DOE/NV/10461--T53

PRELIMINARY

TRAC *Technology and Resource Assessment Corporation*

3800 Arapahoe Avenue, Suite 225
Boulder, Colorado 80303
(303) 443-3700 FAX No. (303) 443-8626

ANNUAL REPORT - NEVADA

Investigations of Natural Groundwater Hazards at the Proposed Yucca Mountain High Level Nuclear Waste Repository

Part A: Geology at Yucca Mountain

Part B: Modeling of Hydro-Tectonic Phenomena Relevant to Yucca Mountain

---

ANNUAL REPORT NO. 1
CONTRACT No. 92/94.0004

ANNUAL REPORT Submitted to the
Nuclear Waste Project Office
State of Nevada

May 1993

Authored by:
J. S. Szymanski
C. M. Schluter
D. E. Livingston
M. R. Somerville
J. B. Davies

ANNUAL REPORT - NEVADA

Investigations of Natural Groundwater Hazards at the Proposed Yucca Mountain High Level Nuclear Waste Repository

---

CONTENTS

Part A: Geology at Yucca Mountain

Part B: Modeling of Hydro-Tectonic Phenomena Relevant to Yucca Mountain

Section I Extension of In-Situ Stress Test Analysis to Fractured Media with Reference to Yucca Mountain Data (J. B. Davies)

Section II Fluid Flows Due to Earthquakes with Reference to Yucca Mountain, Nevada (J. B. Davies)

PART A
Geology at Yucca Mountain

INTRODUCTION

Both advocates and critics disagree on the significance and interpretation of critical geological features which bear on the safety and suitability of Yucca Mountain as a site for the construction of a high-level radioactive waste repository. Critics believe that there is sufficient geological evidence to rule the site unsuitable for further investigation. Some advocates claim that there is insufficient data and that investigations are incomplete, while others claim that the site is free of major obstacles. Regardless what the advocates say, specialists blithely continue to expend hundreds of millions of dollars each year to pursue an incredibly expensive and time-consuming effort to study Yucca Mountain. Little, if any, effort is spent in the DOE program to synthesize and integrate the information that is already available. Such studies as have been done (e.g., U. S. Department of Energy, 1988; Science Applications International Corporation, 1992) have not resulted in the formulation of cost-effective and focused investigations of potentially hazardous conditions at Yucca Mountain.

Some attempts to synthesize and coherently interpret existing data within the DOE have been made (Szymanski, 1987, 1989, and 1992). These attempts have raised serious technical concerns about the suitability of the Yucca Mountain site. The initial attempt was dismissed by the DOE (Dudley et al., 1989) and the latter has not been yet considered. However, some scientists that have reviewed these works agree that the concerns have a valid technical basis (e.g., Archambeau and Price, 1991). Other scientists have examined the earlier attempts and have been provided with the latter efforts, but have dismissed the contents of these reports (NAS/NRC, 1992). These dismissals give evidence of institutional reluctance to consider the possibility that Yucca Mountain is not a site where

safe disposal of high level nuclear waste may be achieved.

It is recognized by those critical of the siting of the proposed repository at Yucca Mountain that their concerns are based on a multitude of site-specific observations and measurements. The principal documentation for these concerns are reports to the management of the U. S. Department of Energy by Szymanski (1989 and 1992) and Archambeau and Price (1991).

During this past year we have expanded our efforts to include both the critical evaluations of existing geological and geochemical data and the collection of field data and samples for the purpose of preparing scientific papers for submittal to scientific journals. Summaries of the reviews of critical evidence are given in the following portions of this report as are the rationales for future efforts. As part of our first annual report we take this opportunity to clarify the technical basis of our concerns and summarize the critical geological field evidence and related information.

GEODYNAMICS

With regard to the suitability of the Yucca Mountain site to accommodate a high level nuclear waste repository, potentially disqualifying conditions arise directly or indirectly from active tectonic processes. The ultimate cause of these processes is terrestrial heat which drives plate tectonics and in some instances, such as in the Basin and Range province, causes rifting of the continental lithosphere. Typically, rifting regions are characterized by a conductive heat flow of 80-120 mW/m^2, about twice the average for stable continental regions. In these geothermal settings transport of heat through the crust, in addition to involving the conductive mechanism, also involves the advective (molten rock) and convective (aqueous and gaseous phases) heat transfer mechanisms. For most of the Basin and Range province the conductive heat flow is typically 80-100mW/m^2; locally, it may be as high as 120mW/m^2 (Sass et al., 1981). Such high flux of thermal energy poses unique problems for repository siting anywhere within the Basin and Range province.

In terms of heat flow the shallow crust at Yucca Mountain represents a small-scale anomaly (less than 10 km in length) of low conductive heat flow (40 mW/m^2) within a local background of 85 mW/m^2 (Sass et al., 1987). Importantly, the Yucca Mountain heat flow anomaly seems to be a transient phenomenon. This is suggested by the fact that the paleogeothermal gradient, reconstructed based on the oxygen isotopic signatures of young calcite/opal-CT/sepiolite veins, is about 34°C/km (Whelan and Stuckless, 1992). This reconstructed gradient is approximately 50 percent higher than the contemporary geothermal gradients measured by Sass et al. (1987). Most of the veins that have been used in paleogeothermal reconstructions carry U/Th ages of <400 ka (Szabo and Kyser, 1985).

Szymanski (1989) pointed out that, similar to the contemporary geothermal field,

the present-day strain and hydrologic field at Yucca Mountain cannot be regarded as a permanent feature. The Yucca Mountain geodynamic system appears as a non-equilibrium dissipative system which, for geologic time spans, fluctuates between high- and low-energy states. This non-equilibrium thermodynamic behavior seems to be facilitated by high-energy flux from the unstable upper mantle.

A small-scale anomaly (less than 20 km in length) in compressional velocity of the crust and upper mantle has been revealed by seismic tomography between western Yucca Mountain and Crater Flat (Evans and Smith, 1992). In the uppermost mantle the compressional velocity is about 2 percent lower than the laterally-averaged background. Because the background velocity itself is representative of a mantle region within which incipient/partial melting occurs, the anomalously low velocities indicate that, beneath western Yucca Mountain and Crater Flat, the degree of mantle melting is greater than elsewhere.

The mantle low-velocity anomaly presumably reflects magma source regions for the Quaternary basaltic cones in Crater Flat and at Lathrop Wells. The latter cone is situated only 15 km away from the proposed repository site and is the youngest of the locally-known magmatic centers in the Yucca Mountain region. Two separate Lathrop Wells lava flows have been dated by Turin and Champion (1991) at 144 ±35 ka and 183 ±21 ka (arithmetic means of $^{40}Ar/^{39}Ar$ ages), and 119 ±11 ka and 141 ±10 ka (combined weighted means of K/Ar and Ar/Ar ages). Wells et al. (1990) inferred that three additional events occurred within the past 20 ka based on soil stratigraphy of eolian sand and silt containing tephra.

In the crust, beneath western Yucca Mountain and Crater Flat, the compressional

velocity is about 1 or 2 percent lower than the laterally-averaged background. The corresponding low-velocity anomaly cannot be uniquely attributed to incipient or partial melting of the crust, however, this anomaly may be regarded as indicating that a degree of mantle-induced heating is greater than elsewhere. This, together with the inferred asymmetry of mantle-induced heating, virtually assures that Yucca Mountain is underlain by a deep-seated geothermal system. In that regard, Sass et al. (1983) state:

> ...heat flow is likely to vary between about 30 and 70 mWm^{-2} (.75 to 1.7 HFU) within the very small area. This in turn suggests very shallow (in the range of 2.5 to 5 km) heat sources and sinks as the cause of the variation. The most likely sources and sinks would be hydrologic... From the present series of measurements, it seems clear that various fluids are moving about in the unsaturated zone, that water is moving in a very complicated manner within the saturated zone to depths on the order of 1 km, and that in the Paleozoic rocks beneath the tuffs, there is also a complex hydrothermal circulation system.

Mantle dynamics have been invoked to explain aberrant crustal strains measured by a large-aperture (60 km E-W, 150 km N-S) array of strain meters operated in the NTS region in 1970-1971 (Smith and Kind, 1972). The southernmost element of the array was located at Yucca Mountain. The array "detected a pulsating strain field that increased over a period of six weeks and decayed over a shorter interval of time" (Smith and Kind, 1972). The maximum regional variation in strain consisted of an extension of 1.3×10^{-5} in a N48°W direction and a compression of 5.8×10^{-6} in the orthogonal direction. Following this episode the rate of strain accumulation abruptly changed polarity. Extension during the strain episode was oriented in the same direction as the axis of minimum compressive stress determined by a variety of methods (Stock et al., 1985). The crustal strain was not associated with either unusual earthquake activity or with known fault displacement. Smith and Kind (1972), therefore, explained the secular strain in terms of crustal response to mantle processes.

Transient crustal deformation is also evidenced by re-leveling surveys along a line from Las Vegas to Tonopah, NV, a line that crosses southern Yucca Mountain and Crater Flat. Data from three surveys, from 1910 to 1984, show 25.5 ± 3.5 cm of subsidence of Crater Flat relative to Yucca Mountain and Bare Mountain in 75 years (Gilmore and Carr, unpublished data, cited by the National Research Council, 1992, p. 106). The subsidence rate, over 3 mm/year, is greater than can have been sustained over the long term.

Long-term strain rates estimated from paleoseismicity are orders of magnitude lower than the transient strain rates determined from geodetic leveling and strain meter data. Of the several Quaternary faults in the Yucca Mountain area, the Windy Wash fault in eastern Crater Flat has the most detailed displacement-chronology. The apparent vertical offset of Pliocene basalts dated at 2.5-3.7 Ma is 40 meters (Ramelli et al., 1991), yielding an apparent vertical slip rate of about .01 mm/year. Four episodes of displacement over the past 270 ka have been documented, the youngest displaced stratum being an eolian silt dated by thermo-luminescence methods at 3.0-6.5 ka, (Whitney et al., 1986). Holocene offset has also been documented on the Solitario Canyon and Black Cone faults using radiocarbon accelerator mass spectrometry methods (Ramelli et al., 1991).

Paleoseismic activity at Yucca Mountain has evidently been accompanied by concurrent rupture of multiple faults and local eruption of basaltic ash. Evidence cited by Ramelli et al. (1991) includes: "the high degree of fault interconnection, similarities in scarp morphology, similarities in ages and amounts of recent offset along multiple faults, and presence of basaltic ash within vertical fractures formed in fault-filling carbonate exposed in trenches across four faults." The four faults cited are the Bow Ridge, Solitario Canyon, Windy Wash, and Fatique Wash faults. Because the ash-filled fissure in the

Windy Wash fault cuts all surficial strata except the youngest, a Holocene silt, the ash probably came from an eruption of the Lathrop Well volcanic center, the youngest basaltic cone in the area. The distributive faulting evidenced at Yucca Mountain has a significant implication as to the maximum earthquake potential. DePolo et al. (1991) documented the distribution of surface ruptures caused by 11 historic earthquakes in the Basin and Range province. All nine events that ruptured multiple geometric or structural segments had magnitudes of 6.8 and greater.

Paleoseismic events at Yucca Mountain have been in the same magnitude range as historic normal-faulting earthquakes in the Basin and Range province that have produced very large outflows of crustal fluids (0.5 km^3 and 0.3 km^3 respectively for the 1959 Hebgen Lake and 1983 Borah Peak events; Wood and King, 1992). For both events, the outflow was equivalent to the earthquake-induced volumetric strain accumulated to a depth of 5 km. The outflow from such an event at Yucca Mountain would appear to be sufficient to inundate the vadose zone, presently 0.5 km deep, or at least flood the proposed repository, 0.3 km deep.

The phenomenon of large outflow from the source regions of normal-faulting events helps to explain the as-yet-poorly-understood hydrologic processes involved in mineralization of the crust in an extensional environment. The observation that Plio-Quaternary alkali-earth zeolitization of the ignimbrites at Yucca Mountain, both within and below the vadose zone, occurs in aureoles around faults and fractures provides strong basis to consider a possible role of tectonism in inducing a variety of fluid flows. Further, the epigenetic zeolitization is distinctly polygenetic, as indicated by geochemical and geochronologic analyses of drillhole cores, and therefore is most likely related to episodic

tectonism (Szymanski, 1992). Likewise, the wide range in ages of vein calcites is indicative of recurrent flow of aqueous solutions through faults and fractures.

To explain the large outflows cited by Wood and King (1992) for major normal-faulting earthquakes, water must be drawn into fractures to a depth of at least 5 km during strain accumulation in the source region. It has been inferred by Szymanski (1989) that the upper crust at Yucca Mountain, south of northernmost drill hole USW G-2, is presently in an advanced stage of strain accumulation. The steep potentiometric gradient, between drill holes G-2 and G-1, marks the northern margin of the pre-seismic strain field. The region between G-2 and G-1 also marks the northern margin of the Yucca Mountain heat-flow anomaly. Deep in the saturated zone of G-2, the conductive heat flow is 71 mW/m^2; elsewhere in the phreatic and vadose zones at Yucca Mountain, it is anomalously-low (Sass et al., 1987). It seems likely that the anomalously-low heat flow and water table are related to the same transient phenomenon.

GEOLOGICAL FIELD RELATIONS AND OBSERVATIONS

Critical geological field observations have been compiled by Szymanski (1992) and also by Hill (1993). This section will summarize the observations, discussions, and conclusions of Szymanski (1992) and discuss how these are variously regarded by advocates and critics of Yucca Mountain.

Volcanism

Of the several elementary geological field observations that can be made at Yucca Mountain, recent volcanism seems to be the one that most readily can be recognized by both trained geologists and others with an appreciation and knowledge of the nuclear regulatory requirements for assuring public and environmental safety. Four partially-eroded volcanoes in Crater Flat, immediately to the west of Yucca Mountain, and one clearly-visible uneroded volcano, the Lathrop Wells cinder cone in southern Yucca Mountain, are all examples of this younger volcanism. Besides these volcanoes there is other, less obvious, evidence of basaltic volcanic activity. This activity is expressed in the existence of basalt flows and fissure vents in southeastern Crater Flat and in a basaltic dike in the upper reaches of Solitario Canyon, immediately adjacent to the western edge of the proposed repository. The ultimate origin of basalt is well understood by geologists: it originates in the mantle of the earth. Basaltic magmas do not necessarily emanate directly from the mantle to the surface, but may reside for a while within the Earth's crust, differentiating and mixing with melted crustal material and then be erupted to the surface later in time.

Reported potassium-argon ages for these five volcanos range from about 120 to

1160 ka. The basaltic flows in southeastern Crater Flat have been dated at about 3.7 Ma and the basaltic dike at about 10 Ma. Both immediately adjacent to and in the larger region surrounding Yucca Mountain, basaltic volcanism has occurred episodically throughout the past 10 million years. The five volcanoes have erupted over Quaternary detritus and thus were erupted within the time span of the direct regulatory concern.

Direct disruption of a repository site by basaltic volcanism and the effects of volcanic eruption on surface facilities, however, are not our greatest concern. We regard basaltic volcanism as direct and unequivocal evidence of deep-seated geologic instability, but more important: What are hydrologic implications of such instability and how do they bear on the future performance of the proposed repository?

Within the context of our involvement with the State of Nevada Nuclear Waste Project Office, we are planning to address these concerns through integration of a two-fold approach. First, we are in a process of examining the local geologic record with the intent of determining whether or not it contains clues to past behavioral patterns of the local hydrologic system (e.g., evidence for post-Timber Mountain alteration and/or mineralization would be of critical importance). Second, we have initiated a numerical simulations program involving a variety of hydro-tectonic interactions. Examples of such interactions are: 1) seismic pumping, 2) gas-assisted seismic pumping, 3) influence of in-situ stresses on fracture aperture and hydraulic conductivity, and 4) intermittent fluid convection in a deforming, fractured medium. Throughout this program we hope to achieve quantitative insight into processes that may have been operating at Yucca Mountain. This understanding, in turn, may be used to help understand the geologic record at Yucca Mountain.

Faulting

Younger faulting has also occurred at Yucca Mountain. Many scientists do not consider faulting important to long-term disposal of high-level radioactive waste (NAS/NRC, 1992; DOE, 1988; SAIC, 1992); others deny its youthfulness (Evernden, 1992).

Major Quaternary faulting has been amply documented at Yucca Mountain (Ramelli et al., 1991). The spectacular Solitario Canyon fault is located adjacent to the western edge of the proposed repository immediately to the west of the ridge line of Yucca Mountain and has documented Quaternary displacement (Scott and Bonk, 1984). Several other faults with documented Quaternary displacement also exist in Crater Flat as well as on the east side of Yucca Mountain (Ramelli et al., 1991).

The local "capable" faults are the subject of on-going studies by scientists working for the U. S. DOE, Yucca Mountain Project. Most of their efforts seem to be directed toward evaluating the impact of fault-induced vibratory ground motion on surface facilities and integrity of underground openings. Again, even though vibratory ground motion is an important aspect of assuring public and environmental safety, our major concern is of a different nature. Specifically, our interest lies in understanding the impact of local faulting on the stability of the shallow hydrosphere, as well as on the stability of the underlying and deep-seated geothermal system. The importance of this subject is not appreciated by many scientists: A prime example of this is the National Academy of Sciences' (1992) report "Groundwater at Yucca Mountain: How High Can It Rise?" in which this important issue is dismissed.

Brecciation

Brecciation along locally-mapped faults is readily apparent at Yucca Mountain. A particularly noteworthy type of brecciation are the so-called "mosaic breccias." In a hand specimen mosaic breccias consist of angular to subrounded, tuffaceous fragments embedded in a matrix of calcite and opal. Mosaic breccias are characterized by: 1) their matrix-supported texture (i.e., individual breccia clasts are not touching); 2) very-large, volumetric strain (dilation) ranging from several percent to tens of percent; and 3) the isotropy of the volumetric strain (i.e., the amount of dilation is comparable in all three mutually perpendicular directions).

Based on textural and compositional characteristics, mosaic breccias are of two distinct varieties: 1) the so-called crushed-tuff-matrix (CTM) breccias, consisting of bedrock clasts in a matrix of finely-crushed bedrock and containing little authigenic cement, and 2) the so-called authigenic-mineral-cemented (AMC) breccias, consisting of very little finely-crushed bedrock and containing matrix material composed almost entirely of authigenic cement (Levy and Naeser, 1991). The CTM breccias contain no plant remains, whereas the AMC breccias contain abundant root casts.

Less commonly observed are occurrences of breccia in soft, unwelded tuffs. Such breccias are typically developed as discontinuous dikes up to 0.3 m thick. They are particularly numerous and well-developed along the eastern flank of Harper Valley. In all of the observed cases, the breccia dikes are of GS-texture and contain allogenic and polymictic clasts. For some breccia dikes compositional clasts are well rounded; for other dikes, however, these clasts are angular. Breccia dike cement consists mainly of opaline silica with lesser micritic calcite. A remarkable feature of these breccia dikes are their

length/width ratio. In one instance, the observed length/width ratio is as small as 5.

A number of observations have been made on the mosaic breccias and breccia dikes and these provide clues as to the origin of the brecciation. Mosaic breccias and breccia dikes occur in both Tertiary pyroclastic rock and in Paleozoic carbonate rock so evidently the eruptive emplacement of pyroclastics, including their cooling and solidification, was not necessarily a factor involved in the formation of all of these breccias. In light of this remark, these breccias appear to be epigenetic rather than auto-breccias (i.e., formed syn-depositionally with the host tuffs); they do not appear to have formed by shear fragmentation associated with ordinary fault-slip because they lack shear fabric; and as previously discussed, they: 1) occur as irregular pods and discontinuous dikes, 2) exhibit very-large volumetric strain that in places ranges from several percent to tens of percent; and 3) as a rule they exhibit a volumetric strain that is remarkably isotropic. Since the Yucca Mountain breccias do not appear to be syn-depositional or shear-fragmentation in origin, then they must be either "denudation" breccias (i.e., formed through in-filling of independently formed bedrock openings by erosionally-derived clasts) or "explosion" breccias (i.e., produced as the result of a large and rapid build-up of fluid/gas pressure).

The true genesis of the Yucca Mountain breccias is suggested by the studies of Levy and Naeser (1991) who found that the AMC breccias (from both Trench 14 and Busted Butte) contain fragments of zircon crystals incorporated in authigenic cements. The separated zircons yielded a wide spectrum of fission-track ages, from 59.7 Ma to as little as 4.8 Ma. Such a wide spectrum indicates that the enclosed zircons originated either from distinct igneous sources or from a differentially-heated source or sources. Significantly, for the two breccia specimens examined, fission-track ages are significantly older and

significantly younger than the K/Ar ages of the host tuffs. The Tiva Canyon member and the Topopah Spring member of the Paintbrush Tuff are 13 and 13.5 Ma, respectively (K/Ar dating method).

From the above discussion it is reasonable to conclude that: 1) the age of formation of some of the AMC breccias postdates both the deuteric alteration of the tuffs and hydrothermal stages of the Timber Mountain Caldera, and 2) at and/or near Yucca Mountain there is a source of fairly young zircons, either juvenile or thermally-reset. It is worth noting that the fission track age of a zircon specimen reflects its so-called "cooling age;" i.e., the time elapsed since the temperature of the specimen dropped below the annealing temperature. The annealing temperature for zircons is as high as 240° ±50°C (Hurford, 1986; Harrison et al., 1979), which fact obviously leads to another important conclusion: at and/or near Yucca Mountain there are rhyolites which were either erupted or became hydrothermally-altered after the late stages of magmatic and hydrothermal activity of the Timber Mountain Caldera.

The fission track ages of zircons embedded in the AMC breccia cements were, however, interpreted differently by the NAS/NRC Panel on Coupled Hydrologic/Tectonic/ Hydrothermal Systems. The Panel (p. 44) stated that:

> ...within the analytical uncertainty, most of the ages are about 10-12 Ma, or about the same as those of the dominant volcanic rocks in the region.

However, the primary authors (Levy and Naeser, 1991) of the work stated that:

> ...there are zircons from multiple sources present. In both samples there are crystals significantly younger and significantly older than the age of the tuff.

Examination of the fission track data shows a multiply-peaked distribution of ages in each breccia sample and that the youngest age is 4.8 Ma. In addition, the 90 percent confidence interval for this age is from 2.3 to 7.3 Ma. Finally, the majority of the twenty-

four most probable ages are actually significantly younger than the age of the host tuffs, which is given by K/Ar dating as 13 Ma. Therefore, contrary to the Panel's description of the fission track data, most of the ages are much younger than the host ignimbrites and provide evidence that hydrothermal activity has occurred at much more recent times than considered by the Panel.

Calcite-Silica Mineralization

Calcite and opal are widely distributed around Yucca Mountain as calcrete and vein material (Szymanski, 1992; Hill, 1993). "Calcrete," as used in this report, is a deposit of calcite and/or silica travertine that is either conformable with a topographic surface (sheet travertine) or which occurs as strata-like (strataform) bodies of greater lateral than vertical extent. Notable localities of calcite/opal calcrete deposits, in the eastern parts of Yucca Mountain, are at Trench-14 and on both the west and east flanks of Busted Butte. Other occurrences are in western Crater Flat near the base of Bare Mountain, in several trenches in eastern Crater Flat, near the mouth of Solitario Canyon west of Yucca Mountain, and in the southern portions of Yucca Mountain, along the trace of the Stagecoach Road fault. The abundance of calcite/opal varies within and among the different exposures. Where calcite and opal completely fill the interstices, the clasts may be either grain-supported (each clast touches its neighbor clasts), or matrix supported (the clasts are totally separated from one another and are "floating"). The calcite/opal cement matrix may amount to as much as 90 percent or more of the volume of the deposit.

Calcite/opal veins are also ubiquitous around Yucca Mountain. These veins range from a few millimeters in thickness to about 1 meter. They occur in all of the stratigraphic

units of the region (including the Ammonia Tanks member of the Timber Mountain Tuff and overlying unconsolidated Quaternary deposits) and in all of the lithologic rock types (including welded and unwelded ignimbrites). Two varieties of veins may be readily distinguished in hand-specimen: an older variety and a younger variety.

The older variety consists of clearly-hydrothermal veins and impregnations. Such veins are composed of calcite and multi-colored opals and typically are accompanied by narrow alteration aureoles. While a hydrothermal origin for these veins is not in dispute, the appropriate question is: Do these veins represent deuteric mineralization (i.e., formed in association with the cooling, syn-depositional devitrification and solidification of the tuffs) or do they represent subsequent epigenetic mineralization? Another critically important question is: Are we reasonably certain that all of these hydrothermal veins are attributable to hydrothermal stages of activity of the Timber Mountain Caldera?

The younger variety of veins consists of white, micritic calcites intercalated with dense, buff-colored, opaline silica. These veins range in thickness from a few centimeters to about 1 meter. They occur in all of the stratigraphic units of the region and also in the sand ramps of Busted Butte. Importantly, the Busted Butte sand ramps occur above the Bishop Ash, so it is known that at least some of these calcite-opaline silica veins are younger than the ~700 ka age of the Bishop Ash. Compositionally, texturally, and spatially, the younger veins are similar to, and associated with, the calcite/opal calcretes and this suggests that both deposits may have precipitated from common solutions. The results of extensive uranium, strontium, oxygen, and carbon isotopic investigations, as performed by the USGS investigators over the last seven years, confirm that such is indeed the case.

A number of U-series age determinations have been performed on the calcite/opal calcretes and veins. This data has been examined by Szymanski (1992) and the primary sources for these data are referenced in his report. The U-series ages for veins and calcretes seem to fall into four discrete groups: 1) ~30 ka, 2) ~75 ka, 3) ~170 ka, and 4) ~280 ka. The youngest episode of mineralization (30 ka) includes surface calcretes as well as veins from a depth of more than 300 meters. The second youngest episode (75 ka) includes calcretes and the two oldest episodes are represented in the subsurface by veins occurring as deep as 600 meters.

Compositionally and texturally the micritic veins and associated calcretes are equivalent to the authigenic cements of the AMC breccias. Furthermore, Whelan and Stuckless (1990) showed that the isotopic character of carbon and oxygen incorporated in the breccia cements is equivalent to that incorporated in the calcretes and veins. Clearly, a single paragenetic assemblage is evident: the breccia cements, micritic veins, and calcretes all precipitated from similar parent fluids.

Many of the breccia cements, calcretes, and surficial micritic veins contain root casts (rhizomorphs). These root casts indicate that, at Yucca Mountain, the surficial calcites and opals formed at or near the topographic surface.

The origin of the calcite-silica mineralization at Yucca Mountain has been the subject of much debate. Essentially there is the "pedogenic-supergene" model of origin and the "hypogene" model of origin. However, these terms have been uncorrectly used and misunderstood. Among the Yucca Mountain Project investigators, it is commonly understood, or implied, that fluids responsible for pedogenic accumulations of calcretes and/or silcretes are necessarily supergene fluids, or infiltrating rainwater. In other words,

for these fluids, the intra-formation residence time in either soil or surficial bedrock is very short, and the depth of their infiltration is very small, no more than a few meters. Such understanding, however, is erroneous. Secondary carbonate and opal may accumulate through a variety of processes to form either calcic-silicic soils or other deposits that resemble such soils (e.g., Goudie, 1973 and Machette, 1985).

Properly understood, "pedogenic" accumulations of carbonate and/or silica are the result of deposition at the topographic surface disposition (through evaporation, evapo-transpiration, run-off, and/or infiltration) of meteoric fluids regardless of their intraformational residence times and histories. These fluids do not have to be supergene; they may also be hypogene. For example, in many arid and semi-arid regions, calcretes and silcretes are commonly regarded as having formed by upward movement of calcium- or silica-rich fluids from the water table via capillary or by other mechanisms, and then by ongoing chemical, biochemical, or evaporative mineral precipitation. Examples of such pedogenic mineral accumulations are common throughout the world (e.g., Summerfield, 1983 and Carlisle, 1983).

In the case of the calcite-silica mineral assemblage the issue is not whether this assemblage is "pedogenic." Rather, the issue is: Are the fluids responsible for this assemblage, hypogene or supergene?

In the supergene model, calcium and/or silica, either introduced at the topographic surface by rainfall and airborne dust or released as the result of various weathering processes, are dissolved in upper soil horizons, transported through these horizons, and then precipitated at depth. In contrast, the hypogene model relies on subsurface fluids, typically deep-seated. For such deep-seated fluids, dissolved calcium and/or silica is derived through leaching of rocks through which the fluids have moved. Precipitation of

calcium carbonate and opaline silica is then the result of a combination of several factors, such as evaporation and/or evapo-transpiration, reduction in fluid temperature, reduction in CO_2 partial pressure, and/or a change in fluid pH.

Critics and advocates of Yucca Mountain being the potential site of a high-level nuclear waste repository are sharply divided as to the character of the fluids out of which the breccia cement-vein-calcrete paragenetic assemblages precipitated. Of course, the advocates maintain that the supergene-pedogenic model applies. In contrast, the critics keep insisting that, in view of the geodynamic setting of Yucca Mountain, the hypogene alternative needs to be seriously considered. Far from being an esoteric concern, the ultimate outcome of the hypogene-supergene debate will determine the future use of Yucca Mountain as the site for the permanent disposal of high-level nuclear waste.

METASOMATISM

As our contribution to a satisfactory resolution of the supergene-hypogene dilemma, we have developed, and have begun pursuing, a promising approach. There are two aspects to this approach, namely: 1) broadening the scope of the controversial paragenetic assemblage, and 2) strengthening genetic linkages between individual elements of this assemblage.

To gain a reliable genetic reference it is necessary to broaden the controversial breccia cement-vein-calcrete assemblage to include an affiliated element whose origin (supergene or hypogene) may be unequivocally established. We believe that this element is the alkaline earth metasomatism of the local alkalic tuffs. Undoubtably, this metasomatism reflects either the ascent or descent of parent fluids for the controversial assemblage. It can be reasonably expected that various characteristics of the corresponding alteration products contain a key to knowing with certainty the operational mode (ascent or descent) of these fluids. In this regard, particularly promising are the following lines of inquiry: 1) spatial distribution of the alteration products; 2) volume of the affected tuffs, and geochemical mass balance calculations; 3) geochemical characteristics of the alteration products such as HREE abundances relative to LREE, relative abundance of ^{87}Sr, trace element concentrations, etc.; 4) mineralogic characteristics of the alteration products (i.e., presence of calcic zeolites such as heulandite, erionite, stellerite, laumontite, etc.); and 5) geochronologic characteristics of the alteration products, mainly K/Ar ages of the calcic zeolites.

It is also necessary to further strengthen the genetic linkage between the reference element (metasomatism) and the controversial elements (breccia cement, vein, and

calcrete). Although this linkage is already sufficiently strong, we believe that it is prudent to implement three lines of inquiry: 1) the REE signature (chondrite-normalized abundance pattern) for each of the elements of the metasomatic assemblage; 2) the isotopic character of strontium incorporated in the alkaline earth alteration products; and 3) the isotopic character of carbon incorporated in both the calcic zeolites and the metasomatically-altered whole rock.

Within the context of the adopted approach the chemical alteration of the tuffs is fundamental to the interpretation of the events that have transpired at Yucca Mountain. To this end we have begun to examine rigorously and in detail, using the already available and extensive geochemical data, the character of the altered tuffs. Two preliminary reports have been prepared, (Livingston, 1992 and 1993). The first was presented to the Las Vegas sub-section of the Association of Engineering Geologists, and later became a part of the third quarterly report submitted by TRAC to the Nuclear Waste Project Office. The second was submitted as the TRAC's fourth quarterly report.

During initial stages of our review of the major-element geochemistry, we have noted that, at Yucca Mountain, most of the whole rock samples are different from glass in their chemistry which argues that most of the tuffs have been altered. This alteration has caused a decrease in the abundance of silica, soda, and potash and an increase in the abundance of lime and magnesia of the altered rocks.

Recognizing the chemical alteration of the tuffs, Broxton et al. (1986) state:

> Zeolitic tuffs at Yucca Mountain formed by diagenetic alteration of rhyolitic vitric tuffs. Despite their similar starting compositions, these tuffs developed compositions that vary both vertically and laterally. Widespread chemical variations were the result of open-system chemical diagenesis in which chemical components of the tuffs were mobilized and redistributed by groundwaters. Alkalies, alkaline earths, and silica were the most mobile elements during

diagenesis.

This statement contains the terms "diagenetic alteration" and "diagenesis." In the context of the known history of the Yucca Mountain site, however, the term "diagenetic alteration" is inappropriate and misleading. At this site the process of diagenetic alteration was completed upon the solidification and compaction of the volcanic glass and upon the completion of isochemical devitrification of the welded tuffs. Any chemical alteration must be regarded as both epigenetic and metasomatic with respect to these processes. This is so because: 1) the chemical solutions which bring about the chemical change must have acquired their chemical character from sources other than the rocks which are being changed in their chemical composition and hence the alteration process must be regarded as metasomatic in character, and 2) these changes must have occurred after the solidification and devitrification of the tuffs, and hence the alteration is epigenetic in nature.

During the course of our review we have confirmed the previous conclusion of Broxton et al. (1986) that the initial chemical composition of the tuffs is best represented by the present-day chemical compositions of volcanic glass (112 analyses). By comparing these compositions with Broxton et al.'s results of 63 whole rock and 436 clinoptilolite chemical analyses we have learned that several chemically-diverse solutions have caused the epigenetic alteration of the tuffs. Two major types of alteration haye occurred, one of which is alkali-rich and calcic-poor and the other of which is calcic-rich and alkali-poor. Two end members of the alkali-rich alteration can be recognized, one of which is potash-rich and soda-poor and the other of which is soda-rich and potash-poor. The chemical compositions of clinoptilolites display three modes in the population distribution. All three

modes, however, are greater in calcium concentrations than the glass. This indicates that several fluids of diverse chemical character caused the alkaline earth metasomatism. As such, it seems unlikely that this metasomatism occurred at the same time, and it must be presumed that the alteration is polygenetic.

We also have examined the mineralogy (Bish and Chipera, 1989), clinoptilolite chemistry (Broxton et al., 1986), and potassium argon ages (WoldeGabriel, 1991) for borehole USW G-1 (Livingston, 1992). With regard to the mineralogy, we recognized the zoning with depth of the silica phases (quartz, tridymite, and cristobalite; in order of decreasing crystal chemical ordering) noted by Bish and Chipera (1989). This zoning shows decreasing abundances of cristobalite and tridymite relative to quartz in deeper levels of the welded devitrified zones. We also recognized the zoning of the zeolites with the relative order and increasing depth: clinoptilolite, mordenite, and analcime, as was noted by the original authors. In addition, we recognized a zone within the densely-welded devitrified Topopah Spring member (about 900 to 1,000 feet deep) that has an association of calcite with low abundances of cristobalite and tridymite relative to an increased abundance of quartz. No doubt this represents a localized alteration event that is epigenetic with respect to the lithification of the ignimbrites. Another possible epigenetic event occurred in the older tuffs (about 5400 to 5700 feet deep) and is represented by the occurrence of clinoptilolite and mordenite within a zone (below about 4000 feet) that is otherwise dominated by analcime as the major alteration phase. These two observations are regarded as supportive of the earlier inferred polygenetic character of the alteration at Yucca Mountain. In addition, these observations indicate that the over-printing alteration events are spatially discrete, such as would be expected for altering solutions sporadically

invading the bedrock along faults and fractures.

Regarding the clinoptilolite chemistry in borehole USW G-1, the single analysis from the Topopah Spring member (1286 feet) is very high in lime and very low in magnesia, soda, and potash, while but 50 feet deeper in the tuffaceous beds of Calico Hills, clinoptilolites are high in soda and potash and low in both lime and magnesia. Deeper in the section, clinoptilolites from the flow breccia (between 3500 and 4000 feet) are high in soda and low in lime, magnesia, and potash. Thus, it is confirmed that clinoptilolites are both chemically and spatially diverse with a strong possibility of being chronologically distinct.

Our review of the potassium-argon data from borehole USW G-1 (WoldeGabriel, 1991) leads us to interesting possibilities with regard to the age of the zeolitic alteration. The reported apparent ages of clinoptilolites are: 1) 10.62 Ma for the Bull Frog member (3288.5 feet), 2) 6.95 Ma (2190.8 feet) and 5.39 Ma (1819 feet) for the Prow Pass member of the Crater Flat Tuff, and 3) 2.23 and 1.99 Ma (2 analyses) for the Calico Hills formation (1561 feet). WoldeGabriel (1991) also reported potassium-argon ages of 14.94 and 15.88 Ma for illite/smectite (3940 feet). Interestingly, Bish (1989) reports a potassium-argon age for illite/smectite (5637 feet) of 10.9 Ma. This age is nearly identical to the oldest zeolite age and occurs at the same depth as the anomalous occurrence of clinoptilolite and mordenite, deep within the analcime zone. Because the oldest zeolite ages agree with the youngest illite/smectite ages, we believe that the zeolitic phases may be equally as good for geochronologic purposes as the illite/smectite phases. Zeolites have not usually been used in geochronologic studies and firm conclusions must await further results and testing. At face value, however, these apparent ages tend to confirm our earlier conclusions that the metasomatism is epigenetic, polygenetic, and may have continued episodically over an

extended period of time.

All together, WoldeGabriel (1991) reported the results of twenty two analyses of samples of clinoptilolite from six boreholes. Corresponding samples were taken from: 1) the Topopah Spring member of the Paintbrush Tuff (one sample), 2) the Calico Hills formation (5 samples), and 3) the three members of the Crater Flat Tuff (11 samples). The clinoptilolite samples from the 13.5 Ma old Crater Flat Tuff range in apparent age from 10.50 to about 2.47 Ma, and the 13.1 Ma old Topopah Spring member of the Paintbrush Tuff contains clinoptilolites with an age of 4.22 ±0.13 Ma. The results indicate that the clinoptilolites were formed, or their ages altered, over a long period of time. The geochronological significance of these results is in need of further scrutiny. The oldest zeolite ages, about 10 Ma, are very similar to the illite/smectite ages reported by Bish (1989) and Aronson and Bish (1987). The latter ~11 Ma ages are younger than the ~15 Ma illite/smectite ages reported by WoldeGabriel (1991). The older ages represent a pre-Paintbrush argillization of the Lithic Ridge Tuff, and the younger corresponding ages may represent argillic over-printing caused by the Timber Mountain hydrothermal episode.

In summary, a review of major element geochemistry, as undertaken by Livingston (1992 and 1993), leads to the following three conclusions. First, the tuffs of Yucca Mountain contain abundant evidence of having experienced alkaline-earth, zeolitic alteration. With respect to the deuteric solidification and devitrification, this alteration is both metasomatic and epigenetic. Second, the apparent K/Ar ages of epigenetic clinoptilolites range from about 10.5 Ma to as little as 2.0 Ma. This wide spectrum of the radiometric ages suggests that the alkaline earth metasomatism is polygenetic and may have been developed episodically and over an extended period of time. Third, the alkaline-

earth metasomatism contains a key to the satisfactory understanding of long-term behavior patterns of the Yucca Mountain hydro-tectonic system. In this regard, the enigmatic metasomatism may be telling us that the accepted hydrologic conventions are inappropriate. Is it possible that, responding to a variety of tectonic processes and disturbances, this hydro-tectonic system has exhibited erratic and diverse behavior during the past, including discharge of upwelling fluids at the topographic surface?

ISOTOPE GEOCHEMISTRY

As their contribution to resolving the supergene-hypogene dilemma at Yucca Mountain, USGS scientists have demonstrated that the isotopic characteristics of uranium, carbon, strontium, and oxygen, inferred to have been incorporated and/or dissolved in parent fluids of the calcite-silica deposits, differ from those contained in contemporary fluids immediately below the water table (representative fluid-sampling depth is about 1.0 km; e.g., Stuckless et al., 1991; Evernden, 1992). Many scientists, including the NAS/NRC Panel, have regarded these isotopic discords as negating the hypogene origin of the micritic veins, isotopically-equivalent calcretes, and authigenic breccia cements. These same scientists have therefore concluded that the controversial paragenetic assemblage must be of supergene-pedogenic origin.

Although we accept the noted isotopic discords without reservation, we strongly disagree with the conclusions drawn by the USGS and NAS/NRC scientists. To begin with, we note that to reach their conclusion, it is essential to introduce an important assumption or premise. This assumption is: during the last 1-2 million years the isotopic characteristics (i.e., $^{234}U/^{238}U$, $\delta^{13}C$, $^{87}Sr/^{86}Sr$, and $\delta^{18}O$ ratios) of the Yucca Mountain crustal fluids were both time- and depth-invariant and, consequently, parent fluids for any hypogene deposits should have been isotopically similar to those currently observed within 0.5-1.5 km of the topographic surface. For this assumption to be true a multitude of factors which control the isotopic characteristics of shallow crustal fluids (i.e., fluid circulation depth, fluid fluxes, conditions of isotopic exchange reactions, etc.) must have remained time- and space-invariant during the last 1-2 million-year time span. Such geochemical tranquility, however, may only be associated with a hydrologic system for which both the

hydraulic conductivity structure and the boundary conditions are time-invariant. In other words, this hypothetical hydrological system behaves as an unperturbed equilibrium or linear dynamic system. For the Yucca Mountain hydrologic system, however, the principal issue that is being addressed, using the isotopic data, is whether or not the above attributes are indeed present (Szymanski, 1989). The assumption that the major premise is true is equivalent to both the hydraulic conductivity structure and the boundary conditions remaining time-invariant and, consequently, the corresponding position of the water table must have also remained time-invariant. Because it does not make sense to investigate a changing water table by assuming that it remains time-invariant, we are left with little choice but to reject the USGS/NAS conclusions and their approach.

Although sceptical of the approach pursued by the advocates, we remain convinced that the isotopic geochemistry of the controversial paragenetic assemblage is fundamental to the interpretation of the events that have transpired at Yucca Mountain. To this end we have begun to rigorously examine, the already-available and extensive isotopic data. This data pertains to: 1) the micritic veins, 2) the affiliated calcretes and breccia cements, and 3) the products of alkaline-earth metasomatism. In this regard, a preliminary report is in preparation and will be submitted to the Nuclear Waste Project Office as part of a forthcoming quarterly report. A condensed summary of this report is given in the following portions of this annual report.

Isotopes Of Uranium

General

The isotopic character of uranium incorporated in various calcareous deposits, both at Yucca Mountain and from the larger surrounding area, are well known based on the results of such studies as those of Szabo et al. (1981), Szabo and O'Malley (1986), Szabo and Kyser (1985), and Winograd et al. (1985). Two important data sets have been developed, namely: 1) the U/Th ages of the micritic veins and the affiliated calcretes, and 2) the present-day values of the $^{234}U/^{238}U$ ratio for both the controversial calcite-silica deposits and calcitic veins whose hypogene origin in known with certainty. The latter veins are referred to as "travertine" veins, and occur in the Amargosa Desert, Nevada, region (including Devil's Hole), and also around Travertine Point, California.

With specific regard to the supergene-hypogene controversy, the uranium isotopic data is important because it may be used to test the following hypothesis: If the controversial calcite-silica deposits are of hypogene origin, then it should be expected that: 1) the isotopic character of uranium incorporated in these deposits is similar to that incorporated in appropriate hypogene analogs, and 2) the U/Th chronology of the precipitation of these deposits should be correlative with the chronology of local tectonic and magmatic activity. The subsequent two sections present the relevant data and a discussion of how they relate to the set-forth hypothesis.

Values of the $^{234}U/^{238}U$ Ratio

As shown in Figure 1, the isotopic character of uranium incorporated in the micritic veins and the affiliated calcretes is characterized by values of the $^{234}U/^{238}U$ ratio ranging from 1.0 to seldom more than 1.5. Based on this observation, what may be inferred with regard to the origin (supergene-pedogenic or hypogene) of these deposits? In arriving at the desired inference, there are two approaches that may be followed.

One approach is to try to obtain an estimate of value of the $^{234}U/^{238}U$ ratio for the parent fluids of the controversial deposits. This is feasible, but only for a deposit behaving as a closed system. For a deposit submerged in a fluid saturated with respect to $CaCO_3$, the assumption of closed system behavior seems appropriate. In this setting vulnerable ^{234}U atoms, which are contained in a previously precipitated part of a travertine vein, are shielded by continuous precipitation of $CaCO_3$. In the vadose zone, however, the circumstances are markedly different. In this setting radiogenic ^{234}U atoms are not armored by ongoing deposition of calcium carbonate and are exposed to leaching by rainwater. Intermittent flushing by infiltrating rainwater may lead to preferential removal of some ^{234}U atoms, resulting in the lowering of the actual value of the $^{234}U/^{238}U$ ratio. This may occur because, relative to parent ^{238}U atoms, radiogenic ^{234}U atoms are more vulnerable to leaching. This relative vulnerability is a consequence of the $^{238}U \rightarrow {}^{234}U$, which involves alpha particle emission (Osmond and Cowart, 1982). The ejection of alpha particles has the effect of damaging the crystal lattice around the parent ^{238}U atom. The resulting daughter nuclide ^{234}U occupies the radiation-damaged site which, consequently, is more susecptible to chemical leaching.

Even in the case of a deposit that demonstrates the desired closed system behavior, knowledge regarding the isotopic character of uranium dissolved in the parent fluid is still of questionable value. This is particularly true for low values of $^{234}U/^{238}U$. Such low values are characteristic of both supergene infiltrating fluids and upwelling hypogene fluids (Osmond and Cowart, 1982).

Another approach is to isotopically compare the controversial deposits with a reference deposit of known hypogene origin. With regard to the deposits at Yucca Mountain, the desired comparative analyses may be performed using as a reference the hypogene deposits (travertine veins) from Devil's Hole (DH), Amargosa Basin, and Furnace Creek Wash. These deposits are of particular importance because they are known to occur both in the vadose zone and below the water table.

The isotopic comparative analyses of the controversial deposits are shown in Figures 1 and 2. From these figures it may be observed that, with respect to the isotopes of uranium, the vadose zone calcites (both the controversial deposits and the unquestionable hypogene deposits) exhibit the expected open system behavior. This is indicated by two independent lines of evidence. First, for a few samples of the controversial deposits, the present-day values of the $^{230}Th/^{234}U$ ratio exceed asymptotic secular equilibrium values (Figure 2a). Such abnormally high ratios indicate that some vulnerable ^{234}U atoms were selectively mobilized. Second, in the case of hypogene veins from the vadose zone, the present-day values of the $^{234}U/^{238}U$ ratio are consistently lower than the corresponding values from the phreatic zone (Figure 2b). The discrepancy, in the relative concentrations of vulnerable ^{234}U atoms, can be attributed to the leaching influences of rainwater and the resulting open system behavior of the vadose zone veins.

From Figures 1 and 2b, it may be further observed that the present-day values of the $^{234}U/^{238}U$ ratio, from the controversial veins and calcites, are indistinguishable from those of the travertine veins at Furnace Creek Wash. At both localities, however, the calcite deposits yield consistently lower values of $^{234}U/^{238}U$ ratio than those of the submerged Devil's Hole vein. In light of this observation, the isotopic incompatibility noted by Stuckless et al. (1991), between the isotopic characters of uranium incorporated in the DH-2 deposit and in the controversial deposits at Yucca Mountain reveals its true nature. Rather than indicating the supergene-pedogenic origin of the controversial deposits, the incompatibility most likely indicates the open system behavior of these deposits. In contrast to the conclusions drawn by the NAS/NRC Panel, therefore, the $^{234}U/^{238}U$ ratios may not be used to rule out the hypogene origin of the Yucca Mountain veins and calcretes.

Apparent U/Th Ages

The results of the U/Th age analyses reveal that the controversial veins and calcretes were developed in association with at least five discrete episodes at Yucca Mountain. As

shown in Figure 3, the mean apparent U/Th ages of these episodes are 30 ka, 75 ka, 170 ka, 280 ka, and more than 400 ka. At and near the topographic surface, only four generations of the controversial deposits are evident. The development of the fifth generation (mean U/Th age of 170 ka) appears to have been restricted to the lower regions of the contemporary vadose zone.

Given the inferred open system behavior of the vadose zone calcites, one may be tempted to reject the U/Th ages of the controversial veins and calcretes as completely erroneous and/or irrelevant. However, this is not necessarily the case because selective mobilization of some ^{234}U atoms has the effect of diminishing the $^{234}U/^{238}U$ ratio while, at the same time, enhancing the $^{230}Th/^{234}U$ ratio. In other words, the partial mobilization of ^{234}U atoms renders U/Th ages positively biased, or too old. This effect is clearly illustrated by the results of ^{14}C and U/Th geochronological studies performed by Schlesinger (1985). These results show that, for coexisting carbonates from the Eagle Mountain area of Mojave Desert, the U/Th ages are consistently older than the corresponding ^{14}C ages. The observed discrepancies, however, are not alarmingly great. For ~20 ka-old carbonates, they amount to about 30 percent. Given that, in the case of the controversial Yucca Mountain deposits, equally substantial error bars accompany the apparent U/Th ages and potential errors of even several tens of percent do not justify complete rejection of these ages.

With regard to the reliability of the U/Th ages, it is worth noting that, at Yucca Mountain, both the direct field observations and the U/Th ages provide analogous histories for the deposition of the local calcretes. At Busted Butte, three distinct depositional episodes can be seen; near the base of, within, and above the local sand ramps (Hill, 1993). Although the youngest age limit for the formation of these sand ramps is unknown, we are reasonably certain that the sand ramps are younger than the underlying Bishop Ash (~700 ka). The U/Th ages of the controversial veins and calcretes reveal four generations of these deposits (30 ka, 75 ka, 170 ka, and 280 ka), subsequent to the deposition of Bishop Ash. However, only three episodes are evident at and near the topographic surface; the fourth

episode (170 ka) is evident only in the lower region of the vadose zone. Agreement in the number (3) of depositional episodes of the local calcretes, from the direct field observations and the U/Th data, suggests that a correlation may exist, but absolute dating of the travertine at Busted Butte (now under way) is needed before this speculation is confirmed.

Also with regard to the supergene-hypogene controversy, it is important to note that the results of radiometric dating of igneous rock/activity and the precipitation of the calcite-silica deposits strongly suggest that the chronologies of both processes are correlative in number of episodes and timings of individual episodes. As shown in Figure 4, average K/Ar and $^{40}Ar/^{39}Ar$ laser fusion ages for samples of local basaltic flows and cinders are in fairly satisfactory agreement with average U/Th ages of the micritic veins and the affiliated calcretes. All five of the recognized igneous episodes of the past one million years seem to have been accompanied by contemporaneous episodes of the precipitation of the controversial calcite-silica deposits. This observation provides additional support for the hypogene hypothesis.

Conclusions

In summary, based on the U-series isotopic data alone, support for the supergene-pedogenic origin of the controversial veins and calcretes, as advocated by the NAS/NRC and USGS scientists, cannot be confirmed. Far from proving such origin, the U-series data instead may be interpreted as favoring a hypogene model. The fact that the development of the deposits seems to be synchronous with the episodes of igneous activity is particularly noteworthy. For both of these processes (igneous activity and calcite-silica mineralization), the cause-effect relationship is well established. Further support for the hypogene origin of the controversial calcite-silica deposits is suggested by the correspondence of the $^{234}U/^{238}U$ ratios from these deposits with the corresponding ratios from the travertine veins of Furnace Creek Wash.

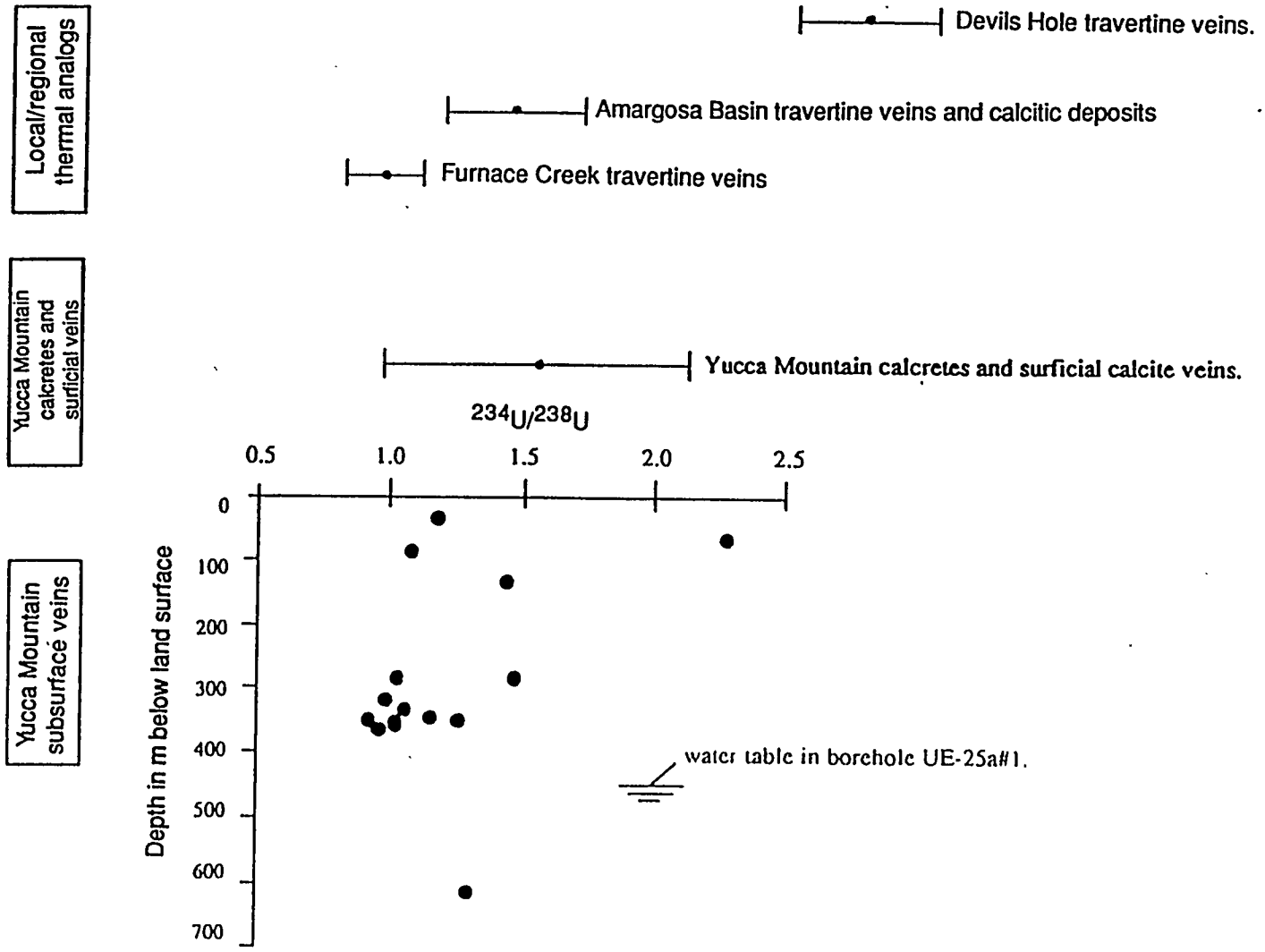

Figure 1. Isotopic character of uranium incorporated in the Yucca Mountain veins and calcretes and the local travertine veins and associated surficial deposits. Isotopic data from Szabo et al. (1981); Szabo and O'Malley (1985); and Szabo and Kyser (1985).

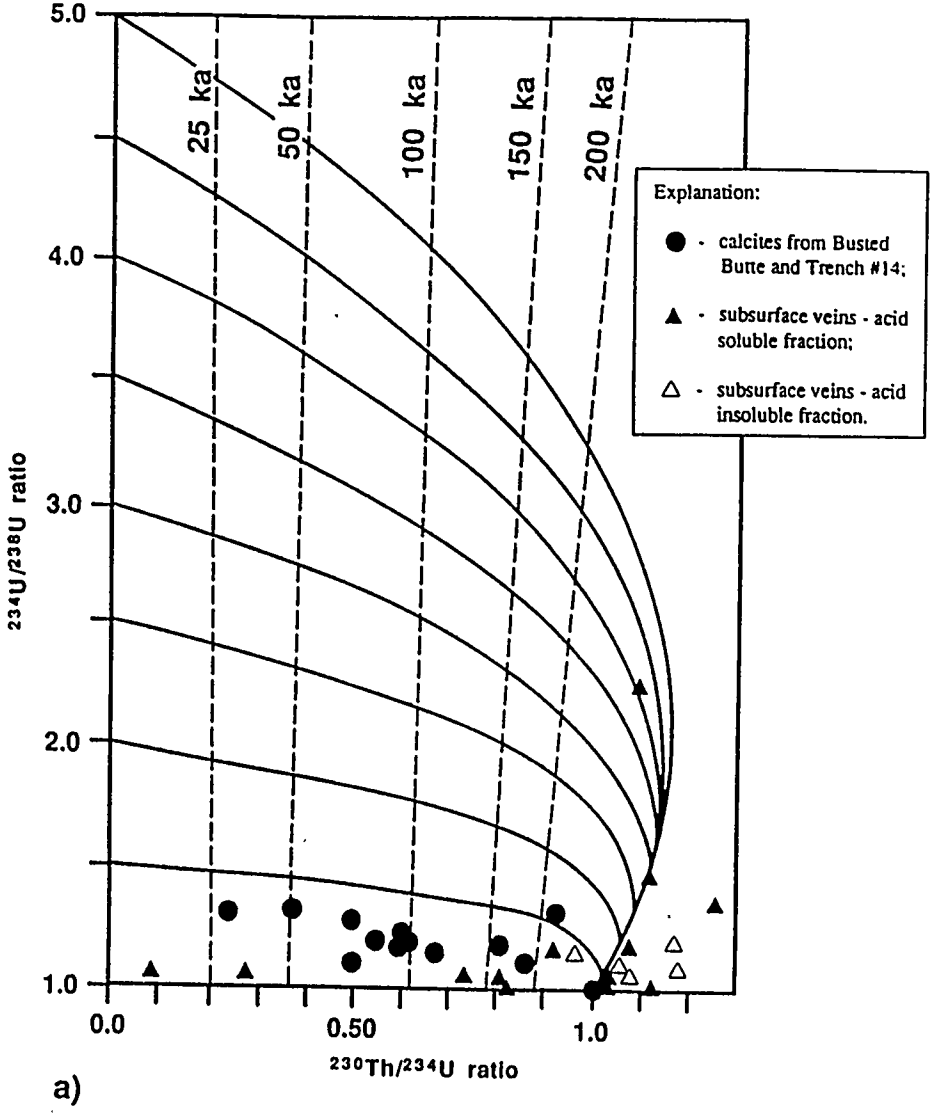

a)

Note:
Isotopic data are from Szabo et al. (1981) and Szabo and Kyser (1985).

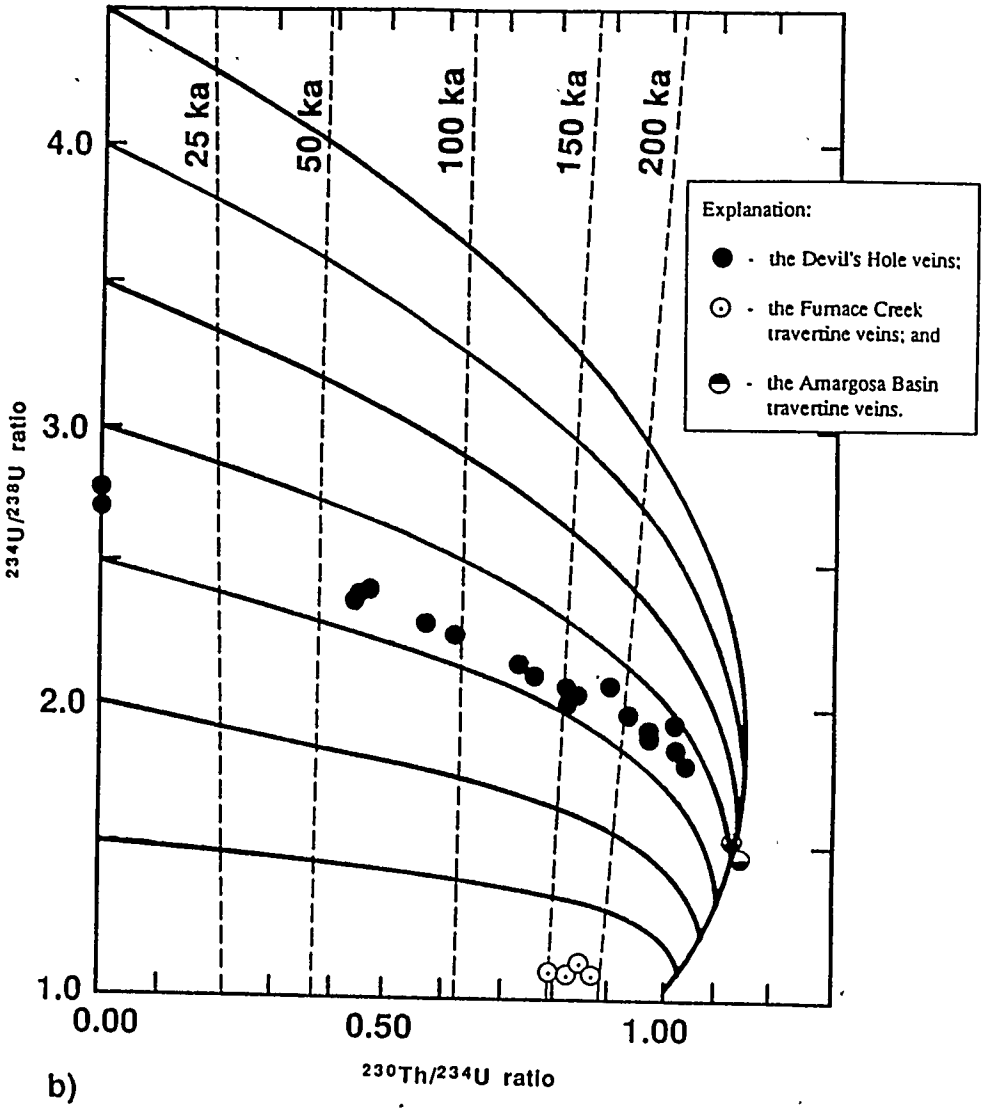

b)

Note:
Isotopic data are from Szabo and O'Malley (1985) and Stuckless (1990).

Figure 2a and 2b. $^{234}U/^{238}U$ vs. $^{230}Th/^{234}U$ ratios from samples of: a) Yucca Mountain calcretes, surficial veins, and subsurface veins, and b) travertine veins from Devils Hole, Amargosa Basin, and Furnace Creek.

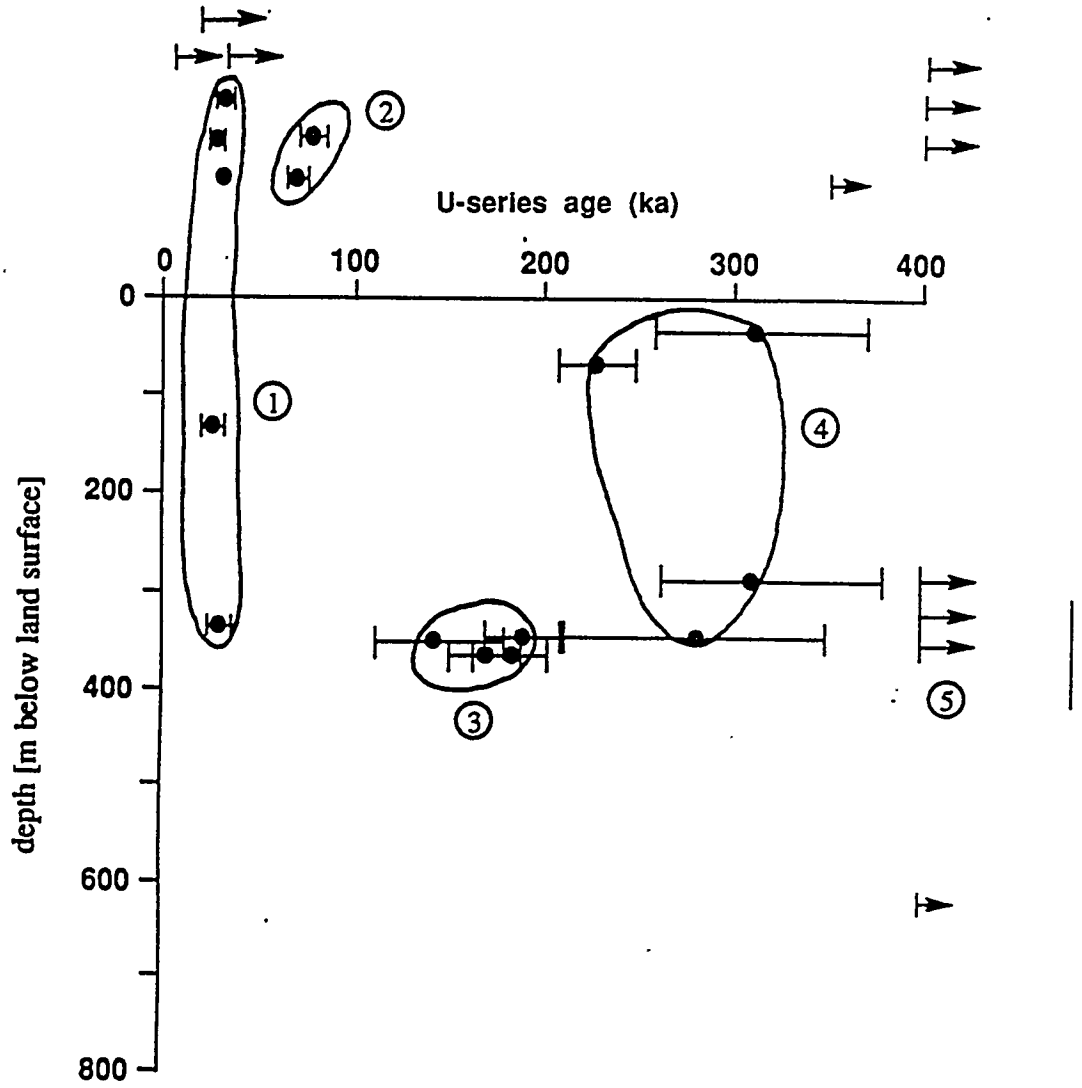

Explanation:

● - the U-series age, bar indicates value of the experimental error, and

⊢► - actual U-series age exceeds value shown.

Note:
U/Th ages are from Szabo et al. (1981); Szabo and O'Malley (1985); and Szabo and Kyser (1990).

Figure 3. U-series ages from samples of Yucca Mountain calcretes, surficial calcitic veins, and subsurface calcitic veins.

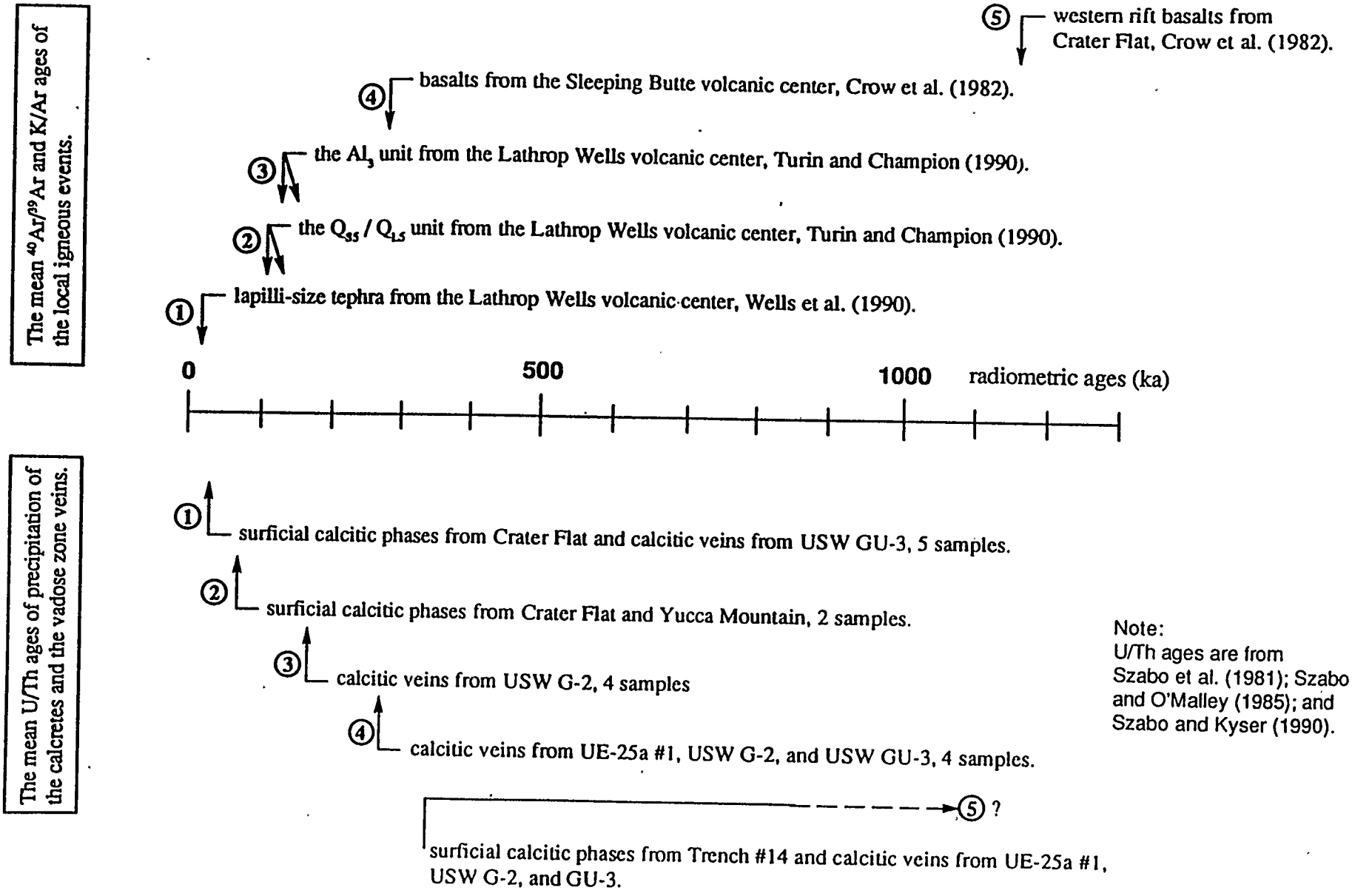

Figure 4. The interpreted chronology of igneous activity and precipitation of the controversial veins and calcretes, Yucca Mountain.

Isotopes Of Carbon

Non-Uniqueness of Carbon Isotopic Signatures

As far as a resolution of the supergene-hypogene controversy is concerned, the results of carbon isotopic analyses do not yield a unique answer. There are two factors which complicate the situation. First, the isotopic character of carbon, either dissolved in a fluid or incorporated in a solid, is not an unequivocal indicator of the origin of this carbon. In particular this is true for carbon that is only slightly depleted in ^{13}C, where corresponding values of the $\delta^{13}C$ ratio range from -3.0 to about -10.0 per mil_{PDB}. There are at least three different ways in which such carbon may originate: 1) from an igneous source (Faure, 1986); 2) through intermixing of biogenically-derived carbon with carbon from an inorganic source (Hoefs, 1987); and 3) through diffusional ^{13}C enrichment of a biogenically-derived carbon. The result of this multiplicity of origin for moderately-light carbon is that supergene-pedogenic carbonates are indistinguishable from hypogene carbonates. For supergene-pedogenic carbonates, for example, Talma and Netterberg (1983) gave $\delta^{13}C$ values ranging from about +4.0 to -8.5 per mil_{PDB}; for hypogene-pedogenic carbonates, the same authors gave values ranging from 0 to -5.5 per mil_{PDB}. Furthermore, for travertine (hypogene) deposits, the range of the $\delta^{13}C$ ratio is inclusive of both of the preceding pedogenic ranges. Turi (1986), for example, notes that this range is from -10.0 to as much as +12.0 per mil_{PDB}. Based solely on the isotopic character of carbon, the origin of pedogenic carbonates is equivocal.

Second, the $\delta^{13}C$ value incorporated in a solid (e.g., calcite) is not a reliable indicator of the isotopic character of carbon dissolved in the corresponding parent fluid. To obtain an estimate for the fluid, based on the carbon isotopic content of the corresponding solid, it is necessary to assume: 1) precipitation conditions of the solid (mainly the crystallization temperature which controls the value of the fractionation factor), 2) rates of precipitation which govern whether carbon isotopic fractionation occurs as an

equilibrium or disequilibrium process, and 3) the degree of fluid CO_2-degassing which controls the degree of diffusional enrichment in ^{13}C in the fluid relative to the pristine (original) state of this fluid.

For isotopes of carbon the temperature-induced $CaCO_3$ <— HCO_3 fractionation effects are fairly small. For example, in the case of equilibrium fractionation at a temperature of less than 100°C, these effects are less than 3.0 per mil_{PDB} (Hoefs, 1987) and for disequilibrium fractionation, these effects are almost non-existent. Usdowski et al. (1979), for example, demonstrated that the kinetic fractionation effects (associated with high rates of $CaCO_3$ precipitation) cause ^{13}C enrichment in solid $CaCO_3$ (relative to HCO_3 in solution) to be very small, less than 1.0 per mil_{PDB}. From this information it may be inferred that potential uncertainties associated with estimates of the $\delta^{13}C$ ratio in a parent fluid based on the corresponding value of a precipitant are fairly small.

In the case of the diffusional ^{13}C enrichment, however, the potential uncertainties are much greater. Although these uncertainties do not involve fluids directly at the precipitation site of a solid, they do involve the pristine state of these fluids. For carbon isotopic considerations of the origin of a fluid (supergene-pedogenic or hypogene) the pristine state of these fluids is of principle interest.

Typically, precipitation of calcite is accompanied by a progressive degassing of CO_2 from a parent solution. During CO_2-degassing, lighter $^{12}CO_2$ molecules escape preferentially and the solution becomes progressively enriched in heavier $^{13}CO_2$ molecules. Therefore, depending upon the degree of CO_2-degassing, a fluid which in the pristine state carries a fixed value of the $\delta^{13}C$ ratio may deposit a solid whose values of the $\delta^{13}C$ ratio are considerably heavier. This effect is clearly illustrated by the results of White et al. (1990) for travertines and associated hydrothermal veins at Long Valley. In this case, the isotopic character of carbon incorporated in the surficial travertines (higher degree of CO_2-degassing) is characterized by values of the $\delta^{13}C$ ratio ranging from -0.7 to +3.5 per mil_{PDB}. For deeper hydrothermal veins, however, where there is lower degree of CO_2-degassing,

the degree of the diffusional ^{13}C enrichment is lower and the resulting calcites carry values of the $\delta^{13}C$ ratio ranging from -3.0 to -7.0 per mil_{PDB}. Similar effects are evident in the results of carbon isotopic studies of surficial calcareous deposits from the Amargosa Basin (Hay et al., 1986). The Amargosa Basin deposits are developed as two distinct facies; the Tpa and Tld calcites represent proximal parts of the spring-fed depositional basin, while the Tpl calcites and dolomites represent the corresponding distal parts. From Figures 5a and 5b, it may be observed that, as the proximal facies grade to become the distal facies, values of the $\delta^{13}C$ ratio increase progressively from -3.0 (proximal facies) to about +3.0 per mil_{PDB} (distal facies). The $\delta^{13}C$ vs. lithofacies gradient most likely represents the progressive CO_2 degassing and the resulting diffusional enrichment in ^{13}C.

Surficial Veins and Calcretes

Numerous carbon isotopic analyses have been performed on the controversial surficial veins and calcretes (Whelan and Stuckless, 1990; Quade and Cerling, 1990). These results reveal that the veins and calcretes contain a moderately-light carbon, $\delta^{13}C \cong$ -3.0 to -8.0 per mil_{PDB} (Figure 6). It may be inferred that, in a pristine state (i.e., prior to near-surface CO_2-degassing and the resulting ^{13}C diffusional enrichment), the parent fluids for these deposits were carrying values of the $\delta^{13}C$ greater or equal to about -10 or -11 per mil_{PDB}. For ambient temperature of 15°C, the equilibrium $CaCO_3$ <— HCO_3 fractionation factor is equal to about 1.75 per mil_{PDB}.

What may be inferred about the origin (supergene or hypogene) of a fluid carrying the -11 per mil_{PDB} values of the $\delta^{13}C$ ratio? In this regard, the only certain inference is that such fluid did not acquire the dissolved carbon solely from an inorganic source of carbon which, at Yucca Mountain, is represented by the early Paleozoic carbonates. For a hypothetical fluid equilibrated with marine limestones, the expected value of the $\delta^{13}C$ ratio falls within a limited range from +4.0 to no less than -2.0 per mil_{PDB}. This expectation indicates that, if the parent fluids for the deposits in question had contained some carbon

dissolved from marine limestones, these fluids must have been intermixed with fluids that have acquired their dissolved carbon from an isotopically-light source, namely, a biogenic and/or deep-seated igneous source of CO_2 gas. Based on the inferred isotopic character of the dissolved carbon alone, however, it is not possible to state unequivocally which one (or both) of the two sources provided the isotopically-light carbon.

On the one hand, one may presume that the source of "light" carbon was a locally-produced biogenic CO_2. For this gas, an estimate of value of the $\delta^{13}C$ ratio may be made based on the results of a botanical survey; these results show that, for Yucca Mountain, the representative proportion of plants having the C-3 metabolic pathway is ~85% (Quade et al., 1989). Therefore for $CO_{2(gas)}$ produced by local biogenic activity, the representative value of the $\delta^{13}C$ ratio is -24.0 per mil_{PDB}. Dissolution of this CO_2 should yield fluids with $\delta^{13}C$ values of about -15.0 per mil_{PDB} (for 15°C, the HCO_3 <—$CO_{2(gas)}$ equilibrium fractionation factor is ~9 per mil_{PDB}). For this inference, some degree of confidence may be derived from the fact that, at Yucca Mountain, shallow interstitial fluids from the vadose zone carry values of the $\delta^{13}C$ ratio ranging from -20.0 to as low as -26.0 per mil_{PDB} (Yang, 1989).

On the other hand, it is equally appropriate to consider that the source of the isotopically "light" carbon is CO_2 gas from an igneous source. Typically, in the pristine state (i.e., prior to near-surface CO_2 degassing and the resulting ^{13}C diffusional enrichment), hydrothermal fluids (which contain dissolved igneous CO_2) carry values of $\delta^{13}C$ as low as about -10 or -12 per mil_{PDB} (Hoefs, 1987; Faure, 1986). The low relative concentrations of ^{13}C may be explained by assuming (conservatively) that igneous $CO_{2(gas)}$, with a $\delta^{13}C$ value ranging from -5.0 to about -8.0 per mil_{PDB}, was dissolved at a temperature of about 200°C. For this temperature, the HCO_3 <— $CO_{2(gas)}$ fractionation factor is about -4.0 per mil_{PDB}. In a low pressure environment (near the topographic surface), escape of CO_2 from ascending solutions is typically accompanied by diffusional ^{13}C enrichment and a resulting progressive increase in the $\delta^{13}C$ ratio. The calcites, formed

under such non-equilibrium conditions, would carry the observed range of the $\delta^{13}C$ ratio from -9.0 (low degree of the diffusional ^{13}C enrichment) to -3.0 per mil_{PDB} (high degree of the diffusional ^{13}C enrichment).

Subsurface Veins

The results of the analyses have also revealed that, at Yucca Mountain, the isotopic character of carbon incorporated in the calcitic veins (both sparry and micritic) displays a clear bi-modal distribution (Whelan and Stuckless 1991, 1992). Specifically, calcites collected from within the upper 1 km of the stratigraphic section have $\delta^{13}C$ values ranging from -3.0 to about -9.5 per mil_{PDB}, whereas calcites sampled from within the 0.5-1.8 km depth interval have heavier values of the $\delta^{13}C$ ratio ranging from -2.0 to about +5.0 per mil_{PDB} (Figure 7):

The bi-modality of $\delta^{13}C$ ratios, and the fact that the controversial veins carry light carbon, was taken as evidence for the supergene-pedogenic origin of these veins (Whelan and Stuckless, 1992; Evernden, 1992). Prior to accepting this conclusion, however, it is prudent to examine the underlying assumption. The assumption is that there are only two sources of circulating carbon at Yucca Mountain, a biogenic source, supplying isotopically-light carbon, and an inorganic source (underlying Paleozoic carbonates) which supply isotopically-heavy carbon. In actuality, however, carbon could originate from three different sources in magmatically-active regions (Faure, 1986; Hoefs, 1987): the two sources identified above and a third deep-seated igneous source. Depending upon the CO_2-dissolution temperature, the latter source may yield fluids for which the isotopic character of dissolved carbon ranges from light to intermediate to heavy.

While searching for a correct explanation of the noted bi-modality of the $\delta^{13}C$ ratio, it is helpful to recognize that, for many magmatically-active regions, the isotopic character of carbon incorporated in hydrothermal calcites varies considerably and can often exhibit a range of $\delta^{13}C$ values similar to the combined range of values at Yucca Mountain (from

-10.0 to about +5.0 per mil_{PDB}; Figure 7). Hoefs (1987) explained the wide range of $\delta^{13}C$ values by pointing out that, in magmatically-active regions, hydrothermal fluids may acquire dissolved carbon from two different sources: marine limestones and an igneous CO_2-gas source. During certain episodes of hydrothermal activity the associated fluids acquire their dissolved carbon largely from marine limestones and these fluids typically are enriched in ^{13}C and carry values of the $\delta^{13}C$ ratio of ~0 ± 2.0 per mil_{PDB}. During other periods of hydrothermal activity, however, a deep-seated igneous source of carbon becomes important and in this case, the associated fluids acquire carbon predominantly through dissolution of igneous CO_2. Typically, such fluids are depleted in ^{13}C and carry $\delta^{13}C$ values ranging from -3.0 to as little as -10.0 per mil_{PDB} (Faure, 1986).

Some support for Hoefs' interpretation may come from Yucca Mountain. Both the ^{13}C-enriched (sparry) and the ^{13}C-depleted (micritic) calcitic veins seem to be spatially associated with calcites yielding elevated fluid inclusions homogenization temperatures. This is indicated by a comparison of the depth distributions of: 1) fluid inclusion homogenization temperatures, and 2) $\delta^{13}C$ ratios from spatially-equivalent samples. From Figure 8, it may be observed that, for the northwestern segment of Yucca Mountain (boreholes USW G-2, G-3, and GU-3), ^{13}C-enriched veins are spatially associated with fluid inclusion homogenization temperatures ranging from 94° to about 240°C. Similarly, some of the shallower and ^{13}C-depleted calcites also seem to be associated with calcites yielding high homogenization temperatures. These temperatures range from 101° to as much as 227°C.

Conclusions

In summary, based on the carbon isotopic data alone, we are not able to find firm support for the supergene-pedogenic origin of the micritic veins and the affiliated calcretes, as advocated by USGS scientists. Far from proving such an origin, the carbon isotopic data are readily explainable within the context of a hypogene model. Furthermore, the fact that

the controversial veins are spatially associated with calcites yielding high fluid inclusion homogenization temperatures may be regarded as favoring the hypogene origin.

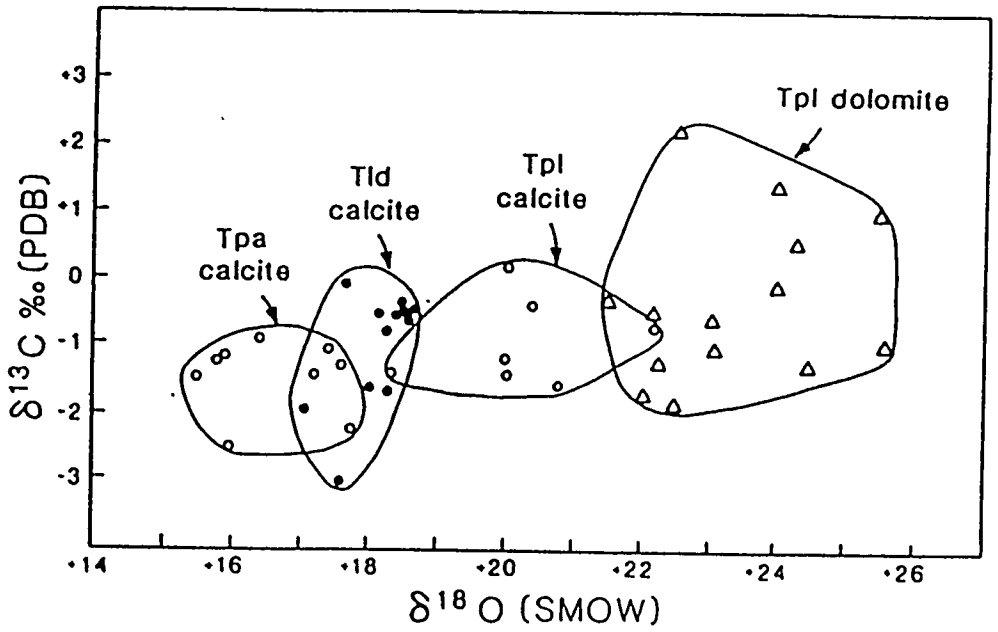

a) Dolomite is represented by triangles and calcite by circles, which are closed for limestones of Tld. Tpa samples are of chalky limestones, most of which are soft; Tld samples are mostly of dense nodular and fenestral limestone; and Tpl samples include both carbonate rocks and carbonate minerals disseminated in claystones.

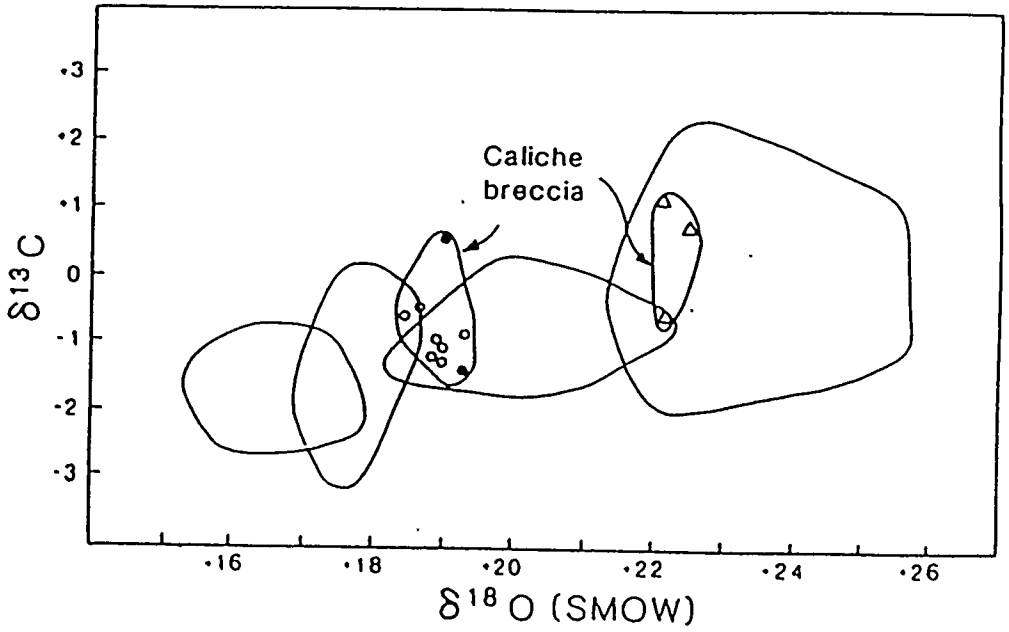

b) Solid circles represent caliche breccia from East Playa, and open circles represent samples from the westernmost caliche breccia. Dolomite is from caliche breccia of East Playa.

Figure 5a and 5b. Explanation of the lithologic notations as employed by Hay et al., 1986. a) composition of carbonate minerals in bedded claystones and carbonate rocks; b) composition of calcite and dolomite in caliche breccia

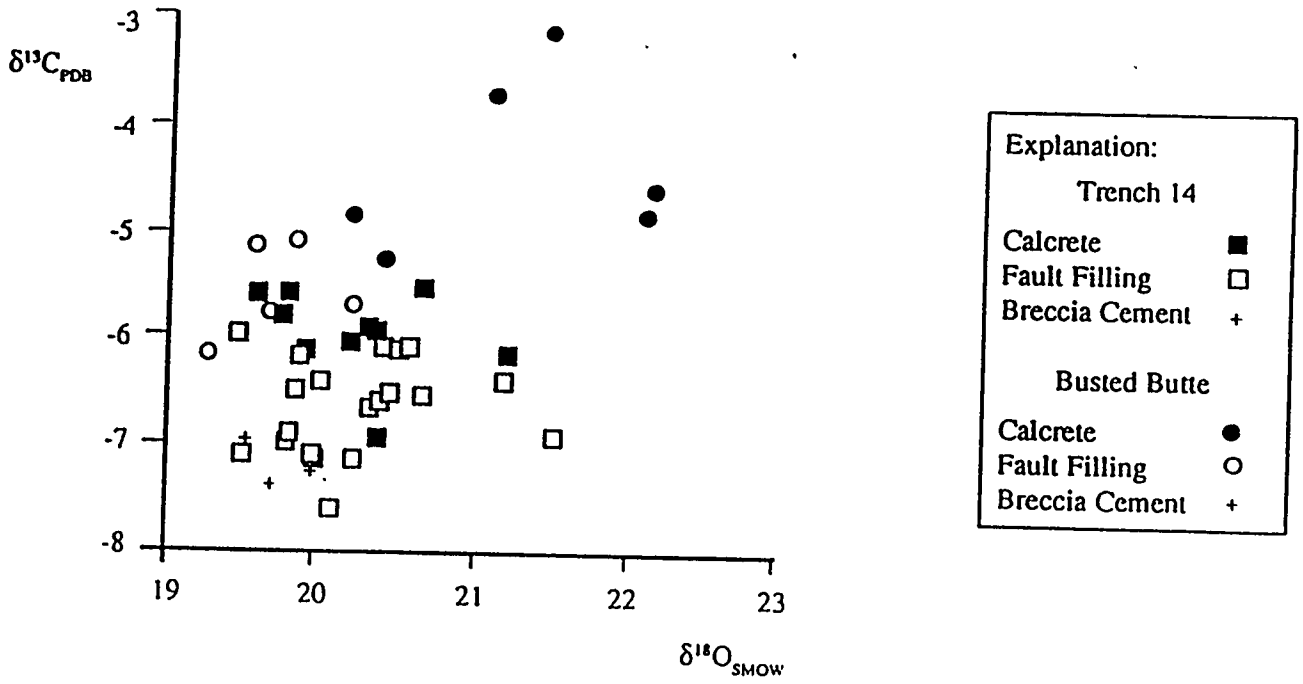

Note:
Isotopic data are from Whelan and Stuckless (1990).

Figure 6. Isotopic characters of carbon and oxygen incorporated in the Yucca Mountain surficial deposits.

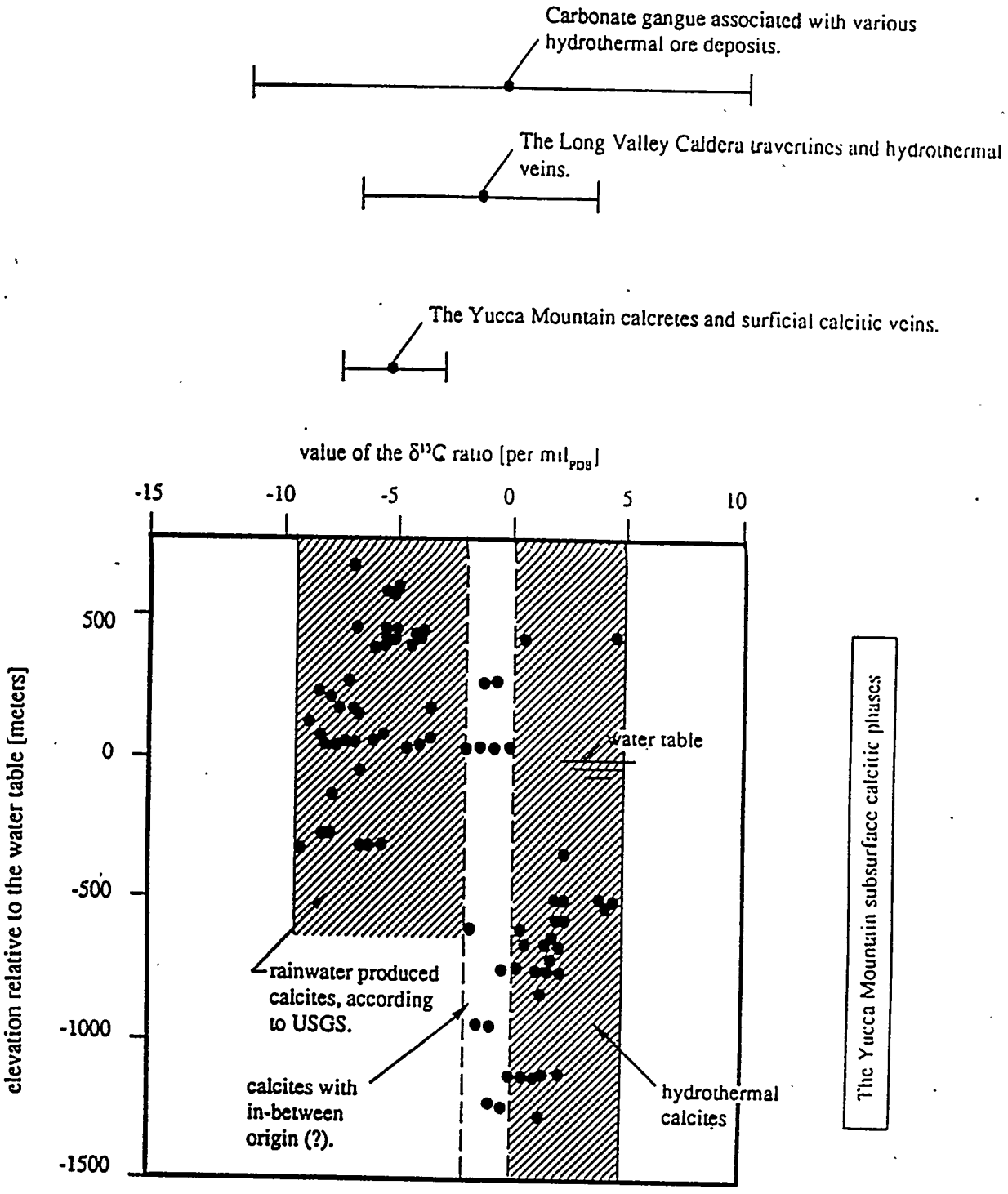

Figure 7. Isotopic data from Whelan and Stuckless (1990, 1991), White et al. (1990), and Hoefs (1987).

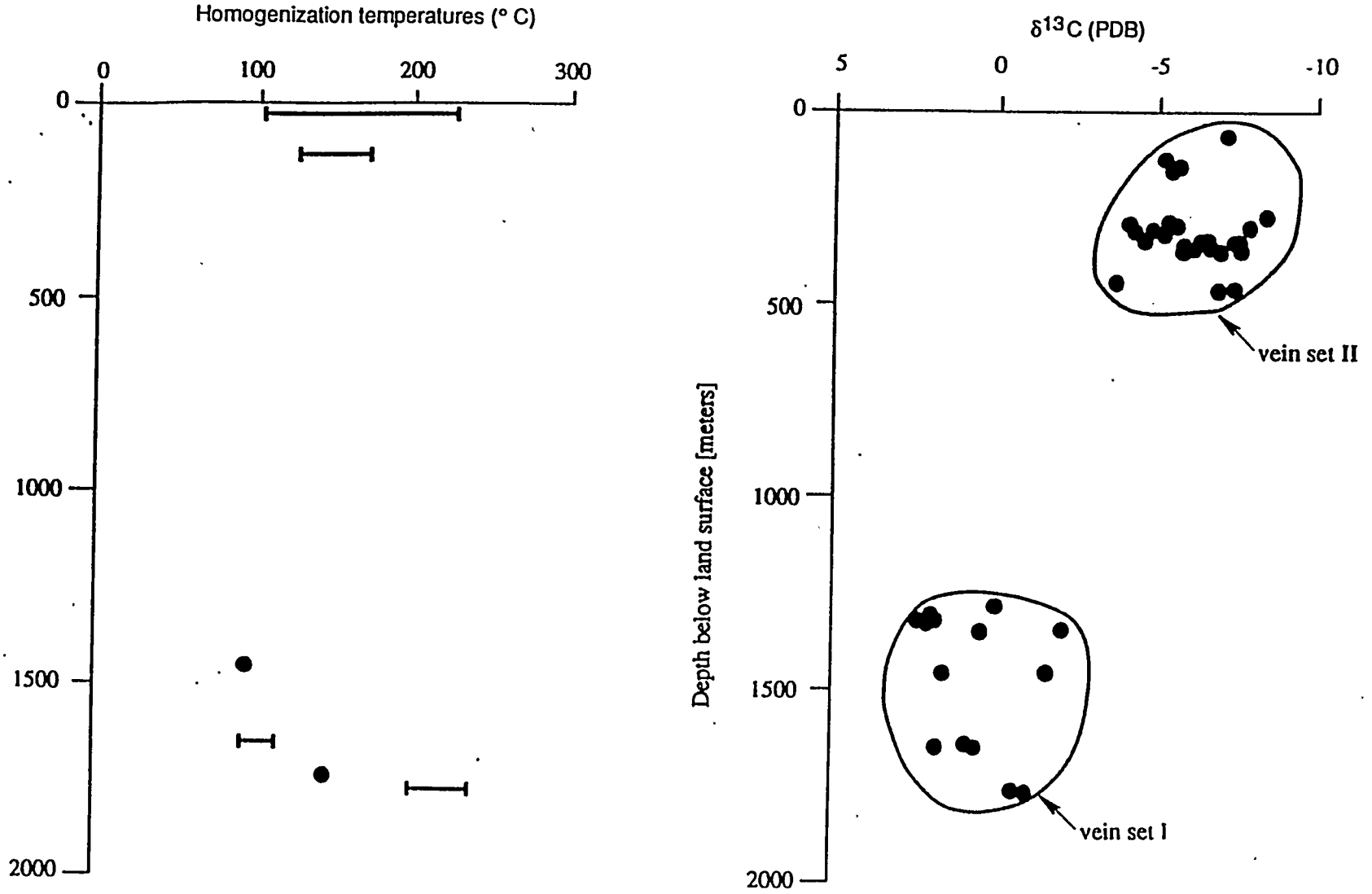

Note:
Isotopic data are from Whelan and Stuckless (1991); fluid inclusion data are from Bish (1989).

Figure 8. Comparison of fluid inclusion homogenization temperatures with $\delta^{13}C$ values. All data are from the northwestern sector of Yucca Mountain (boreholes USW G-2, G-3, and GU-3).

Isotopes Of Strontium

Relative Uniqueness of Strontium Isotopic Signature

As far as a resolution of the supergene-hypogene dilemma is concerned, the isotopic character of strontium incorporated in the controversial paragenetic assemblage (i. e., the alkaline earth alteration products, the micritic veins, the breccia cements, and the calcretes) is particularly noteworthy. This is so because of two well known isotopic properties of strontium. These properties make it feasible to know and/or calculate the isotopic character of strontium dissolved in the corresponding fluid phase, and to infer the corresponding depth of circulation for this fluid phase. These attributes are the result of the absence of strontium fractionation effects and the isotopic uniqueness of strontium incorporated in the local reservoirs of strontium.

With regard to fractionation effects, it is well known that during common geochemical reactions strontium isotopes do not fractionate (Faure, 1986). Consequently, the isotopic character of strontium initially incorporated in a solid compound is identical to that dissolved in the corresponding parent fluid. Furthermore, for most carbonates the in-situ production of radiogenic ^{87}Sr is negligible and thus, the actual value of the $^{87}Sr/^{86}Sr$ ratio represents the corresponding initial value. This is so because ^{87}Rb atoms, which are parent atoms for ^{87}Sr, are too large to be incorporated in the calcite lattice. The oversized ^{87}Rb atoms are excluded from this lattice and, consequently, the in-situ $^{87}Rb \longrightarrow {}^{87}Sr$ production is small or nil (Rankama, 1954).

With regard to the depth of fluid circulation it is important to recognize that three lithostratigraphic units which may serve as reservoirs for strontium at and around Yucca Mountain. These are: 1) the Tertiary ignimbritic complex; 2) the Paleozoic carbonate complex; and 3) the Precambrian basement. The isotopic character of strontium incorporated in these three complexes is markedly different. Specifically, for the Precambrian basement, values of the $^{87}Sr/^{86}Sr$ ratio range from about 0.7120 to as much as

0.7360 or greater (Faure, 1986); for the overlying Paleozoic carbonates, the $^{87}Sr/^{86}Sr$ ratios range from about 0.7082 to 0.7099 (Peterman, 1990); and for the Tertiary ignimbrites, the unaltered (and initial) values of the $^{87}Sr/^{86}Sr$ ratio are inferred to be lower than about 0.7080. With respect to the latter values, equally-low relative concentrations of radiogenic ^{87}Sr are commonly found in association with young rhyolites and compositionally equivalent granites (Faure, 1986). For example, the estimated value of the $^{87}Sr/^{86}Sr$ ratio for rhyolitic magma from the Yellowstone area was reported as 0.7094 by Leeman et al. (1977); for Quaternary rhyolites from the Long Valley Caldera values ranged from 0.7060 to 0.7074 (Goff et al., 1990); and for southeastern-California granites, $^{87}Sr/^{86}Sr$ values have been reported at about 0.7070 (Kiestler and Peterman, 1973)..

The greater enhancement of strontium ratio from the Precambrian basement, relative to the overlying lithostratigraphic complexes, allows for inferences to be drawn with regard to depth of circulation of fluids which were involved in both the alkaline earth metasomatism and the precipitation of micritic veins and calcretes. Fluids involved in shallow circulations (i.e., the Tertiary ignimbrites and underlying Paleozoic carbonates) may be expected to yield both the alteration products and the calcitic veins whose values of the $^{87}Sr/^{86}Sr$ ratio are low, less than 0.7080. For fluids involved in deeper circulation, however, (i.e., the Precambrian basement) the corresponding isotopic values may be expected to be definitively higher, in excess of 0.7120.

Concentrations of Strontium, Whole Rock

A review of the strontium concentration data reveals that, in addition to lime and magnesia metasomatism, the Yucca Mountain tuffs display evidence of having been subjected to a spatially-discrete strontium metasomatism. This is indicated by two lines of evidence. First, for unaltered alkali tuffs the expected total abundance of strontium is uniform and low, typically much less than 100 ppm (Faure, 1986). This expectation has been confirmed by the results of chemical analyses of samples of Yucca Mountain glass. Specifically, Peterman et al. (1991) have reported that, for the unaltered lower vitrophyre

of the Topopah Spring member, the representative concentration of strontium is as low as 19 ± 6 ppm. This is a mean value derived from six samples of fresh vitrophyre from three different boreholes. From Figures 9a and 9b, it may be observed that, in the present-day state, the tuffs contain surprisingly large concentrations of strontium. These concentrations, however, are highly erratic and range from 10 to as much as 700 ppm indicating that epigenetic, spatially-discrete enrichment of total strontium has occurred. This enrichment is best expressed through a normalized plot of trace element analyses (five samples) from the altered lower vitrophyre of the Topopah Spring member (Figure 10). It may be observed that, relative to the devitrified interior of the Topopah Spring ash-flow sheet, the altered vitrophyre exhibits substantial gains in both calcium and strontium.

Second, for a given stratigraphic unit, average concentrations of strontium do not remain constant but instead vary laterally. The lateral variability of the average concentration of strontium may be illustrated by examining these concentrations for the Topopah Spring member at three different locations. In the southern end of Yucca Mountain (near Highway 95), the average concentrations are uniformly-low, approximately 25 ppm, Figures 9a, b. At the northern end, however, the corresponding concentrations are decisively higher. These concentrations range from 50 ppm, for the northwestern segment (boreholes USW G-1 and G-2), to 190 ppm for the southeastern segment (borehole UE-25a#1) (Figures 11a, b).

The fact that the tuffs have been epigenetically-enriched in strontium at Yucca Mountain bears directly on interpretations of the origin of strontium incorporated in the controversial veins and calcretes. Specifically, this fact introduces the possibility that both the strontium enrichment of the tuffs and the emplacement of the veins and calcretes are linked to a common process. In view of this possibility, and without demonstrating that both of the effects are unrelated, the strontium-enriched tuffs may not be regarded as a source of strontium which is incorporated in the controversial deposits.

$^{87}Sr/^{86}Sr$ Ratios, Whole Rock

A review of strontium isotopic data ($^{87}Sr/^{86}Sr$ ratios) reveals that the strontium metasomatism developed sequentially in response to two distinct allogenic fluids, each having distinct strontium isotopic characteristics. This is indicated by the depth distributions of values of the $^{87}Sr/^{86}Sr$ ratio for whole-rock samples of the tuffs (Figures 12a, b). For deeper tuffs (altered during the Timber Mountain hydrothermal metamorphism) the present-day values of the $^{87}Sr/^{86}Sr$ ratio are low, generally slightly less than 0.7100 and the corresponding initial ratios range from 0.7083 to no more than 0.7101 (Peterman, 1990). These initial ratios were calculated assuming that the present-day values reflect both the relative concentration of ^{87}Sr acquired from solution and the ^{87}Sr produced in-situ through decay of ^{87}Rb. It was further assumed that the ^{87}Sr produced in-situ has been accumulating for about 13 million years (the age of emplacement of the host rock). Because the actual timing of the whole-rock alteration (9.5-11 Ma) does not differ appreciably from the assumed age of strontium introduction, the calculated initial values of the $^{87}Sr/^{86}Sr$ ratio, from 0.7081 to 0.7101, may be regarded as accurately reflecting the isotopic character of strontium dissolved in the Timber Mountain hydrothermal fluids. For the tuffs altered in association with the alkaline earth metasomatism, however, the present-day values of the $^{87}Sr/^{86}Sr$ ratio are decisively higher. They range from 0.7095 to as much as 0.7202 and the corresponding initial ratios range from 0.7104 to 0.7129 (Peterman, 1990; Peterman et al., 1991); (Figures 11a, b). These ratios were calculated by erroneously assuming that the ^{87}Sr produced in-situ was accumulating for about 13 Ma years and, therefore, are too low. For fluids responsible for the alteration of the lower vitrophyre of the Topopah Spring member in borehole UE-25a#1, an estimate of the $^{87}Sr/^{86}Sr$ ratio was reported by Peterman et al. (1991). The reported value is 0.7119 ±0.0002, and was said to be identical to that from samples of purified alteration minerals from the altered zone in borehole UE-25a#1. Although too low (because of the erroneously assumed age for the introduction of strontium), the 0.7119 value may be regarded as conservatively

representative of relative concentrations of ^{87}Sr dissolved in fluids involved in the alkaline earth metasomatism.

The strontium (whole-rock) isotopic data (whole-rock) identify an important problem: What is the origin of fluids responsible for the alkaline earth metasomatism and what is a source of the corresponding and highly-radiogenic strontium?

It seems likely that the abnormal enrichment in ^{87}Sr post-dates the Timber Mountain hydrothermal metamorphism and is related to alkaline earth metasomatism (Livingston, 1993). The evidence for alkaline-earth metasomatism (calcium, magnesium, and strontium) cannot be dismissed lightly as being supergene-pedogenic in origin because it involves millions of tons of rock at Yucca Mountain. Furthermore, it is difficult to postulate that the source of the alkaline earth elements is dust derived from Paleozoic carbonates, which elements have been dissolved and carried into the interior of Yucca Mountain by infiltrating rainwater. The difficulty is to explain the alteration of tuffs with the strontium isotopic ratio ($^{87}Sr/^{86}Sr$) of more than 0.7120 as caused by rainwater that has dissolved wind-blown dust with the strontium isotopic ratio of 0.709.

$^{87}Sr/^{86}Sr$ Ratios, Micritic Veins, and Calcretes

The results of the strontium isotopic analyses further reveal that the relativey-high strontium ratios ($^{87}Sr/^{86}Sr \cong 0.7125$) characterize the controversial veins and the affiliated calcretes at Yucca Mountain. For surficial veins and calcretes, $^{87}Sr/^{86}Sr$ ratios range from 0.7112 to as much as 0.7130; for the micritic veins, from a depth of up to 500 m, the corresponding range is from 0.7110 to 0.7127 (Figures 13a, b).

With the supergene-hypogene controversy in mind it is worth noting that: 1) the isotopic character of strontium incorporated in the Devil's Hole (DH-2) deposit is characterized by $^{87}Sr/^{86}Sr$ values ranging from 0.7123 to about 0.7128 (Marshall et al., 1990), and 2) the bi-modality of the $\delta^{13}C$ ratios, noted earlier is clearly reflected through spatially-corresponding bi-modality of the $^{87}Sr/^{86}Sr$ ratios (Figure 14). The apparent

equivalency of the $^{87}Sr/^{86}Sr$ ratios allows for considering the possibility that both the DH-2 deposit and the controversial veins and calcretes at Yucca Mountain were precipitated from fluids that have acquired their dissolved strontium from the Precambrian basement (the only known primary reservoir of sufficiently radiogenic strontium). In addition to being involved in the precipitation of the micritic veins and calcretes, such hypothetical and deep-seated fluids could have also been involved in alkaline earth metasomatism, including the ^{87}Sr aspects of this metasomatism.

The spatially-equivalent Yucca Mountain calcites concurrently: 1) contain high fluid inclusion homogenization temperatures; 2) are depleted in ^{13}C, 3) are enriched in ^{87}Sr; and 4) are temporally correlative with local episodes of magmatic activity. This evidence further strengthens the possibility formulated earlier concerning the igneous origin of carbon incorporated in the controversial veins and calcretes. During their residence in the deep subsurface (say more than 5.0 km), the hypothetical fluids could have acquired their dissolved light carbon through the correspondingly high temperature dissolution of igneous CO_2 in addition to acquiring the highly radiogenic strontium.

The above remarks indicate that the hypogene hypothesis offers a resolution of the dilemma regarding the origin of the controversial paragenetic assemblage. This hypothesis accounts for all of the isotopic data and observations thus far considered. Within the context of this possibility there is not a single piece of isotopic information that is difficult to explain or has been left unaccounted for. There is no scientific reason, therefore, to regard the hypogene hypothesis as either inappropriate or inferior to the supergene-pedogenic hypothesis.

The demonstrated attributes of the hypogene hypothesis are in sharp contrast to the competing supergene hypothesis where a number of isotopic observations are either difficult to explain or must be regarded as fortuitous. With regard to the "difficult to explain" category, the most outstanding problems are: 1) the source of the highly-radiogenic strontium dissolved in parent fluids of the controversial paragenetic assemblage

(alkaline earth metasomatism, micritic veins, and calcretes), 2) temporal correspondence of episodes of calcite precipitation with episodes of local magmatic activity; and 3) origin of the volumetrically-extensive and chemically-diverse alkaline earth metasomatism. With regard to the "fortuitous" category, the outstanding observations are those pertaining to the noted isotopic equivalencies, namely: 1) the equivalence of the $^{234}U/^{238}U$ ratios (reference deposits are the travertine veins from Travertine Point); 2) the equivalence of the $\delta^{13}C$ ratios (reference deposits are the travertine veins from the Long Valley Caldera); and 3) the equivalence of the $^{87}Sr/^{86}Sr$ ratios (reference deposit is the DH-2 vein).

Even if both the hypogene hypothesis and the supergene-pedogenic hypothesis are regarded as being on an equal footing, and considering potentially catastrophic consequences that may result from a malfunction of the proposed nuclear facility, it is clear that the hypogene hypothesis must be sincerely considered. This is the area of deepest concern with regard to the NAS/NRC report.

Conclusions

In summary, based on the strontium isotopic data alone, we are not able to find a firm support for the supergene-pedogenic origin, of the controversial micritic veins and the affiliated calcretes. Far from proving such origin the strontium isotopic data are readily explicable within the context of the hypogene model. The fact that both alkaline earth metasomatism and the micritic veins and calcretes owe their existence to fluids carrying equally and highly radiogenic strontium is particularly noteworthy. Further support for the hypogene origin of the controversial calcite-silica deposits is suggested by the correspondence of the $^{87}Sr/^{86}Sr$ ratio from Yucca Mountain with the ratios from the DH-2 travertine vein.

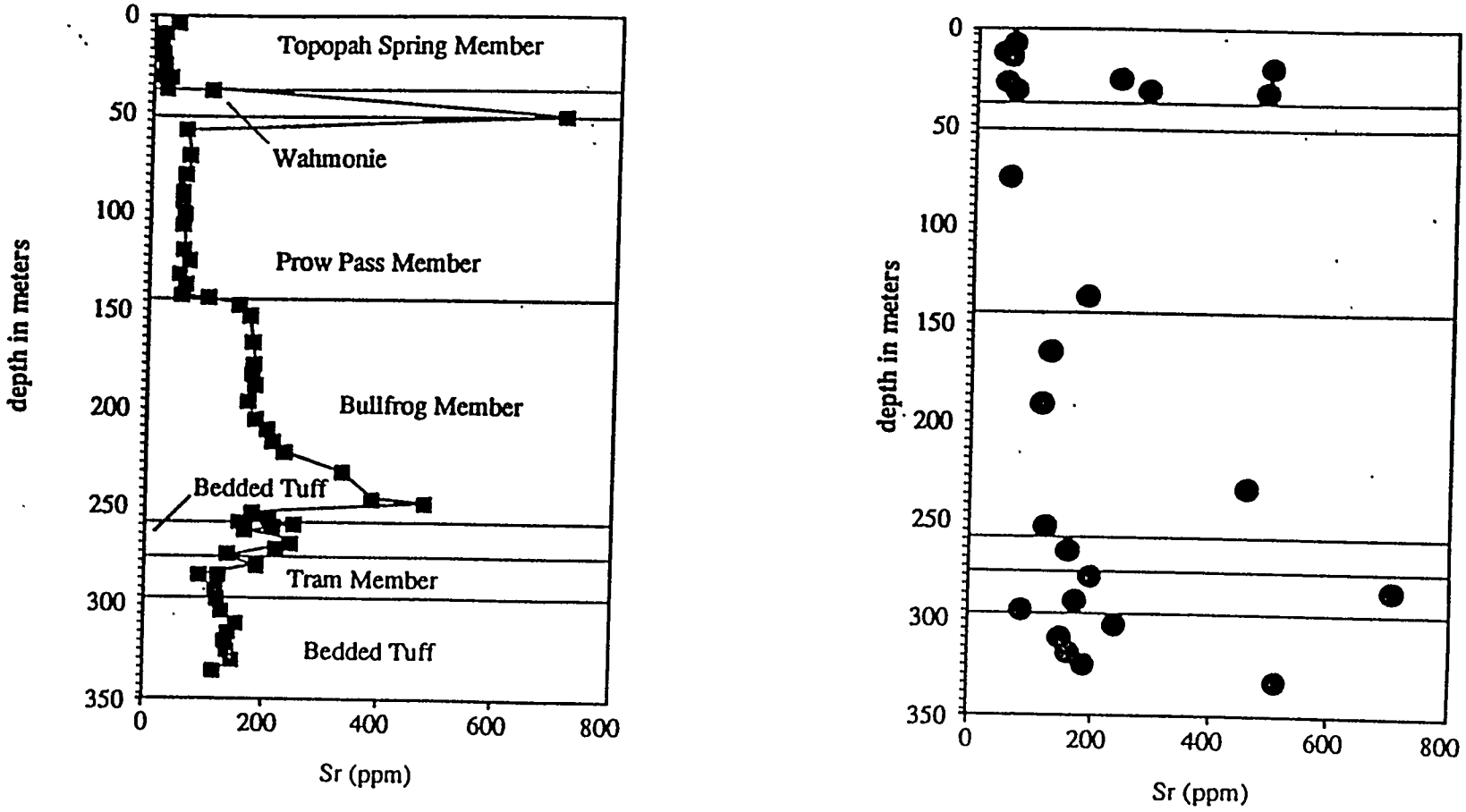

a) southernmost end of Yucca Mountain.

b) northernmost end of Yucca Mountain.

Note:
Strontium concentration data are from Peterman et al. (1991) and Peterman (1989).

Figure 9a and 9b. Concentrations of strontium, whole-rock samples of the stratigraphically equivalent ignimbrites.

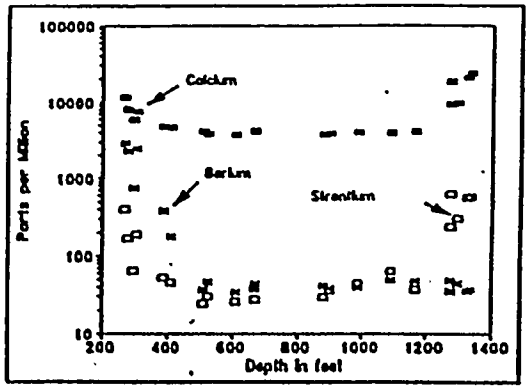

a) Ca, Ba, and Sr, in the Topopah Spring Member.

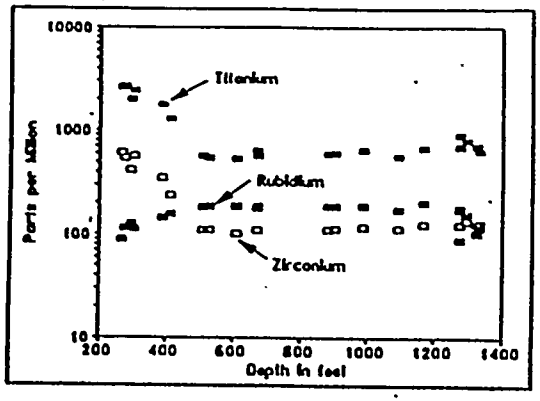

b) Ti, Rb, and Zr, in the Topopah Spring Member.

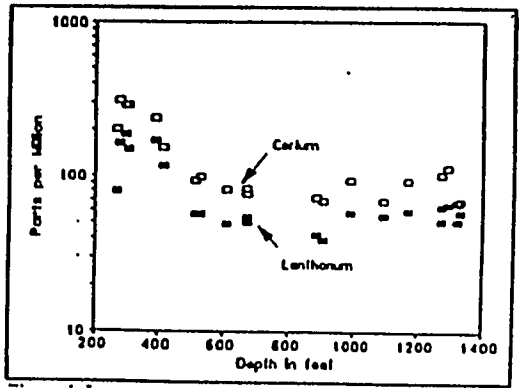

c) La and Ce, in the Topopah Spring Member.

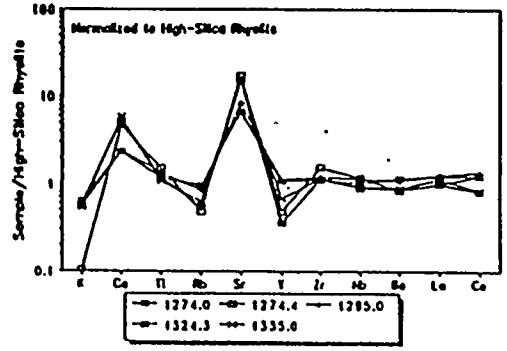

d) normalized concentrations, altered lower vitrophyre of the Topopah Spring Member.

Note:
Sample 268.0 is from the zone of nonwelded vitric tuff at the top of the unit and consists of approximately 90 percent pumice and sparse lithic fragments. Samples 277.8 through 413.0 are moderately to densely welded quartz latite with phenocrysts generally decreasing in abundance with depth. Samples 510.4 to 1170.0 are from the densely welded, devitrified zone composed of high-silica rhyolite. Samples 1274.0, 1274.4, and 1295.0 are from the lower vitrophyre and represent various degrees of alteration. Sample 1274.0 is a dull black vitrophyre with abundant fractures and veining. Sample 1274.4 is predominantly smectite and clinoptilolite, and sample 1295.0 is approximately half smectite and clinoptilolite. Sample 1324 is 80 ± 12 percent clinoptilolite and 6 ± 2 percent mordenite; the remainder is alkali feldspar and silica minerals. Sample 1335.0 is from a non- to partially welded, slightly altered zone near the base of the unit.

Figure 10. Major and trace element concentrations, whole-rock ignimbrites from the vadose zone, borehole UE-25a#1. (from Peterman et al., 1991)

	Rb	Sr	Y	Zr	Nb	Rb/Sr	Ma	87Sr/86Sr	IR(Sr)
	Parts per million								
Tiva Canyon									
MD-18	192	24	36	187	32	8.00	12.9	0.71574	0.7115
MD-29	222	10	25	64	30	22.20	12.9	0.72024	0.7084
MD-32-1	208	49	29	67	33	4.24	12.9	0.71353	0.7113
MD-34	148	44	37	326	24	3.36	12.9	0.71267	0.7109
Yucca Mt. 2AA-6	175	31	34	193	32	5.65	13.0	0.71495	0.7119
Topopah Spring(12)	176	22	26	109	22	8,07	13.4	0.71603	0.7116
2AA-5(upper)	146	57	25	320	21	2.56	13.4	0.71231	0.7109
2AA-2 (bas.vit)	192	58	22	118	25	3.31	13.4	0.71239	0.7106
2AA-1(basal)	204	63	28	104	24	3.24	13.4	0.71345	0.7117
Calico Hills(4)	159	66	24	91	19	2.41	13.4	0.71328	0.7119
2A-1-1	85	77	10	53	12	1.10	13.4	0.71239	0.7118
2A-1-2	158	92	18	99	18	1.72	13.4	0.71239	0.7114
Prow Pass(2)	155	52	30	148	27	2.99	13.5	0.71172	0.7101
3A-7	116	196	21	93	19	0.59	13.5	0.71139	0.7111
Bullfrog(16)	139	124	29	135	24	1.12	13.5	0.70953	0.7089
3A-6 (upper)	159	122	26	108	20	1.30	13.5	0.70976	0.7090
3A-4 (ba. vit.)	165	239	27	177	31	0.69	13.5	0.70879	0.7084
3A-3 (ba. vit.)	151	464	27	251	26	0.33	13.5	0.70834	0.7082
3A-2 (basal)	169	118	25	131	23	1.43	13.5	0.70944	0.7086
Air Fall 31-1	144	149	29	204	31	0.97	13.5	0.71012	0.7096
Tram(11)	131	196	20	149	19	0.67	13.6	0.70974	0.7094
4A-1	219	705	27	179	32	0.31	13.6	0.71026	0.7101
4B-4	161	178	21	108	17	0.90	13.6	0 71042	0.7099
4B-6	149	79	17	113	20	1.89	13.6	0.71105	0.7100
Flow Breccia(4)	103	729	32	331	17	0.14	13.7	0.70928	0.7092
Lithic Ridge(6)	131	240	24	165	21	0.55	13.8	0.70909	0.7088
1C-3	151	144	19	128	26	1.05	13.8	0.70947	0.7089
Unit A(6)	157	161	25	151	27	0.98	14.0	0.70955	0.7090
Unit B(1)	131	183	26	186	23	0.72	14.0	0.70921	0.7088
Unit C(7)	130	511	23	244	17	0.25	14.0	0.70892	0.7088
Yucca Flat 1C-1	108	105	32	177	32	1.03	14.0	0.71013	0.7095

a)

Depth feet	Rb, ppm	Sr, ppm	$^{87}Rb/^{86}Sr$	$^{87}Sr/^{86}Sr$	IR(Sr)	Sm, ppm	Nd, ppm	$^{147}Sm/^{144}Nd$	$^{143}Nd/^{144}Nd$	ϵ_{Nd}
268.0	89.7	401	0.65	0.71044	0.71032					
277.8	115	169	1.97	0.70953	0.70917					
304.0	92.7	114	1.75	0.70977	0.70946					
387.7	144	52.9	7.88	0.71287	0.71145					
510.4	185.9	26.03	20.68	0.71663	0.71290	5.57	26.48	0.1271	0.51206	-11.2
609.6	185.3	28.16	19.05	0.71638	0.71294					
669.5	181.8	35.53	14.81	0.71538	0.71271					
990.0	187.4	46.44	11.68	0.71451	0.71240					
1093.0	171	64.0	7.74	0.71397	0.71257					
1170.0	200	37.2	15.57	0.71530	0.71249	6.15	29.07	0.1280	0.51205	-11.4
1274.0	178	237	2.02	0.71243	0.71207					
1274.4	76.6	582.0	0.38	0.71198	0.71191	4.30	20.98	0.1238	0.51207	-11.0
1295.0	160.4	296.3	1.57	0.71236	0.71208	6.44	30.17	0.1290	0.51207	-11.0
1324.3	102.8	568.0	0.52	0.71099	0.71090	5.03	24.72	0.1231	0.51206	-11.2

b)

Note:
Strontium data are from Peterman (1989) and Peterman et al. (1991).

Figure 11a and 11b. Isotopic character of strontium and strontium concentrations, whole-rock samples from: a) boreholes USW G-1 and G-2, and b) borehole UE-25a#1

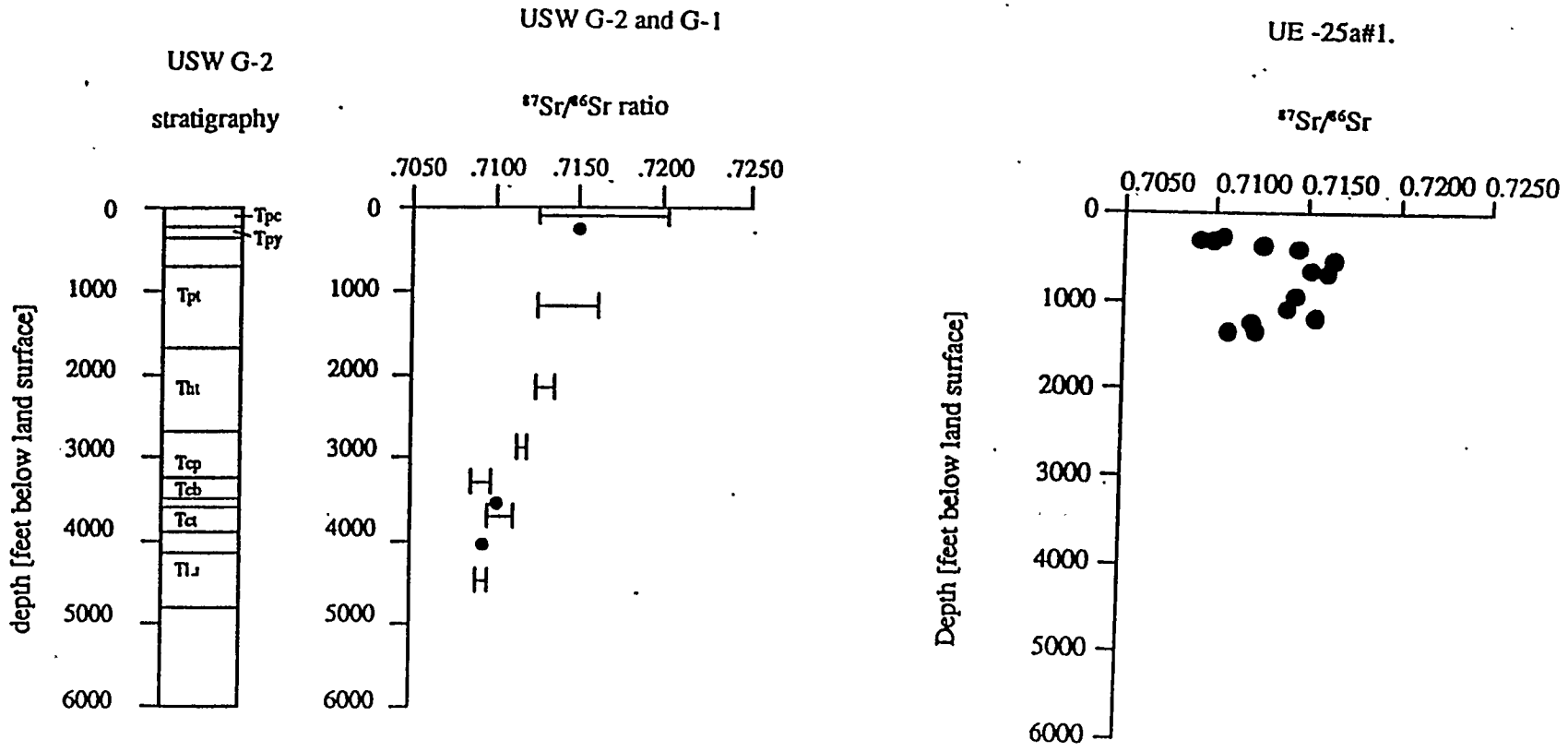

Explanation:

bar indicates range of values for either $^{87}Sr/^{86}Sr$ ratio or concentrations of Sr, whole-rock samples; and
Tpc - the Tiva Canyon Member, Tpy - the Yucca Mountain Member, Tpt - the Topopah Spring Member, Tht - the Tuffs of Calico Hills, Tcp - the Prow Pass Member, Tcb - the Bullfrog Member, Tct - the Tram Member, and Tlr - the Lithic Ridge Tuff.

Note:
Isotopic data from Peterman (1989) and Peterman et al. (1991).

Figure 12a and 12b. Depth comparison of the $^{87}Sr/^{86}Sr$ ratios. Whole-rock samples from: a) USW G-2 and G-1; and b) UE-25a#1.

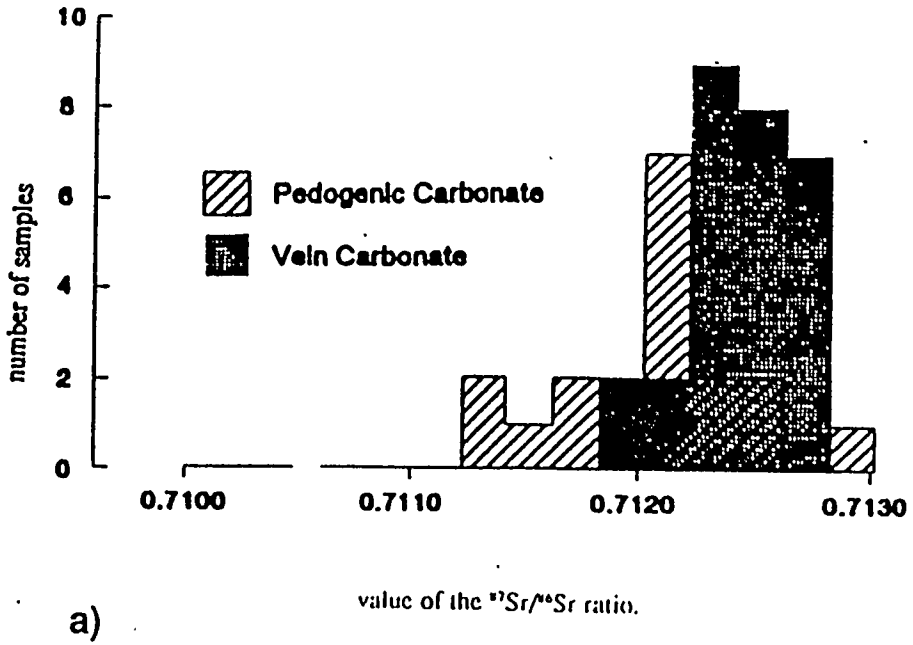

a)

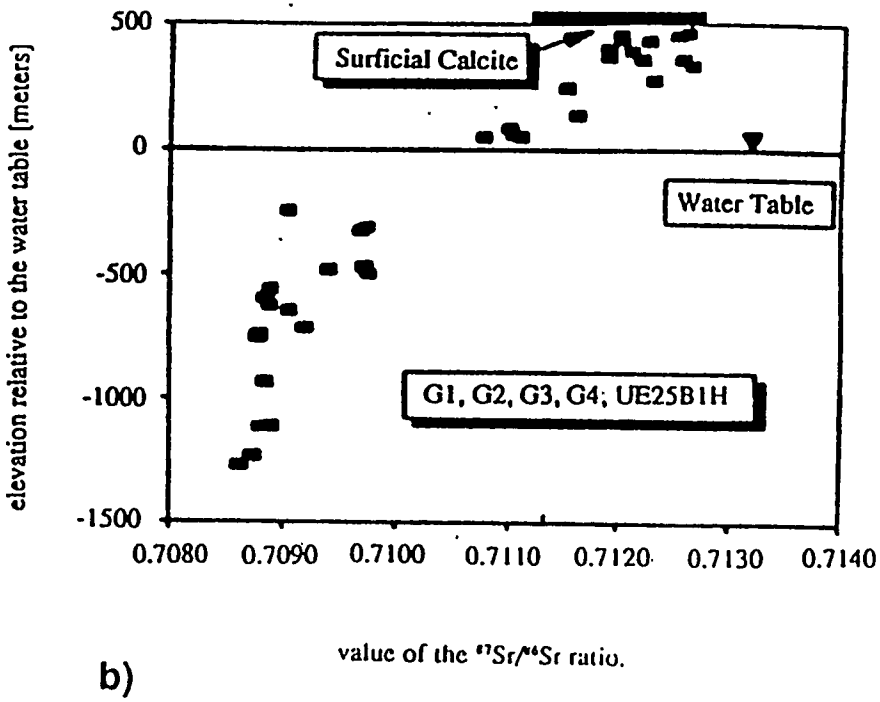

b)

Note:
Isotopic data are from Stuckless (1990) and Peterman et al. (1991).

Figure 13a and 13b. Isotopic character of strontium incorporated in samples of Yucca Mountain subsurface veins, calcretes, and surficial veins.

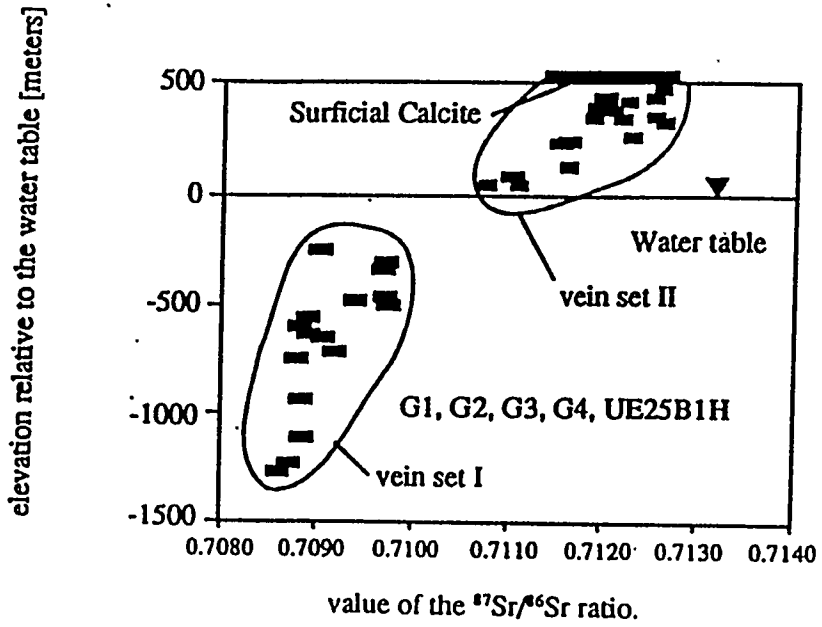

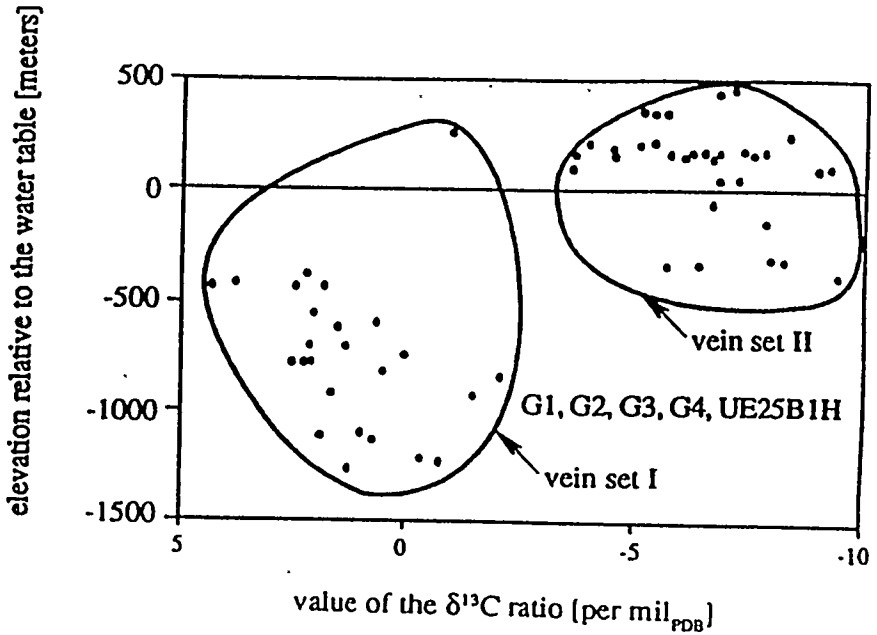

Note:
Isotopic data are from Whelan and Stuckless (1991) and Peterman et al. (1990).

Figure 14. Comparison of the $^{87}Sr/^{86}Sr$ ratios with the $\delta^{13}C$ ratios, samples of the corresponding calcitic veins.

Isotopes Of Oxygen

Non-Uniqueness of Oxygen Isotopic Signatures

Hypogene-type travertine deposits are typically characterized by a variability in the isotope of oxygen. Turi (1986), for example, compiled $\delta^{18}O$ values for travertines from the western United States (California, Wyoming, and Montana) and from south-central Europe (central and southern Italy, Germany, and Czechoslovakia). These results show $\delta^{18}O$ values ranging from 2.0 to as much as 34.0 per mil_{SMOW}. Even for a single orographic setting, the oxygen isotopic variability is still significant. Travertines from central Italy yield a range of $\delta^{18}O$ values, from 16.0 to 32.0 per mil_{SMOW}, and travertines from California, show an even greater variability, from 11.0 to as much as 34.0 per mil_{SMOW}.

The variability of the $\delta^{18}O$ of travertines is commonly attributed to a variety of interactions among three main factors: 1) the oxygen isotopic characteristics of parent fluids, 2) isotopic fractionation effects, and 3) near-surface isotopic modification of parent fluids by diffusional, evaporative, and diluting mechanisms.

The isotopic composition of ground water in addition to being highly variable at a time of atmospheric precipitation and reservoir recharge, is also variably modified through a variety of rock <—> water isotopic exchange reactions. The magnitude of the so-called "oxygen isotopic shift" is dependent upon a number of factors, and is known to vary from fairly small (e.g., Clayton and Steiner, 1975; Lamber and Epstein, 1980) to as much as 12.0 per mil_{SMOW} (Williams and McKibben, 1989). Furthermore, relative to their pristine (intra-reservoir) state, travertine-depositing fluids may undergo additional and highly-variable isotopic modifications. During ascent to a discharge point, these fluids may acquire isotopic inputs which cause them to depart from their pristine (original) state. Intermixing with infiltrating rainwater, as well as either diffusional or evaporative ^{18}O enrichments, are the main processes that are responsible for these additional modifications and resulting isotopic deviations.

The isotopic character of oxygen incorporated in travertine deposits is also known

to be strongly controlled by fractionation effects. Magnitude of these effects is highly dependent upon: 1) temperature under which travertine precipitation occurs, and 2) conditions of the $CaCO_3$ <— H_2O isotopic fractionation. For equilibrium fractionation, the temperature dependence of the $CaCO_3$ <— H_2O fractionation factor is well known. It is also well known that, for most travertine deposits, the equilibrium isotopic fractionation is seldom attained and precipitation of travertines occurs as an isotopic disequilibrium process instead. The disequilibrium fractionation effects may cause, relative to the equilibrium $CaCO_3$ <— H_2O fractionation factor, the actual fractionation factor to be either smaller or larger. The observed magnitude of this discrepancy may be as large as ± 5.0 per mil_{SMOW} (e.g., Turi, 1986).

Finally, during residence of a crustal fluid at the topographic surface, both the oxygen isotopic composition of this fluid and the conditions of the $CaCO_3$ <— H_2O isotopic fractionation do not remain constant. As sheet-travertine deposits precipitate from a fluid, they undergo progressive isotopic evolution. As a fluid degasses and evaporates it becomes increasingly enriched in ^{18}O due to both diffusional and evaporative-enrichment mechanisms. Concurrently, as the fluid cools, the $CaCO_3$ <— H_2O fractionation factor becomes progressively larger. Responding to both of these isotopic modifications, the precipitated sheet-travertine deposits become progressively enriched in ^{18}O. These isotopic enrichments are well represented in the Amargosa Basin spring and marsh deposits (Hay et al., 1986). From these results (Figures 5a, b), it may be observed that, relative to calcareous deposits from the proximal parts of the spring-fed depositional basin, the corresponding distal deposits are progressively enriched in ^{18}O, from 16.0-18.0 to a maximum of 26.0 per mil_{SMOW}.

From the above discussions, it is evident that the isotopic character of oxygen incorporated in a moderately heavy deposit ($\delta^{18}O \geq \sim 14$ per mil_{SMOW}) may not be used as a unequivocal indicator of the origin of this deposit. Both the multitude and variability of factors that control this character virtually assure that each hypothesis, put forth with regard

to the origin of a deposit, may be contested by the equally valid counter-hypotheses. By its very nature the oxygen-based genetic interpretation does not have a unique resolution unless, of course, oxygen isotope gradients are considered. These gradients (i.e., rate of change of the $\delta^{18}O$ ratio as a function of either depth or lateral distance) may reveal the conditions of precipitation of the controversial deposits at Yucca Mountain. In turn, these inferred conditions may be employed to test each one of the competing hypotheses. In that regard, the following two tests are particularly promising.

On the one hand, a depth distribution of the $\delta^{18}O$ ratio from calcitic veins (the $\delta^{18}O$ vs. depth gradient) may be employed to reconstruct the corresponding rate of the depthward increase of temperature (i.e., paleogeothermal gradient) under which these veins were precipitated. If the questionable veins were precipitated via the supergene-pedogenic mechanism, then these veins should yield values of the paleogeothermal gradient that are equivalent to contemporary observed values. In contrast, noticeably-higher relative values of the reconstructed geothermal gradient may be regarded as favoring the competing hypogene genesis.

On the other hand, a lateral distribution of the $\delta^{18}O$ ratios from calcretes (i.e., the $\delta^{18}O$ vs. lateral distance gradient) may be employed to ascertain whether or not the isotopic composition of the corresponding parent fluids were undergoing the expected isotopic modification or enrichment. For a calcrete with the same age, the presence of a noticeable isotopic gradient is supportive of the hypogene hypothesis. The absence of such gradient, however, allows for further considerations of the competing supergene-pedogenic hypothesis.

Surficial Veins and Calcretes

From the stable isotope data published by Whelan and Stuckless (1990) and by Quade and Cerling (1990) it is known that the $\delta^{18}O$ values of the controversial surficial veins and calcretes at Yucca Mountain range from 19.0 to about 22.0 per mil_{SMOW} (Figure

6). Based on these data, what may reasonably be inferred with regard to the origin of these deposits (i.e., supergene-pedogenic or hypogene)? Considering the substantial uncertainties that are involved in interpretations of oxygen isotopic data, the frank answer must be: not too much. Although one can be reasonably certain that the deposits in question were precipitated at relatively low temperatures it is not possible to: 1) specify a reliable and fairly narrow (only a few degrees Celsius) range for these temperatures, and 2) use the inferred temperatures to discriminate one possible origin against the other. To illustrate this point, the following two examples may be considered.

On the one hand, recognizing that a weighted average value of $\delta^{18}O$, for the local contemporary atmospheric precipitation, is about -12.0 per mil_{SMOW}, (Ingraham et al., 1990), it can be speculated that the controversial veins and calcretes could have precipitated from supergene-pedogenic fluids at an ambient temperature of ~15°C. For this temperature and under the conditions of equilibrium isotopic fractionation (the $CaCO_3$ <— H_2O fractionation factor is ~30 per mil_{SMOW}), supergene-pedogenic fluids could yield calcareous deposits with $\delta^{18}O$ values of about 18.0 per mil_{SMOW}. Small differences between the computed and observed values may readily be attributed to, for example, a ^{18}O evaporative-enrichment of the parent fluids.

On the other hand, it is equally feasible to maintain that the supergene-pedogenic origin is not uniquely evident and that the controversial deposits could have been precipitated from hypogene-epithermal fluids. Within the context of this speculation it is reasonable to expect that the deposits could have been precipitated under circumstances commonly observed in association with near-surface geothermal systems. Specifically, epithermal calcites are known to commonly precipitate: 1) from fluids that underwent rock <—> fluid isotopic exchange reactions and, consequently, exhibit the so-called "oxygen isotopic shift", 2) from fluids that are undergoing CO_2 degassing and, relative to their pristine state, are slightly enriched in ^{18}O via the diffusional enrichment mechanism, and 3) under the conditions of disequilibrium isotopic fractionation whereby the actual $CaCO_3$

<— H_2O fractionation factor is both smaller (as much as 6.0 per mil_{SMOW}) and higher (as much as 5.0 per mil_{SMOW}) than the equilibrium fractionation factor (Turi, 1986). There is no way to know what significance each of these factors could have played in controlling the isotopic character of the oxygen incorporated in the Yucca Mountain surficial veins and calcretes. Based on information presently available, and if these veins and calcretes are of the epithermal origin, they may have precipitated at a temperature anywhere within a range from 15°C to as much as 55°C.

From the above considerations it is evident that the oxygen isotopic data can hardly be regarded as supportive of supergene-pedogenic origin for the controversial veins and calcretes at Yucca Mountain. This cautioning remark is somewhat reinforced by noting that the isotopic character of the incorporated oxygen of these deposits is similar to that incorporated in calcareous material whose hypogene origin is unquestionable. The Amargosa spring-marsh deposits and carbonate gangue associated with the Carlin and Cortez gold deposits of Nevada are particularly relevant. For the former $\delta^{18}O$ values range from 16.0 to 26.0 per mil_{SMOW} (Hay et al., 1986); for the latter, the corresponding range is from 12.0 to 24.0 per mil_{SMOW} (Rye, 1985). Both of these ranges are similar to the 19.0-22.0 per mil_{SMOW} range observed at Yucca Mountain.

Subsurface Calcitic Veins

Calcitic veins are present throughout the entire ~2 km of stratigraphic section at Yucca Mountain. The oxygen isotopic character of these deposits is known from the isotopic analyses of Whelan and Stuckless (1991). These analyses reveal that for an explored depth range of 77m to as much as 1794m, the calcitic veins occur as two texturally and isotopically distinct facies (Figures 15 and 16). The first facies consists of calcitic veins which, in terms of incorporated oxygen, are isotopically-light ($\delta^{18}O \cong 4.0$ to 12.0 per mil_{SMOW}). Sometimes such veins are associated with barite, fluorite, and pyrite and typically they exhibit a sparry texture. The second facies consists of calcitic veins

which are distinctly heavier ($\delta^{18}O$ 13.0 to 22.0 per mil_{SMOW}). These veins can be associated with opal-CT and sepiolite and are micritic in texture.

The bi-modality of both the $\delta^{18}O$ values and calcite textures may reflect the existence of two chemically- and isotopically-distinct alteration and mineralization assemblages, as inferred earlier in this text (Figure 16). The Timber Mountain assemblage, in addition to the alkalic pro-grade zeolitization and illitization (brought about by the ^{87}Sr depleted fluids with the soda-potash bulk composition) also includes the calcitic veins which concurrently are depleted in both ^{87}Sr and ^{18}O, and enriched in ^{13}C. The earlier deduced hydrothermal origin of this entire assemblage seems to be confirmed by the paleogeothermal reconstructions of Whelan and Stuckless (1991). Based on the depth distribution of the ^{18}O-depleted calcites (i.e., the rate of increase of the $\delta^{18}O$ ratios as a function of depth), the reconstructed value of the paleogeothermal gradient is as large as 140° C/km (Figure 17).

In addition to the alkaline-earth zeolitization (brought about by the ^{87}Sr enriched fluids with the lime-magnesium bulk composition) the subsequent assemblage also includes the calcitic veins which concurrently are enriched in both ^{87}Sr and ^{18}O, and depleted in ^{13}C. The controversial origin of this assemblage may be further scrutinized by noting that, in addition to being associated with the abnormal strontium isotopic characteristics and the alkaline earth metasomatism, this assemblage seems to be also associated with an abnormal depth distribution of oxygen isotopes. The abnormal character of this distribution becomes apparent by noting that the value of the paleogeothermal gradient is as large as ~34°C/km (Whelan and Stuckless, 1992, Figure 17).

Present-day (contemporary) and spatially corresponding geothermal gradients are known from downhole measurements (Sass et al., 1987). These geothermal gradients are: 1) UE-25a#1, dT/dz~22°C/km; 2) USW G-2, dT/dz~24°C/km; 3) USW G-3, dT/dz~22°C/km; and 4) USW G-4, dT/dz~20°C/km. As can clearly be seen from these

values, the reconstructed paleogeothermal gradient significantly exceeds the contemporary gradient. The minimum discrepancy is about 50% and by any standard of judgment this is a significant discrepancy.

A significance of comparing the paleo and contemporary geothermal gradients is that this discrepancy in value is not consistent with, or supportive of, a supergene-pedogenic origin for the micritic and ^{18}O enriched calcites. Reconstructed paleogeothermal gradients for supergene calcites ought to be equal to contemporary gradients. This is because it is totally unreasonable to associate infiltrating rainwater with a noticeable warming of rock through which this rainwater percolates. For ascending hypogene fluids, however, the opposite is true. Even minor heating of rock volumes measured in km^3 requires very large amounts of energy and, for natural circumstances, is conceivable only with the involvement of deep-seated hot or warm fluids.

Conclusions

In summary, based on the oxygen isotopic data alone, we are not able to find firm support for a supergene-pedogenic origin of the controversial micritic veins and the affiliated calcretes, as advocated by the USGS and NAS/NRC scientists. Far from proving such an origin, the oxygen isotopic data may be interpreted as favoring a hypogene origin. The elevated value of the paleogeothermal gradient, reconstructed based on the rate of depthward change of the $\delta^{18}O$ ratio from the calcitic veins, is particularly noteworthy. Further support for the hypogene origin of the controversial calcite-silica deposits is suggested by the correspondence of $\delta^{18}O$ values with corresponding values from the hypogene deposits of the Amargosa Basin and Carlin and Cortez gold deposits of Nevada.

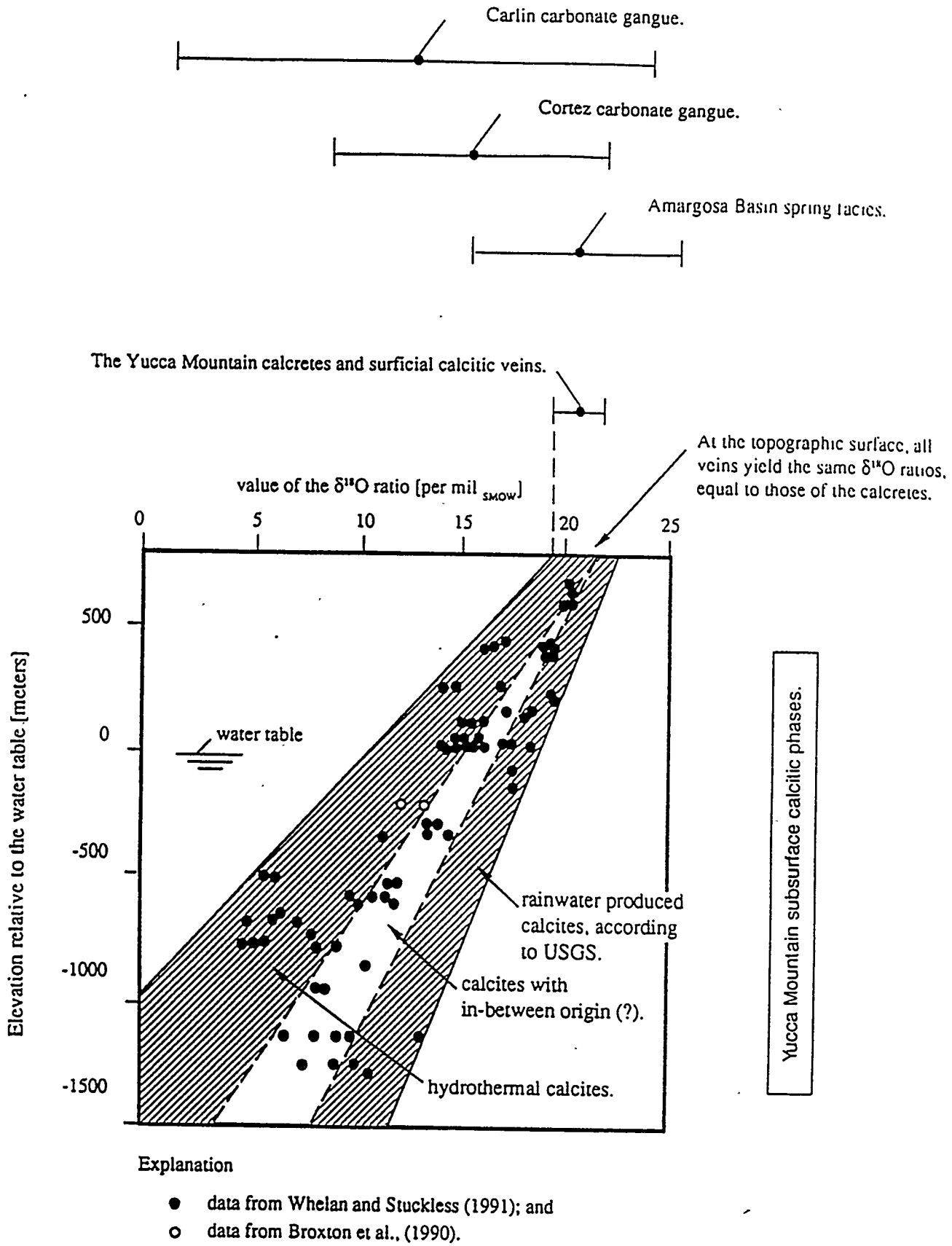

Note:
The remaining isotopic data are from Hay et al. (1986) and Rye (1985).

Figure 15. Isotopic character of oxygen incorporated in the Yucca Mountain calcitic phases.

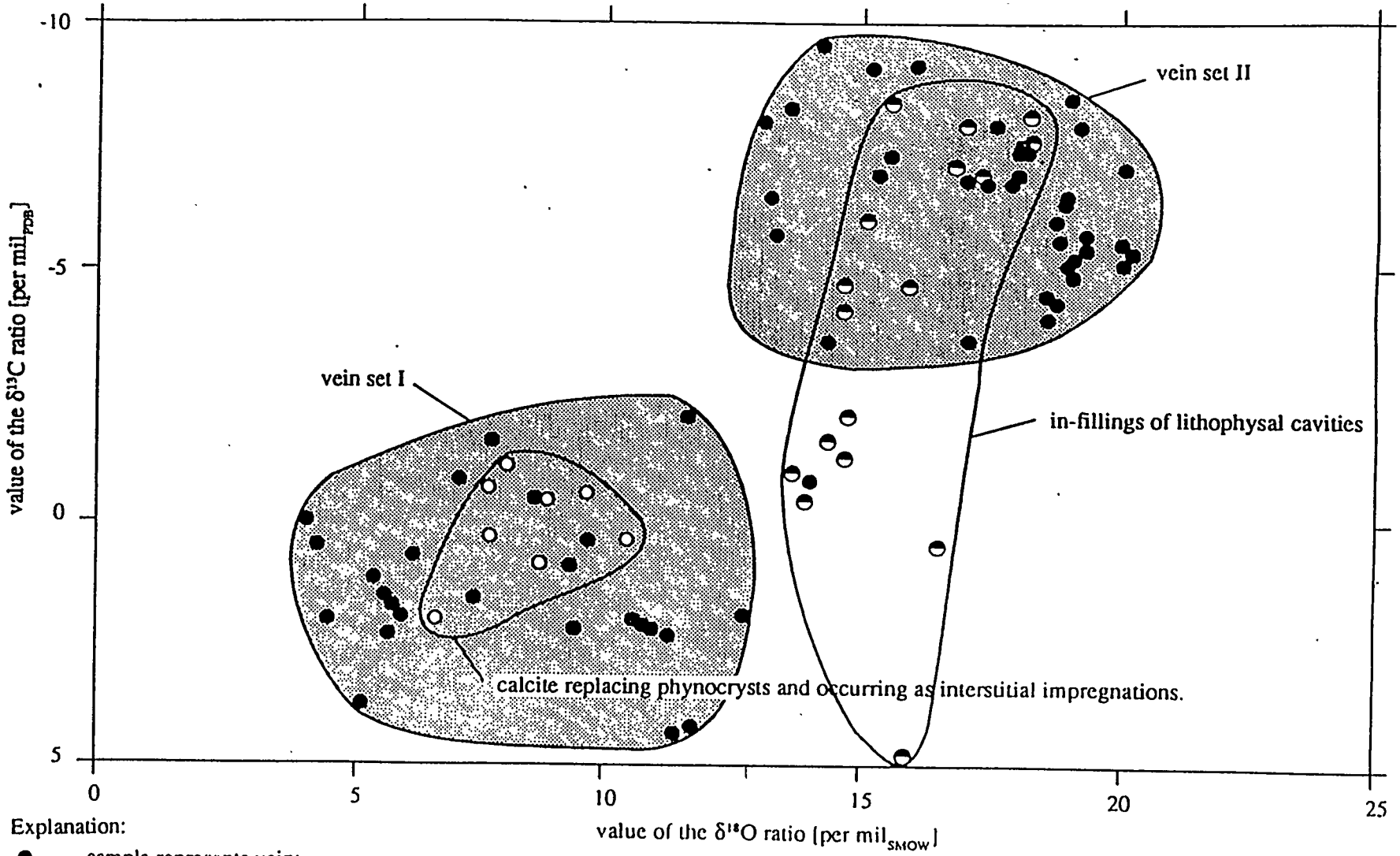

Explanation:

- ● - sample represents vein;
- ◑ - sample represents in-filling of lithophysal cavities; and
- ○ - sample represents calcite replacing phynocrysts and occurring as interstitial impregnations (cements)

Note:
Isotopic data are from Whelan and Stuckless (1991).

Figure 16. The $\delta^{13}C$ ratios vs. the $\delta^{18}O$ ratios for samples of calcitic phases from the Yucca Mountain ignimbrites.

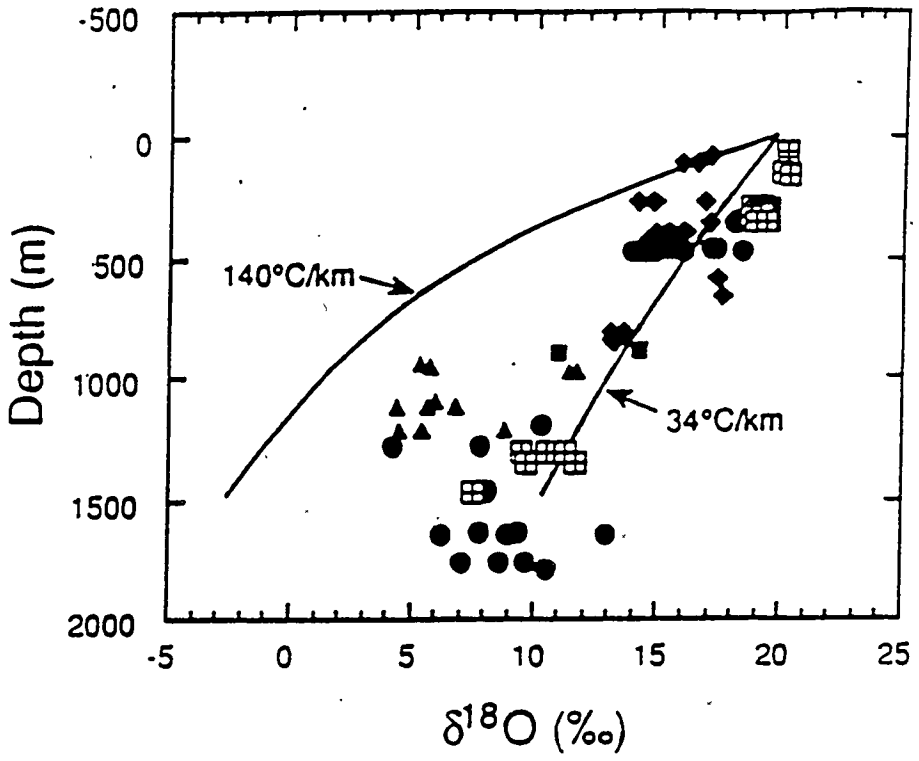

Note:

a) the paleo-geothermal reconstructions shown are based on the depth-distribution of values of the $\delta^{18}O$ ratio, as observed in boreholes USW G-1, G-2, G-3, GU-3, G-4, and UE-25b #1;

b) the actually measured values of the contemporary geothermal gradient range from 18 to no more than 24° C/km (USW G-1 - 18° C/km; G-2 - 24° C/km; G-3 - 22° C/km; G-4 - 24° C/km; and UE-25 b#1 - 20° C/km, Sass et al., 1987);

c) a factor of $\geq$ 1.5 discrepancy, between the observed and the reconstructed values of the geothermal gradient, indicates that the Yucca Mountain veins were formed exclusively in association with hypogene geothermal processes; and

Figure 17. Results of paleo-geothermal reconstructions, the Yucca Mountain calcitic veins. From Whelan and Stuckless (1992).

Isotope Geochemistry Overall Conclusions

A critical examination of the extensive isotopic data, as presented in the preceding sections, leads to the following three conclusions. **First, the currently available isotopic data do not provide any known support for the supergene-pedogenic origin of the controversial calcite-opal CT-sepiolite assemblage. Far from reliably establishing such an origin, the isotopic data provide as much as five independent lines of evidence against this origin.** These five are: 1) the depth distribution of $\delta^{18}O$ is not in accord with geothermal conditions that can be reasonably associated with the supergene-pedogenic mechanism, but instead suggests crystallization of the controversial veins occurred under elevated geothermal gradients; 2) the isotopic character of the incorporated strontium is not in accord with infiltrating rainwaters which have Paleozoic carbonate derived dust dissolved in them; 3) temporally, the controversial veins may have formed contemporaneously with periods of local magmatic activity; 4) spatially, the controversial veins appear to be accompanied by calcites containing fluid inclusion homogenization temperatures well in excess of the ambient temperature; and 5) spatially and isotopically (strontium ratio), the controversial veins seem to be associated with alkaline earth metasomatism where large volumes of rock have been enriched in ^{87}Sr, which enrichment strongly favors a hypogene origin.

Second, in contrast to the supergene-pedogenic model, the competing hypogene model is not contradicted by any of the examined isotopic data. In favor of the hypogene origin are lines of evidence which involve a number of independent elements. Among these are: 1) the isotopic character of uranium, carbon, strontium, and oxygen of the controversial deposits is explainable within the context of the postulated hypogene origin, 2) the isotopic character of incorporated uranium, carbon, strontium, and oxygen in these deposits is clearly equivalent to hypogene analogs, and 3) crystallization of the controversial veins seems to be contemporaneous with local magmatism and displays

paragenetic affinity with the alkaline earth metasomatism.

Finally, within the context of considering a suitability of Yucca Mountain, for either site characterization or for the development of a high-level nuclear waste repository, both the calcite-opal CT-sepiolite veins and the affiliated calcretes are of two-fold significance. First, the fact that the vein-calcite assemblage may be identified at the topographic surface seems to contribute to a reliable resolution of the dilemma involving the expected magnitudes of co-seismic or co-magmatic hydrologic effects. In contrast to assurances given by many scientists, rather than being measured in terms of feet and meters, these effects seem to be measured in terms of hundreds of meters. Second, the calcite-opal CT-sepiolite assemblage and the metasomatic alteration products (zeolites) display a wide range of U/Th and K/Ar ages (from 8.5 Ma to as little as 30 ka). Rather than being restricted to an isolated and distant-past episode, these processes seem to be operating on an intermittent basis instead and probably extend to the present. The directly observed field relationships, the K/Ar ages of metasomatic clinoptilolites, and the U/Th ages of the calcitic veins all seem to be unanimous in that regard.

LIST OF FIGURES

REFERENCES

Archambeau, C. B., and N. J. Price, 1991. *An Assessment of J. S. Szymanski's Conceptual Hydro-Tectonic Model and Its Relevance to Hydrologic and Geologic Processes at the Proposed Yucca Mountain Nuclear Waste Repository.* Minority Report of the Special DOE Review Panel. U. S. Department of Energy. Las Vegas, Nevada.

Aronson, J. L., and D. L. Bish, 1987. *Distribution, K/Ar Dates, and Origin of Illite/Smectite in Tuffs from Cores USW G-1 and USW G-2, Yucca Mountain, Nevada, a Potential High-Level Radioactive Waste Repository.* Clay Mineral Society, 24th Annual Meeting. Socorro, New Mexico.

Bish, D. L., 1989. *Evaluation of Past and Future Alterations in Tuff at Yucca Mountain, Nevada, based on the Clay Mineralogy of Drill Cores USW G-1, G-2, and G-3.* Los Alamos National Laboratory, LA-10667-MS. Los Alamos, New Mexico.

Bish, D. L., and S. J. Chipera, 1989. *Revised Mineralogical Summary of Yucca Mountain, Nevada.* Los Alamos National Laboratory, LA-11497-MS. Los Alamos, New Mexico.

Broxton, D. E., R. G. Warren, R. C. Hagan, and G. Luedemann, 1986. *Chemistry of Diagenetically Altered Tuffs at a Potential Nuclear Waste Repository, Yucca Mountain, Nye County, Nevada.* Los Alamos National Laboratory, La-10802-MS. Los Alamos, New Mexico.

Carlisle, D., 1983. *Concentration of Uranium and Vanadium in Calcretes and Gypcretes.* In Residual Deposits: Surface Related Weather in Precesses and Materials. R. C. L. Wilson (ed.). The Geological Society of London, Blackwell Scientific Publications.

Carlos, B. A., 1987. *Minerals in Fractures of the Saturated Zone from Drill Core USW G-4, Yucca Mountain, Nye County, Nevada.* LA -10927, Los Alamos National Laboratory. Los Alamos, New Mexico.

Carlos, B. A., D. L. Bish, and S. J. Chipera 1990. *Manganese - Oxide Minerals in Fractures of the Crater Flat Tuff in Drill Core USW G-4, Yucca Mountain, Nevada.* Los Alamos National Laboratory, LA-11787-MS. Los Alamos, New Mexico.

Clayton R. N., A. Steiner, 1975. *Oxygen Isotope Studies of the Geothermal System at Warakei, New Zealand.* Geochimica at Cosmochimica Acta, 39.

dePolo, C. M., D. G. Clark, D. B. Slemmons, and A. R. Ramelli, 1991. *Historical Surface Vaulting in the Basin and Range Province, Western North America: Implications for Fault Segmentation.* Journal of Structural Geology. Vol. 13, No. 2, pp. 123-136.

Dudley, W. W., Jr., G. E. Barr, D. A. Chesnut, and C. J. Fridrich (eds.), 1989. *Review of a Conceptual Model and Evidence for Tectonic Control of the Ground-Water System in the Vicinity of Yucca Mountain, Nevada.* U. S. Department of Energy. Las Vegas, Nevada.

Evans, J. R., and M. Smith, 1992. *Teleseismic Tomography of the Yucca Mountain Region: Volcanism and Tectonism.* High-Level Radioactive Waste Management Proceedings. American Nuclear Society. Las Vegas, Nevada.

Evernden, J. F. 1992. *Safety of Proposed Yucca Mountain Nuclear Repository as Regards Geological and Geophysical Factors: Evaluation of Minority Report by Archambeau and Price.* U. S. Geological Survey Open-File Report 92-516.

Faure, G., 1986. *Principles of Isotope Geology.* John Wiley and Sons, Inc. New York, NY.

Goff, F., H. A. Wollenberg, D. G. Brookins, and R. W. Kistler, 1990. *A Sr-Isotope Comparison Between Thermal Waters, Rocks and Hydrothermal Calcites, Long Valley Caldera, California.* Draft Paper Accepted by Journal of Volcanology and Geothermal Research.

Goudie, A., 1973. *Duricrusts in Tropical and Subtropical Landscapes.* Oxford, Clarendon Press.

Hay, R. L., R. E. Pexton, T. T. Teague, and T. K. Kyser, 1986. *Spring-Related Carbonate Rocks, Mg Clays, and Associated Minerals in Pliocene Deposits of the Amargosa Desert, Nevada and California.* Geological Society of American Bulletin, 97.

Harrison, T. M, R. L. Armstrong, C. W. Naeser, and J. E. Harakal, 1979. *Geochronology and Thermal History of the Coast Plutonic Comples, Near Prince Rupert, British Colombia.* Canadian Journal of Earth Sciences. Vol. 16.

Hill, C. A., 1993. *Trip Report, Yucca Mountain, December 5-9, 1992.* Special Report No. 2. Submitted to the State of Nevada Agency For Nuclear Projects, Nuclear Waste Project Office. Technical and Resource Assessment Corporation. Boulder, Colorado.

Hoefs, J., 1987. *Stable Isopope Geochemistry.* Springer-Verlag.

Hurford, A. J., 1986. *Cooling and Uplift Patterns in the Lepontine Alps, South Central Switzerland and an Age of Vertical Movement on the Insubric Fault Line.* Contributions to Mineralogy and Petrology. Vol. 92.

Ingraham, N. L., R. L. Jacobson, J. W., Hess, and B. F. Lyles, 1990. Stable Isotopic Study of Precepitation and Sping Discharge on the Nevada Test Site. Water Resources Center. Desert Research Institute. University of Nevada System Publication #45078.

Kistler, R. W., and Z. E. Peterman, 1973. *Variations in Sr, Rb, K, Na and Initial $^{87}Sr/^{86}Sr$ in Mesozoic Cranite Rocks and Intruded Wall Rocks in Central California.* Geological Society of America Bulletin, 84.

Lambert, S. J., S. Epstein, 1980. *Stable Isotope Investigations of an Active Geothermal System in Valles Caldera, Jemez Mountains, New Mexico.* Journal of Volcanology and Geothermal Research. Vol. 8.

Levy, S. and C. W. Naeser, 1991. *Bedrock Breccias Along Fault Zones Near Yucca Mountain, Nevada.* Draft report submitted for publication by the U. S. Geological Survey. Los Alamos National Laboratory. Los Alamos, New Mexico.

Leeman, W. P., B. R. Doe, and J. Whelan, 1977. *Radiogenic and Stable Isotope Studies of Hot-Spring Deposits in Yellowstone National Park and Their Genetic Implications.* Geochem. J., 11.

Livingston, D. E., 1992. *Some Aspects of Alteration and Metasomatism at Yucca Mountain, Nevada. Presentation to: The Association Of Engineering Geologists, Southwestern Section, Las Vegas Subsection.* Las Vegas, Nevada.

Livingston, D. E., 1993. *A Review of the Major Element Geochemistry of Yucca Mountain, Nevada.* Quarterly Report No. 4. Submitted to the State of Nevada Agency For Nuclear Projects, Nuclear Waste Project Office. Technical and Resource Assessment Corporation. Boulder, Colorado.

Machette, M. N., 1985. *Calcic Soils of the Southwestern United States.* Geological Society of America Special Paper 203. Weide, D. L. (ed.).

Maldonado, F., and S. L. Koether,1983. *Stratigraphy, Structure, and Some Petrographic Features of Tertiary Volcanic Rocks at the USW G-2 Drill Hole, Yucca Mountain, Nye County, Nevada.* U. S. Geological Survey Open File Report 83-732.

Marshall, B. D., Z. E. Peterman, K. Futa, J. S. Stuckless, S. A. Mahan, J. S. Downey, and E. D. Gutentag, 1990. *Origin of Carbonate Deposits in the Vicinity of Yucca Mountain, Nevada: Preliminary Results of Strontium-Isotope Analyses.* High-Level Radioactive Waste Management Proceedings. American Nuclear Society. Las Vegas, Nevada.

NAS/NRC, 1992. *Ground Water at Yucca Mountain How High Can It Rise?* Final Report of the Panel on Coupled Hydrologic/Tectonic/Hydrothermal Systems at Yucca Mountain. National Research Council. National Academy Press. Washington, D. C.

Peterman, Z. E., 1990. *Material Provided to the Special DOE Panel.*

Peterman, Z. E., R. W. Spengler, K. Futa, B. D. Marshall, and S. A. Mahan, 1991. *Assessing the Natural Performance of Felsic Tuffs Using the Rb-Sr and Sm-Nd Systems - A Study of the Altered Zone in the Topopah Spring Member, Paintbrush Tuff, Yucca Mountain, Nevada.* Materials Research Society Symposium Proceedings. Vol. 212.

Peterman, Z. E., J. S. Stuckless, B. D. Marshall, S. A. Mahan, and K. Futa, 1991. *Strontium Isotope Geo-chemistry of Calcite Fracture Fillings in Deep Core, Yucca Mountain, Nevada.* Draft USGS Paper.

Quade, J., T. E. Cerling, and J. R. Bowman, 1989. *Systematic Variations in the Carbon and Oxygen Isotopic Composition of Pedogenic Carbonate Along Elevation Transects in the Southern Great Basin, United States.* Geological Society of America Bulletin. Vol. 101.

Quade, J., and T. E. Cerling, 1990. *Stable Isotopic Evidence for a Pedogenic Origin of Fracture-Filling Carbonates in Trench 14 Near Yucca Mountain, Nevada.* Science. Vol. 250.

Ramelli, A. R., J. W. Bell and C. M. dePolo, 1991. *Late Quaternary Faulting at Crater Flat, Yucca Mountain, Southern Nevada.* Annual Progress Report, Task 1, Appendix E. Prepared by the Center for Neotectonic Studies. University of Nevada, Reno, for the State Agency for Nuclear Projects, Nuclear Waste Project Office.

Rankama, K., 1954. *Isotope Geology.* McGraw-Hill Book and Pergamon Press.

Rye, R. O., 1985. *A Model for the Formation of Carbonate-Hosted Disseminated Gold Deposits Based on Geologic, Fluid-Inclusion Studies of the Carlin and Cortez Deposits, Nevada.* USGS Bulletin 1646.

Sass, J. H., A. H. Lachenbruch, and C. W. Mase, 1980. *Analysis of Thermal Data from Drill Holes UE24a-3 and UE25a-1, Calico Hills and Yucca Mountain, Nevada Test Site.* U. S. Geological Survey Open File Report 80-826.

Sass, J. H., A. H. Lachenbruch, H. Grubb, and T. H. Moses, 1983. *Status of Thermal Observations at Yucca Mountain, Nevada.* USGS Letter Report.

Sass, J. H., A. H. Lachenbruck, W. W. Dudley, Jr., S. S. Priest, and R. J. Munroe, 1987. *Temperature, Thermal Conductivity, and Heat Flow Near Yucca Mountain, Nevada: Some Tectonic and Hydrologic Implications.* U.S. Geological Survey Open-File Report 87-649.

Sass, J. H., D. D. Blackwell, D. S. Chapman, J. K. Costain, E. R. Decker, L. A. Lawver, and C. A. Swanberg, 1981. *Heat Flow from the Crust of the United States.* Physical Properties of Rocks and Minerals. Y. S. Touloukin, W. R. Judd, and R. F. Roy (eds.). McGraw-Hill, New York. Vol. II, Chapter 13, pp. 503-540.

Schlesinger, W. H., 1985. *The Formation of Caliche in Soils of the Mojave Desert, California.* Geochimica at Cosmochimica Acta, 49. Pergamon Press.

Scott, R. B. and M. Castellanos, 1984. *Stratigraphic and Structural Relations of Volcanic Rocks in Drill Holes USW GU-3 and USW G-3, Yucca Mountain, Nye County, Nevada.* U. S. Geological Survey Open File Report 84-491.

Scott, R. B., and J. Bonk, 1984. *Preliminary Geologic Map of Yucca Mountain, Nye county, Nevada.* With Geologic Sections. U. S. Geological Survey Open File Report 84-494.

Science Applications International Corporation, 1992. *Report of Early Site Suitability Evaluation of the Potential Repository Site at Yucca Mountain, Nevada.* SAIC-91/8000. Prepared for the Office of Civilian Radioactive Waste Management. Las Vegas, Nevada.

Sheppard, R. A., A. J. Gude, 3rd and J. J. Fitzpatrick, 1988. *Distribution, Characterization, and Genesis of Mordenite in Miocene Silicic Tuffs at Yucca Mountain, Nye County, Nevada.* U.S. Geological Survey Bulletin-1777.

Smith, S. W., and R. Kind, 1972. *Regional Secular Strain Fields in Southern Nevada.* Tectonophysics. Vol. 14, pp. 57-69.

Spengler, R. W., and M. P. Chornack, 1984. *Stratigraphic and Structural Characteristics of Volcanic Rocks in Core Hole USW G-4, Yucca Mountain, Nye County, Nevada.* U. S. Geological Survey Open File Report 84-789.

Spengler, R. W., F. M. Byers, and J. B. Warner, 1981. *Stratigraphy and Structure of Volcanic Rocks in Drill Hole USW-G1, Yucca Mountain, Nye County, Nevada.* U. S. Geological Survey Open File Report 81-1349.

Stock, J. M., J. H. Healy, S. H. Hickman, and M. D. Zoback, 1985. *Hydraulic Fracturing Stress Measurements at Yucca Mountain, Nevada, and Relationship to the Regional Stress Field.* Journal of Geophysical Research. Vol. 90, No. B10, pp. 8691-8706.

Stuckless, J. S., Z. E. Peterman, and D. R. Muchs, 1991. *U and Sr Isotopes in Ground Water and Calcite, Yucca Mountain, Nevada: Evidence Against Upwelling Water.* Science. Vol. 254.

Summerfield, M. A., 1983. *Silcrete in Chemical Sediments and Geomorphology: Precipitates and Residue in the Near-Surface Environment.* Academic Press. Goudie, A. S., and Pye, K., (eds.).

Szabo, B. J., W. J. Carr, and W. C. Gottschall, 1981. *Uranium - Thorium dating of Quaternary Carbonate Accumulations in the Nevada Test Site Region, Southern Nevada.* U. S. Geological Survey Open File Report 81-119.

Szabo, B. J., and T. K. Kyser, 1985. *Uranium, Thorium Isopotic Analyses and Uranium-Series Ages of Calcite and Opal, and Stable Isotopic Compositions of Calcite from Drill Cores UE25a#1, USW G-2, and USW G-3/Gu-3, Yucca Mountain, Nevada.* U.S. Geological Survey Open-File Report 85-224.

Szabo, B. J., and P. A. O'Malley, 1985. *Uranium-Series Dating of Secondary Carbonate and Silica Precipitates Relating to Fault Movement in the Nevada Test Site Region and of Caliche and Travertine Samples from the Amargosa Desert.* U.S. Geological Survey Open-File Report 85-47. Denver, Colorado.

Szymanski, J. S., 1987. *Conceptual Considerations of the Death Valley Groundwater System with Special Emphasis on the Adequacy of this System to Accommodate a High-Level Nuclear Waste Repository.* DOE Internal Report. U.S. Department of Energy. Las Vegas, Nevada.

Szymanski, J. S., 1989. *Conceptual Considerations of the Yucca Mountain Groundwater System with Special Emphasis on the Adequacy of this System to Accommodate a High-Level Nuclear Waste Repository.* DOE Internal Report. U.S. Department of Energy. Las Vegas, Nevada.

Szymanski, J. S., 1992. *The Origin and History of Alteration and Carbonatization of the Yucca Mountain Ignimbrites.* DOE Internal Report. U.S. Department of Energy, Las Vegas, Nevada.

Talma, A. S., and F. Netterberg, 1983. *Stable Isotope Abundances in Calcretes. In Residual Deposits: Surface Related Weathering Processes and Materials.* Wilson, R. C. L. (ed.). The Geological Society of London.

Turi, B., 1986. *Stable Isotope Geochemistry of Travertines.* P. Fritz and J. C. Fontes (eds.). Handbook of Environmental Isotope Geochemistry. Vol. 2.

Turrin, B. D., and D. E. Champion, 1991. *$^{40}Ar/^{39}Ar$ Laser Fusion and K-Ar Ages from Lathrop Wells, Nevada and Cima, California: The Age of the Latest Volcanic Activity in the Yucca Mountain Area.* Proceedings of the Second International High-Level Radioactive Waste Conference. Las Vegas, Nevada. pp. 68-75.

U. S. Department of Energy, 1988. *Site Characterization Plan: Yucca Mountain Site, Nevada Research and Development Area, Nevada.* DOE/RW 0199. Office of Civilian Radioactive Waste Management. Washington, D. C.

Usdowski, E., J. Hoefs, and G. Menschel, 1979. *Relationship Between ^{13}C and ^{18}O Fractionation and Changes in Major Element Composition in a Recent Calcite-Depositing Spring. A Model of Chemical Variations with Inorganic $CaCO_3$ Precipitation.* Earth Planetary Sciences Letters, 42.

Wells, S. G., L. D. McFadden, C. E. Renault, and B. M. Crowe, 1990. *Geomorphic Assessment of Late Quaternary Volcanism in the Yucca Mountain Area, Southern Nevada:* Implications for the Proposed High-Level Radioactive Waste Repository. Geology. Vol. 18, pp. 599-553.

Whelan, J. F., and J. S. Stuckless, 1990. *Reconnaissance $d^{13}C$ and $d^{18}O$ data from Trench 14, Busted Butte, and Drill Hole G-4, Yucca Mountain, Nevada Test Site.* International High Level Radioactive Waste Management Conference.

Whelan, J. F., and J. S. Stuckless, 1991. *Paleohydrologic Implications of the Stable Isotope Composition of Secondary Calcite Within theTertiary Volcanic Rocks of Yucca Mountain, Nevada.* Draft USGS Paper.

Whelan, J. F., and J. S. Stuckless, 1992. *Paleohydrologic Implications of the Stable Isotope Composition of Secondary Calcite Within theTertiary Volcanic Rocks of Yucca Mountain, Nevada.* High Level Waste Management. LaGrange Park, Illinois. Vol. 2.

White, A. F., M. L. Peterson, H. Wollenberg, and S. Flexer, 1990. *Sources and Fractionation Processes Influencing the Isotopic Distribution of H, O, and C in the Long Valley Hydrothermal System, California.* U. S. A. Applied Geochemistry. Vol. 5.

Whitney, J. W., and R. R. Shroba, F. W. Simonds, and S. T. Harding, 1986. *Recurrent Quaternary Movement of the Windy Wash Fault, Nye County, Nevada.* Geological Society of America. Abstracts with programs. Vol. 18, No. 6, p. 787.

WoldeGabriel, Giday, 1991. *Diagenetic Minerals, K/Ar Data, and Alteration History in The Yucca Mountain, Nevada; A Candidate High-Level Radioactive Waste Repository.* Los Alamos National Laboratory. Draft Report. Los Alamos, New Mexico.

Wood, R. M., and G. C. P. King, 1992. *Hydrological Signatures of Earthquake Strain.* Submitted to Journal of Geophysical Research.

Yang, I. C., 1989. *Conceptual Model of Unsaturated Zone Ground Water Flows at Yucca Mountain in Nevada, Based on Geochemical Isotope Data.* Draft USGS Report Submitted for Release as Proceedings for the April 1990 International High-Level Radioactive Waste Management Conference.

PART B - Section I

Extension of In-Situ Stress Test Analysis to Fractured Media with Reference to Yucca Mountain Data

J. B. Davies

Extension of In-Situ Stress Test Analysis to Fractured Media with reference to Yucca Mountain Data

Dr. John Bruce Davies

ABSTRACT

Yucca Mountain is underlain by highly fractured rock containing a deep water table. Stress tests have been performed in boreholes in-situ and under high head pressures. For a pre-fractured rock system, data analysis must incorporate the effects of opening and closing of fractures. As the head pressure increases from ambient, the aperture of the existing dilated fractures increase. The fracture surface area remains constant until the excess head increases to above a critical pressure, when induced fractures can open and existing fractures may propagate. These will furnish a larger rock surface area thereby allowing a more rapid percolation of the water into the rock matrix. We have extended previous models by specifying a functional dependence of both existing fracture aperture and induced fracture surface area and volume on the excess water pressure. Relationships are obtained through the mass conservation laws and these predictions are used as discriminative graphs, with the most useful being pressure versus rate of pressure change. Such type-curves are applied to Yucca Mountain data with interpretation in terms of the applicable fracture systems and the critical pressure. Estimates of the critical pressure are obtained and usually lie in the range of 10 to 30 bars which is appreciably lower than that expected from the lithostatic pressure effects. This implies that large dilational stresses exist at Yucca Mountain.

INTRODUCTION

The water table below Yucca Mountain is abnormally low compared to its surrounding hydrological environment. No general consensus has developed for an explanation of this abnormal depth of the water table which is of the order of 500 meters. One explanation is that the subsurface is a deforming fractured medium where dilatation of fractures has increased the storativity and hydraulic conductivity in this region and thereby depressed the water table. If large regions are subject to dilatational strains, any earthquake releasing such strains can be expected to alter the in-situ stress field, the hydraulic conductivity structure and, thus, the depth of the water table.

In order to investigate the state of stress above and below this abnormal water table, both hydrofracture and slug tests have been performed by injecting water into boreholes at and near Yucca Mountain. These in-situ stress tests will be analyzed to discover if existing and induced fractures can open and close under external pressure heads of water. In order to accomplish this analysis, we develop a simple but comprehensive model of these borehole and fracture flows. This flow model incorporates pre-existing fractures that readily dilate with increasing water head. New fractures can open above the critical pressure producing induced fracture surfaces, allowing more rapid drainage into the surrounding rock matrix. The model is flexible enough to incorporate loss of water out of the system through fractures that act as conduits to the external environment.

Drill-hole stress tests are usually performed by charging a small section along the hole, termed the "packed-off interval", with a head of water under its own and/or externally applied pressure. When tests are done under high pressures in a pre-

fractured rock system, it is necessary to extend the usual low-pressure test analysis to incorporate the effects of opening and closing fractures. Pre-existing fractures may dilate as soon as the pressure head increases from ambient, with apertures increasing while the surface area of the fractured system remains essentially constant. When the head is above the fracture closure pressure or critical pressure, previously induced fractures will open and thereby furnish a larger rock surface area that will allow a more rapid percolation of the water into the rock matrix, as pointed out by Hayashi and Haimson (1991).

This situation is mathematically and numerically modeled by developing a formulation that accounts for variable fracture area and volume. To this end, we formulate the conservation laws of mass, momentum and energy of the borehole-fracture system and adopt constitutive laws which specify exiting fluxes and fracture properties as a function of the existing excess pressure head. Only the mass conservation law need be applied if we assume a functional dependence of the area and aperture of the fracture systems on the excess pressure head. These assumptions allow us to obtain general relationships for the rate of change of the excess head in terms of the total rock surface area exposed and the rate of change of the volume of water in the fractured region.

These model solutions are used to determine discriminative graphs that are typical of different fracture systems and behaviour. For determining the critical pressure, one important type-curve is that of head versus rate of head change, as demonstrated previously by Baumgartner and Zoback (1989). The head drop rate is linearly related to the excess head when it is below the critical pressure and when either no fractures are

involved or when existing fractures have opened with aperture change linearly dependent on the excess head. However, above this closure pressure, the slope of the curve increases rapidly, as either induced fractures form or existing fractures propagate.

When the fractures open only a small amount under excess head, then most of the surplus water is stored in the drill-hole. When the fractures open a large amount under excess head, then most of the surplus water is stored in the fracture system. If both these cases have the same exiting flux, i.e. a fixed fracture area, permeability and porosity, the excess head in the borehole will decrease more rapidly in the first case as the largest fraction of water is in the borehole. When the existing fractures open readily under excess head, the storativity of the fracture system is much greater than that of the drill-hole. Thus, under the condition that the same amount of water drains out of the system per unit time, the fraction exiting from the drill-hole, and therefore the pressure head drop rate at that particular head of pressure, will be much smaller when the fractures dominate storativity.

Type-curves and analyses, based on this modeling, are applied to Yucca Mountain data from slug tests performed by other investigators. The limited data allows initial analyses categorizing the observed curves in terms of the synthetic curves for different fracture systems. Closure pressures are determined, whenever possible, from inspection and non-linear curve fitting. The values of the fracture parameters for representative test data is found by curve matching. Areas, volumes and stiffness of both existing and induced fractures are obtained. The results are compared to previous qualitative arguments based on the same data.

CONSERVATION LAWS

Any fluid-rock system obeys the conservation laws of mass, momentum and energy. The interaction of the different components, together with stress-strain relations, are governed by constitutive laws. We shall develop the general equations of conservation for the simplest system which is composed of a borehole and a fractured rock system of variable geometry. A stylized representation of such a system is illustrated in Figure 1 and is similar to that used by Hayashi and Haimson (1991). It is assumed that water can exit the borehole-fracture system either by percolation into the surrounding rock or by flow out along conduits. The walls of the borehole and fractures are assumed to transmit the fluid into the porous rock matrix. The water is considered to be incompressible, so the density will be removed from all equations.

The conservation of mass under these conditions is given by:

$$\frac{d}{dt}(V_c + V_p) = Q \tag{1}$$

where V_c is the volume of water in the fractures at time t and V_p is the volume of water in the borehole. Q is the rate at which water exits the system either along conduits or by percolation into the rock face from the fractures and the borehole. This relation assumes no water is injected into the system after the head is allowed to free-fall. The volume of water in the borehole is given by the product of the cross-sectional area, $A_p = \pi R_p^2$, where R_p is the radius of the borehole pipe, times the height of the column of water. This height is equal to the sum of the excess head, h(t), and the depth of the borehole below the water table above the test region, which is a constant. Thus, conservation of mass can be written as:

$$A_p \frac{dh(t)}{dt} + \frac{d}{dt} V_c(t) = Q(t) \tag{2}$$

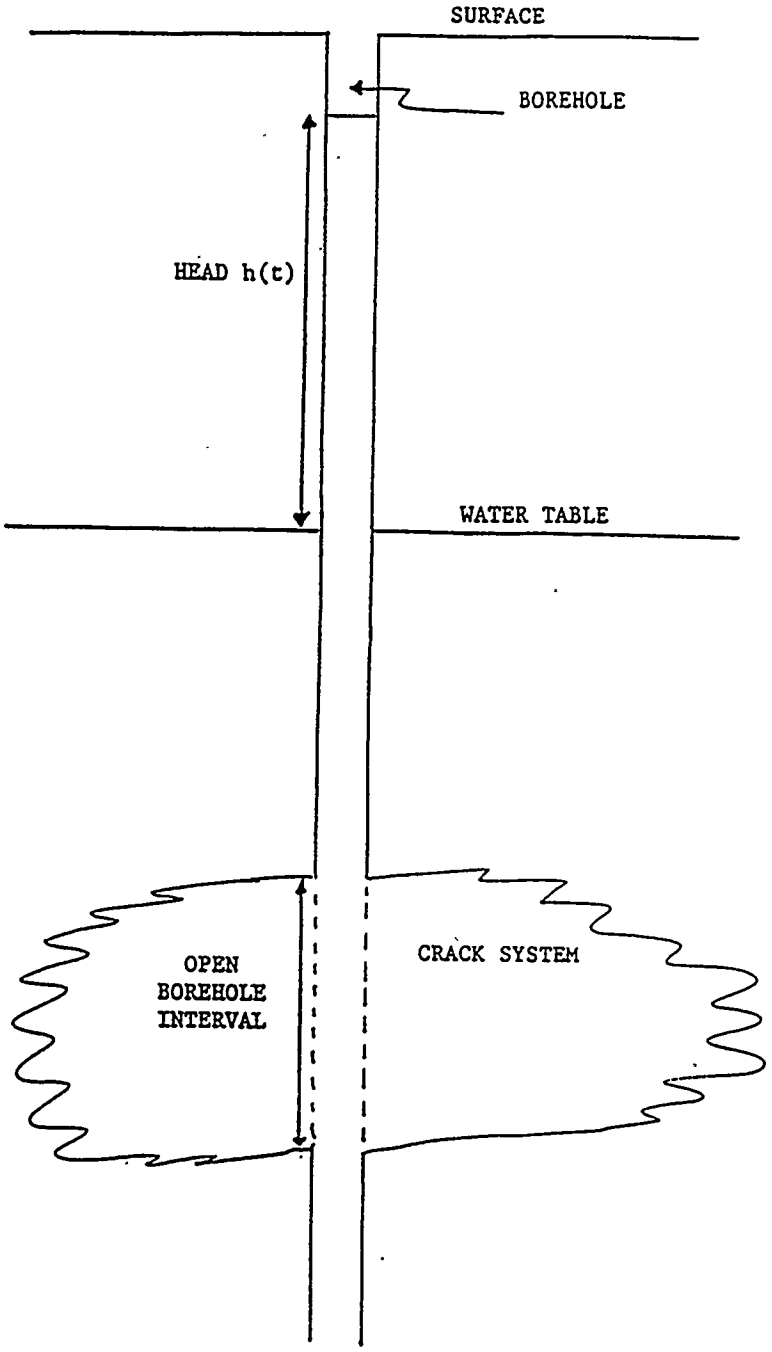

Figure 1 - Conceptual diagram of the borehole-fracture system subject to a head h(t) of water above the present water table.

Similarly, momentum conservation gives the relation:

$$\frac{d}{dt}(v_c V_c + v_p V_p) = Q v_r \tag{3}$$

where v_c is the velocity of the fluid in the fractured region, v_p is the fluid velocity in the borehole (i.e. dh/dt) and v_r is the velocity of fluid percolation into the rock matrix.

The law of conservation of energy can be stated:

$$\frac{d}{dt}(\text{ Potential Energy + Kinetic Energy + Strain Energy + Crack Energy }) = 0 \tag{4}$$

where, as usual, the density is taken as constant and removed from the relevant equations. As only the excess head above the water table contributes to the potential energy, this term is:

$$E_p = A_p\, g\, h^2/2 \tag{5}$$

The rate of change of kinetic energy of the water throughout the system is :

$$\frac{d}{dt}E_e = \frac{d}{dt}\left[\frac{1}{2}v_c^2 V_c + \frac{1}{2}\left[\frac{dh}{dt}\right]^2 V_p\right] + \frac{1}{2} Q v_r^2 \tag{6}$$

As the water is deemed incompressible, the strain energy of the water is taken as zero. The energy of the fractured system is given by Lardner (1974) from dislocation theory:

$$E_c = \int_{S(t)} \sigma_{ij} u_i n_j ds \tag{7}$$

where S(t) is the area of the fractured surface at time t, σ_{ij} is the stress on the fractured system at time t and u_j is the j component of displacement along the fracture surface with normal n_j at time t. This fracture energy equation can be evaluated, but, for the present argument, this will not be done as the constitutive relations assumed will be such that only the conservation of mass will be necessary.

CONSERVATION OF MASS

In order to examine the effect of the changing excess head, certain simple constitutive relations must be formulated for the storativity volume and the exiting flux. These will be inserted into the mass conservation law; that is in the equation :

$$A_p \frac{dh(t)}{dt} + \frac{d}{dt} V_c(t) = Q(t) \qquad (2)$$

We see that the fracture volume is an important property of the system whose value is the fracture area times the aperture. The surface area of pre-existing fractures is assumed constant when the excess water head is below the critical pressure, though their aperture will be a function of the applied head. When the head is greater than the critical pressure, we assume a constitutive relation whereby the volume and surface area of induced fractures is a function of the difference between the excess head and the critical pressure.

The volume of the pre-existing fractured region can be approximated by the product of the fractured area and an effective displacement orthogonal to the surface. We shall assume that any fractures present below the closure pressure have initial values of fracture surface area A_e and fracture volume V_e. Thus, for $h(t) < P_c$ we assume A_e is a constant, and $V_e = A_e * D_e$, where the fracture aperture D_e varies with changing head. As the imposed head increases, we shall expect the aperture of these pre-existing fractures to increase functionally with the applied head, i.e.

$$D_e = D_o + F(h) \qquad (8)$$

where D_o is the aperture at ambient pressures, F(h) is assumed to be a power-law or logarithmic function of head h and measures how readily the existing open fractures dilate under external head. Thus, for $h(t) < P_c$ we obtain the time derivative of

fracture volume as :

$$\frac{d}{dt}V_e(t) = A_e \cdot \frac{dF}{dh} \cdot \frac{dh}{dt} \tag{9}$$

When the external head is greater than the fracture closure pressure, induced fractures will open which have induced surface area and a finite volume. It will be assumed, to the first order, that the area of the induced fractured region, A_c, is a function of the head above the critical pressure, P_c. Thus, for $h(t) > P_c$, we assume:

$$A_c = G(h-P_c) \tag{10}$$

where G is a measure of the change of area with excess head. The function G is expected to be positive definite which may, for example, be a power-law or logarithmic function of the excess head above the critical pressure $h-P_c$. We will not assume initial knowledge of these functions, but will advance the analysis as far as possible without a specific functional form assumed. We shall use a functional dependence of aperture on head, as in the case of pre-existing fractures, but with different parameters for these initially closed fractures. We take :

$$D_c = J(h-P_c) \tag{11}$$

where the aperture is zero when $h = P_c$. The function J may be of power-law or logarithmic form, depending on the constitutive relation assumed. Incorporating these constitutive assumptions, for $h>P_c$, the rate of change of fracture volume is :

$$\frac{d}{dt}V_e = (A_e\frac{dF}{dh} + [G\frac{dJ}{dh} + J\frac{dG}{dh}])\cdot\frac{dh}{dt} \tag{12}$$

EXITING WATER FLOWS

Nature displays a wide range of flow phenomena in the subsurface where water can flow slowly through pores and rapidly along fractures. When water is pumped

into a well for in-situ stress tests, it can display head rate drops ranging in time from slow percolation into tight rocks to the most rapid drop possible i.e. free-fall. In free-fall no excess head can be determined, implying that the water is exiting the system through open fractures and/or is flushed out by subsurface flows along open conduits.

We must incorporate these flow characteristics into the functional dependence of Q, the exiting flux. Consequently, we divide flow in this fractured system of porous and permeable rocks into two components :

1. Flow into the rock matrix through the fracture and borehole surfaces.

2. Flow along fractures that are open conduits to the external environment.

For the latter case, account must be taken of pre-existing conduits in order to model the functional form and magnitude of the appropriate exiting flux. Observations of near free-fall fluid heads have been observed at Yucca Mountain where such phenomena were encountered in drilling and stress testing, c.f. Healy (1988). However, in this study, we shall examine data that has reasonable decay times for its drop in excess head. This implies that a finite fracture system is involved and that the exiting flux is dominated by percolation into the surrounding rock matrix. Further work is expected to extend the analysis to incorporate exiting fluxes dominated by fluid flow along conduits.

A constitutive relation must be developed for Q, the rate at which water percolates into the rock matrix through the exposed surface area of the borehole and fractured region. From D'Arcy's Law, using the Dupuit approximation, c.f. Bear (1972), Harr (1991), this is assumed to be proportional to the product of a power-law function of the head, h(t), and the exposed area, which is the sum of the fracture area and the

borehole area in the open zone. For this case, the percolation rate is given by :

$$Q = -kh^q (A_e + A_c + A_o) \tag{13}$$

where A_o is the surface area of the open "packed-off interval" of the borehole, of length d_o, so that $A_o = 2\pi R_p d_o$. Here k is a constant which can be determined from D'Arcy's law and represents the rock wall permeability and porosity.

In order to estimate the expected value of q, we apply Dupuit's approximation to flow out of a well surrounded by a finite thickness of permeable rock. We note, Harr (1991), that for cylindrical symmetry, integration of the total flow out of the external boundary gives q = 1, but we can expect the observed value to vary when asymmetric fractures are present.

APPLICABLE EQUATIONS

These specific constitutive relations can be incorporated into the equation governing conservation of mass. For $h > P_c$ we obtain the general equation :

$$\frac{dh}{dt}(A_p + A_e\frac{dF}{dh} + [G\frac{dJ}{dh} + J\frac{dG}{dh}]) = -kh^q(A_* + G(h-P_c)) \tag{14}$$

where $A_* = A_o + A_e$ and is the total surface area through which the fluid percolates into the rock matrix when no head is applied. This complicated equation reduces, in the lower pressure regime where $h < P_c$, to the simpler equation :

$$\frac{dh}{dt}(A_p + A_e\frac{dF}{dh}) = -kh^qA_* \tag{15}$$

It is useful to examine the approximate solutions to the above equations for particular types of media and fractures under differing pressure regimes.

CASE 1 : Low head, no existing fractures.

When the head is very low, $h \rightarrow 0$, and there are no pre-existing fractures, then $A_e = 0$, we have the standard equation, derived from (15) :

$$\frac{dh}{dt} = -kh^q A_o / A_p \tag{16}$$

which on integration gives, for $q > 1$:

$$\log h = (\log t)/(1-q) + \text{constant} \tag{17}$$

which allows us to relate the slope of the log h versus log t plot to the power q as the head approaches zero. For the case $q = 1$, we obtain an exponential solution :

$$h(t) = h_c \exp\left[\frac{-kA_o\, t}{A_p}\right] \tag{18}$$

where h_c is a constant which can be determined. In a log h versus log t plot, such an exponential solution will manifest a slope that rapidly approaches infinity as the pressure head approaches zero. This contrasts, for example, with the case $q = 2$ where the asymptotic slope would be -1 and thus much less in magnitude than that of the exponential solution.

These problems in the log [h] versus log [t] domain can be easily circumvented by examing curves of log [dh/dt] against log [h], where the value of q can be determined readily. This is the approach we will follow.

CASE 2 : Low head, existing fractures tight, i.e. difficult to open.

In this situation, $h < P_c$, and $dF/dh \rightarrow 0$, which results in the equation :

$$\frac{dh}{dt} = -kh^q A_* / A_p \tag{19}$$

This gives the logarithmic relation :

$$\text{Log}\frac{dh}{dt} = q \cdot \text{Log}(h) + \text{Log}(-kA_* / A_p) \tag{20}$$

that is similar to the previous case, but with A_o replaced by $A_* = A_o + A_e$, so that the

head decay rate will be correspondingly greater due to the larger surface area through which the fluid can percolate. However, the slope q will be the same as in Case 1, in which no fractures are present.

CASE 3 : Low head, existing fractures have large area and are loose, i.e. are easy to open.

The next important subset of solutions occur when the head is low, $h < P_c$, yet the surface area of the existing fractures greatly exceeds the drill-pipe area, $A_e \gg A_p$. In addition, the fractures open easily to increased head, implying dF/dh large. We can then derive an applicable, though approximate, equation from (15), that is :

$$\frac{dh}{dt} = -kh^q A_* / (A_p + A_e \frac{dF}{dh}) \qquad (21)$$

Here the numerator is the same as in Case 2, while the denominator shows the effect of aperture change with excess head on the pre-existing fracture volume. For the simplest linear effect, where $F = \gamma h$, and γ is an arbitrary constant, we see that for large $A_e\gamma$, this term dominates the A_p term and the rate of drop of excess head is correspondingly less. In this linear case, there is no head dependence in the denominator, so the slope of the head gradient versus head curve should be q, the same as the previous cases. When non-linear dependences of F(h) are considered, the denominator will change with head thereby producing a continuously changing slope in the head gradient versus head curves.

The amount that existing fractures open under excess head affects the storativity of the system and we can examine the two extreme cases. When existing fractures have large area and open easily under excess pressure heads, most of the excess water is stored in the fracture system, whereas, in the tight case, the largest fraction of the

water is stored in the borehole. Thus, assuming identical fracture area, porosity and permeability (k) for both cases, and therefore the same rate of volume loss into the surrounding rock matrix, the head will drop faster in the tight case as a greater fraction of borehole water is removed per unit time than in the loose fracture case.

CASE 4 : High head, no induced fractures

This implies that the applied head in the slug test was not high enough to create any induced fracture surfaces, and so the equations valid at low head will also be valid in this domain.

CASE 5 : High head, existing fractures tight and induced fractures have small and tight apertures.

Here $h>P_c$, but $dF/dh \rightarrow 0$ and both dJ/dh and J(h) approach 0, so we can reduce equation (15) to

$$\frac{dh}{dt} = -kh^q \frac{(A_* + G(h-P_c))}{A_p} \qquad (20)$$

Depending on the magnitude and functional form of G on h, the area of induced fractures may increase rapidly above the closure pressure. This implies that the numerator may increase rapidly with head and so we can expect a sharp break at P_c with increased slope in the $\frac{dh}{dt}$ versus h curve.

CASE 6 : High head, existing fractures loose and of large area, induced fractures tight.

Here $h>P_c$, but J(h) and dJ/dh approach 0, and $A_e \gg A_p$, yielding the approximate equation :

$$\frac{dh}{dt} = -kh^q(A_* + G(h-P_c))/(A_e\frac{dF}{dh}) \qquad (21)$$

so that, as before, we may get a sharp break at P_c and an increase in slope in the high

pressure regime, depending on the parameter values so chosen and the functional forms of G and F. If G changes more rapidly with excess head than dF/dh, this type-curve will be similar to the previous case. Conversely, when dF/dh is more affected by excess head than G, the denominator will control the rate of head change.

CASE 7 : High head, existing fractures few and tight, induced fractures many.

For this, we return to equation (14) and consider only the terms involving G as these will dominate at sufficiently high head. Then the high pressure slope will depend intimately on J(h), the amount the induced fractures open with increasing head. If this is large, at high head, most of the contained water is enclosed in these induced fractures, so the head in the borehole will drop relatively slowly above the critical pressure. However, as soon as these fractures close, most of the storativity will be in the borehole and relatively rapid rates of head drop will occur.

ESTIMATIONS

It is instructive to determine the expected size of the parameters in these equations. The critical pressure varies in rock, ranging from zero upward with many values found in the 20-50 bar range, i.e. of the order of stress drops during earthquakes in fluid saturated media. However, in dilatant zones subjected to high fluid pressures, these closure pressures may be much lower.

The borehole is usually of a diameter of the order of 0.1m giving a value of its cross-sectional area of $A_p \approx 10^{-2}m^2$. The open part of the borehole, through which the water moves into the rock, is usually between 10m and 100m long. Assuming this range of interval lengths, then we can expect the surface area of the open test interval

to range between $3m^2 < A_o < 30m^2$ and so the ratio A_o/A_p is in the approximate range of 300 to 3000, and is usually known from the measured experimental data. Minor changes in the experimental values of borehole radius and area occur if there is a skin effect i.e. erosion and/or pitting and/or mud effects on the borehole surface.

The total fracture area is composed of initial fracture area and pressure-dependent fracture area. In regions of the Earth's crust where dilatant fractures abound, we can expect that the existing fractured area can be much higher than the open borehole area. Observations of fracture systems produced by high pressure water injection in laboratory samples, indicates that such fracture areas may be orders of magnitude greater than the borehole area.

THEORETICAL DECAY CURVES

For various values of the critical pressure we solve these equations numerically in order to determine type-curves that can illustrate the effects of the various parameters. These type-curves can subsequently be compared to experimental data.

Below the critical pressure, we can expect the denominator function dF/dh in equation (15) to be of prime importance. As the aperture of the existing fractures increases, we get an attendant increase in storativity of the fractured region. Under conditions of identical exit fluxes, the greater the fraction of the total stored water in the fractured region relative to that in the borehole, the less the rate of head drop in the borehole. In order to comprehend the effect of this aperture change, various functional forms of F, and thus dF/dh, will be assumed. We take $F = \gamma h^n$ where γ is an arbitrary constant and n is a number greater than zero implying that aperture increases with pressure. If n is less than 1, then dF/dh may decrease with pressure head thereby

altering the slope of the log [dh/dt] versus log [h] curve. We shall also use logarithmic dependence of F(h) on excess head in order to see this effect. Such a logarithmic dependence has been observed in the closure of rock joints under external pressure, c.f. Goodman (1976), Brown and Scholz (1985,1986). It has also been found that even a small amount of shear can affect the aperture of fractures due to the effect on the apertures spatial and frequency distribution caused by the shear displacement, Vickers et al. (1992).

Above the critical pressure, both G(h) and J(h) will be important as they govern the area and aperture of the induced fracture region. We can see that as G(h) increases the area of opened induced fractures will increase and expedite the exiting of the fluid. Thereby, an increase in the pressure gradient is to be expected above the critical pressure P_c. As J(h) increases, the aperture of these induced fractures increases, thereby increasing the storativity of this fractured region. Thus, the head in the borehole will drop slower when J(h) is large, as then the greatest fraction of the water charge is in the induced fractured region.

We wish to garner some comprehension of how the area and aperture of these induced cracks vary with increasing pressure above the critical value. From the Griffiths' propagation criterion, we can expect the length of the crack to increase with increasing head pressure. Also, Hayashi and Sakurai (1989) have argued that the rate of pressure decay increases with the height of the crack. Thus, we shall assume that the area function is of the form $G = \alpha(h-P_c)^m$ with an initial value of m=2 assumed for illustrative purposes and where α is an arbitrary constant. As in the case of existing cracks and their aperture dependence on pressure, we can expect the aperture of

the induced fractures to increase with increasing pressure above the critical value. Thus, we assume $J = \beta(h-P_c)^r$ with values of r of order 1 assumed for numerical experiments and where β is an arbitrary constant.

Incorporating these assumed constitutive relations into the mass conservation relation, gives :

$$\frac{dh}{dt} = -kh^q(A_* + \alpha(h-P_c)^m) \,/\, (A_p + nA_e\gamma h^{n-1} + \alpha\beta(m+r)(h-P_c)^{m+r-1}) \qquad (22)$$

where $\alpha=0$ when $h<P_c$ and $A_* = A_o + A_e$.

NUMERICAL SOLUTIONS

We shall solve equation (22) for various values of the parameters in order to plot pressure versus time, or, as prevalent in the industry, pressure versus log time, with time measured in minutes.

These equations are integrated numerically. We obtain graphs of h versus t, plots of (dh/dt), the rate of head change, versus the head, h, which obviously requires no integration of the basic equations, and their logarithmic equivalents. We shall examine these synthetic curves in order to obtain an understanding of the three main effects :

1. the critical pressure, P_c.

2. the aperture change of existing cracks as pressure increases toward the critical pressure, which is controlled by the function $F = \gamma h^n$.

3. the aperture and area change of induced cracks as pressure increases above the critical pressure, controlled by the functions $J = \beta(h-P_c)^r$ and $G = \alpha(h-P_c)^m$ respectively.

We have estimated the expected or typical values of the area terms in this conservation equation. The borehole diameter is about 0.1m so its cross-sectional area will

be taken as $A_p=10^{-2}m^2$. For an open borehole length of about 30 meters, we shall assume that the surface area of the open test interval is $A_o=10m^2$. Assuming an existing crack having the same height as the borehole open area and a length of about 3 meters, we thus assume $A_e=100m^2$.

We have previously shown that Dupuits' approximation to cylindrically symmetric flow out of a well gives the value q = 1 and this is the theoretical powerlaw we shall use. Examination of equation (22) shows that the slope of the head rate of change against head scales with k, the permeability parameter. We use the range of values of k from 10^{-5} to 10^{-2} as this gives a time for pressure drop from maximum to zero in the range of 10 to 100 minutes which is similar to that observed in Yucca Mountain slug tests, Szymanski (1989).

In the following examples, or type-curves, we take an initial head of 500 meters of water, similar to the heads used at Yucca Mountain, which is equivalent to 50 bars of pressure. We also assume a critical pressure of 20 bars for these examples as this is close to the values qualitatively measured in the Yucca Mountain data, Szymanski (1989).

Example A.

Consider the case where the aperture change of the existing cracks is linear in the excess pressure, i.e. n=1, which implies that no effect of increasing pressure is observed below the critical pressure. This is because differentiation of F with h produces a constant, namely γA_e. We shall assume for this case that γ=0.001, which implies that the existing fractures open 1mm for each 1 bar increase in pressure. Thus the denominator term γA_e has the value 0.1, which is a factor of ten larger than the

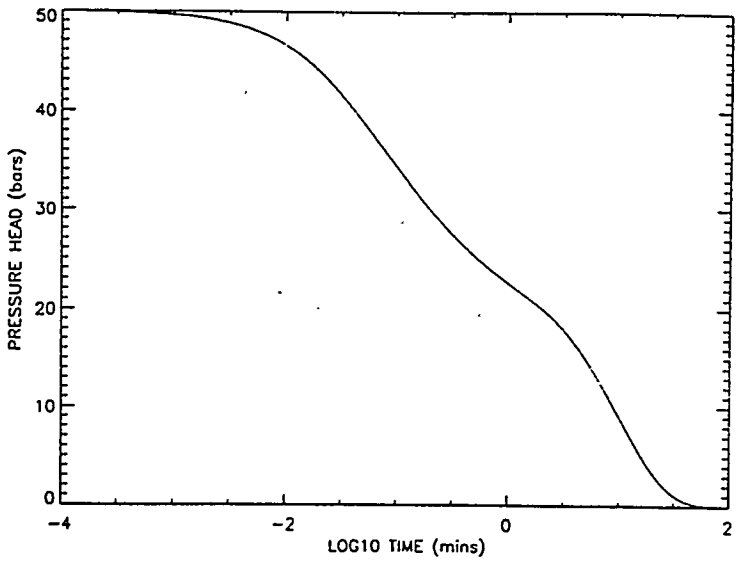

Figure 2a - Theoretical graph of head versus log time. The initial pressure head of water in the borehole is 50 bars. The parameters used in the model synthesis are:
$P_c = 20$bars, $k = 0.0001$,
$A_0 = 0.01m^2$, $A_p = 10m^2$,
$A_e = 100m^2$, $q = 1$, $m = 2$,
$n = 1$, $y = 0.0011$, $\alpha = 10$,
$\beta = 0$.

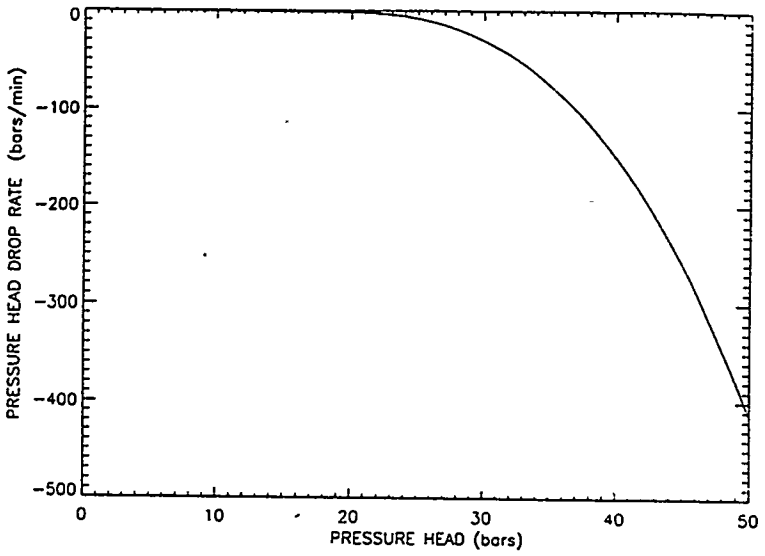

Figure 2b - Theoretical graph of head versus rate of head change. The parameters used are as in Figure 2a.

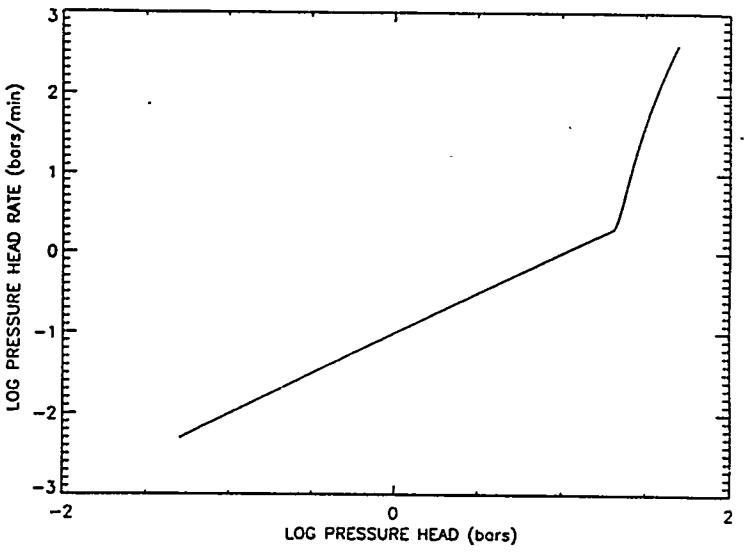

Figure 2c - Theoretical graph of log head versus log rate of head change. The parameters used are as in Figure 2a.

borehole term, A_p.

For behaviour above the critical pressure, we examine the situation where induced fractures have small aperture change but appreciable area change with incresing pressure. In the limit we ignore the aperture changes, i.e. $\beta=0$, and assume that the area obeys $G = \alpha(h-P_c^2)$. We take an initial example of $\alpha=10$, which implies that the surface area of the induced fracture region, when the pressure is 10 bars above critical, is about 1000 m^2. This is ten times the area of the existing fracture surface so this term will eventually dominate the numerator of equation (22).

In Figure 2a, we plot head versus log time, in order for comparison with the in-situ stress measurements. There is an appreciable bend in the head decay curve just above the closure pressure of 20 bars, but it's gradual change of slope hinders an exact prediction of the critical pressure. In Figure 2b, we plot rate of pressure change against pressure and we see that a sharp gradient increase occurs at 20 bars, the critical head. In Figure 2c, we show the synthetic curve for the log of pressure rate versus the log pressure. The lower part of this curve is dominated by the h^q term where $q=1$ in this case. At P_c a sharp slope change occurs as the induced fractures open up.

Example B.

In Figures 3a,b,c we have dropped α to 1, a factor of one tenth that of Example A. This implies that the surface areas of the existing fractures and induced fractures will be of the same order above the critical pressure. All other parameters remain the same as Example A. We see that no bend is observed at P_c in the pressure versus log time curve in Figure 3a. However, the curve in Figure 3b is seen to deviate from a straight line when the pressure exceeds the critical pressure of 20 bars. In Figure 3c

Figure 3a - Theoretical graph of head versus log time. The parameters used are the same as in Figure 2a except that α = 1, a factor of ten less than Figure 2a.

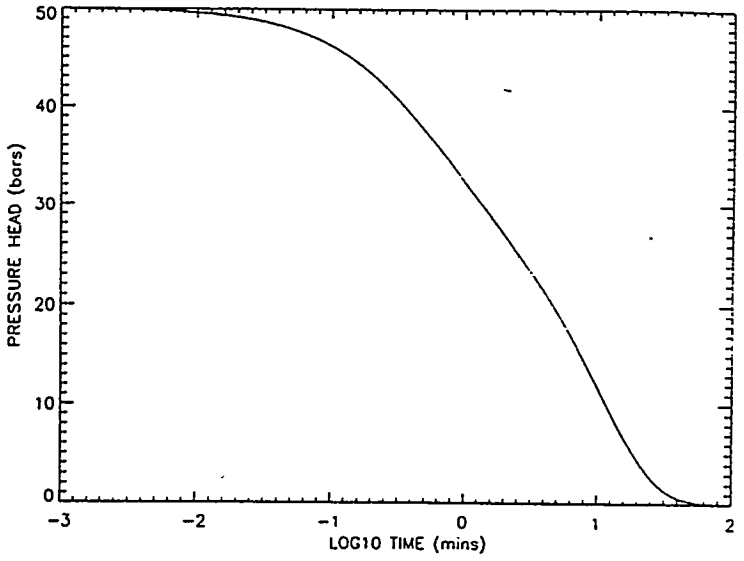

Figure 3b - Theoretical graph of head versus rate of head change. The parameters used are as in Figure 3a.

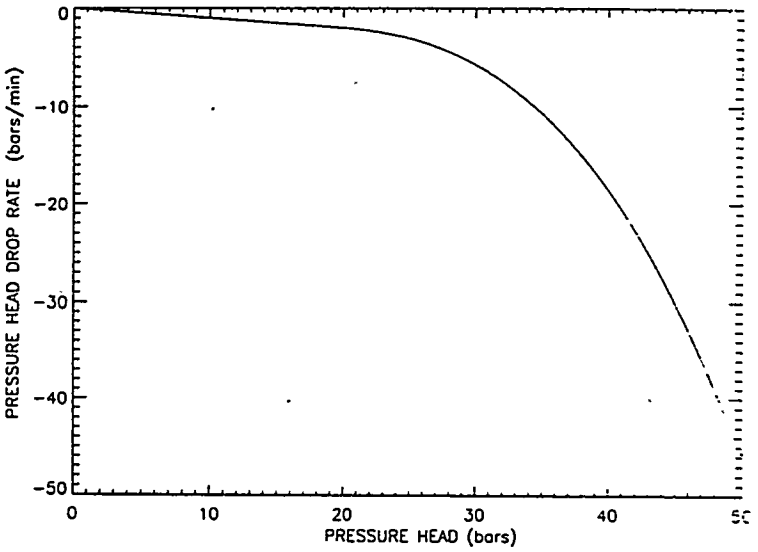

Figure 3c - Theoretical graph of log head versus log rate of head change. The parameters used are as in Figure 3a.

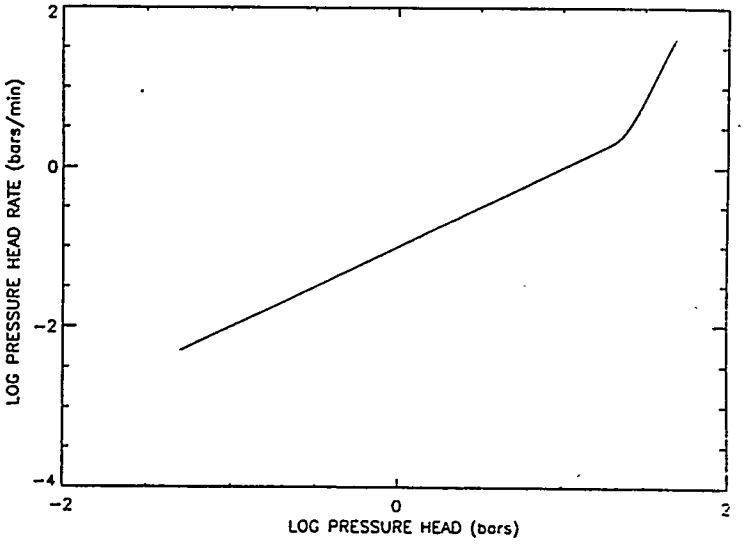

we see that the abrupt change in slope at the critical pressure is less than in Example A. Below the critical pressure, the log [dh/dt] versus log [h] has a slope of 1 reflecting the value of q assumed.

In these two examples, we illustrate the effect of opening induced fracture surfaces above the critical pressure. We can argue from these examples that the ratio of induced crack surface area to existing surface area decides whether an observable bend occurs in the head decay curve at the critical pressure. As this ratio of terms decreases, we obtain synthetic head decay curves in which there may be no apparent bend at the critical pressure. However, there is still a sharp break in gradient at the critical pressure in the corresponding rate of head change versus head as is readily seen in Figure 3b. We immediately see how much more useful the plots using gradients vs head are compared to head vs log time graphs. The sharp break at $h = P_c$ manifests much more strongly in the rate plot. From these general principles, we can see that the effect of changing P_c would be to move the slope change along the curve. Obviously, if the critical pressure is greater than the maximum excess head, then we will not expect such a slope change in any of the graphs.

Example C.

We now examine the effect of changing the functional dependence of the aperture of existing fractures on excess pressure, F(h) . The linear examples, where $F(h) = \gamma h$, have been shown in Figures 2 and 3. Here the slope of the curves in the log[dh/dt] versus log [h] graphs below the critical pressure are equal to q which is 1 for this experiment, and thus the linear case does not affect this slope. If the aperture of these existing fractures opens more readily with pressure than the linear case, we can expect

Figure 4a - Theoretical graph of head versus log time. The parameters used are the same as in Figure 2a except that n = 2, a factor of two times that of Figure 2a.

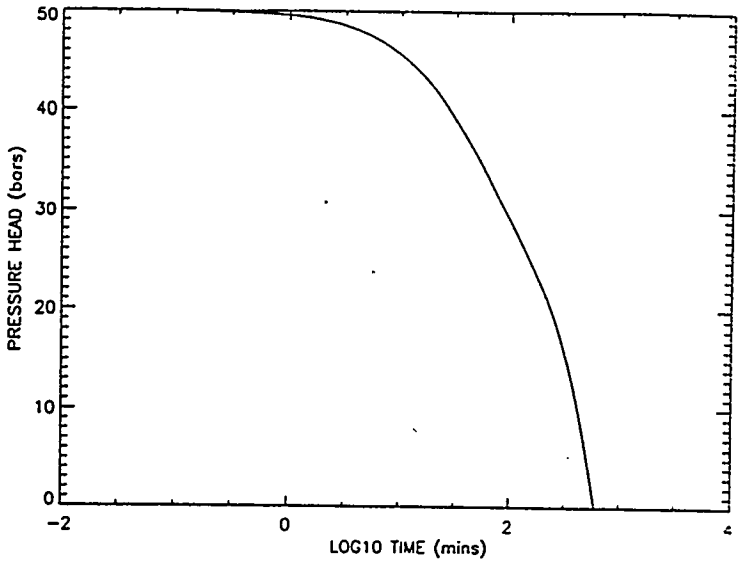

Figure 4b - Theoretical graph of head versus rate of head change. The parameters used are as in Figure 4a.

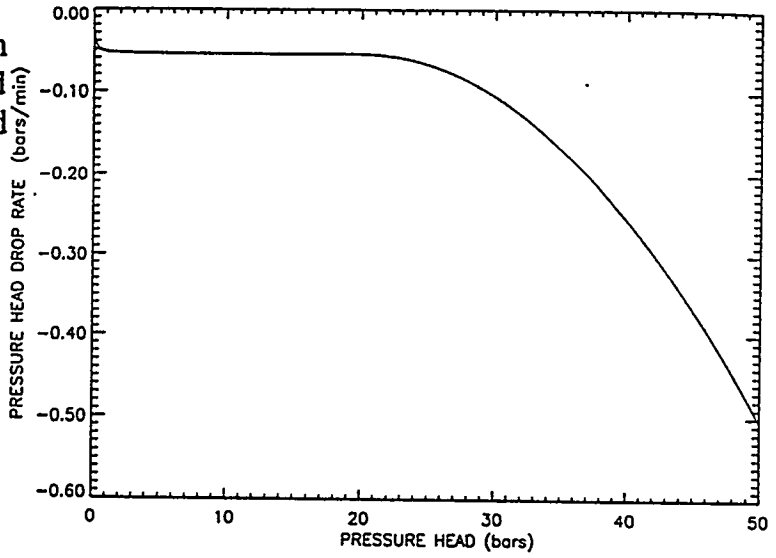

Figure 4c - Theoretical graph of log head versus log rate of head change. The parameters used are as in Figure 4a.

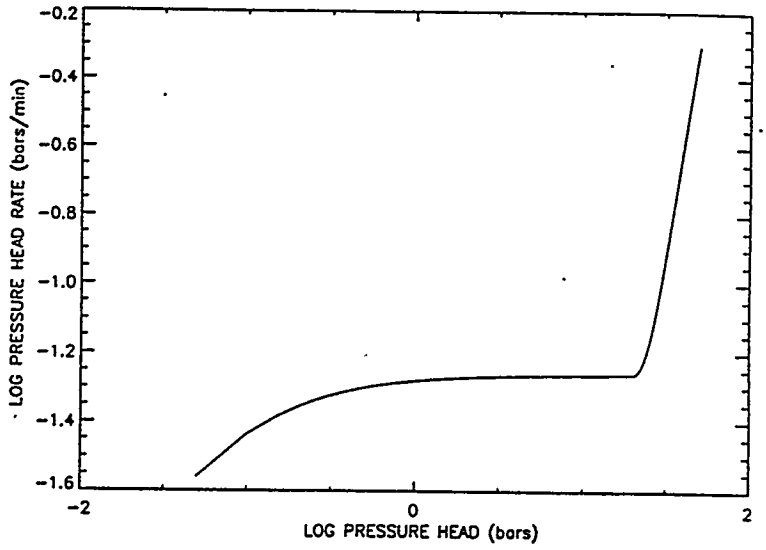

an effect on this log-log slope. When $F(h) = \gamma h^2$, we expect the log [dh/dt] vs log [h] curve to start with a slope of 1 at lowest pressure and, as this term takes effect, the slope drops off to zero, as shown in Figure 4c. All the parameters in Figures 4a,b,c are the same as in Figures 3a,b,c except for n=2. Thus, we see that the effect of opening existing fractures more readily is to increase the storativity of the fracture system and thereby increase the time for the pressure head to drop to zero, as seen in comparing Figure 4a with Figure 3a.

If the aperture of these existing fractures opens less readily with pressure than the linear case, we also expect an effect on this log-log slope. We assume that for this case a power law dependence of aperture on pressure will have the power less than 1, where we take $F(h) = \gamma h^n$, where $n < 1$. The log [dh/dt] versus log [h] curve will have a slope that increases with head even below the critical pressure, but this will only manifest on the type-curves if the existing fracture storativity is comparable to the borehole storativity, as expected from the theoretical relationship, equation (22).

Example D.

In order to determine the complete effect of induced fractures opening above the critical pressure, we must take into account that volume as well as area of the the induced fracture region can increase rapidly with pressure. The effect of aperture change with head above the critical pressure is modeled by using a non-zero J(h) and we shall initially assume a powerlaw dependence $J(h) = \beta(h-P_c)^r$. Just as for the existing fracture system, we shall assume initially a linear relation with r=1 for these examples. We shall assume a β of one tenth γ, i.e. 0.0001, implying that the aperture will open only 0.1mm for each bar of pressure above the critical value. In Figure 5a,b,c

we show examples of graphs from such a situation where all other parameters are the same as in Figure 2. The β term affects the head vs log time curve mainly above the critical pressure but no change in slope is observed at the critical pressure of 20 bars. However, the head rate vs head curves are similar to those in Figure 2b,c though the change in slope at P_c is not as steep.

Figure 6a,b,c show the effect of a larger β term, 0.0005, implying greater increases of induced fracture volume with pressure than in Figure 5. Again no change in slope at the critical pressure is observed in the head vs. log time curve. However, the head rate vs head curves are very different to those in Figure 5b,c with a kink at P_c and with similar slope gradients on either side of the critical pressure.

Figure 7a,b,c show the effect of an even larger β term, 0.001, which is the same value as γ, implying greater increases of induced fracture volume with pressure than in Figure 6. Again no change in slope at the critical pressure is observed in the head vs. log time curve. The pressure rate versus pressure curve has a more pronounced kink at the critical pressure than in Figure 5b,c.

This sequence of Figures, 5,6 and 7, shows the effect of an increasing storativity of the fractures which open above the critical pressure. It takes an increasingly longer time for the head to drop to the critical pressure in Figure 7a than in Figure 6a and Figure 5a. Also, if the storativity increases more rapidly than the surface area of the induced cracks, just above the critical pressure the pressure rate of drop of the borehole head will momentarily decrease as relatively more water will be stored in and thus removed from the induced fracture system rather than from the borehole.

These synthetic solutions are representative of the types of curves we can expect

Figure 5a - Theoretical graph of head versus log time. The initial pressure head of water in the borehole is 50 bars. The parameters used are as in Figure 2 but with $\beta = 0.0001$, $r = 1$. This solution investigates the effect of aperture changes in the induced fractures opening above the critical pressure.

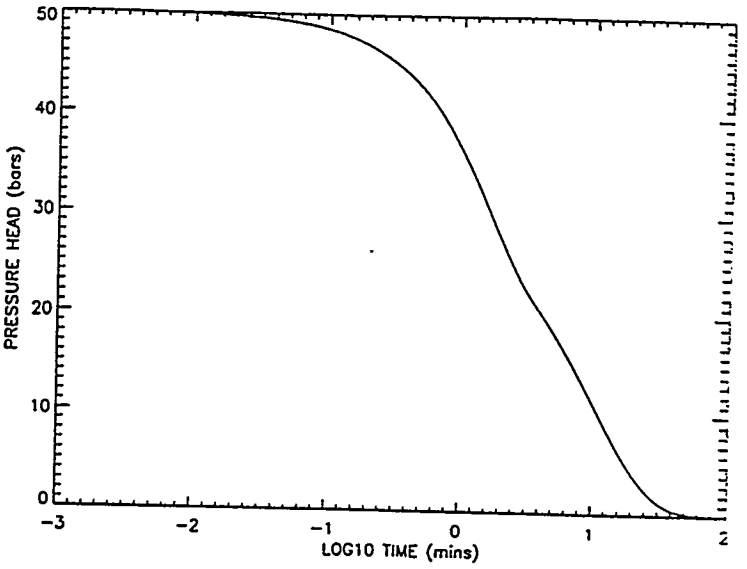

Figure 5b - Theoretical graph of head versus rate of head change. The parameters used are as in Figure 5a.

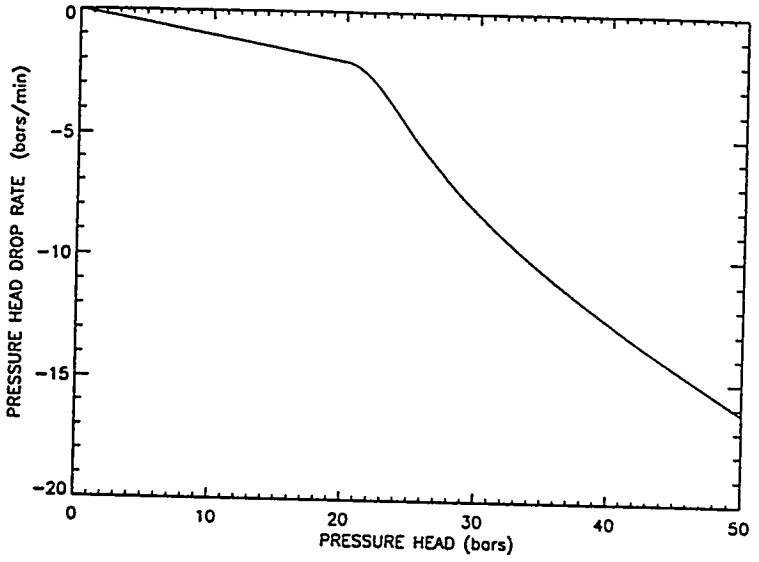

Figure 5c - Theoretical graph of log head versus log rate of head change. The parameters used are as in Figure 5a.

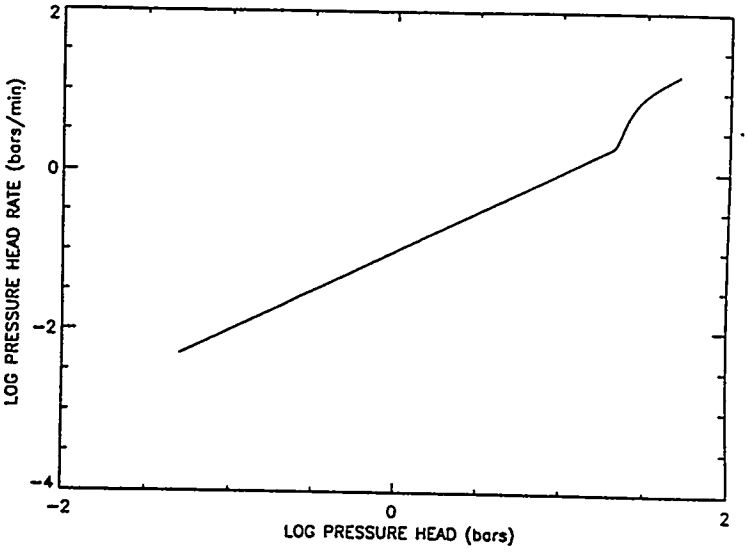

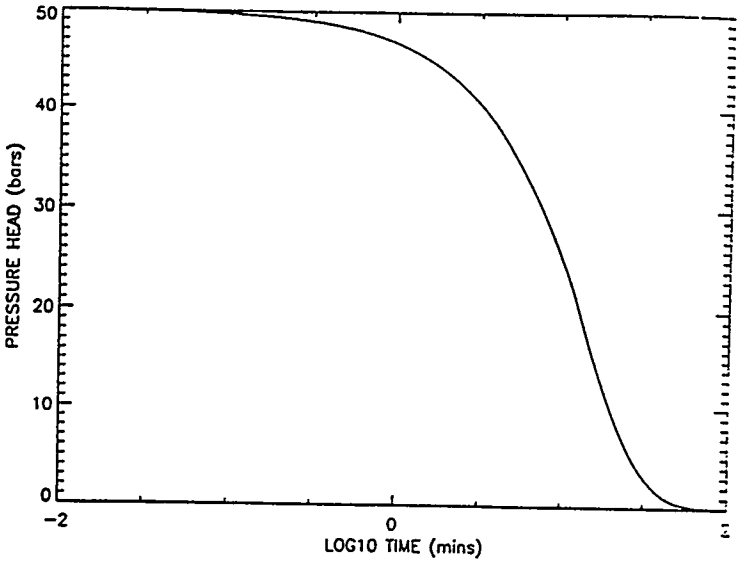

Figure 6a - Theoretical graph of head versus log time. The initial pressure head of water in the borehole is 50 bars. The parameters used are as in Figure 5a but with β five times the value used in Figure 5.

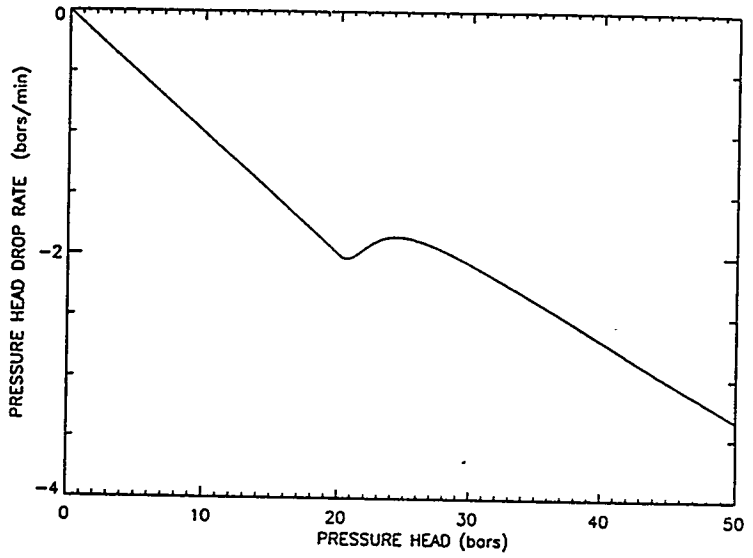

Figure 6b - Theoretical graph of head versus rate of head change. The parameters used are as in Figure 6a.

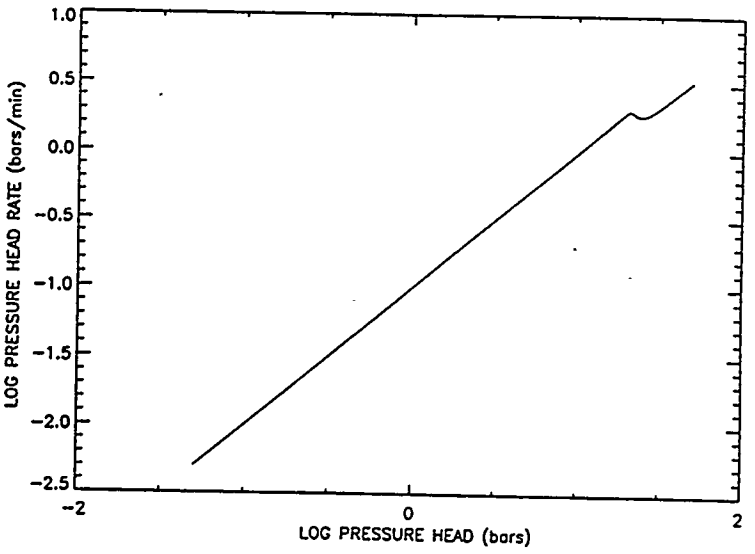

Figure 6c - Theoretical graph of log head versus log rate of head change. The parameters used are as in Figure 6a.

Figure 7a - Theoretical graph of head versus log time. The initial pressure head of water in the borehole is 50 bars. The parameters used are as in Figure 5a but with β ten times the value used in Figure 5.

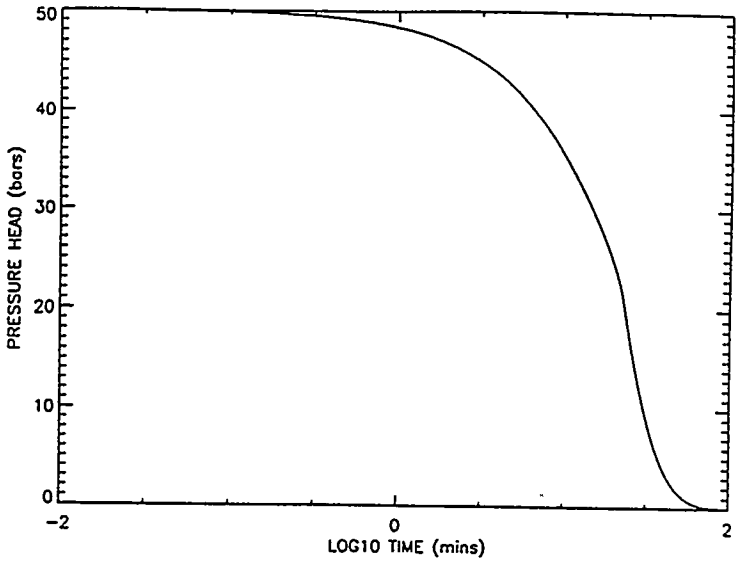

Figure 7b - Theoretical graph of head versus rate of head change. The parameters used are as in Figure 7a.

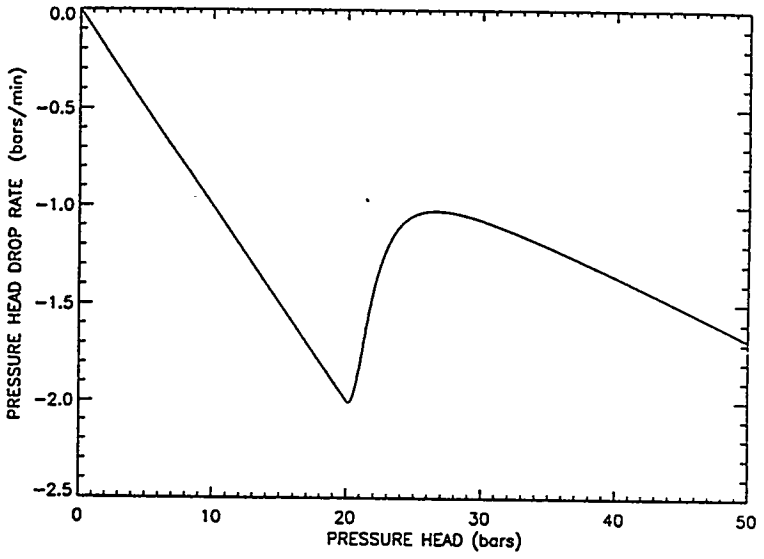

Figure 7c - Theoretical graph of log head versus log rate of head change. The parameters used are as in Figure 7a.

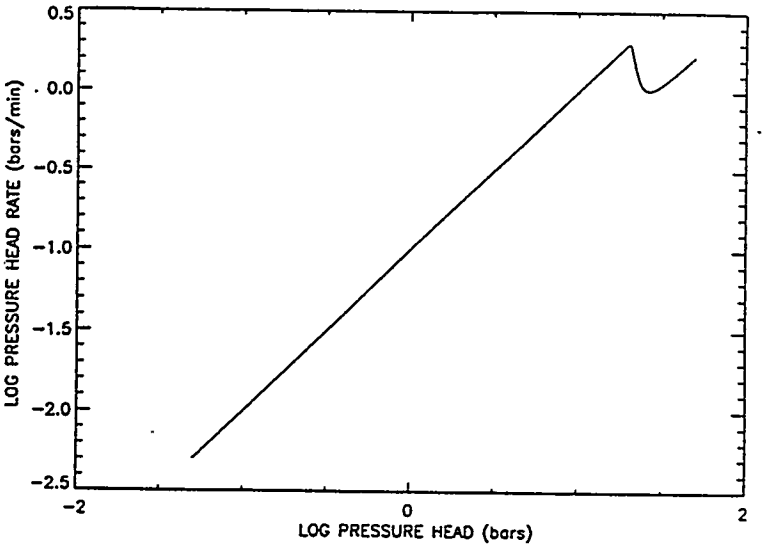

in real data from stress tests in fractured media. They allow us to examine such data and determine the most likely fracture systems operable in the subsurface.

YUCCA MOUNTAIN DATA

A number of boreholes have been drilled in and near Yucca Mountain, Nevada, the proposed site for a nuclear waste depository. Healy (1988) has discussed the problems of drilling boreholes in and near Yucca Mountain. He comments :

"At Yucca Mountain, drill crews talked about 'underground rivers', a description that attempts to explain the large amount of drilling fluids that were lost in the hole during drilling. Drilling conditions on Yucca Mountain are very unusual. The natural water table is about 1700 ft. below the surface and when the hole is drilled with standard methods with circulating fluid, no fluid or drill cuttings return to the surface."

Certain of these holes have been subjected to in-situ stress tests utilizing both hydro-frac and slug tests. This depository site was mainly chosen for its very low anomalous water table which is of the order of 500 metres below the surface. Thus the slug tests so performed were under high pressure, of the order of 50 bars, as the boreholes were usually filled to the top with water at the start of the test. A realistic analysis necessitates incorporation of the effects of such high water pressures on the fractured rock system.

The data used was digitized from graphical information published in Szymanski (1989), which itself was obtained from USGS documents. We are, at present, trying to obtain the original data from various investigators as we lack information on borehole size, leakage factors, flow rate, total water volume input as a function of head and time, televiewer logs and density data etc.

The original and derived data for representative sections of each hole is displayed in the Appendix. There are 3 figures for each test; the 'a' figures show the raw data from the slug test, Szymanski (1989); the 'b' figures show head pressure drop rates versus excess head, and the 'c' figures show the log [dh/dt] versus log [h] curves. Because of inherent errors in the digitization process and the lack of accurate data, at the highest pressures there is often much scatter in the derived gradient values. We have used simple averaging algorithms for smoothing of the original digitised data in order to improve the differentiated data.

DATA INTERPRETATION

This interpretation will be mainly qualitative until adequate information is available to make more quantitative predictions. However, where recognisable changes in slope occur at specific heads, we do obtain a quantitative estimate of the critical pressure. In the following analysis, we examine a few representative sections from various boreholes. We shall compare the data with synthetic curves in order to determine the applicable fracture phenomena. Comments on each specific test are included in the Appendix.

In Table 1, for the selected Yucca Mountain data, we list the estimated values of the critical pressure determined from the pressure rate versus pressure graphs. The closure pressures lie mainly in the range of 10 to 30 bars. The depths at which these tests sampled the in-situ stress were in the range of 500 to 1200 meters which corresponds to lithostatic gravity pressures in the range of 150 to 360 bars. For a medium under lithostatic pressure alone, the minimum principle stress is at least 0.25 times the lithostatic pressure. Thus, for such a medium without non-lithostatic

pressures, we should observe critical closure pressures in the range of 40 to 90 bars. Our observed closure pressures are much less than the lithostatic values implying that other forces must be operating on the medium. These must be dilatational forces whose stresses must be the difference between the computed lithostatic estimates and the observed values of closure pressures. From Table 1. we can see that, at Yucca Mountain, dilatational stresses are estimated to be in the range of 15 to 70 bars, with most values in the 30 to 40 bar range. Such high dilatational stresses and low closure pressures indicate that, at Yucca Mountain, the region could be close to failure.

In order to estimate values of the other parameters governing the system, we have created synthetic solutions that match the observed data for a subset of the tests. These solutions are displayed in the Appendix under the particular test for comparison with the observed data curves. We find that the value of k, the porosity-permeability parameter, is in the range 10^{-3} to 10^{-4} and is the main parameter affecting how rapidly the pressure decays to zero. Values of q, the powerlaw parameter affecting the exiting flow, are observed to be in the range of 0.5 to 2 with most values near 1. The expected value of q for cylindrically symmetric flow out of a well is 1 so we are confident of our estimated values.

The area terms in the model equation are known for the borehole and give an A_o, the open borehole surface area, of about 10 to 50 square meters. Using representative values from the synthetic solutions matching observed data, estimated areas of existing fracture surface is of the same order, 10 to 50 m^2. Similarly, representative values of γ, the amount the fracture opens under increasing water pressure, are of the order of 10^{-3} meters per bar. Thus, under 10 bars of pressure, the existing fractures may open

about 1 cm and store a total volume of water of about 0.1 to 1 cubic meter. This is in contrast to the storativity of the 500m borehole which is about 15 cubic meters of water.

For the induced fractures, we obtain values for β, the amount that the induced fractures open under excess pressure above the closure pressure, in the range 10^{-4} to 10^{-3} meters per bar. These induced fractures are usually stiffer than the existing fractures, i.e. $\beta<\gamma$. We obtain estimates of the value of α, the multiplier term affecting the area of induced fracture surface, in the range of 1 to 10. The powerlaw of induced area as a function of excess head, m, is found to be in the range of 1.5 to 2. Thus, for a pressure exceeding the closure pressure by 10 bars, we obtain an area of fracture surface on the order of 100 to 1000 square meters. Associated with this area is a volume storativity in the range of 10^{-1} to 10 cubic meters.

All these estimated parameter values are well within expected ranges for such a fractured system. The critical pressure values and estimated dilatational stresses show how close to failure is the rock-water system. Induced fracture areas imply fracture lengths up to hundreds of meters long. Such easily opened and long fractures imply that these are ancient fractures which have been cemented by low-strength materials which fracture easily under low excess stress.

CONCLUSIONS

Our results indicate that the critical closure pressure varies in depth and spatial location over the Yucca Mountain region. The results are consistent with models of a deforming fractured medium whose hydraulic conductivity is a sensitive function of in-situ and applied stress. Yucca Mountain is an anomalous geological and

hydrological system. It differs from its surrounding environment in possessing a much deeper water table stored in a highly fractured rock. This fractured system has been shown to be dilated under in-situ stress, and these dilational stress values have been estimated above. This dilatation has been considered the cause of the deep water table, Szymanski (1989), Archambeau and Price (1991). Both changes in in-situ stress and water pressure can affect the fracture dilatation and hence the water storativity and the level of the water table. If these open fractures return to the closed fractures of the rocks to the north of Yucca Mountain, we can expect the water table under Yucca Mountain to become of the same level as that to the north. This would entail a rise from the present level of 500 meters to a much shallower one of only 50 meters.

Stock (1985) and U.S.G.S. associates have performed numerous in-situ tests at Yucca Mountain. Televiewer monitoring of holes showed long fractures parallel to the borehole that Healy argues were formed during drilling when high drill-fluid pressures were used. Hydraulic tests were used in order to determine in-situ stress in this rock-water system. They examined head versus time curves for sharp gradient changes and concluded that these occurred at the minimum principle stress. From these results, Healy (1988) concludes that the "rocks penetrated by the drill hole USWG1 are near a state of incipient failure" and are "subject to stresses that may be close to their long-term strength". This has been emphasised recently by the earthquake of June 1992 at Little Skull Mountain, which did serious damage to DOE buildings near the proposed Yucca Mountain site.

Szymanski, (1989), has examined these slug tests using qualitative fits to the data. He has claimed that for heads higher than the "closure pressure", induced fractures

open. For heads less than the "closure pressure", he claims that the fractures will be closed thereby allowing only slow percolation of water into the rock matrix through the borehole open surface area. Using representative type-curves for each situation, he has qualitatively determined the state of stress in the tested formation by examining the curves of head versus log time. When a change in slope occurs in such curves, he has argued that this point is the value at which the head is equal to the closure pressure. When no change in slope occurs, but there is rapid drop in head at all pressures, he argues for a "singular point" which is essentially where the closure pressure approaches zero and fractures are open even under low head.

Both Szymanski and Healy only used the raw data of head versus time to make an estimate of the critical pressure. Our model with its synthetic results show that under a wide variety of conditions, no break is observable in this curve of head versus time even though a finite and reasonable critical pressure is acting. We have used the more discriminative curves of head versus head rate to determine this critical pressure. In the straightforward curves which contain change in slopes in the head versus time data, Szymanski's qualitative measure of closure pressure is very near our determination based on the rapid change in gradient in the head rate versus head data. In the cases where Szymanski has argued for a "singular point" where no obvious change in slopes occur in the head decay curve, our analyses indicate that the determination of closure pressure is available from the pressure rate versus pressure curves. Our estimates of the closure pressure show that the system is close to failure.

Earthquakes can cause rapid changes in near-field stresses and thereby causing transient fluid flows, Archambeau and Price (1991), with observed extrusion of water

over large areas, Wood and King (1991). That both USGS scientists and these independent analyses have shown that the tectonic system at Yucca Mountain is highly dilated and close to failure should be taken into account in any site evaluation and estimate of earthquake and flooding risk.

COMPARISON OF TEST ANALYSES

Borehole	Interval	Lith-Pc	Data-Pc	Dil. Stress
USW H-6	649-683	50	23	27
USW H-6	835-869	65	19	46
USW H-6	606-640	45	26	19
USW G-4	792-838	60	16	44
USW G-4	899-915	70	10	60
USW G-4	850-875	65	8	57
USW H-5	949-1010	75	17	58
USW H-5	888-949	70	30	40
USW H-5	1033-52	80	40	40
USW H-4	555-604	40	17	23
USW H-4	735-767	55	17	38
USW H-4	873-892	65	26	39
USW H-4	928-1219	85	10	75
UE-25p#1	600-650	45	29	16
UE-25p#1	974-1044	75	?	?
UE-25b#1	1006-1220	85	?	?
UE-25b#1	505-579	40	4	36
UE-25b#1	820-860	65	7	58

The closure pressure as 1/4 of the lithostatic pressure is labeled "Lith-Pc". The critical pressure determined by examination of the pressure rate versus pressure data is labeled "Data-Pc". The estimated dilatational stress is labeled "Dil. Stress".

HOLE USW G-4: Interval 792-838 meters.

Figure 8a shows the raw data of hole USW G-4, test G-4.1, depth interval 792 to 838 meters, and with a packed-off open test interval of length 46 meters. Szymanski's qualitative estimate of the pressure at which the change in slope in the raw data occurs is 19 bars, which pressure he terms the "closure pressure" of the induced fractures. Figure 8b, showing dh/dt versus h, has a sharp directional change at about 16 bars corresponding to the critical pressure and close to Szymanski's value. The Figures, 8a,b,c are similar to the synthetic curves, shown in Figures 2a,b,c, in which large surface areas but small apertures of induced fractures are produced when the head exceeds the critical pressure. However, below 16 bars, the slope of the log dh/dt versus log h curve in Figure 8c is approximately 0.5 and is appreciably less than the expected value of 1. We can thus tentatively infer that, below the critical pressure, the apertures of existing fractures are opening with increasing head with consequent increase in stored water in the open fracture volume. Above the critical pressure, the log dh/dt - log h slope is about 3 and the general pattern is that in which the area of induced fractures created has a greater effect than the rate of change of volume due to these induced fractures.

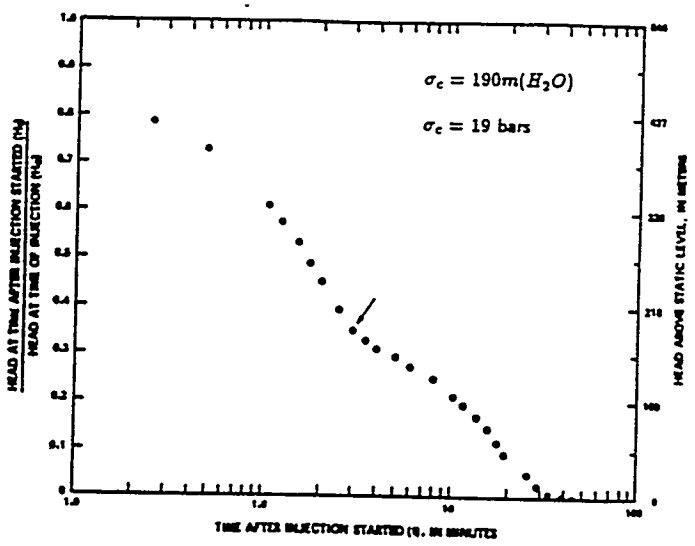

Figure 8a - Raw data of hole USW G-4, test G-4.1, depth interval 792 to 838 meters, and with open test interval of length 46 meters.

Figure 8b - Graph of head versus rate of head change, derived from raw data shown in Figure 8a.

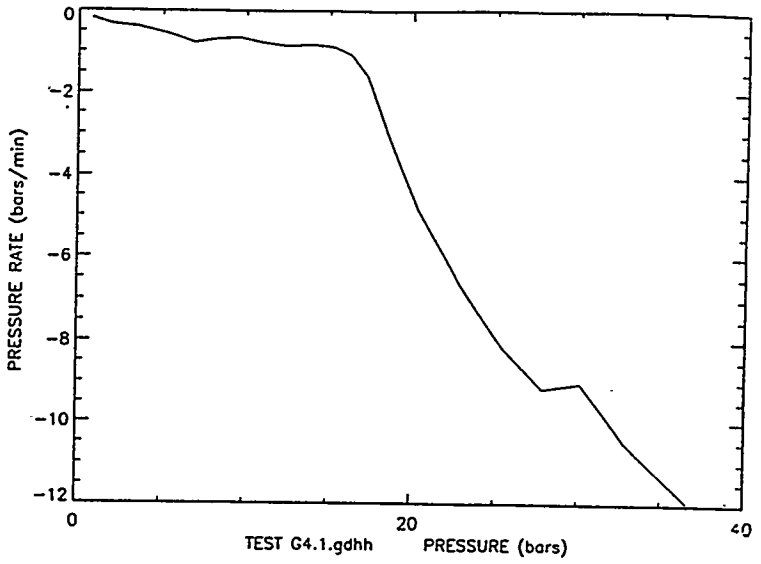

Figure 8c - Graph of log head versus log rate of head change, derived from raw data shown in Figure 8a.

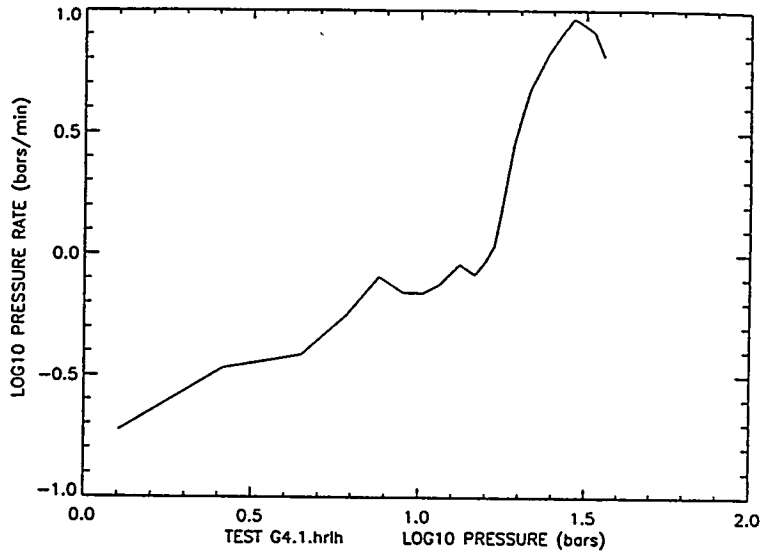

Figure 8d - Theoretical graph of head versus log time with model curve designed to match raw data of Figure 8a. The initial pressure head of water in the borehole is 40 bars. The parameters used in the model synthesis are:
P_c = 16bars, k = 0.0001,
A_o = 27m², A_p = 0.03m²,
A_e = 20m², q = 1, m = 2,
n = 1, y = 0.0001, α = 20,
β = 0.0001

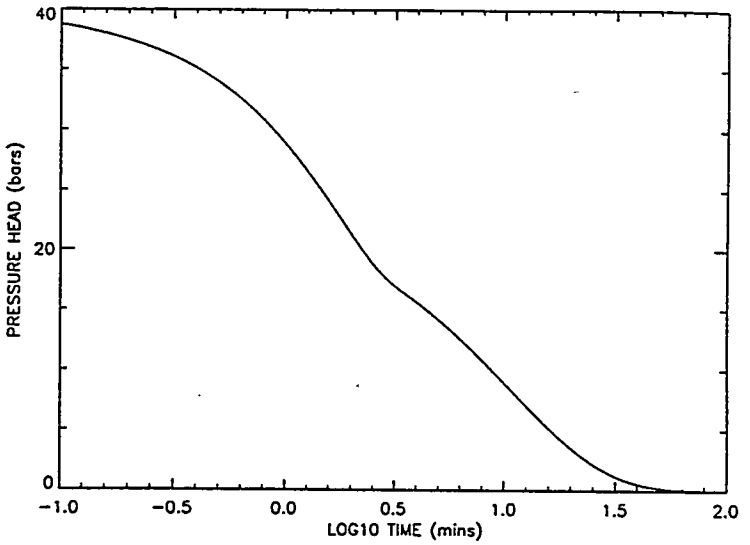

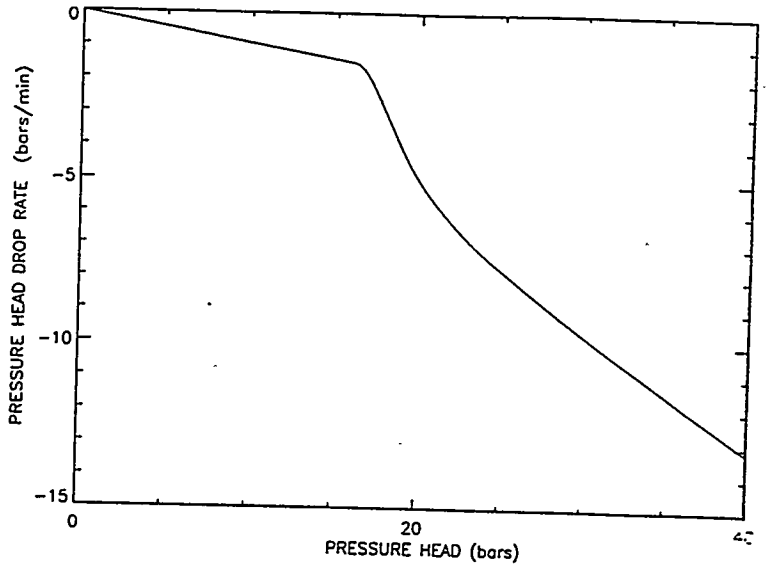

Figure 8e - Theoretical graph of head versus rate of head change. The parameters used are as in Figure 8d.

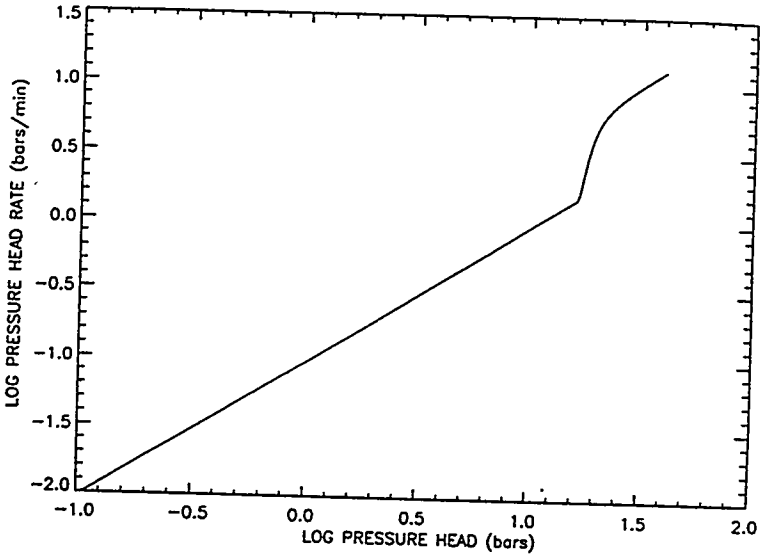

Figure 8f - Theoretical graph of log head versus log rate of head change. The parameters used are as in Figure 8d.

HOLE USW G-4: Interval 899-915 meters.

Figure 9a shows the raw data of hole USW G-4, test G-4.2, depth interval 899 to 915 meters, and with test interval of length 16 meters. No change in slope or bend is observable in this raw data. However, Figure 9b is similar to the synthetic Figure 6b,

which curve shape is manifested when induced fractures form above the critical pressure and are easily opened with rapid volume changes. Examination of the curve in Figure 9c indicates that the slope of log dh/dt versus log h is approximately 1 in the low pressure regime. There is a break in slope at about 10 bars in both graphs, Figures 9b,c, which we may estimate as the critical pressure.

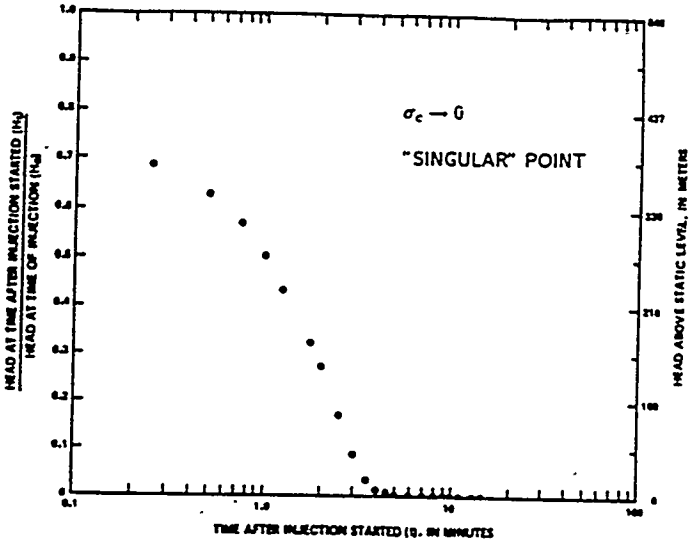

Figure 9a - Raw data of hole USW G-4, test G-4.2, depth interval 899 to 915 meters, and with open test interval of length 16 meters.

·Pacter-injection test for depth interval from 899 to 915 meters.

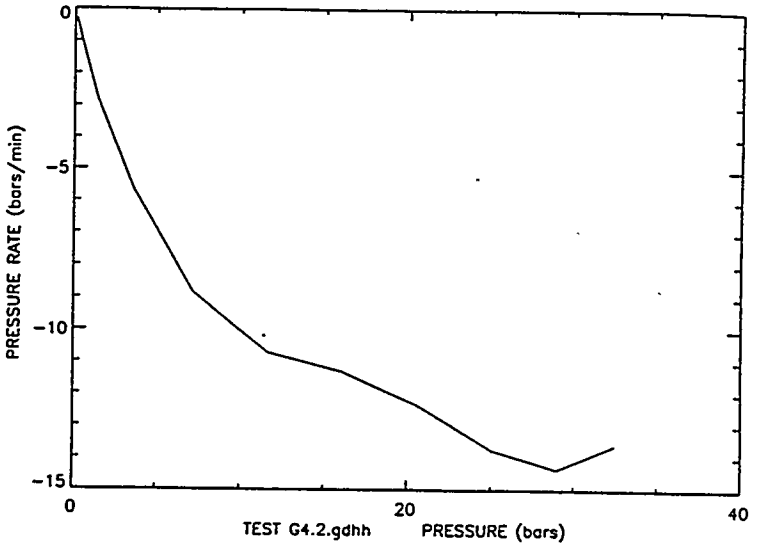

Figure 9b - Graph of head versus rate of head change, derived from raw data shown in Figure 9a.

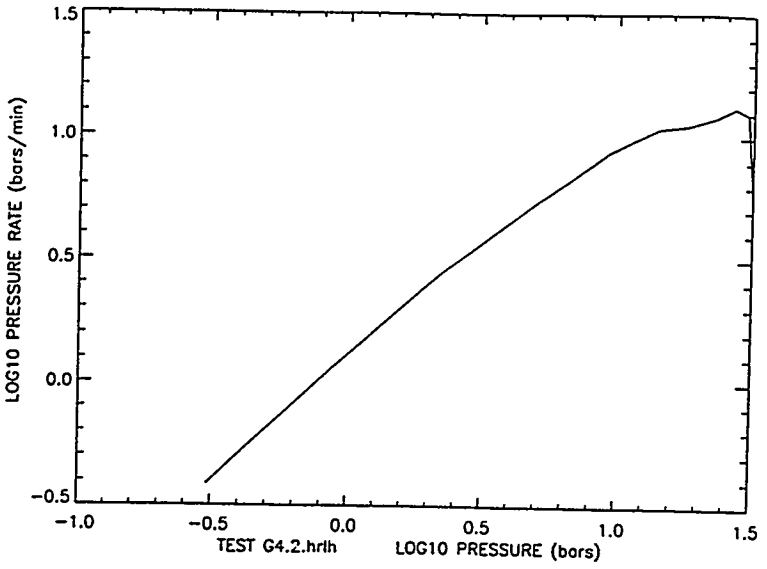

Figure 9c - Graph of log head versus log rate of head change, derived from raw data shown in Figure 9a.

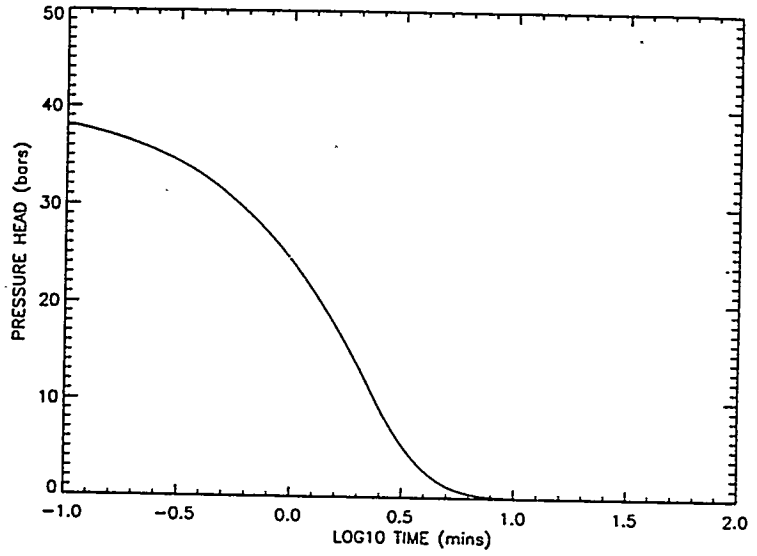

Figure 9d - Theoretical graph of head versus log time, with model curve designed to match raw data of Figure 9a. The initial pressure head of water in the borehole is 40 bars. The parameters used in the model synthesis are:
P_c = 10bars, k = 0.001,
$A_o = 9m^2$, $A_p = 0.03m^2$,
$A_e = 60m^2$, q = 1, m = 1.5,
n = 1, y = 0.0009, α = 2.5,
β = 0.0009

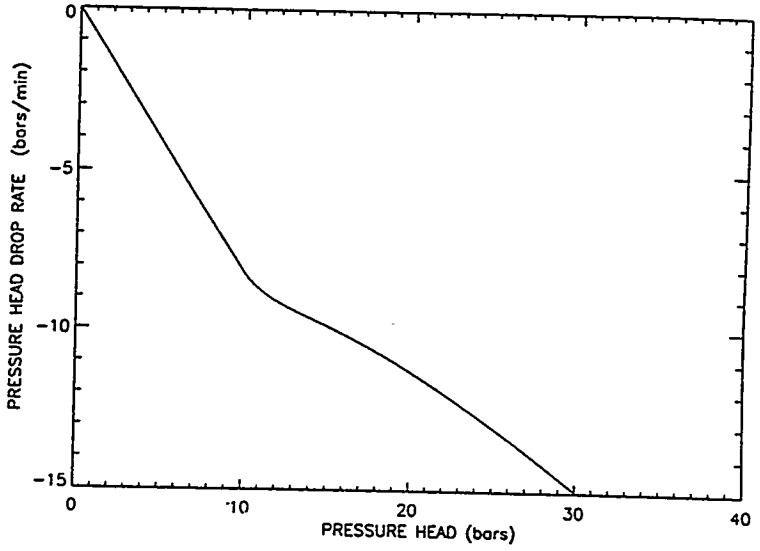

Figure 9e - Theoretical graph of head versus rate of head change. The parameters used are as in Figure 9d.

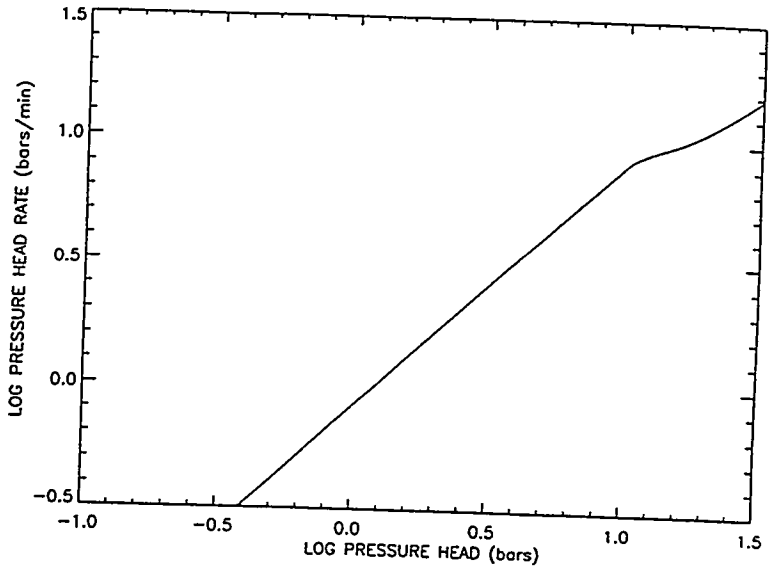

Figure 9f - Theoretical graph of log head versus log rate of head change. The parameters used are as in Figure 9d.

HOLE USW G-4: Interval 850-875 meters.

Figure 10a shows the raw data of hole USW G-4, test G-4.3, depth interval 850 to 875 meters, and with test interval of length 25 meters. No change in slope or bend is observable in this raw data. However, Figures 10b,c are similar to the previous Figures 9b,c with a deviation from a linear trend at about 8 bars. Similar remarks concerning the induced fractures forming with large volume changes are applicable.

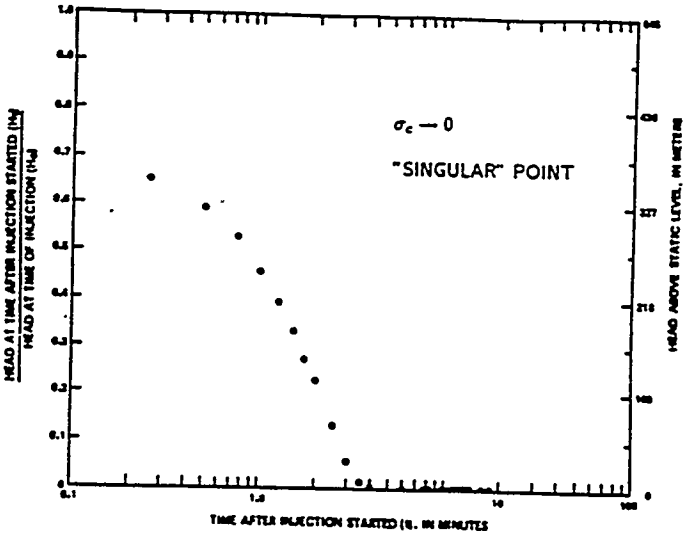

Packer-injection test for depth interval from 850 to 875 meters.

Figure 10a - Raw data of hole USW G-4, test G-4.3, depth interval 850 to 875 meters, and with open test interval of length 25 meters.

Figure 10b - Graph of head versus rate of head change, derived from raw data shown in Figure 10a.

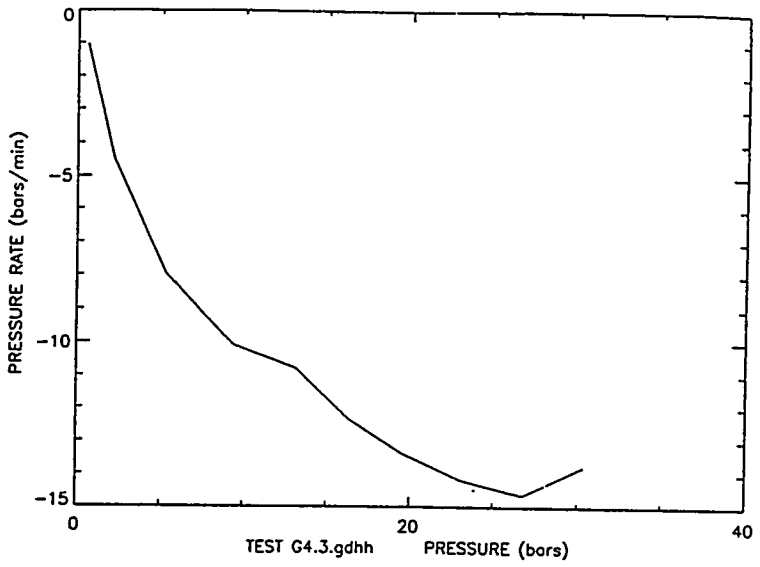

Figure 10c - Graph of log head versus log rate of head change, derived from raw data shown in Figure 10a.

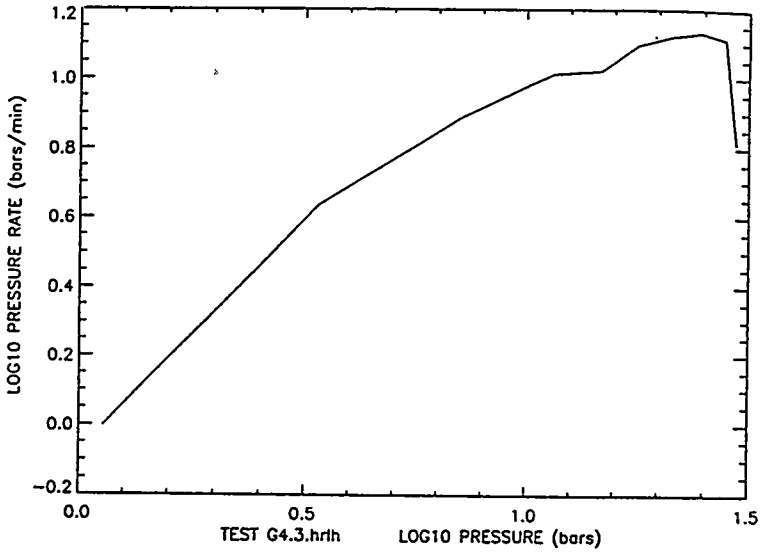

Figure 10d - Theoretical graph of head versus log time, with model curve designed to match raw data of Figure 10a. The initial pressure head of water in the borehole is 40 bars. The parameters used in the model synthesis are:
P_c = 10bars, k = 0.001,
A_o = 14m², A_p = 0.03m²,
A_e = 30m², q = 1, m = 2,
n = 1, y = 0.0007, α = 5,
β = 0.0005

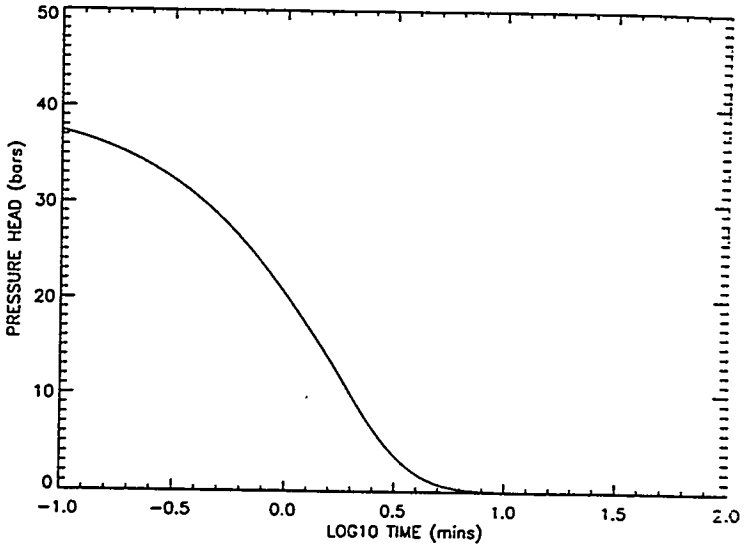

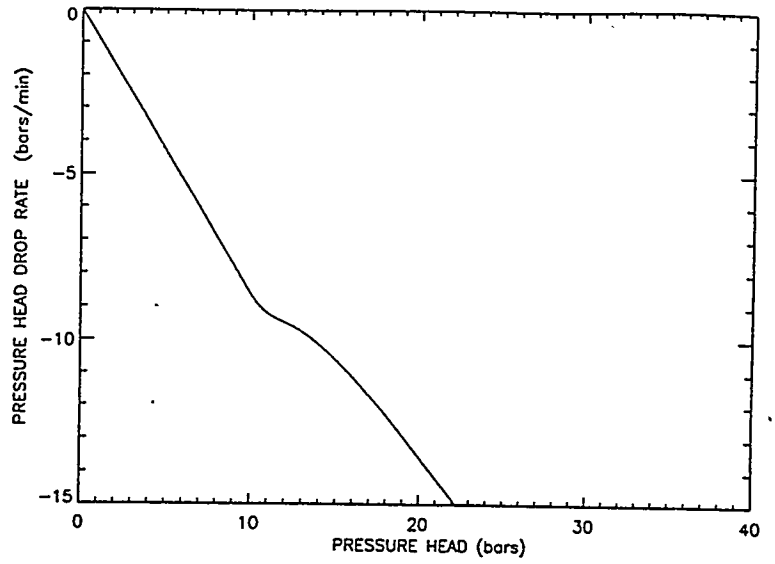

Figure 10e - Theoretical graph of head versus rate of head change. The parameters used are as in Figure 10d.

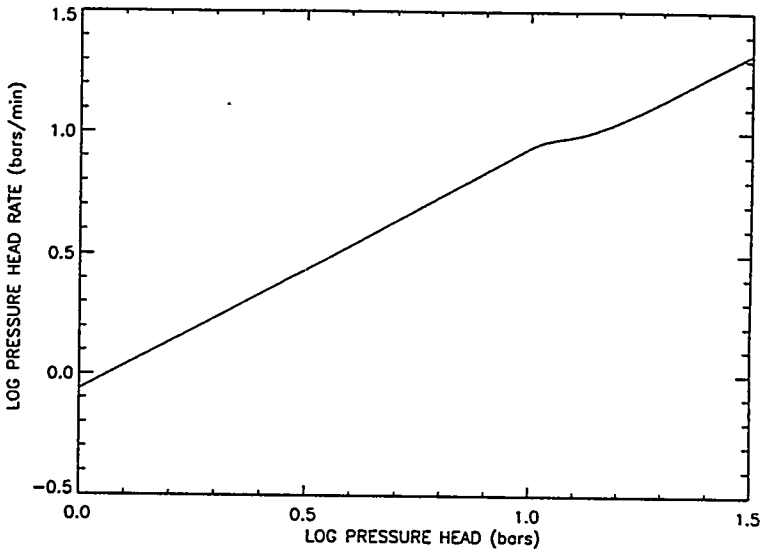

Figure 10f - Theoretical graph of log head versus log rate of head change. The parameters used are as in Figure 10d.

HOLE USW H-4: Interval 555-604 meters.

Figure 11a shows the raw data of hole USW H-4, test H-4.1, depth interval 555 to 604 meters, and with open test interval of length 49 meters. Szymanski's qualitative estimate of the "closure pressure" at which the change in slope in the raw data occurs is 17.5 bars. Figure 11b, showing dh/dt versus h, has a sharp directional change at about 17 bars corresponding to the critical pressure and close to Szymanski's value. The

Figures 11a,b,c are similar to the synthetic curves, shown in Figures 2a,b,c, in which large areas of induced fracture surface rather than volume change is produced above the critical pressure. Below this critical pressure, we can see that the slope of the log dh/dt versus log h plot increases from about 1 at the lowest pressure to about 2 at the critical pressure. This indicates that existing fractures are dilating even under these low pressure heads.

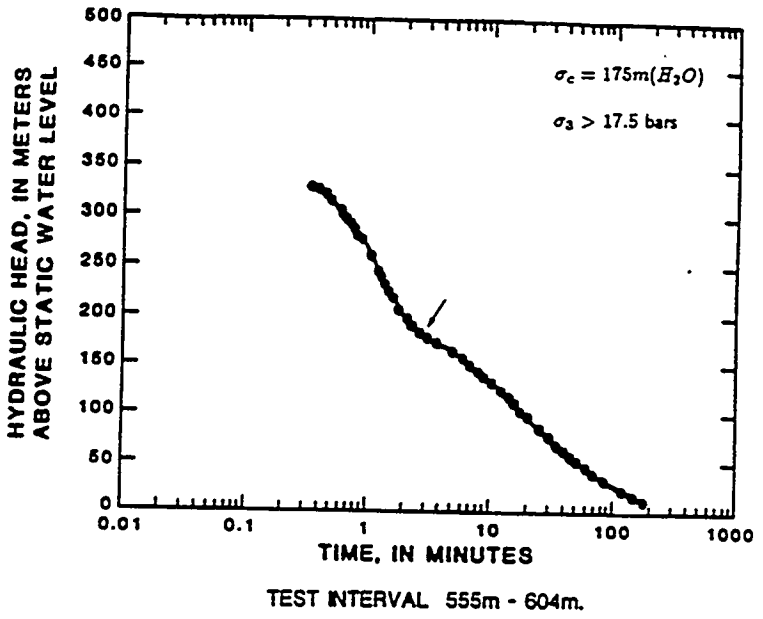

Figure 11a - Raw data of hole USW H-4, test H-4.1, depth interval 555 to 604 meters, and with open test interval of length 49 meters.

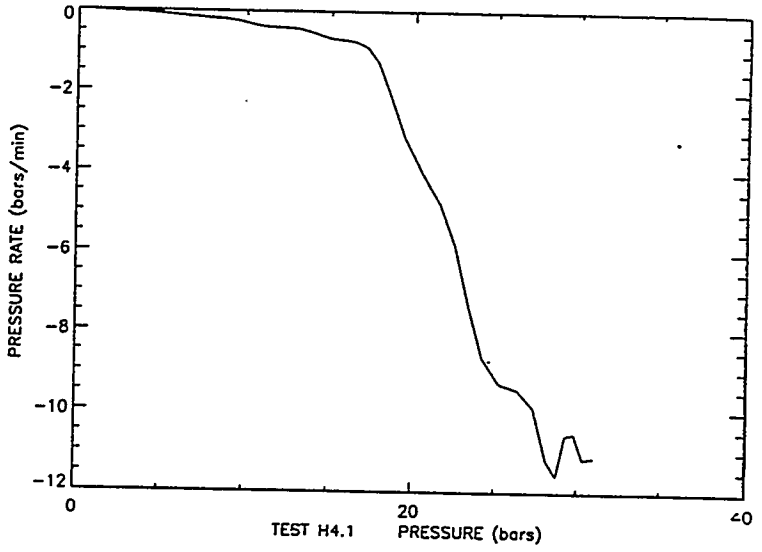

Figure 11b - Graph of head versus rate of head change, derived from raw data shown in Figure 11a.

Figure 12a - Raw data of hole USW H-4, test H-4.2, depth interval 735 to 767 meters, and with open test interval of length 32 meters.

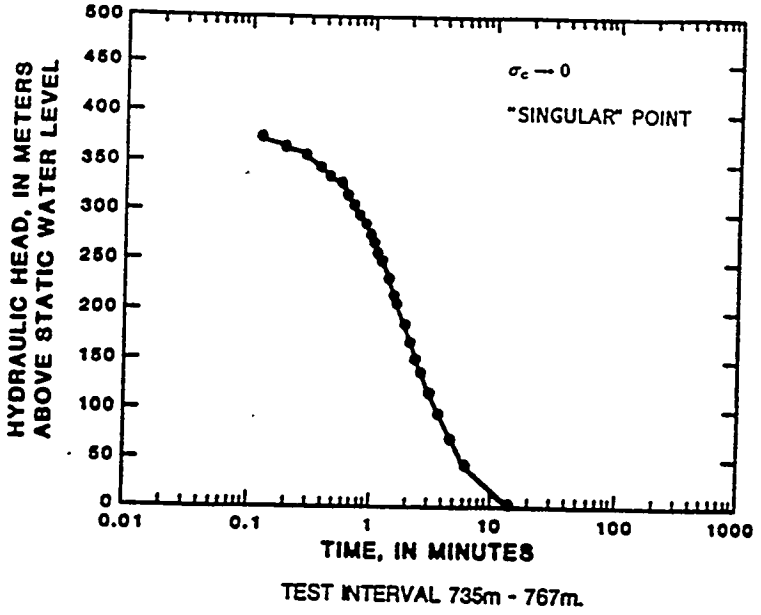

Results of the Cooper-Bredehoeft injection tests in Well USW H-4. From Whitfield et al., 1984.

Figure 12b - Graph of head versus rate of head change, derived from raw data shown in Figure 12a.

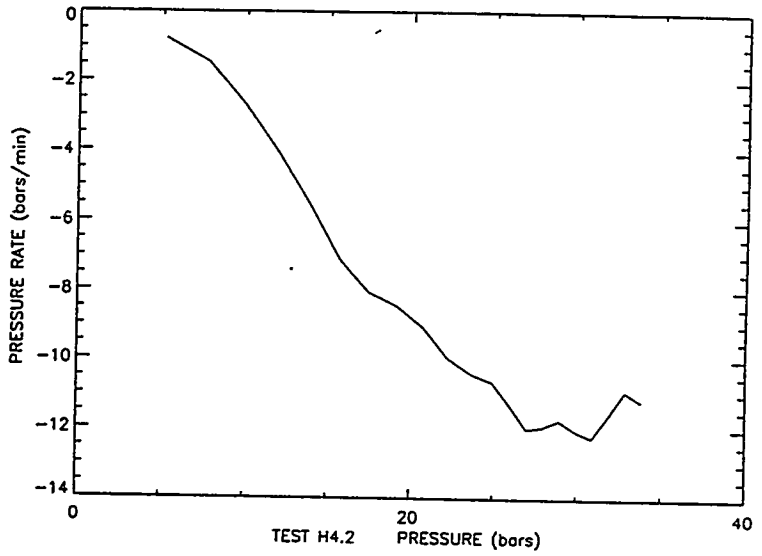

Figure 12c - Graph of log head versus log rate of head change, derived from raw data shown in Figure 12a.

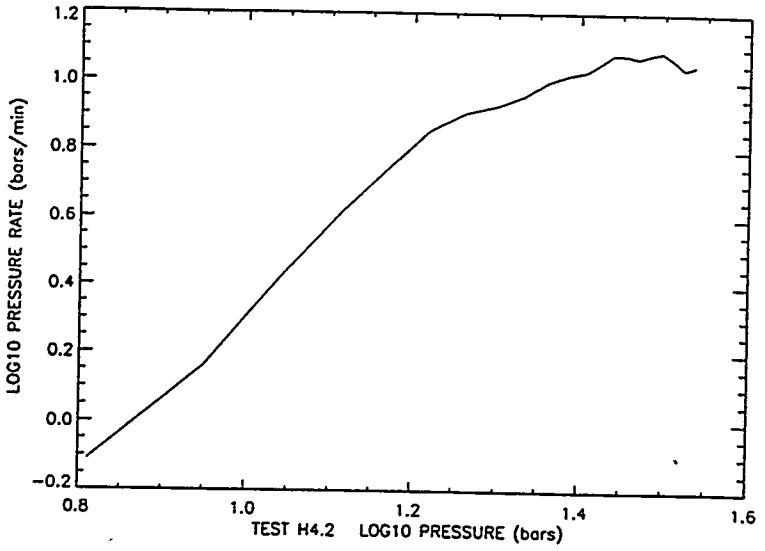

7b,c with a deviation from a linear trend at about 10 bars. This pattern of behavior is characteristic of induced fractures that dilate above the critical value of 10 bars. The low pressure region has a slope of log dh/dt versus log h of about 1 between 1 and 10 bars.

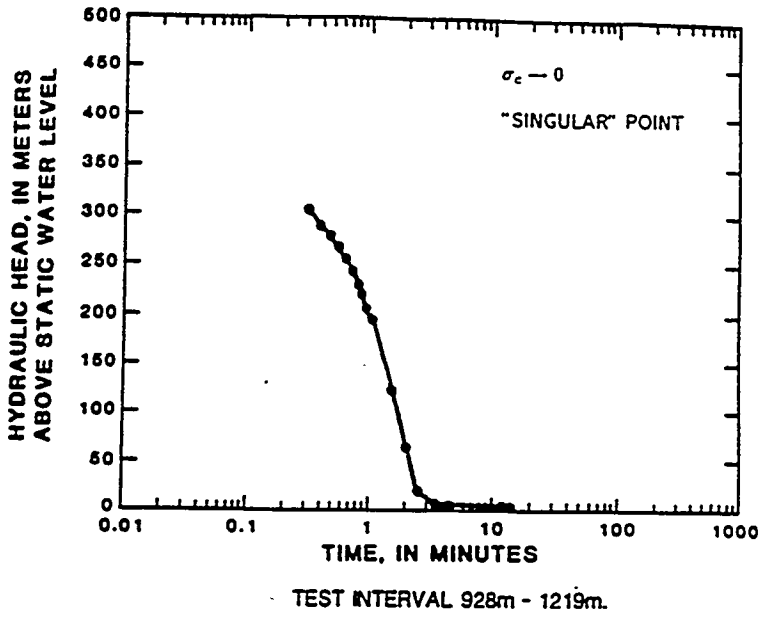

Figure 14a - Raw data of hole USW H-4, test H-4.4, depth interval 928 to 1219 meters, and with open test interval of length 291 meters.

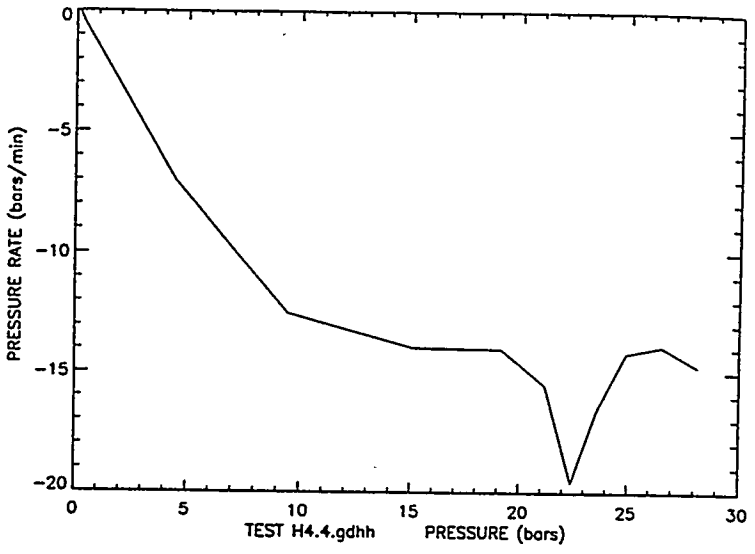

Figure 14b - Graph of head versus rate of head change, derived from raw data shown in Figure 14a.

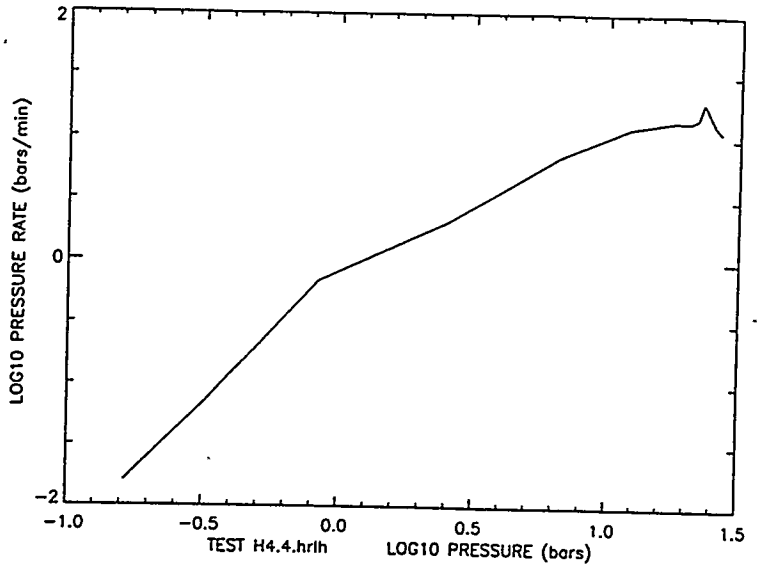

Figure 14c - Graph of log head versus log rate of head change, derived from raw data shown in Figure 14a.

HOLE USW H-5: Interval 949-1010 meters.

Figure 15a shows the raw data of hole USW H-5, test H-5.1, depth interval 949 to 1010 meters, and with open test interval of length 61 meters. Szymanski's qualitative estimate of the "closure pressure" at which the change in slope in the raw data occurs is 17.5 bars. Figure 15b, showing dh/dt versus h, has a sharp directional change at about 17 bars corresponding to the critical pressure and close to Szymanski's value. The Figures 14a,b,c are similar to the synthetic curves, shown in Figures 2a,b,c, in which large areas of induced fracture surface rather than volume change is produced above the critical pressure. Below this critical pressure, we can see that the slope of the log dh/dt versus log h plot is only about 0.3. This indicates that existing fractures are dilating even under these low pressure heads.

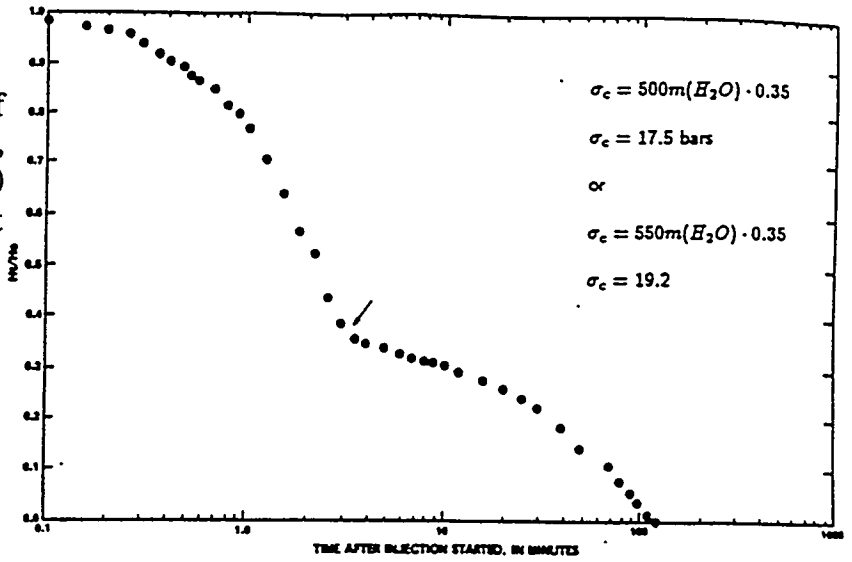

—Packer-injection test for depth interval from 949 to 1,010 meters.

Figure 15a - Raw data of hole USW H-5, test H-5.1, depth interval 949 to 1010 meters, and with open test interval of length 61 meters.

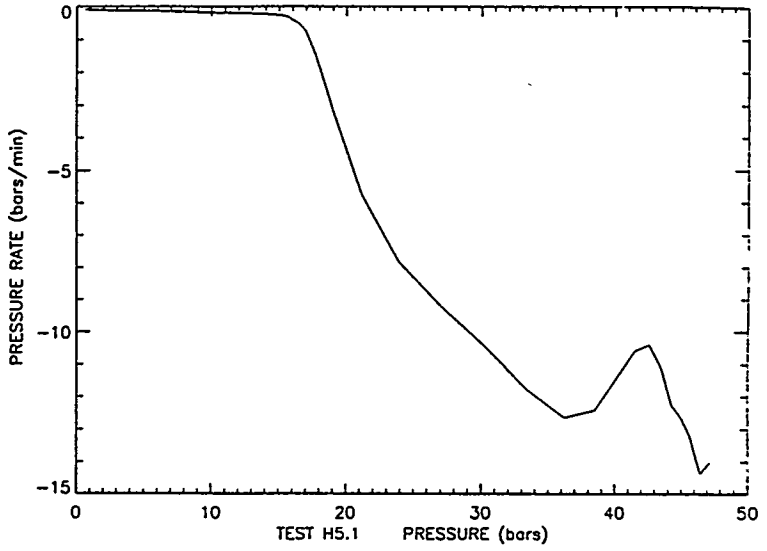

Figure 15b - Graph of head versus rate of head change, derived from raw data shown in Figure 15a.

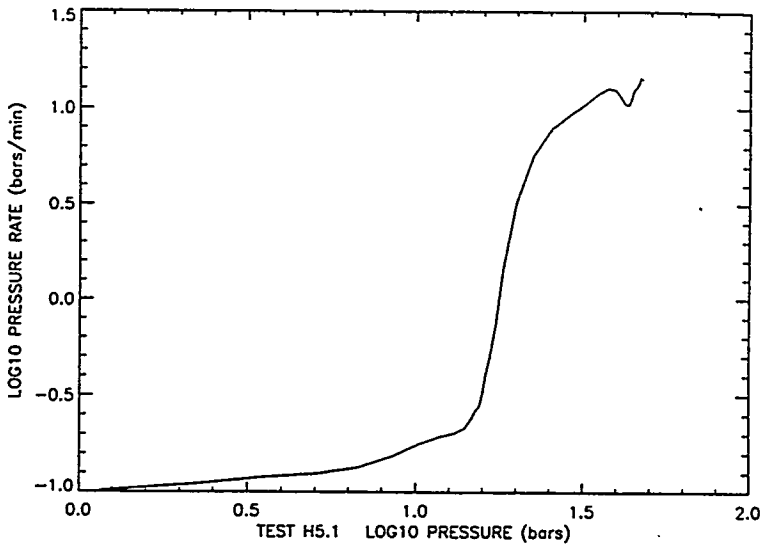

Figure 15c - Graph of log head versus log rate of head change, derived from raw data shown in Figure 15a.

HOLE USW H-5: Interval 888-949 meters.

Figure 16a shows the raw data of hole USW H-5, test H-5.2, depth interval 888 to 949 meters, and with open test interval of length 61 meters. This interval is of the same length and adjacent to but deeper than the previous case. No change in slope or bend is observable in this raw data, and it has a faster drop in head than the previous case. However, Figures 16b,c are similar to the synthetic Figures 7b,c with a deviation from a linear trend at about 0.6 times the maximum head, 50 bars, which gives a critical pressure of about 30 bars. This pattern of behavior is characteristic of induced fractures that dilate above the critical value of 30 bars. The low pressure region has a slope of log dh/dt versus log h of about 1.

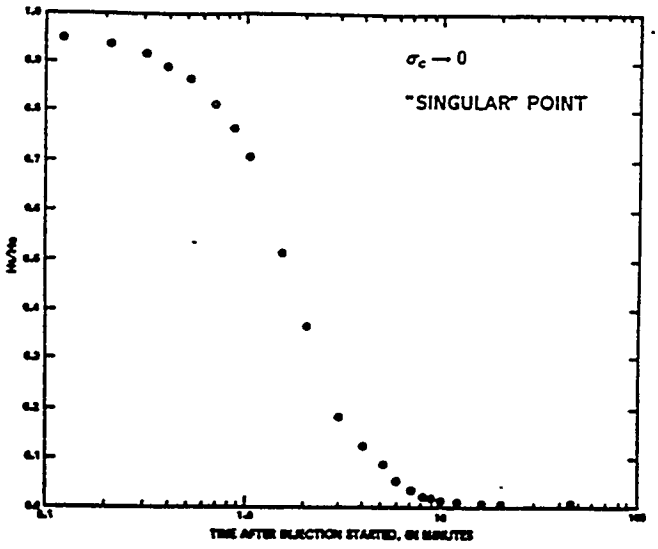

-Packer-injection test for depth interval from 888 to 949 meters.

Results of the Cooper-Bredehoeft injection tests in Well USW H-5. From Bentley et al., 1983.

Figure 16a - Raw data of hole USW H-5, test H-5.2, depth interval 888 to 949 meters, and with open test interval of length 61 meters.

Figure 16b - Graph of head versus rate of head change, derived from raw data shown in Figure 16a.

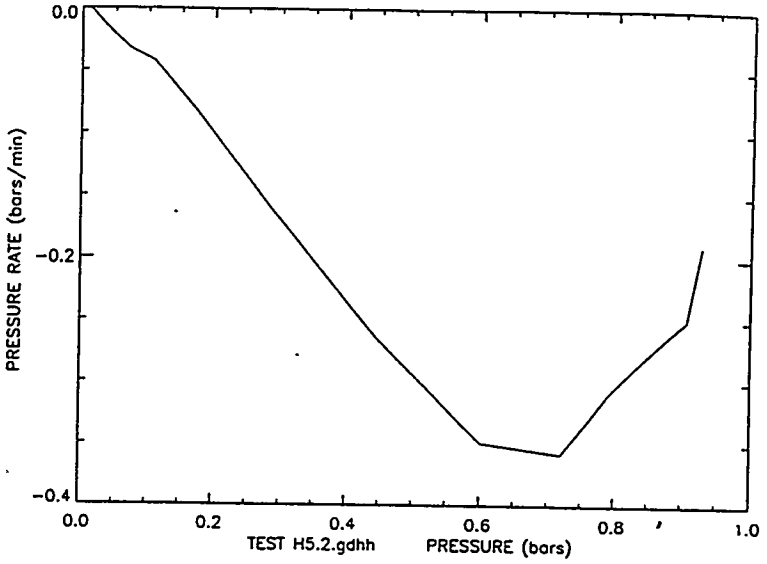

Figure 16c - Graph of log head versus log rate of head change, derived from raw data shown in Figure 16a.

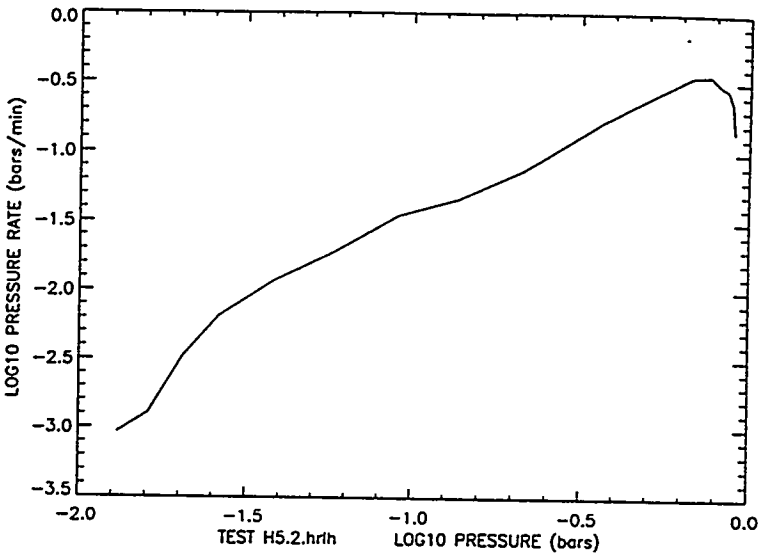

HOLE USW H-5: Interval 1033-1052 meters.

Figure 17a shows the raw data of hole USW H-5, test H-5.3, depth interval 1033 to 1052 meters, and with open test interval of length 19 meters. No change in slope

or bend is observable in this raw data, however, Figures 17b,c are similar to the synthetic Figures 7b,c with a deviation from a linear trend at about 0.8 times the maximum head, 50 bars, which gives a critical pressure of about 40 bars. This pattern of behavior is characteristic of induced fractures that dilate rapidly above the critical value of 40 bars. The low pressure region has a slope of log dh/dt versus log h of about 1.

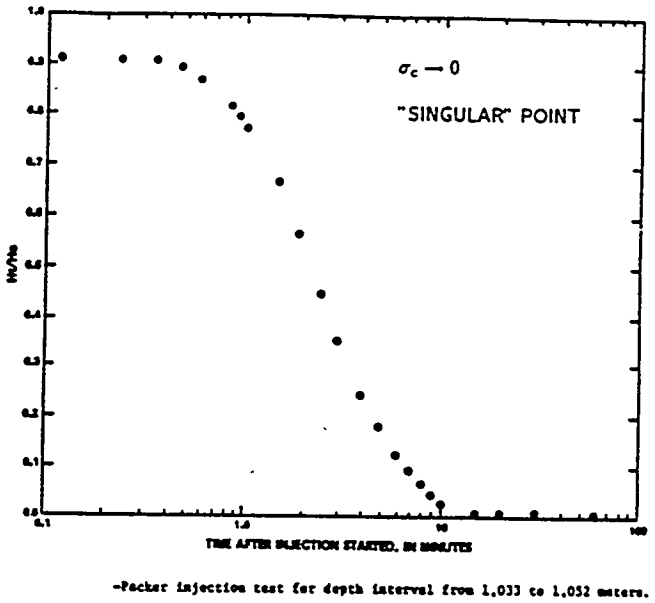

Figure 17a - Raw data of hole USW H-5, test H-5.3, depth interval 1033 to 1052 meters, and with open test interval of length 19 meters.

-Packer injection test for depth interval from 1,033 to 1,052 meters.

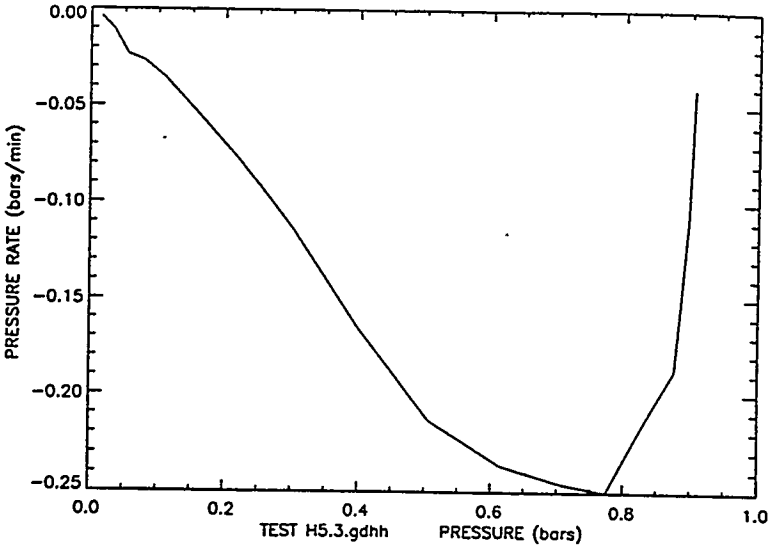

Figure 17b - Graph of head versus rate of head change, derived from raw data shown in Figure 17a.

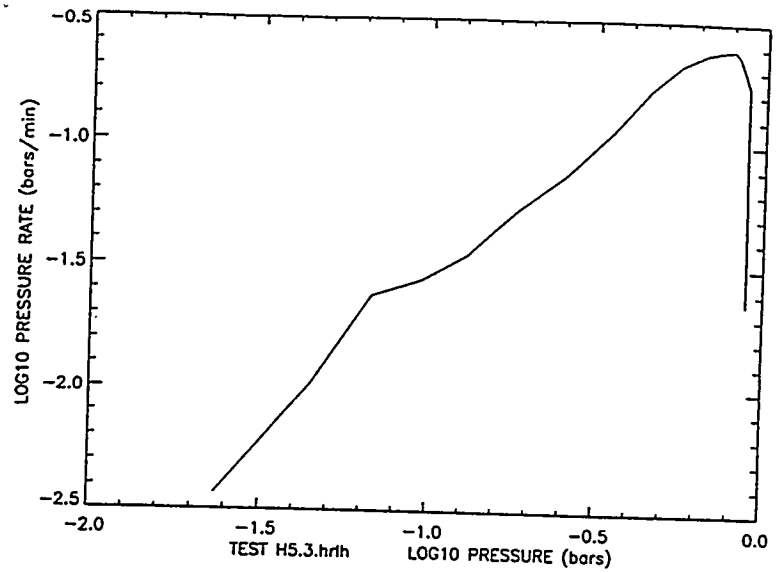

Figure 17c - Graph of log head versus log rate of head change, derived from raw data shown in Figure 17a.

HOLE USW H-6: Interval 649-683 meters.

Figure 18a shows the raw data of hole USW H-6, test H-6.1, depth interval 649 to 683 meters, and with open test interval of length 34 meters. No change in slope or bend is observable in this raw data, which has a very long time decay. However, Figures 18b,c are similar to the synthetic Figures 3b,c with a deviation from a linear trend at a critical pressure of about 23 bars. This pattern of behavior is characteristic of induced fractures that grow rapidly in area above the critical value. The low pressure region has a slope of log dh/dt versus log h of initially about 1 but this increases to about 2 just below the critical pressure. This indicates that the pre-existing fractures are dilating further as the head increases. Szymanski's qualitative estimate that the critical pressure is higher than the maximum head achieved in the slug test is doubtful, as our gradient curves enable the determination of the critical pressure more accurately.

Figure 18a - Raw data of hole USW H-6, test H-6.1, depth interval 649 to 683 meters, and with open test interval of length 34 meters.

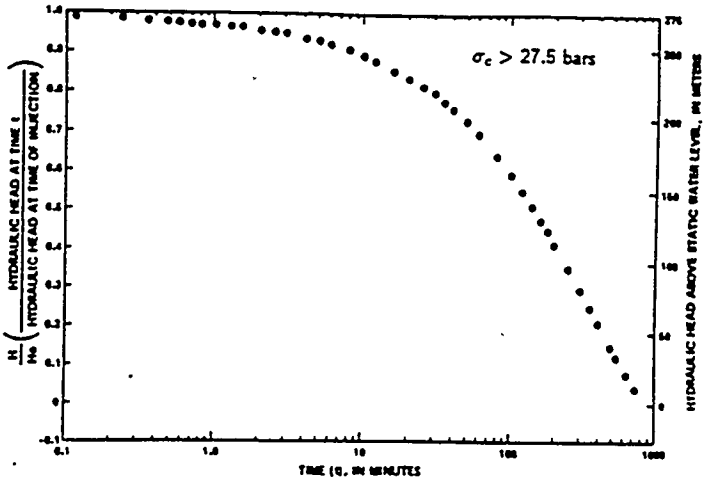

-Packer-injection test 3A, depth interval from 649 to 683 meters.

Figure 18b - Graph of head versus rate of head change, derived from raw data shown in Figure 18a.

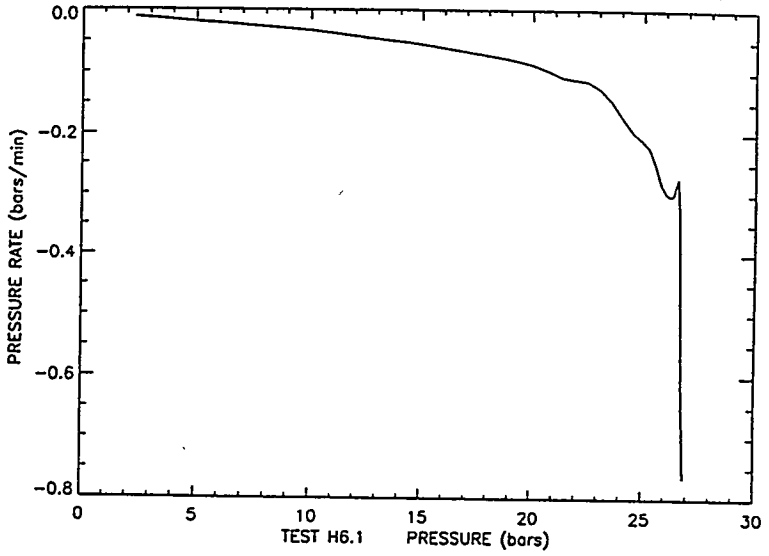

Figure 18c - Graph of log head versus log rate of head change, derived from raw data shown in Figure 18a.

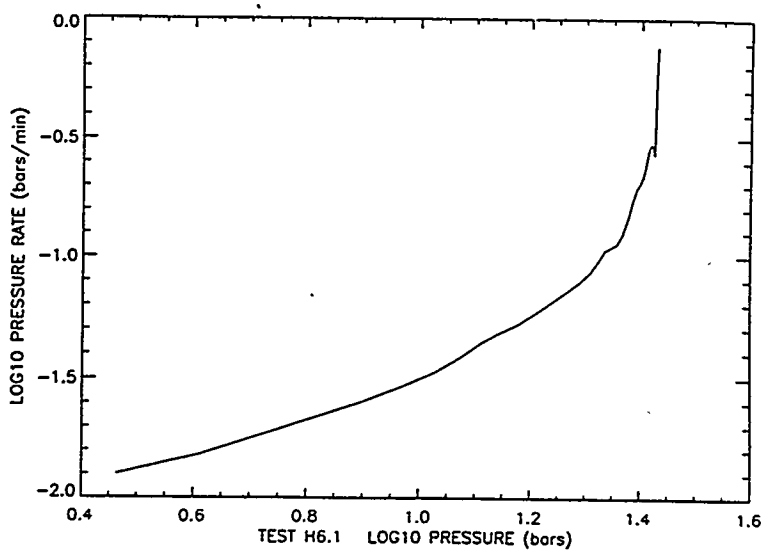

HOLE USW H-6: Interval 835-869 meters.

Figure 19a shows the raw data of hole USW H-6, test H-6.2, depth interval 835 to 869 meters, and with open test interval of length 34 meters. Szymanski's qualitative estimate of the "closure pressure" at which the change in slope in the raw data occurs is 20 bars. Figure 19b, showing dh/dt versus h, has a sharp directional change at about 19 bars corresponding to the critical pressure and close to Szymanski's value. The Figures 19a,b,c are similar to the synthetic curves, shown in Figures 2a,b,c, in which large areas of induced fracture surface rather than volume change is produced above the critical pressure. Below this critical pressure, we can see that the slope of the log dh/dt versus log h plot is initially less than 1 and then increases with increasing head. This indicates that existing fractures are dilating even at low heads.

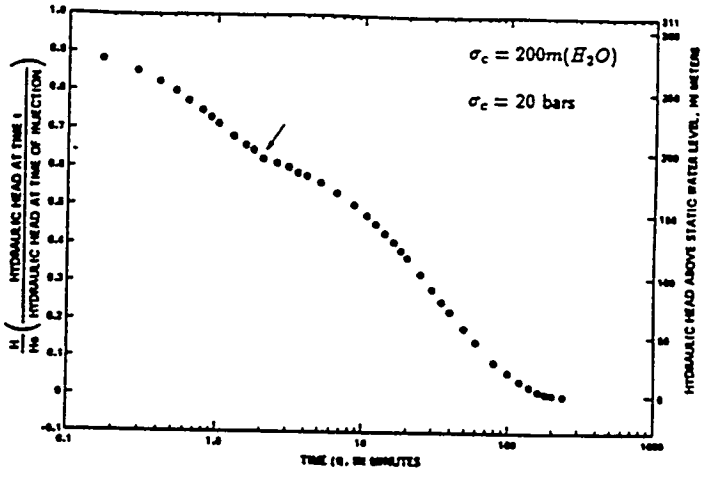

Packer-injection test 7, depth interval from 835 to 869 meters.

Figure 19a - Raw data of hole USW H-6, test H-6.2, depth interval 835 to 869 meters, and with open test interval of length 34 meters.

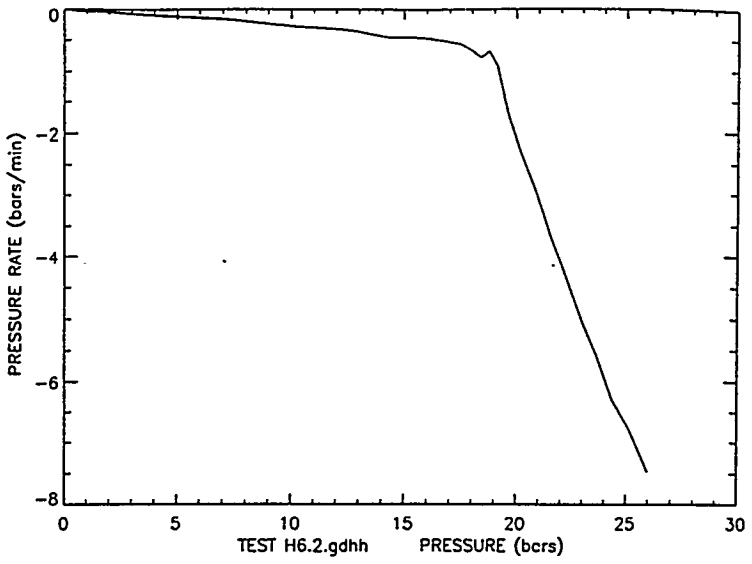

Figure 19b - Graph of head versus rate of head change, derived from raw data shown in Figure 19a.

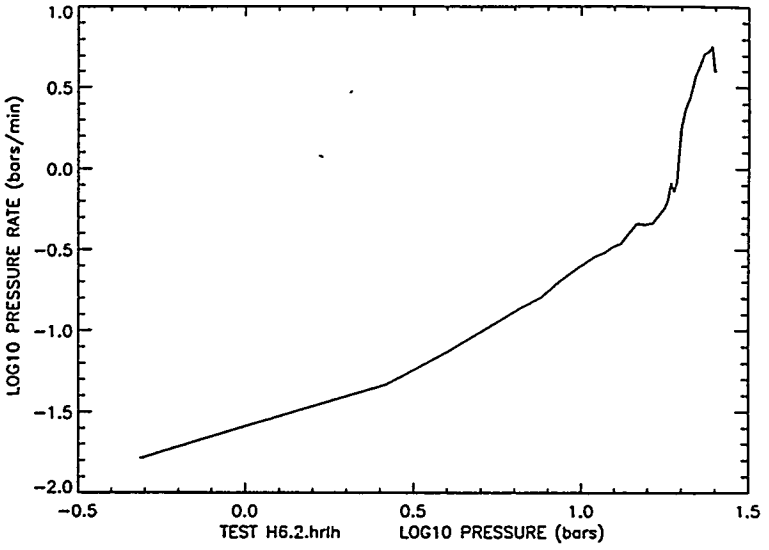

Figure 19c - Graph of log head versus log rate of head change, derived from raw data shown in Figure 19a.

HOLE USW H-6: Interval 606-640 meters.

Figure 20a shows the raw data of hole USW H-6, test H-6.3, depth interval 606 to 640 meters, and with open test interval of length 34 meters. This interval is of the same length but shallower than the previous case. No change in slope or bend is

observable in this raw data, and it has a much faster drop in head than the previous case. However, Figures 20b,c are similar to the synthetic Figures 6b,c with a deviation from a linear trend that is difficult to determine. This pattern of behavior is characteristic of induced fractures that, above the critical pressure, dilate more than they create induced area. The low pressure region has a slope of log dh/dt versus log h of about 1, which decreases above about 10 bars. This indicates existing fractures are dilating under increased pressure heads of water so that the effect of induced fractures opening is not sufficiently dramatic to cause a radical break in slope at the critical pressure. A qualitative estimate of critical pressure is approximately 26 bars.

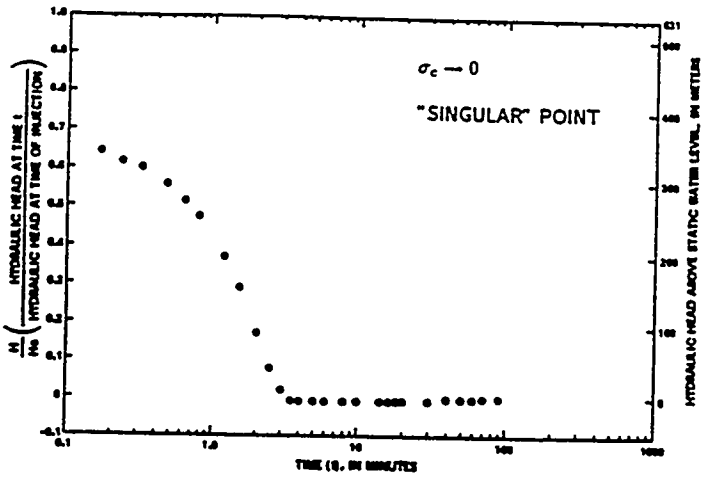

Figure 20a - Raw data of hole USW H-6, test H-6.3, depth interval 606 to 640 meters, and with open test interval of length 34 meters.

-Packer-injection test 2, depth interval from 606 to 640 meters.

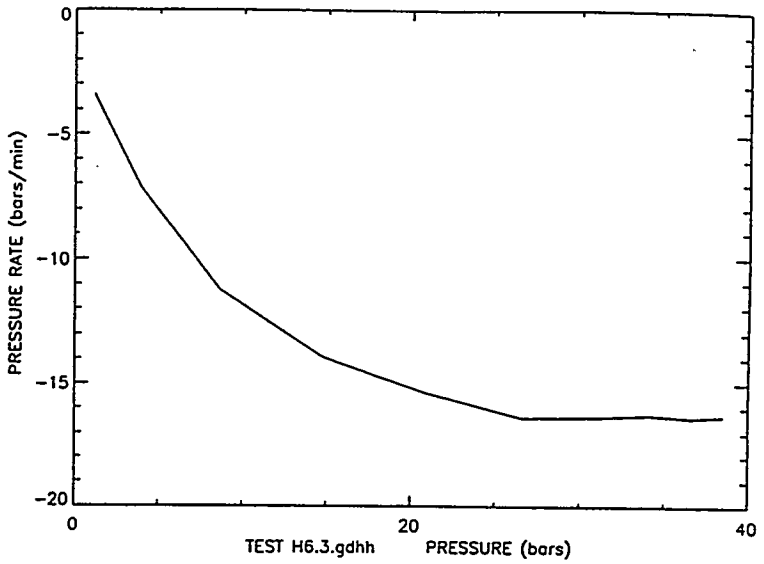

Figure 20b - Graph of head versus rate of head change, derived from raw data shown in Figure 20a.

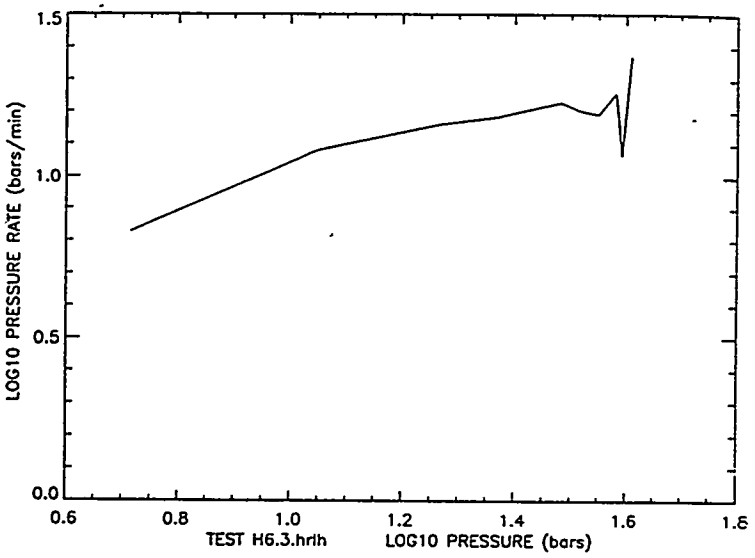

Figure 20c - Graph of log head versus log rate of head change, derived from raw data shown in Figure 20a.

HOLE UE25b: Interval 1006-1220 meters.

Figure 21a shows the raw data of hole UE25b, test UE25b.1, depth interval 1006 to 1220 meters, and with long open test interval of length 214 meters. No change in slope or bend is observable in this raw data, which has a very long time decay. However, Figures 21b,c are similar to the synthetic Figures 3b,c with a deviation from a linear trend

at a critical pressure in the range of about 32 to 42 bars. This pattern of behavior is characteristic of induced fractures that grow rapidly in area above the critical value. The low pressure region has a slope of log dh/dt versus log h of initially about 3/2 though there is much scatter in the data. This indicates that the pre-existing fractures are dilating further as the head increases. Szymanski's estimate that the critical pressure is higher than the maximum head achieved in the slug test is probably not correct, as our gradient curves enable the determination of the critical pressure more accurately.

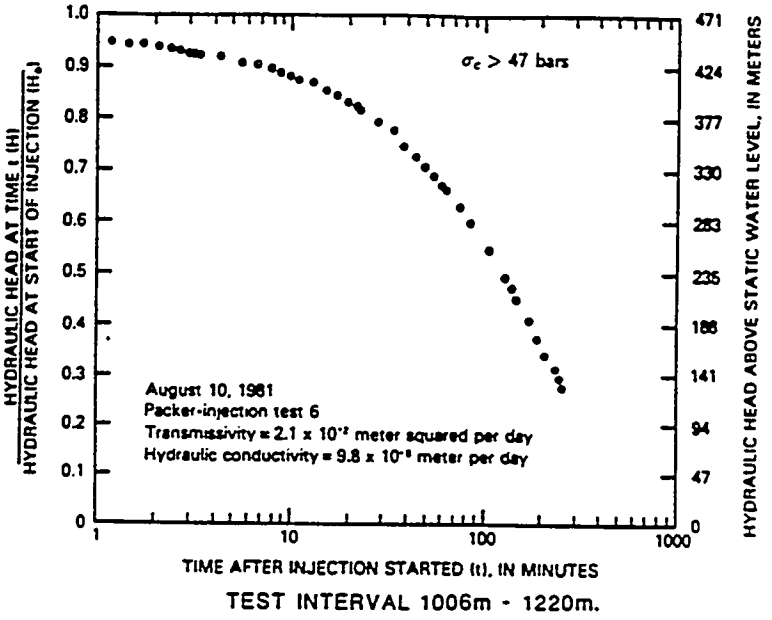

Figure 21a - Raw data of hole UE25b, test UE25b.1 depth interval 1006 to 1220 meters, and with long open test interval of length 214 meters.

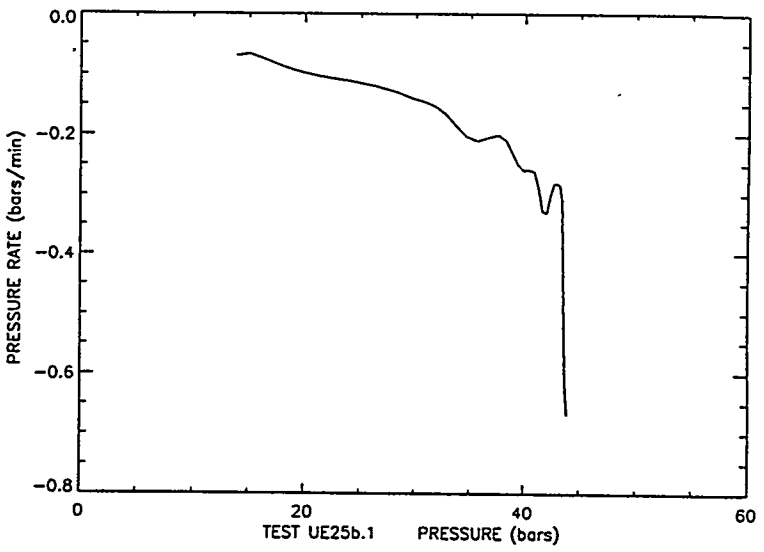

Figure 21b - Graph of head versus rate of head change, derived from raw data shown in Figure 21a.

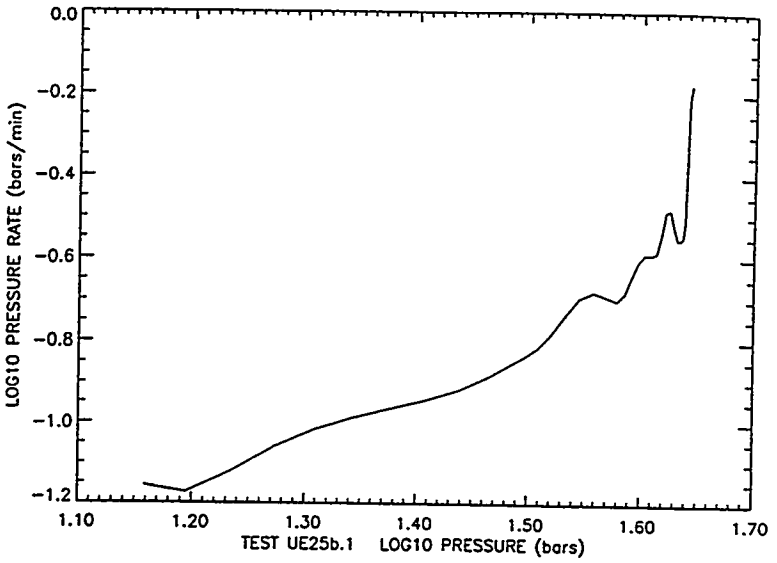

Figure 21c - Graph of log head versus log rate of head change, derived from raw data shown in Figure 21a.

HOLE UE25b: Interval 505-579 meters.

Figure 22a shows the raw data of hole UE25b, test UE25b.2, depth interval 505 to 579 meters, and with open test interval of length 74 meters. No change in slope or bend is observable in this raw data, and it has a much faster drop in head than the previous case. Indeed, data was only collected below 10 bars of head due to the initial rapid drop. However, Figures 22b,c are similar to the synthetic Figures 6b,c with a deviation from a linear trend at about 3.5 bars. This pattern of behavior is characteristic of induced fractures that dilate above the critical pressure more than they create induced area. The low pressure region has a slope of log dh/dt versus log h of about 1.

Figure 22a - Raw data of hole UE25b, test UE25b.2 depth interval 505 to 579 meters, and with open test interval of length 74 meters.

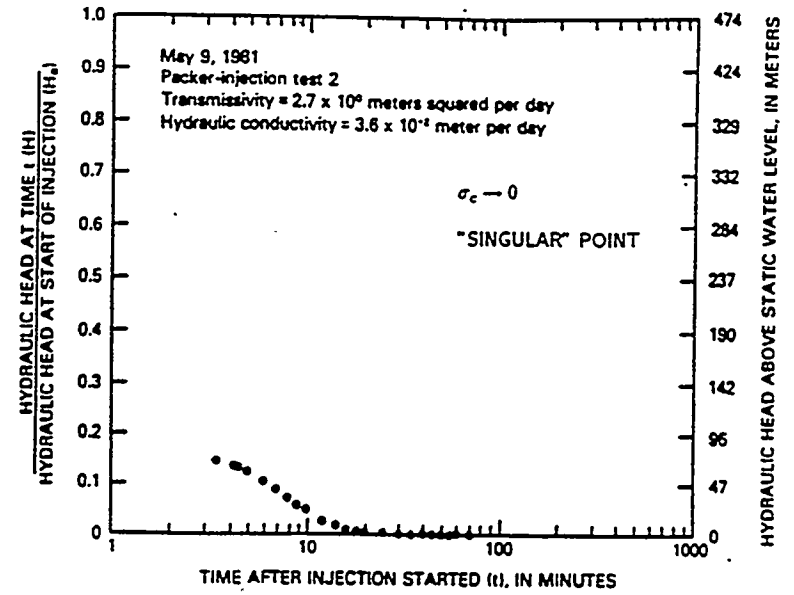

Results of the Cooper-Bredehoeft injection tests in Well UE-25b#1. From Lahoud et al., 1984.

Figure 22b - Graph of head versus rate of head change, derived from raw data shown in Figure 22a.

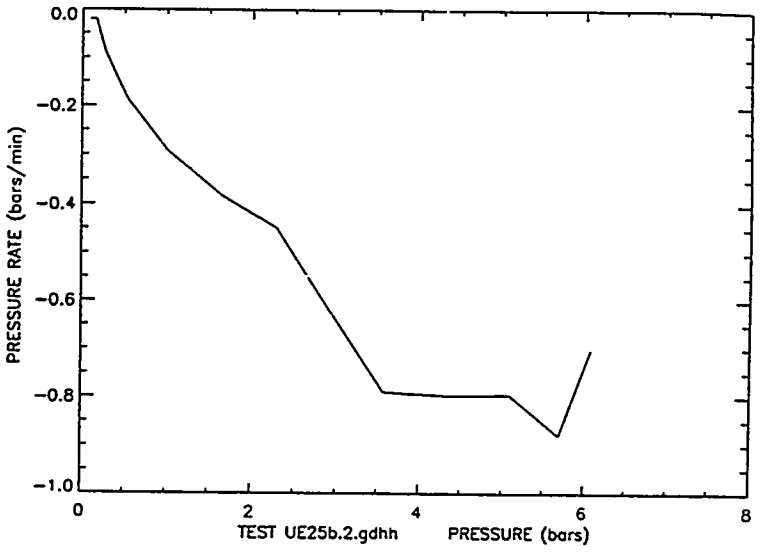

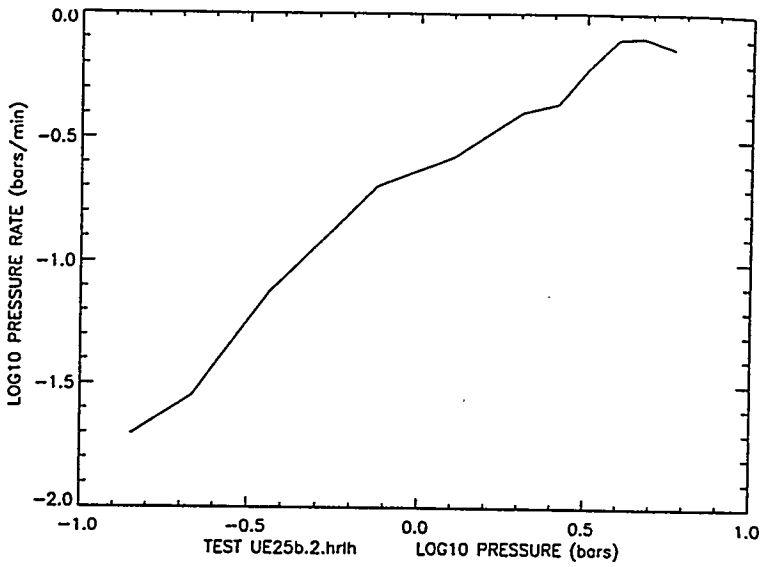

Figure 22c - Graph of log head versus log rate of head change, derived from raw data shown in Figure 22a.

HOLE UE25b: Interval 820-860 meters.

Figure 23a shows the raw data of hole UE25b, test UE25b.3, depth interval 820 to 860 meters, and with open test interval of length 40 meters. No change in slope or bend is observable in this raw data, and it has a fast drop in head like the previous case. Indeed, data was only collected below 20 bars of head due to the initial rapid drop. However, Figures 23b,c are very noisy though similar to the synthetic Figures 6b,c with a deviation from a linear trend at about 7 bars. This pattern of behavior is characteristic of induced fractures that dilate above the critical pressure more than they create induced area. The low pressure region has a slope of log dh/dt versus log h of about 1.

Figure 23a - Raw data of hole UE25b, test UE25b.3 depth interval 820 to 860 meters, and with open test interval of length 40 meters.

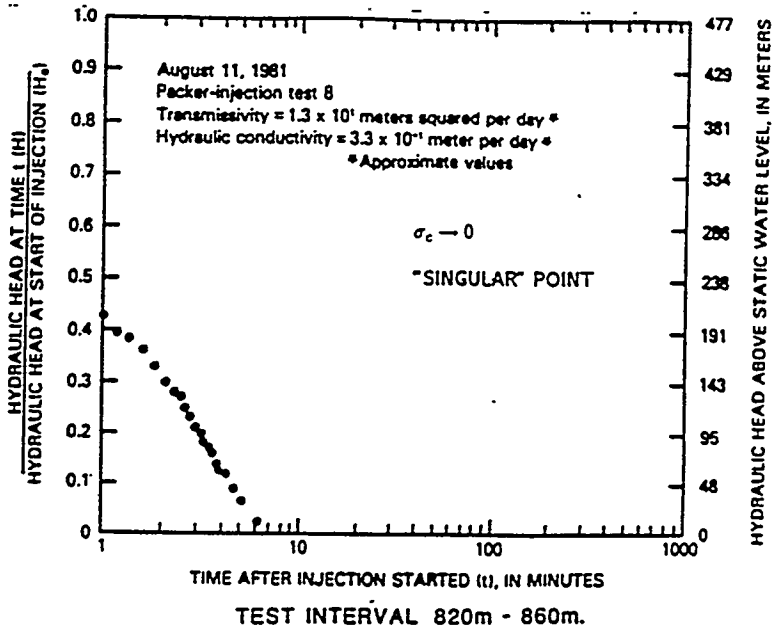

Results of the Cooper-Bredehoeft injection tests in Well UE-25b#1. From Lahoud et al., 1984.

Figure 23b - Graph of head versus rate of head change, derived from raw data shown in Figure 23a.

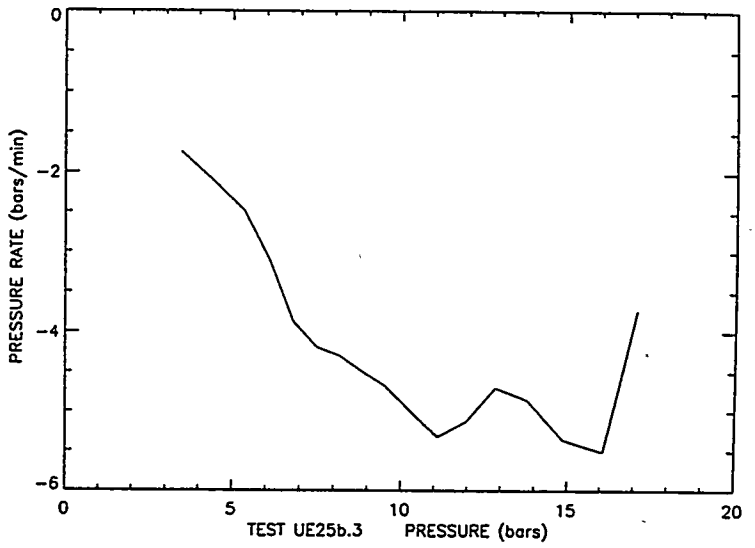

Figure 23c - Graph of log head versus log rate of head change, derived from raw data shown in Figure 23a.

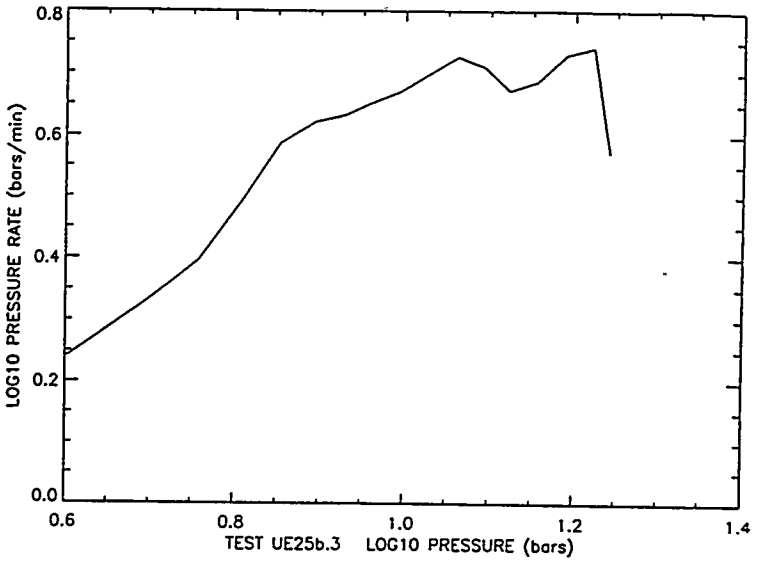

HOLE UE25p: Interval 600-650 meters.

Figure 24a shows the raw data of hole UE25p, test UE25p.1, depth interval 600 to 650 meters, and with open test interval of length 50 meters. No change in slope or bend is observable in this raw data, however, Figures 24b,c are similar to the synthetic Figures 5b,c with a deviation from a linear trend at a critical pressure in the range of about 28 to 30 bars. This pattern of behavior is characteristic of induced fractures that grow more rapidly in volume than in area above the critical value. The low pressure region has a slope of log dh/dt versus log h of initially about 5 decreasing to a value 1 just below the critical pressure. This indicates that the pre-existing fractures are dilating further as the head increases.

Figure 24a - Raw data of hole UE25p, test UE25p.1 depth interval 600 to 650 meters, and with open test interval of length 50 meters.

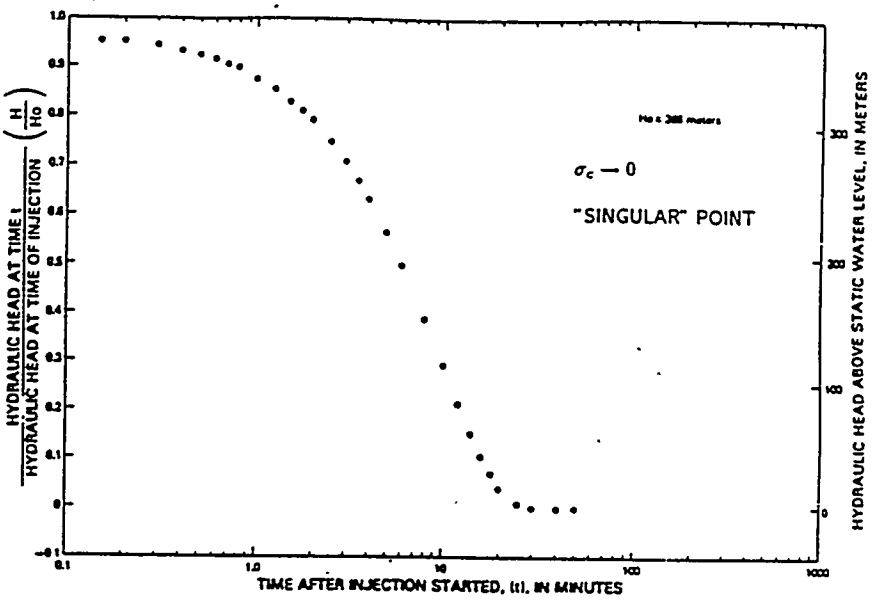

Packer-injection test 4, depth interval from 600 to 650 meters.

Results of the Cooper-Bredehoeft injection tests in Well UE-25p#1. From Craig and Johnson, 1984.

Figure 24b - Graph of head versus rate of head change, derived from raw data shown in Figure 24a.

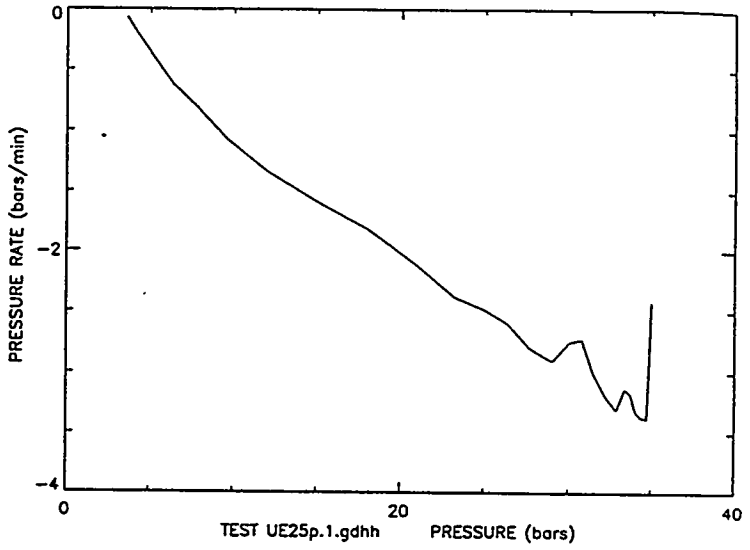

Figure 24c - Graph of log head versus log rate of head change, derived from raw data shown in Figure 24a.

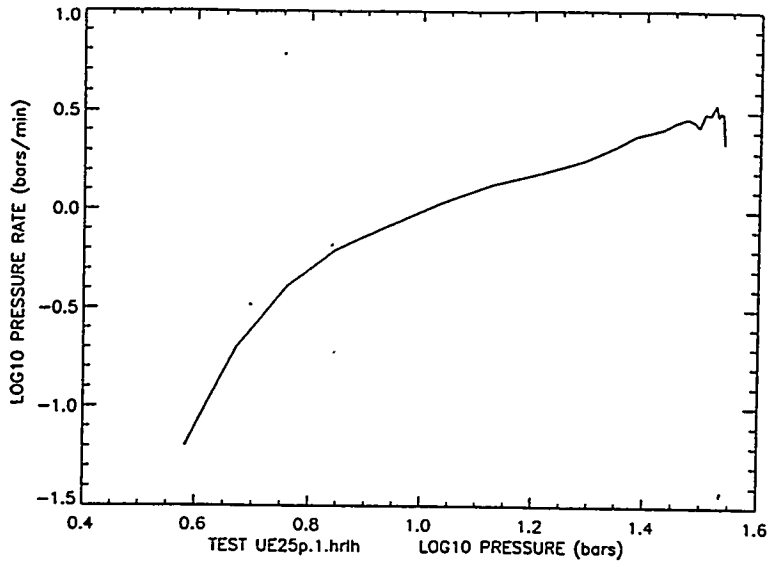

HOLE UE25p: Interval 974-1044 meters.

Figure 25a shows the raw data of hole UE25p, test UE25p.2, depth interval 974 to 1044 meters, and with open test interval of length 70 meters. No change in slope or bend is observable in this raw data, however, Figures 25b,c are similar to the synthetic solution where no induced fractures are formed even under the highest head as no appreciable deviation from a linear trend is seen. The low pressure region has a slope of log dh/dt versus log h of initially about 5 decreasing to a value 1 at high pressure. This indicates that the pre-existing fractures are dilating further as the head increases.

Figure 25a - Raw data of hole UE25p, test UE25p.2 depth interval 974 to 1044 meters, and with open test interval of length 70 meters.

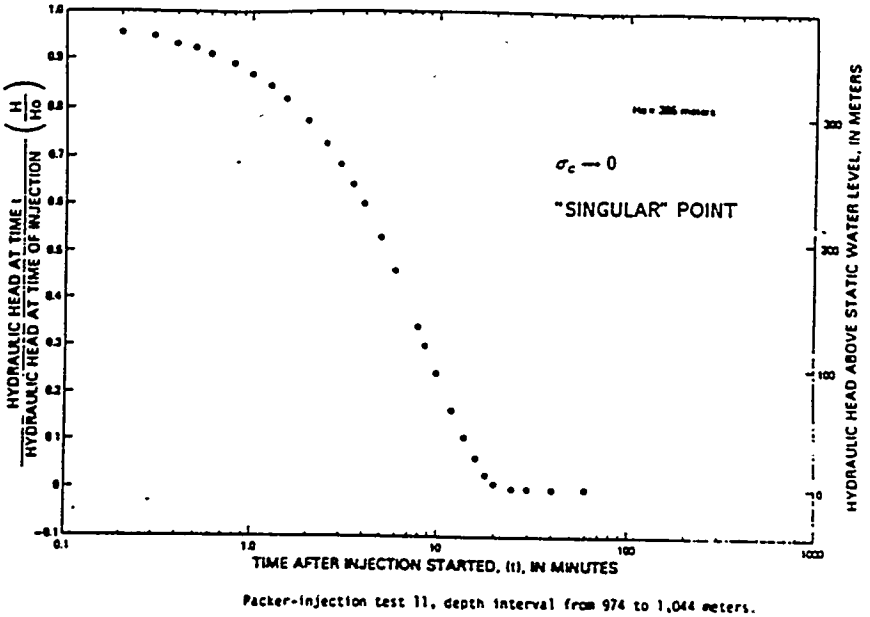

Figure 25b - Graph of head versus rate of head change, derived from raw data shown in Figure 25a.

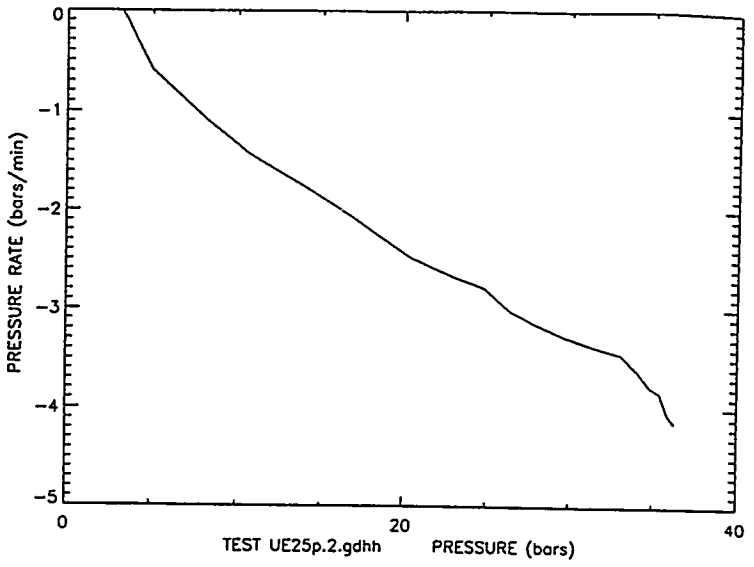

Figure 25c - Graph of log head versus log rate of head change, derived from raw data shown in Figure 25a.

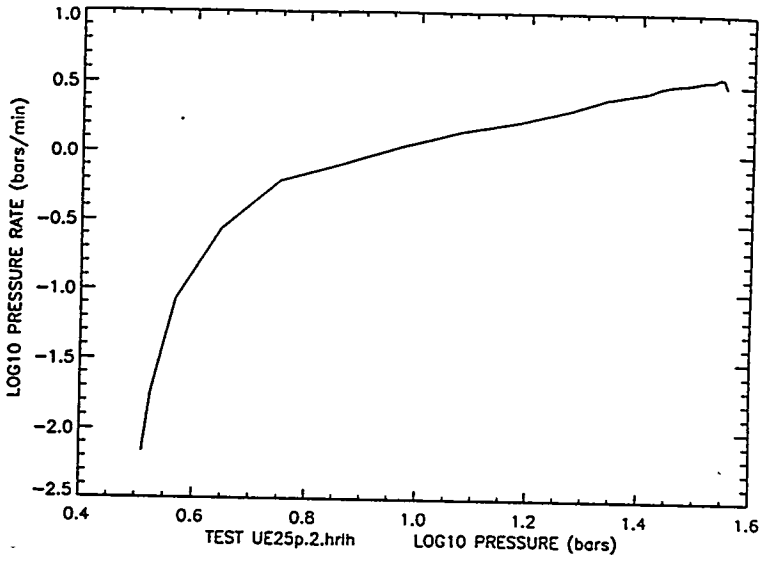

REFERENCES

Archambeau, C. B., and N. J. Price, 1991. *An Assessment of J. S. Szymanski's Conceptual Hydro-Tectonic Model and Its Relevance to Hydrologic and Geologic Processes at the Proposed Yucca Mountain Nuclear Waste Repository.* Minority Report of the Special DOE Review Panel. U. S. Department of Energy. Las Vegas, Nevada.

Baumgartner, J., and M. D. Zoback, 1989. *Interpretation of Hydraulic Fracturing Pressure-Time Records Using Interactive Analysis Methods.* International Journal of Rock Mechanics, Mineral Science and Geomechanics Abstract. Vol. 26, #6, pp, 461-469

Bear, J., 1972. *Dynamics of Fluids in Porous Media.* Elsevier Press.

Brown, S. R., and C. H. Scholz, 1985. *Closure of Random Elastic Surfaces in Contact.* Journal of Geophysical Research. Vol. 90, B7, p. 5531.

Brown, S. R., and C. H. Scholz, 1986. *Closure of Rock Joints.* Journal of Geophysical Research. Vol. 91, B5, p. 4939.

Goodman, R. E., 1976. *Methods of Geological Engineering in Discontinuous Rocks.* West Publishing.

Harr, M. E., 1991. *Groundwater and Seepage.* Dover Press

Hayashi, K., and B. C. Haimson, 1991. *Characteristics of Shut-In Curves in Hydraulic Fracturing Stress Measurements and Determination of In-Situ Minimum Compressive Stress.* Journal of Geophysical Research. Vol. 96, B11, pp. 18,311 - 18,321.

Hayashi, K., and I. Sakurai, 1989. *Interpretation of Hydraulic Fracturing Shut-In Curves for Tectonic Stress Measurements.* International Journal of Rock Mechanics, Mineral Science and Geomechanics Abstract. Vol. 26, #6, p. 477.

Healy, J. H., 1988. *Stress Measurements at Yucca Mountain.* Draft to USGS (personal communication).

Lardner, R. W., 1974. *Mathematical Theory of Dislocations and Fracture.* University of Toronto Press.

Stock, J. M., et al., 1985. *Hydraulic Fracturing Stress Measurements at Yucca Mountain, Nevada, and Relationship to the Regional Stress Field.* Journal of Geophysical Research. Vol. 90, B10, p. 8691.

Szymanski, J. S., 1989. *Conceptual Considerations of the Yucca Mountain Groundwater System with Special Emphasis on the Adequacy of the System to Accommodate a High-Level Nuclear Waste Repository.* DOE Internal Report, Las Vegas, Nevada.

Wood, R. M., and G. D. P. King, 1991. *Hydrological Signatures of Earthquake Strain.* Submitted to Journal of Geophysical Research.

PART B - Section II

Fluid Flows Due to Earthquakes with Reference to Yucca Mountain, Nevada

J. B. Davies

Fluid Flows Due to Earthquakes with Reference to Yucca Mountain, Nevada

Dr. John Bruce Davies

ABSTRACT

Yucca Mountain geohydrology is dominated by a deep water table in volcanic tuffa beds which are cut by numerous faults. Certain zones in these tuffas and most of the fault apertures are filled with a fine-grained calcitic cement. Earthquakes have occurred in this region with the most recent being of magnitude 5.6 and at a distance of about 20 km. Earthquakes in the western U.S.A have been observed to cause fluid flows through and out of the crust of the Earth. These flows are concentrated along the faults with normal faulting producing the largest flows. An earthquake produces rapid pressure changes at and below the ground surface, thereby forcing flows of gas, water, slurries and dissolved salts. In order to examine the properties of flows produced by earthquakes, we simulate the phenomena using computer-based modeling. We investigate the effects of faults and high permeability zones on the pattern of flows induced by the earthquake. We demonstrate that faults act as conduits to the surface and that the higher the permeability of a zone, the more the flows will concentrate there. Numerical estimates of flow rates from these simulations compare favorably with data from observed flows due to earthquakes. Simple volumetric arguments demonstrate the ease with which fluids from the deep water table can reach the surface along fault conduits.

INTRODUCTION

Yucca Mountain, Nevada, is in the Basin and Range geologic province, which is dominated by extensional stresses. These are the cause of normal faulting which has had a large effect on the Yucca Mountain region. The major faults are shown in Figure 1, while many other smaller faults are not shown on this regional map. The upper geological column at Yucca Mountain consists mainly of volcanic tuffas deposited during previous extensive volcanic action in the area. During an initial field survey, it was readily obvious that extensive calcite deposits occur, with certain tuffa zones being more likely to be impregnated with calcite. Most importantly, almost all faults observed in the field were filled with calcite deposits composed of a fine-grained compact cement located between the walls, Figure 2. There is also evidence of high pressure brecciation in the midst of a large calcite-rock system, located at drill hole USW-WT-7, Figure 3. All these phenomena lend credence to the source of these calcites being upwelling fluids and slurries. It has been proposed, Szymanski (1989), that earthquakes provide the power that could push these fluids to the surface. That earthquakes occur in the Yucca Mountain region was emphasised by the June, 1992, earthquake at Little Skull Mountain, magnitude 5.6 and only 20 km distant from the proposed repository site. This earthquake caused much destruction at the DOE site at Yucca Mountain.

In many seismically active regions, substantial transient outflows of water along spring-lines in the vicinity of faults are often observed following moderate shallow earthquakes, Briggs and Troxell (1955), Wood and King (1991). The Matsushiro earthquake swarm, which was energetically equivalent to a single event of magnitude

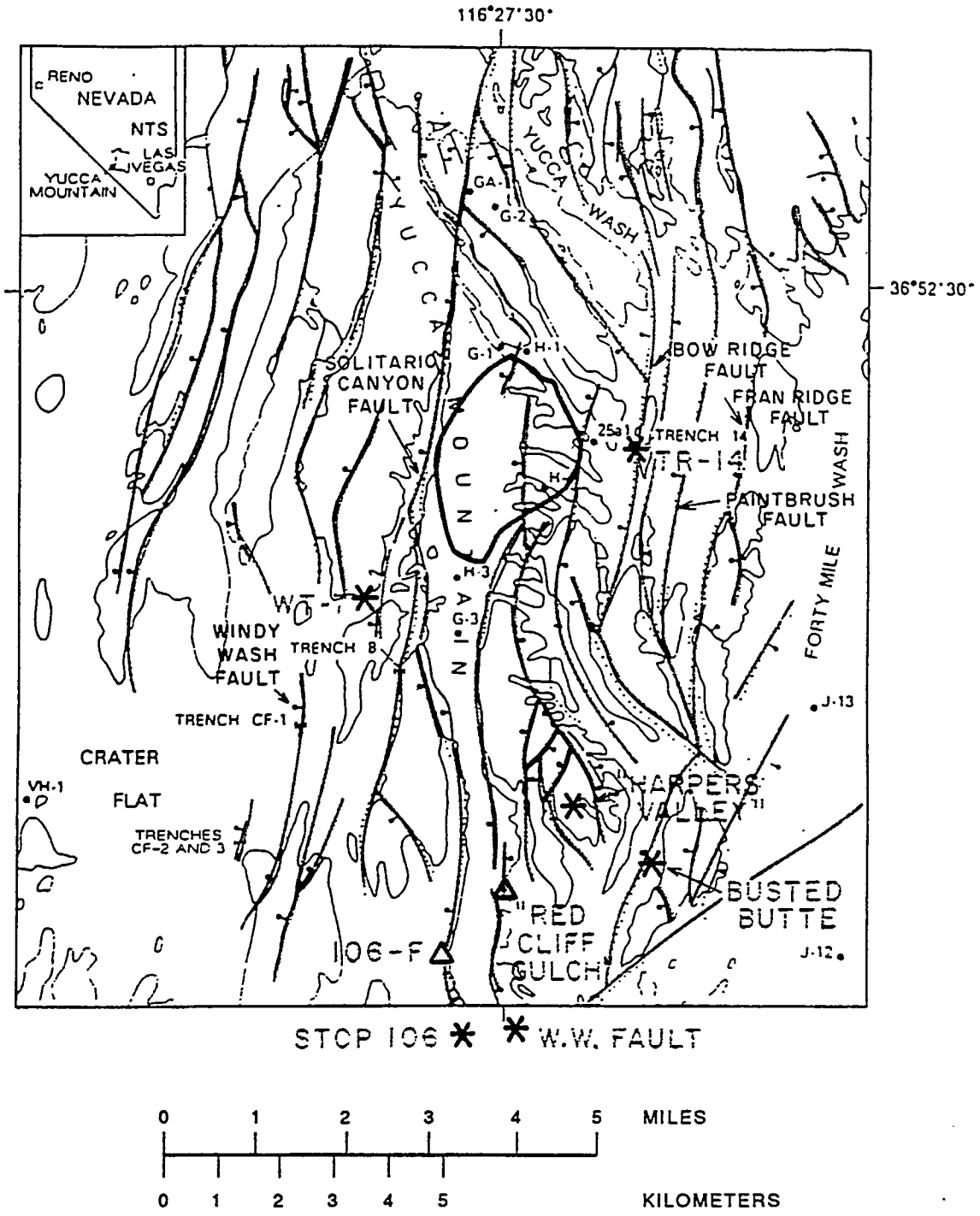

Figure 1. Map of Yucca Mountain and surrounding region with major faults and site locations.

Figure 2. Calcite-filled faults and fractures in Yucca Mountain.

Fig. 3 . - Evidence of hydrothermal activity can be found at many sites in the Yucca Mountain area. These views show veins and breccias which have developed adjacent to the western flank of Yucca Mountain itself, at the well site "WT-7" near the Solitario Canyon Faults shown in Figure 1.

6.3, resulted from strike-slip movements about a buried wrench fault about 10 km in length. It was accompanied by the surface explulsion in one year of about 10^7 cubic meters of warm Na-Ca-Cl brine, saturated with CO_2.

There have been numerous observations of the flow of water and gas out of the surface near earthquake hypocenters in the Basin and Range province, c.f. Wood and King (1991) for a historical survey. Massive flows with initial high velocities have been recorded, with explosive ejection of water and gas at localized areas during certain earthquakes, as at Borah Peak, Idaho,(M7.3,1983), as documented by Waag and Lane (1985). After these initial violent outbursts, ejection of excess water, usually from new and existing springs along pre-existing faults, occurred, Wood (1985). These initial flows usually peak in volume discharge rate soon after the earthquake, the discharge rate subsequently decaying in amplitude over a period of months. Similar flows were monitored after the M7.3 earthquake at Hebgen Lake in Montana in 1959. For the Borah Peak event, total excess flow is estimated to be between 0.2 and 0.5 cubic km, while Hebgen Lake excess flows are between 0.3 and 0.8 cubic km, Wood and King (1991). Excess flows have also been recorded from two Nevada earthquakes produced by normal faulting. The M6.9 Dixie Valley earthquake in 1954 produced excess discharge from springs upto 18 months after the event, Zones (1957). The 1915 Pleasant Valley earthquake produced increased flow in streams and the breaking out of new springs within 50 miles of the epicenter, Jones (1915). Numerous other occurrences of increases in groundwater flow have been observed following earthquakes in the Basin and Range province, Wood and King (1991). These authors conclude that: "The predicted volume strain associated with these events can be compared

with the total amount of water expelled and requires that nearly all of the seismic volume strain is accommodated by fissure closure and fluid expulsion. A well-connected fissure system extending throughout much of the brittle crust must exist to permit the water to escape."

In this paper, we investigate the effects of earthquakes on fluid flow in the sub-surface through computer simulations. Previous modeling has assumed a simple medium with usually a D'Arcy flow model and isotropic porosity and permeability, Carrigan et al.(1991). Such models are not valid for a Yucca Mountain environment which is dominated by fracture flow and with anisotropic permeabilities that depend on the fracture distribution and hydraulic conductivity properties. We have developed computer models which specifically include these non-uniform types of phenomena. Results from these simulations allow us to investigate the earthquake-induced fluid motions so produced. Our computer models use the total set of fluid conservation equations with no assumptions of steady-state and/or isotropy and solve them for both gas and water flows. We show that fracture flow will dominate the distribution patterns and that these conduits can transmit fluid to and above the present water table. These fluids can spread rapidly through the more porous and permeable zones in the tuffa beds. As the proposed Yucca Mountain repository is to be only 200 meters above the present water table, the effect of such induced fluid flows must be taken into account.

Earthquakes are due to tectonic strain changes in the subsurface rock system caused by slip along faults. Faults are long, broad yet narrow cracked zones where most of the displacement is located when the earthquake occurs. The type of faulting

most important for hydrological effects is normal dip-slip, Wood and King (1991), wherein one side slips downward with respect to the other. We have calculated the strain changes produced by normal displacement on a cross-section of a semi-infinite fault. These strain and corresponding elastic stress changes are obtained using a dislocation model with finite element numerical methods. The stress changes impose pressure gradients on the fluids enclosed in the rock matrix.

In order to simulate flows of gas and liquid, we use a multiphase system of flow equations which, for each constituent, are the conservation laws of mass, momentum and energy, which are integrated numerically with stable time steps. This complex non-linear system incorporates advection, bouyancy, compressibility, dissipation and thermal conductivity. In regions where the imposed pressure decreases, gas will be released from solution, the quantity of gas being controlled by the ideal gas equation of state. Gas, relative to liquid, will move upward toward the surface due to bouyancy forces. The main drag forces are on the water flows and are due to the rock walls. A velocity dependent drag force can be equated to permeability using D'Arcy's Law under steady-state conditions.

We use the simulations to demonstrate the importance of fractures as conduits for the subsurface flows. Numerical experiments are performed in order to investigate the effects of varying initial fluid concentrations, permeabilities (drag) and the locations of fracture conduits and anomalous zones in the tuffas. The results of our investigations indicate that fracture flow dominates over the usual porous medium flow and controls the transient flow structure and its temporal and spatial character. Observed flows and their properties compare favourably with the results of these simulations. Simple argu-

ments, using the volumetric results of Carrigan et al. (1991), show that flow up the fractures due to typical earthquakes can reach levels two or three orders of magnitude greater than for flows in isotropic porous media.

CONSERVATION LAWS

There are two main approaches to obtaining the continuity equations that govern the thermodynamic fields for each component of the multiphase system. One approach is based on a set of equations of motion for mean quantities that represent the density, momentum and energy of the mixture. These are then decomposed into separate components. We shall use the alternative approach, Oran and Boris (1987,p.497], which is a generalisation of the two-fluid equations presented by Stewart and Wendroff (1984). A set of fluid equations can be written for each phase, labeled α. The mass per unit volume of the α'th constituent is equivalent to the product of its volume fraction or concentration ϕ^α and its density ρ^α. Thus the mean density of the fluid system $\bar{\rho}$ is given by $\Sigma_\alpha \phi^\alpha \rho^\alpha$. For each constituent, the conservation law for mass is,

$$\frac{\partial(\phi^\alpha \rho^\alpha)}{\partial t} = -\frac{\partial}{\partial x_j}(\phi^\alpha \rho^\alpha v_j^\alpha) + r^\alpha \qquad (1)$$

where v_j^α is velocity in the x_j direction of the α'th component with r^α the mass transfer terms representing the rate of creation. Conservation of total mass implies $\Sigma_\alpha r^\alpha = 0$. Conservation of momentum for each constituent is similarly expressed as :

$$\frac{\partial(\phi^\alpha \rho^\alpha v_i^\alpha)}{\partial t} = -\frac{\partial(\phi^\alpha \rho^\alpha v_j^\alpha v_i^\alpha)}{\partial x_j} + X_i^\alpha + \frac{\partial}{\partial x_j}(\phi^\alpha P_{ij}^\alpha) + s_i^\alpha \qquad (2)$$

where X_i^α are external forces which includes both gravity and drag forces, P_{ij}^α is the generalized stress and s_i^α is the rate of momentum creation proportional to r^α of the

α'th component. Such a momentum source can be due to gas coming out of solution and having the instantaneous velocity of the liquid. Conservation of total momentum implies $\Sigma_\alpha s_i^\alpha = 0$. Also, after differentiation of (2) by parts and, as usual, using (1) we get :

$$\phi^\alpha \rho^\alpha \frac{\partial v_i^\alpha}{\partial t} = -\phi^\alpha \rho^\alpha v_j^\alpha \frac{\partial v_i^\alpha}{\partial x_j} + X_i^\alpha + \frac{\partial}{\partial x_j}\phi^\alpha P_{ij}^\alpha + (s_i^\alpha - r^\alpha v_i^\alpha) \qquad (3)$$

Conservation of energy of each constituent is :

$$\frac{\partial}{\partial t}(\phi^\alpha E^\alpha) = -\frac{\partial}{\partial x_j}(\phi^\alpha v_j^\alpha E^\alpha) + \frac{\partial q_j^\alpha}{\partial x_j} - p^\alpha \frac{\partial \phi^\alpha}{\partial t} - p^\alpha \frac{\partial \phi^\alpha v_j^\alpha}{\partial x_j} + \Phi^\alpha + L^\alpha + M^\alpha \quad (4)$$

where E^α is total energy, p^α is pressure, q_j^α is heat flow, Φ^α is the internal viscous dissipation and L^α is the rate of energy change due to the mass transfer, r^α, where $\Sigma_\alpha L^\alpha = 0$. M^α is the dissipated energy rate due to the external forces.

ASSUMPTIONS

We are able to simplify these equations through application of certain assumptions without sacrificing too much generality. Our most important assumption is that the earthquake will release gas in regions where the imposed pressure is negative. The amount of gas is calculated and fixed as an initial condition so that, because there is no time dependence of the gas release, then the terms concerning rate of creation are zero in the above continuity equations. The conservation of mass equation becomes :

$$\frac{\partial \phi^\alpha \rho^\alpha}{\partial t} = -\frac{\partial}{\partial x_j}(\phi^\alpha \rho^\alpha v_j^\alpha) \qquad (5)$$

Also, after differentiation of (2) by parts and, as usual, using (1) we get :

$$\phi^\alpha \rho^\alpha \frac{\partial v_i^\alpha}{\partial t} = -\phi^\alpha \rho^\alpha v_j^\alpha \frac{\partial v_i^\alpha}{\partial x_j} + X_i^\alpha + \frac{\partial}{\partial x_j}\phi^\alpha P_{ij}^\alpha \qquad (6)$$

We are only interested in the effects of the imposed pressure p^r on the fluids due to the compaction or expansion of the rock matrix. The subsequent changes in pressure, due to the flow of fluids, are assumed small compared to the imposed pressures in the time immediately after the earthquake. We also ignore spatial and temporal gradients in concentration so that the equation for energy conservation can be written :

$$\phi^\alpha \frac{\partial}{\partial t} E^\alpha = -\phi^\alpha \frac{\partial}{\partial x_j} (v_j{}^\alpha E^\alpha) + \frac{\partial q_j{}^\alpha}{\partial x_j} - p^r \phi^\alpha \frac{\partial v_j{}^\alpha}{\partial x_j} + \Phi^\alpha + M^\alpha \qquad (7)$$

In order to reduce this equation to one governing temperature, the total energy term can be decomposed into thermal and kinetic energy components :

$$E^\alpha = C_v{}^\alpha T^\alpha + \frac{1}{2} \rho^\alpha v_i{}^\alpha v_i{}^\alpha$$

where T^α is the temperature and $C_v{}^\alpha$ is the specific heat at constant volume of the α'th constituent.

The dependent and independent variables are normalized with respect to characteristic invariants in order to form dimensionless variables. Distances are normalized through the characteristic depth, which is taken to be 10 Km, which is the typical depth of a crustal earthquake, and velocities are normalized with respect to c_s, the sound velocity in water. Similarly density, pressure and temperature are normalized to surface values, and the independent variable, time t, is normalized using the characteristic depth and velocity. The magnitude of the dimensionless parameters, obtained by this process, are readily related to the usual dimensionless Rayleigh and other numbers and provide a measure of the relative importance of the terms in the basic equations. These equations are now split into two sets, one governing the ambient field, with the other controlling the transient flows due to stress changes. The ambient field is assumed to be that of water under hydrostatic pressure gradients with zero

velocities. This ambient solution gives a hydrostatic pressure gradient which balances the gravitational forces and is readily removed from equation (2) leaving similar equations for the transient flows of each component.

CONSTITUTIVE RELATIONS

Because this multiphase system assumes the presence of free gas and allows dissolved gas to be emitted in regions of initial imposed pressure drops, the constitutive relation between pressure and density/temperature will be dominated by the gas as it is much more compressible than the liquid. The effect of dilatation of the rock matrix on the gas-water system will be to release sufficient gas to keep the pressure at ambient. The effect of contraction of the rock matrix on the gas-water system is to decrease the volume available to the constituents. This volume change will take place mainly in the free gas due to its higher compressibility. The equation of state for the gas is taken to be ideal i.e.

$$P^1 = \frac{k_B}{m^1} \cdot \rho^1 \cdot T^1 \tag{8}$$

where k_B is Boltzmann's Constant and m^1 is mean molecular weight of the gas, component 1. The generalised stress tensor has off-diagonal components which can be related to strain rates in order to derive a Navier-Stokes relation for dissipative effects within the fluids, i.e.

$$P_{ij} = -p\delta_{ij} + 2\mu\dot{e}_{ij} - \frac{2}{3}\mu\delta_{ij}\dot{e}_{kk} \tag{9}$$

where μ is the coefficient of viscosity and $\dot{e}_{ij}$ is the rate of increase of strain given by :

$$\dot{e}_{ij} = \frac{1}{2}\left(\frac{\partial v_i}{\partial x_j} + \frac{\partial v_j}{\partial x_i}\right) \tag{10}$$

For each constituent, these relations can be input into the equations of momentum conservation, (2), with μ allowed to be variable for each phase. The viscosity also contributes to the conservation of energy, the internal dissipation term Φ being for such a material :

$$\Phi = 2\mu\dot{e}_{ij}^{\,2} - \frac{2}{3}\mu\dot{e}_{jj}^{\,2} \tag{11}$$

this dissipation being internal to the fluid.

The other important dissipative mechanism for flow through narrow orifices are the drag forces. The water, as it flows through the rock matrix, is subject to drag by the walls on the adjacent liquid boundary layer, which, at low speeds, gives a drag force proportional to their velocity difference. In general, such a drag force can be taken to have the form :

$${}_dF_j^{(n)} = \sum_{m \neq n} \beta_{jk}^{(n,m)} \left[v_k^{(n)} - v_k^{(m)} \right] \tag{12}$$

where the $\beta_{jk}^{(n,m)}$ is the drag coefficient tensor between the n*th* and m*th* constituents and consists of spatially variable randomized functions, while $v_k^{(n)}$ is the k*th* particle velocity component of the n*th* constituent. This is equivalent to D'Arcy's Law for a liquid in a permeable medium when the flow is slow, steady-state and with a constant permeability and pressure gradient in the medium, Bear (1972). Because its specific gravity is much less than the surrounding liquid, gas rises upward due to bouyancy, and thus will move relative to the water and will thereby be subject to a drag force proportional to their velocity differences.

SEISMIC SOURCES

Normal faulting is observed to cause the largest hydrological effects and these will be used in most of the simulations. The synthetic dip-slip source is an equivalent dislocation, with field variables constant in the y-direction. Using finite element methods, the strain changes produced by a dislocation source can be obtained numerically, Frazier and Petersen (1974), and these are converted into pressure changes that act on the fluids. The length, depth, dip, strength and displacement of the dislocated fault are chosen to represent the expected earthquake. Linear elastic equations are iteratively solved to determine the initial strain changes in the rock, Figure 4. The largest strains occur near the bottom tip of the fault as the displacements must go to zero at this location. Listric faults, which are normal faults with non-planar faces, have also been numerically modeled and give similar strain patterns though with increased strains near regions of large curvature on the fault, Figure 4.

FINITE DIFFERENCE SCHEME

The set of non-linear partial differential equations are converted to a corresponding set of finite difference equations in order for computer integration in time and space. Upwind and other differencing algorithms are used for first order spatial gradients with the advection velocity terms treated non-locally on the lattice for stability. The updated velocity variable is projected not from just the old dependent variable, a process that is inherently unstable, but from a distributed smoothed average of the variable at locations surrounding the specific spatial location. Such a smoothing method brings stability to the differencing scheme, and also helps in stabilising the

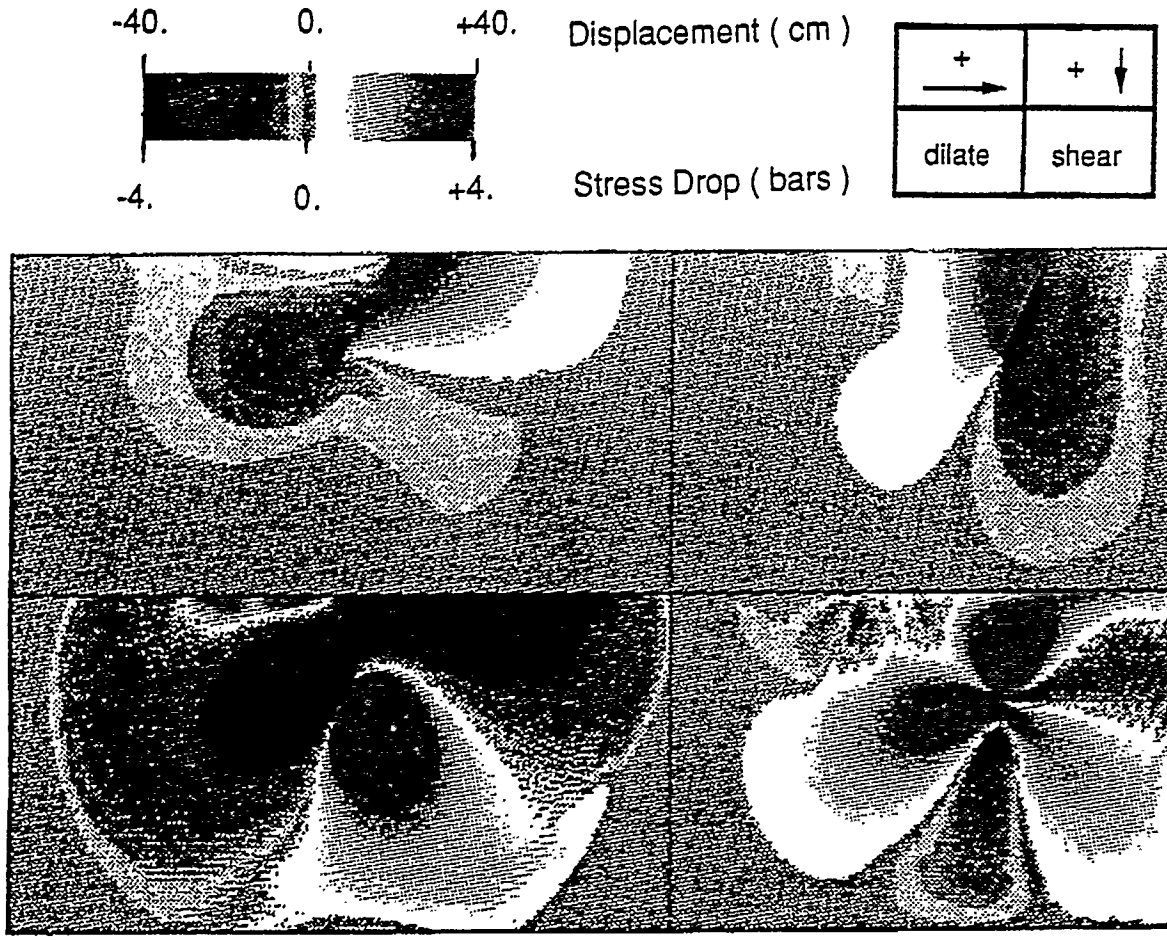

Fig. 4 . - Displacements, shear stress and dilatation in the upper crust in the vicinity of a dip-slip (60°) and a listric (60° to 0°) fault with hypocenters at 12 km. depth. The inset at the upper right indicates the field variable plotted for each fault type in the four vertical cross-sections shown. (Horizontal and vertical displacements, dilatation and shear stress.)

integration at grid corners and boundaries. Numerical diffusion is produced by this process, but is constrained by having no smoothing of the density variable while allowing velocities and temperature to be smoothed sufficiently for long-term stability, given a sufficiently small time-step. In the integration scheme, the flow velocities, temperature and density are obtained via their continuity equations while pressure is obtained from insertion of the updated density and temperature into the equation of state. Boundary conditions are necesary for integration over a finite grid. The ground surface is a complex boundary, which must model the effect of a water table together with a partially saturated zone, which is the ground above the water table. The artificial grid vertical sides are open boundaries that allow free flow in either direction. Open boundary conditions also apply at the lower sub-surface boundary; for free flow, velocities are not taken as zero but, instead, zero velocity and density gradients are assumed in the direction normal to the open boundary.

INTEGRATION PROCEDURE

Cartesian coordinates, xyz, were used to model the 3-dimensional system. By using an earthquake fault whose length is long compared to its width and depth, grid size can be reduced to 50*10*50 with the y direction being that along the fault strike.

The method of integration of these equations is outlined below :

1. Set initial values of ambient dependent variables, and values and spatial variability of the drag coefficients.

2. Read in seismic source pressures as imposed values, constant in time.

3. Where these imposed pressures are negative, gas is emitted from solution in sufficient amounts to increase the total pressure to ambient. The gas density increase is determined from the ideal gas equation of state. Thus in these zero pressure gradient regions, no flows occur due to the absence of imposed pressures.

4. In regions of positive pressure imposed by the rock matrix, the fluids are forced to flow by these pressure gradients.

5. The conservation laws, in finite difference form, are integrated with a stable time step.

6. The resultant change in the density and temperature of the gas are used in the ideal gas equation to compute the change in gas pressure. This is very small compared with the imposed pressures in the compressive regions and is of small effect even in the expansive regions.

7. Drag forces are applied to the water and gas flows.

8. Viscous forces can be applied but are set to zero in this experiment.

9. Boundary conditions are satisfied.

10. Reloop on the time step.

SIMULATIONS

We have performed a sequence of simulations of the flows of water and gas from a typical normal fault earthquake. The faulting was simulated for our typical case with a fault of length 10 km and depth 10 km with a displacement of 1m. This corresponds to an earthquake of magnitude about 6 on the Richter scale. Its induced pressure changes are as shown in Figure 4.

We now examine the fluid flows produced by these pressure changes. We assume that the water initially is concentrated inversely with depth below the water table, though this affects only the total volume of flow and not the particular velocity. Figure 5. shows the vertical and horizontal fluid velocities within a few seconds after the earthquake, for the simplest case where the drag forces, and thus the permeabilities, are uniform and constant in space. On the left are shown the water velocities, on the right the gas velocities. The upper simulations are for the vertical velocity with blue color for upward motions and red for downward motions. The lower simulations are for the horizontal velocity with blue color for leftward motions and red for rightward motions. Each picture depicts a cross-section across the fault with the top of the fault at the top right hand corner and the bottom of the fault motion at the center of the diagram. The dimensions of the diagrams are 20 km deep by 20 km wide. We can see from the simulations that an intense upward flow of water occurs near the surface on the hanging wall, a result observed in normal earthquakes in the western U.S. At the surface, there is also a motion of water away from the fault though the gas mimics these effects but with less velocity. At the depth of the earthquake, 10 km, we see that the vertical and horizontal velocities are similar for both water and gas.

In Figure 6, we show the effect of enhanced permeability along the main fault where the drag forces are assumed to be much less than those operating on the uniform background medium. The fault can readily be seen to have much faster fluid flows along its conduit compared to the surrounding uniform rock.

In Figure 7, we simulate the effect of a parallel but inactive fault conduit on the hanging wall side. This higher permeability zone has much faster fluid flows than the

WATER VERTICAL VELOCITY GAS VERTICAL VELOCITY

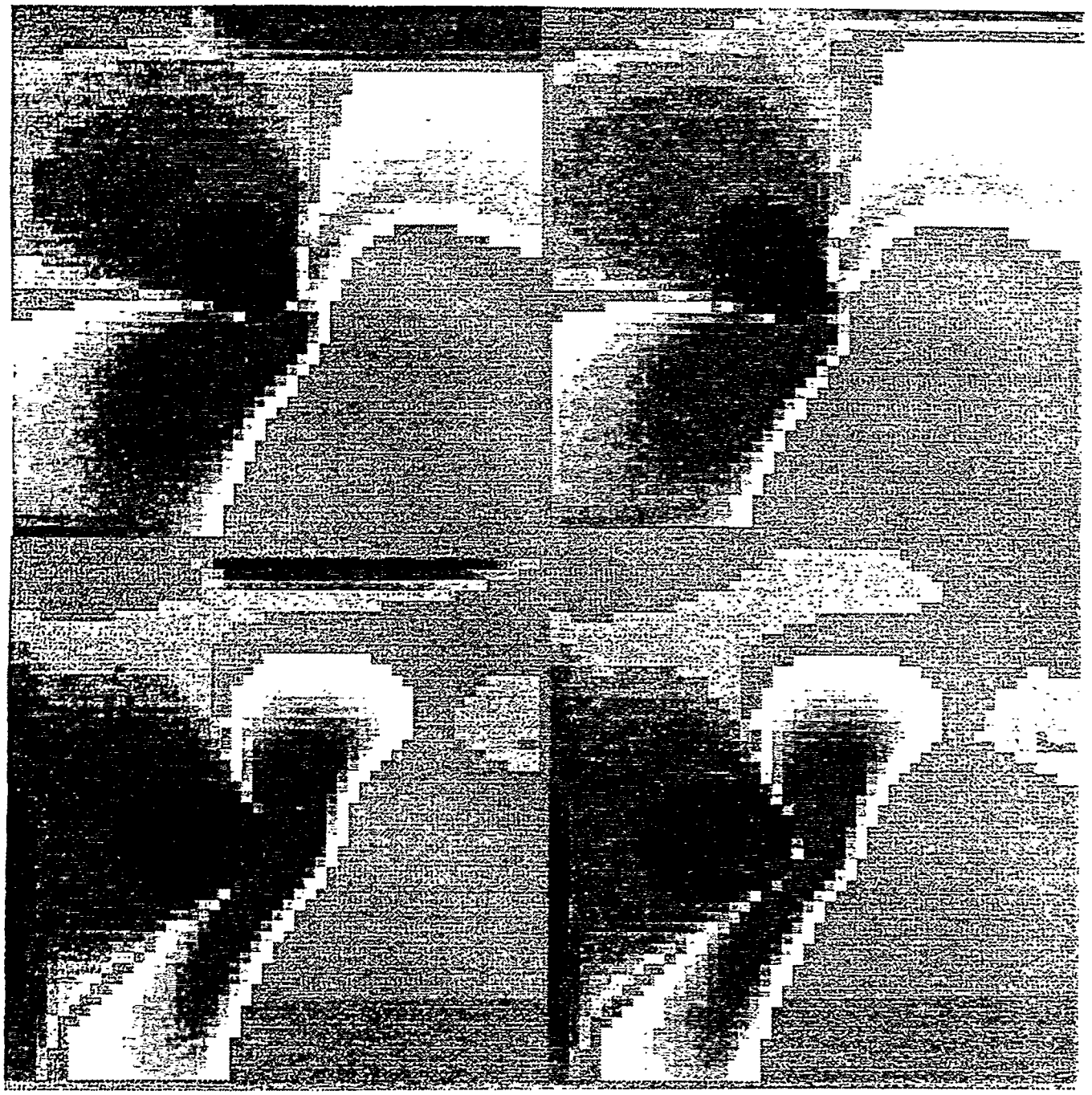

WATER HORIZONTAL VELOCITY GAS HORIZONTAL VELOCITY

Figure 5. Water and gas velocities in an uniformly permeable medium. Each cross-section is 20 km deep by 20 km wide. Upward vertical motions are blue and downward motions red; leftward motions are blue and rightward motions are red.

WATER VERTICAL VELOCITY GAS VERTICAL VELOCITY

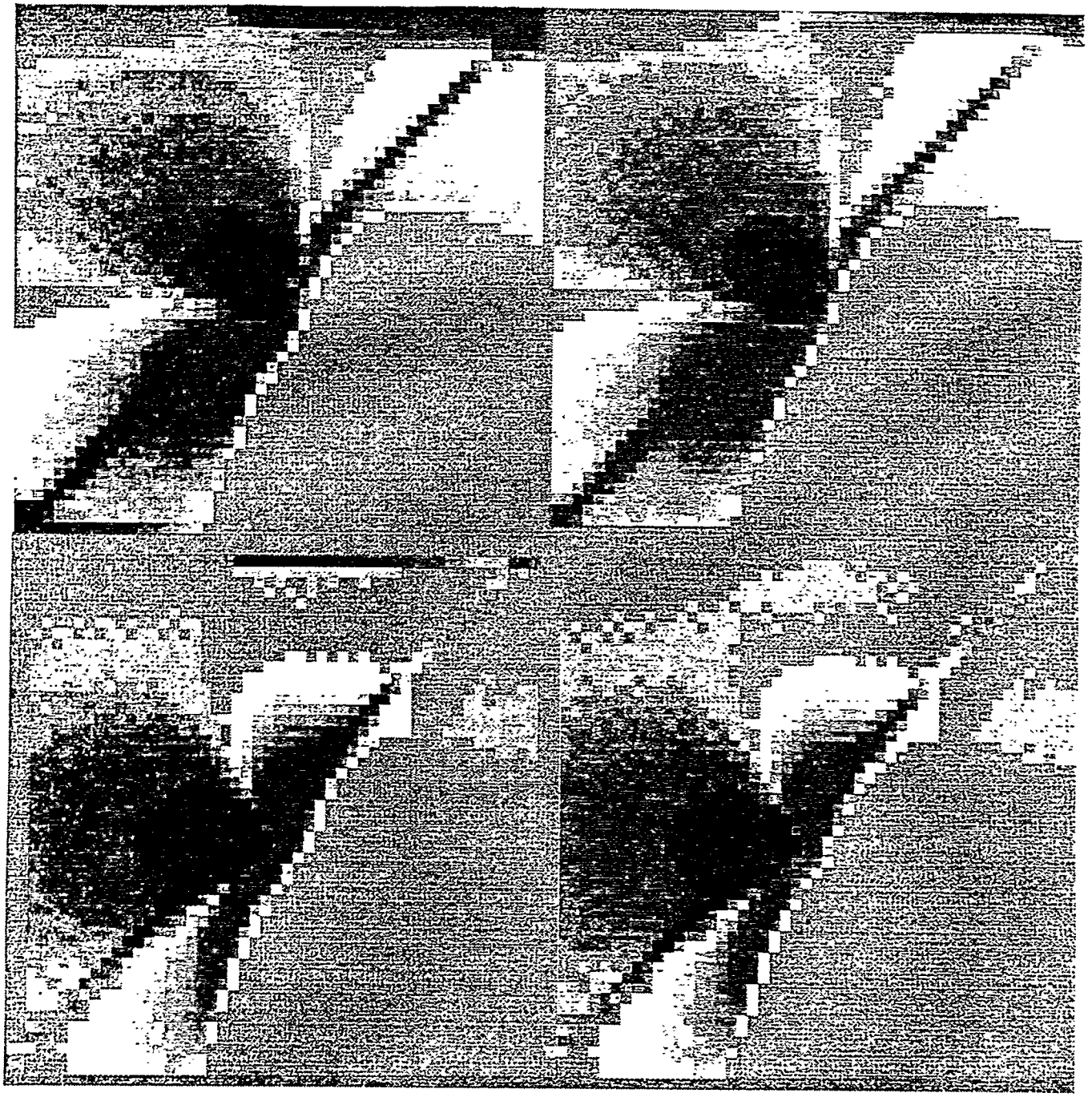

WATER HORIZONTAL VELOCITY GAS HORIZONTAL VELOCITY

Figure 6. Water and gas velocities where the permeability is enhanced along the main fault. Each cross-section is perpendicular to the fault, with the breaking faultline at the top righthand corner and the end of the fault break at the center of each diagram.

WATER VERTICAL VELOCITY GAS VERTICAL VELOCITY

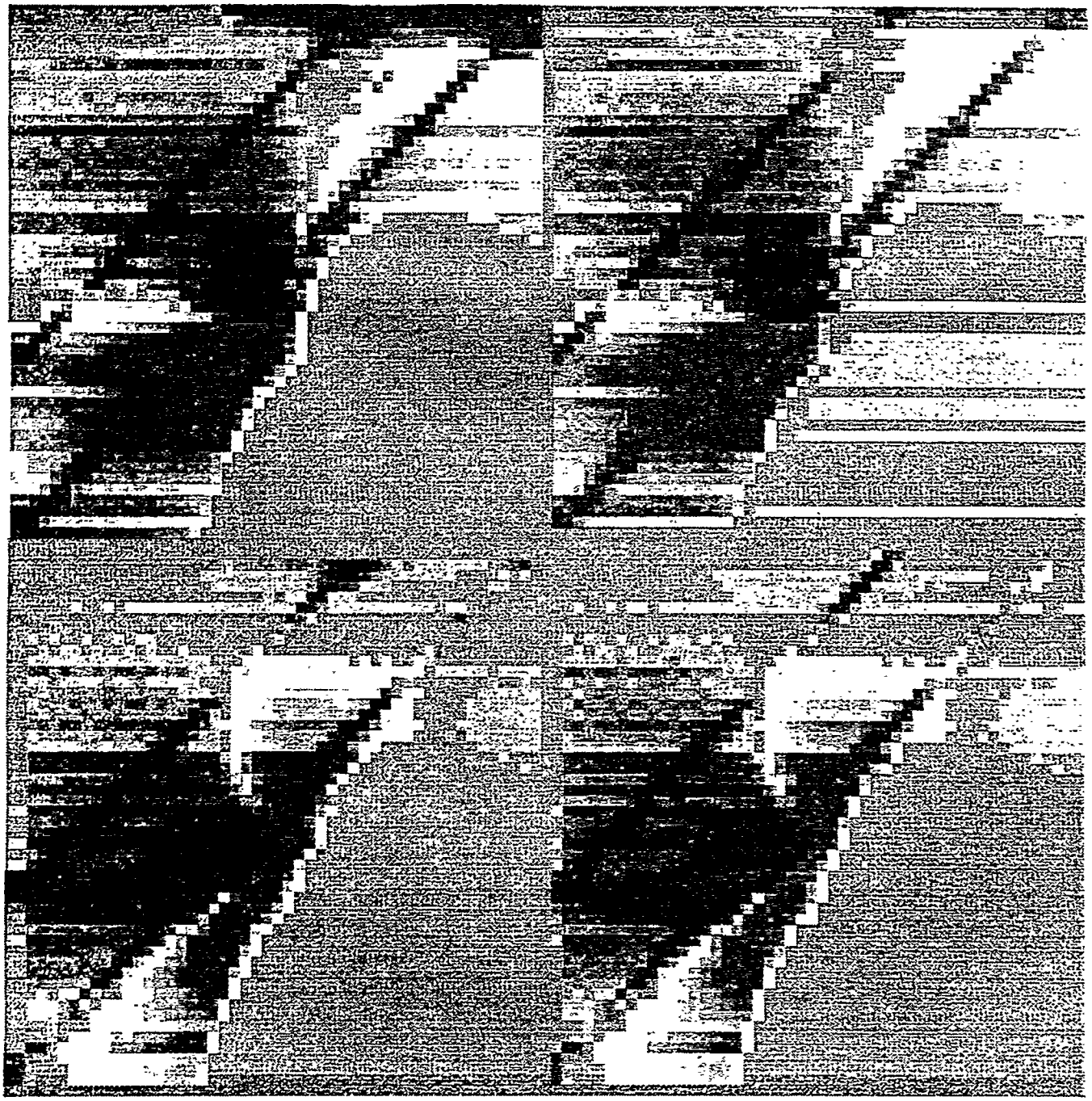

WATER HORIZONTAL VELOCITY GAS HORIZONTAL VELOCITY

Figure 7. Water and gas velocities where the permeability is enhanced along the main fault and along a parallel inactive fault. Each cross-section is 20 km deep by 20 km wide. Upward vertical motions are blue and downward motions red; leftward motions are blue and rightward motions are red.

surrounding medium with both water and gas moving up it on the hanging-wall side. Thus, we can conclude that such parallel faults concentrate the flows along these preferential conduits.

In Figure 8, we show the upward velocity, horizontal velocity and change in concentration of water flows due to our standard earthquake. In this case, we not only have the main fault and a parallel inactive fault as high permeability zones, but also allowed a simulated bed at about 3 km depth to have a similar permeability contrast with the rest of the uniform medium. We see that, as before, the faults act as preferential flow conduits and flows are also enhanced in the specific bed. The concentration changes are seen to be correlated with the flows, as expected, with increased concentration in the regions where the flows are headed and decreased concentrations in their wake. Such phenomena is well known in geology where oil, gas and water are found in traps beneath impervious rocks; and, similarly, vein deposits of minerals and metals are found adjacent to impervious country rock. A similar simulation is shown in Figure 9, where the preferential bed is about 6 km deep. The lower right hand graph shows the flow along the fault plane.

In Figure 10, we examine the effect of a random permeability component acting on top of the uniform permeability. Because the randomness is on a scale of each grid block dimension, i.e. 400 meters, no large scale effect is observed with essentialy similar flow patterns as in the uniform case. In Figure 11, however, we have restricted the random component to the vertical direction with intent to model the effect of a layered medium with differing permeabilities for each bed. We see that the same basic flow pattern is achieved but with the more permeable beds controlling the flow.

WATER VERTICAL VELOCITY WATER HORIZONTAL VELOCITY

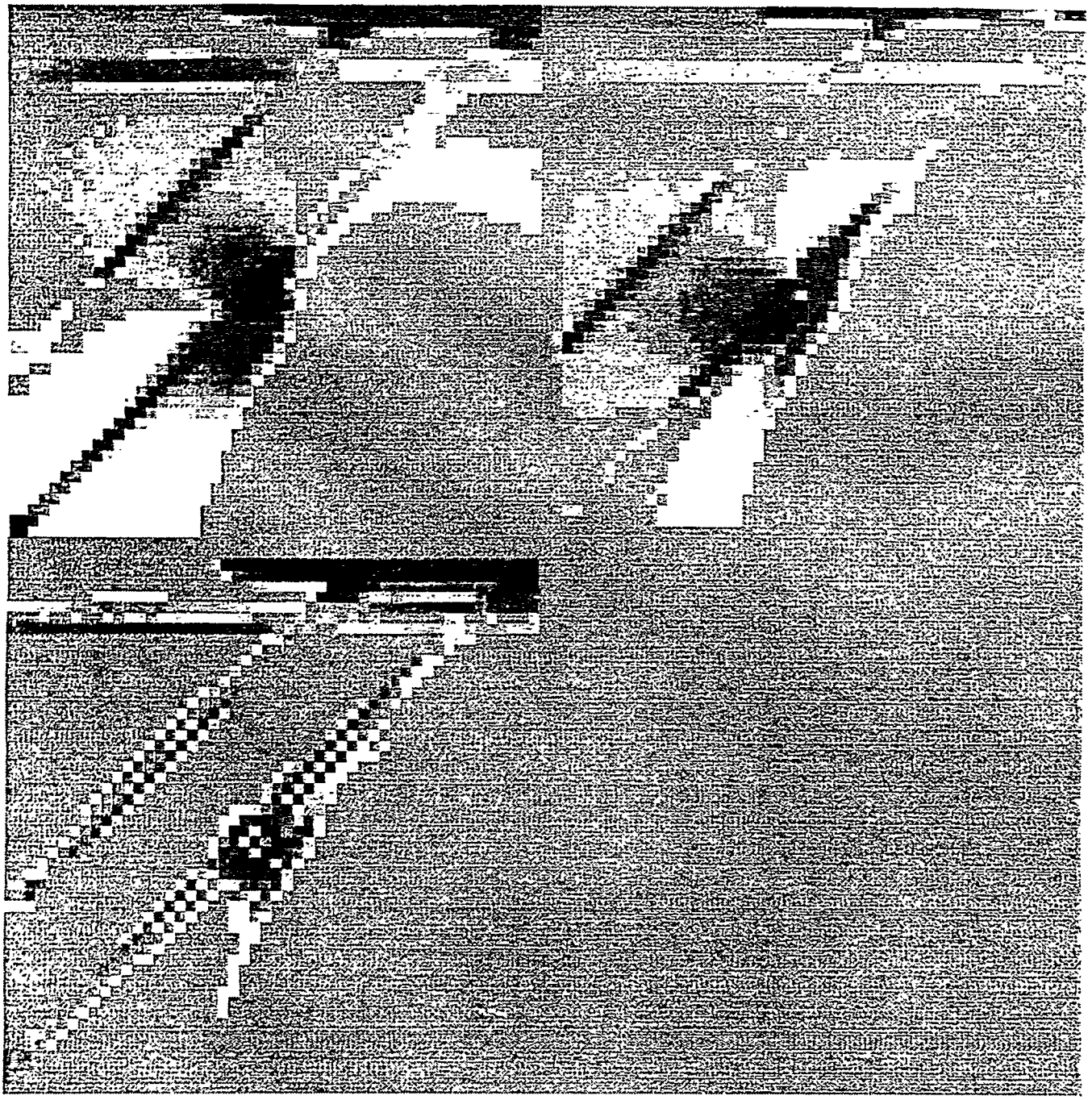

WATER CONCENTRATION CHANGES

Figure 8. Water velocities and concentration changes for the case where the permeability is enhanced along both the main fault and a parallel inactive fault, as well as along a horizontal zone at about 3 km depth. In the lower left diagram, concentration increases are red and decreases are blue.

WATER VERTICAL VELOCITY WATER HORIZONTAL VELOCITY

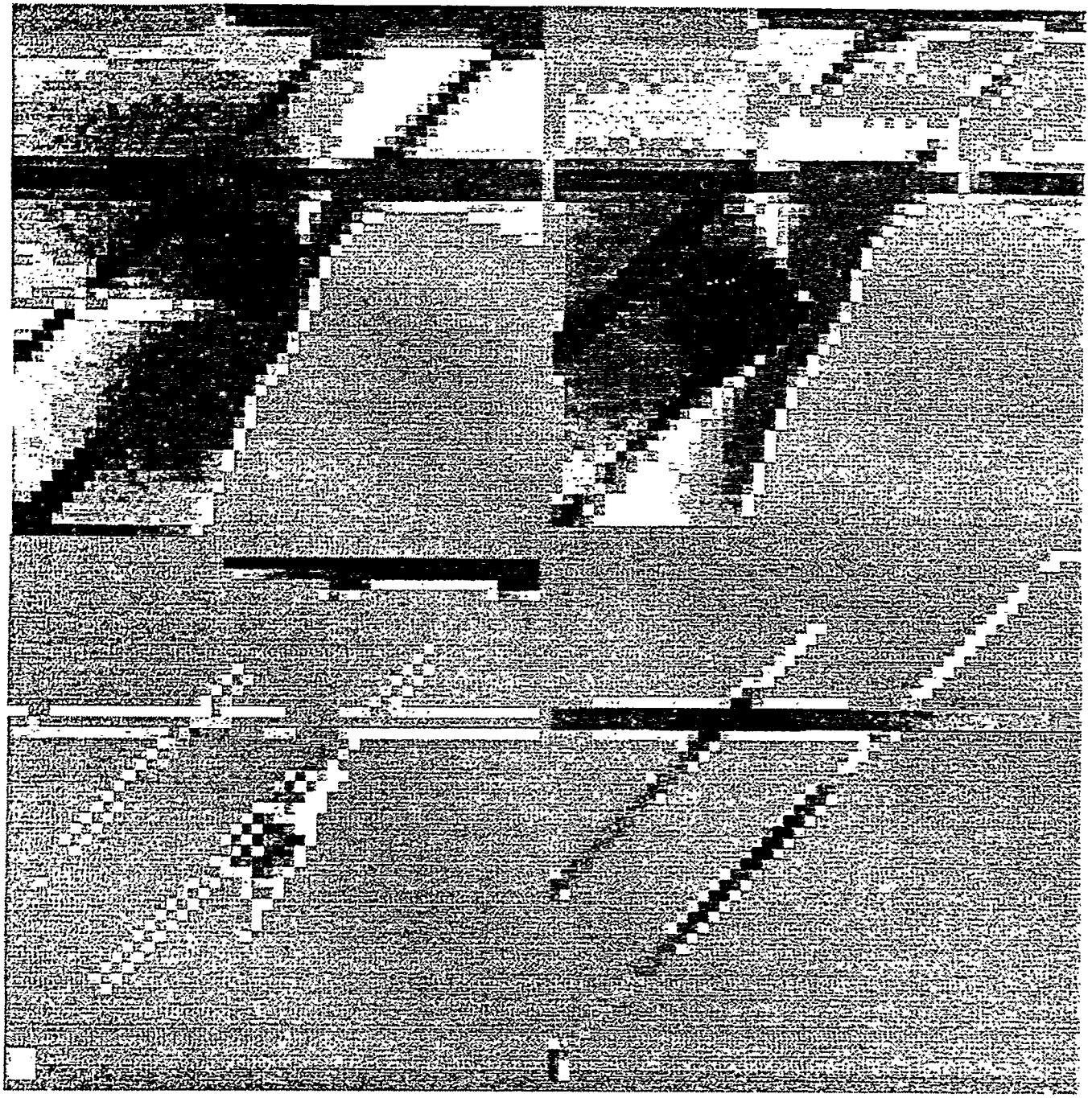

WATER CONCENTRATION CHANGES WATER VELOCITY

Figure 9. Water velocities and concentration changes for the case where the permeability is enhanced along both the main fault and a parallel inactive fault, as well as along a horizontal zone at about 6 km depth. In the lower right diagram, water is flowing into the paper along the enhanced permeability regions.

WATER VERTICAL VELOCITY GAS VERTICAL VELOCITY

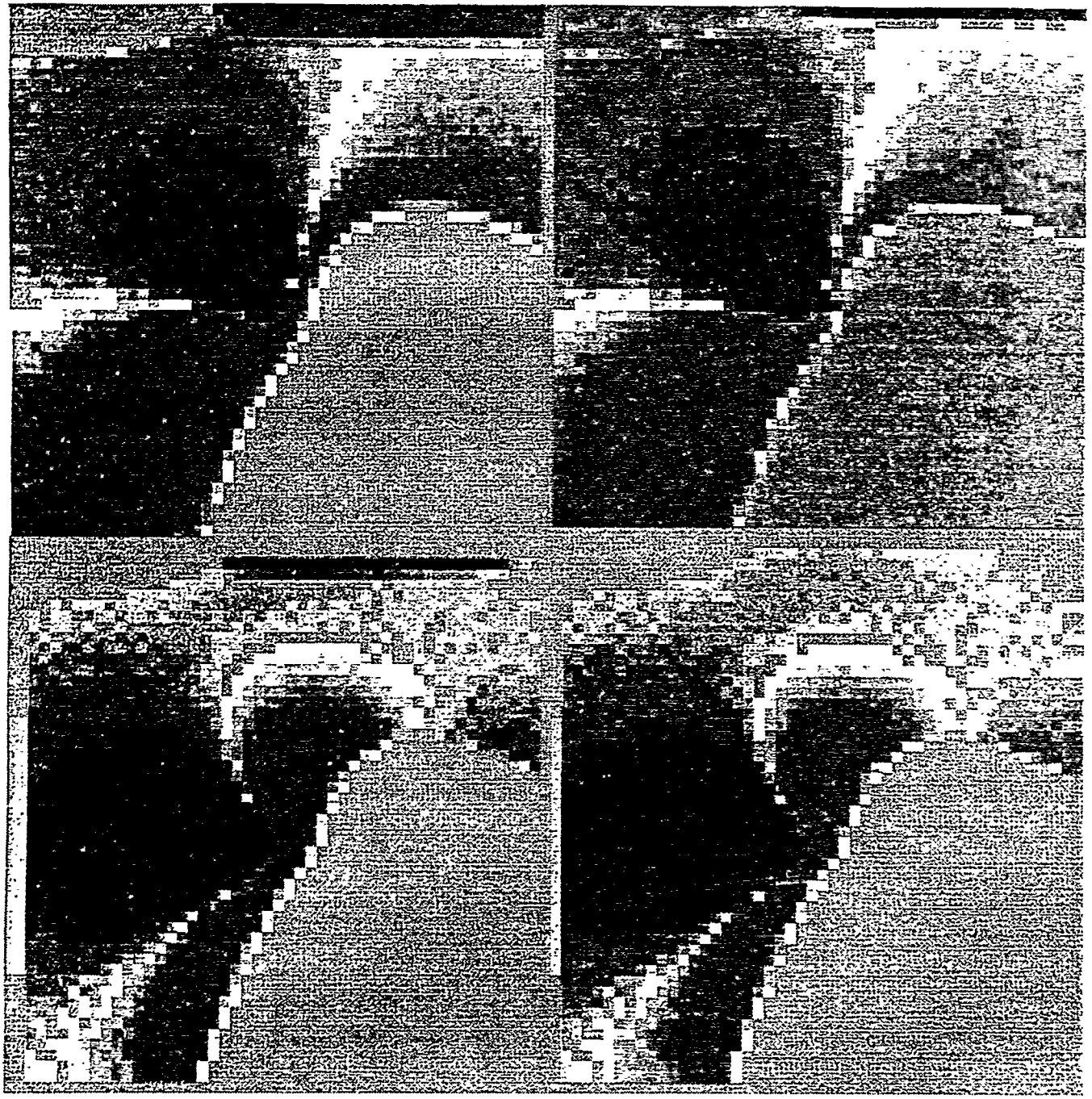

WATER HORIZONTAL VELOCITY GAS HORIZONTAL VELOCITY

Figure 10. Water and gas velocities where the permeability is random superimposed on top of the uniform permeability. Each cross-section is 20 km deep by 20 km wide. Upward vertical motions are blue and downward motions red; leftward motions are blue and rightward motions are red.

WATER VERTICAL VELOCITY GAS VERTICAL VELOCITY

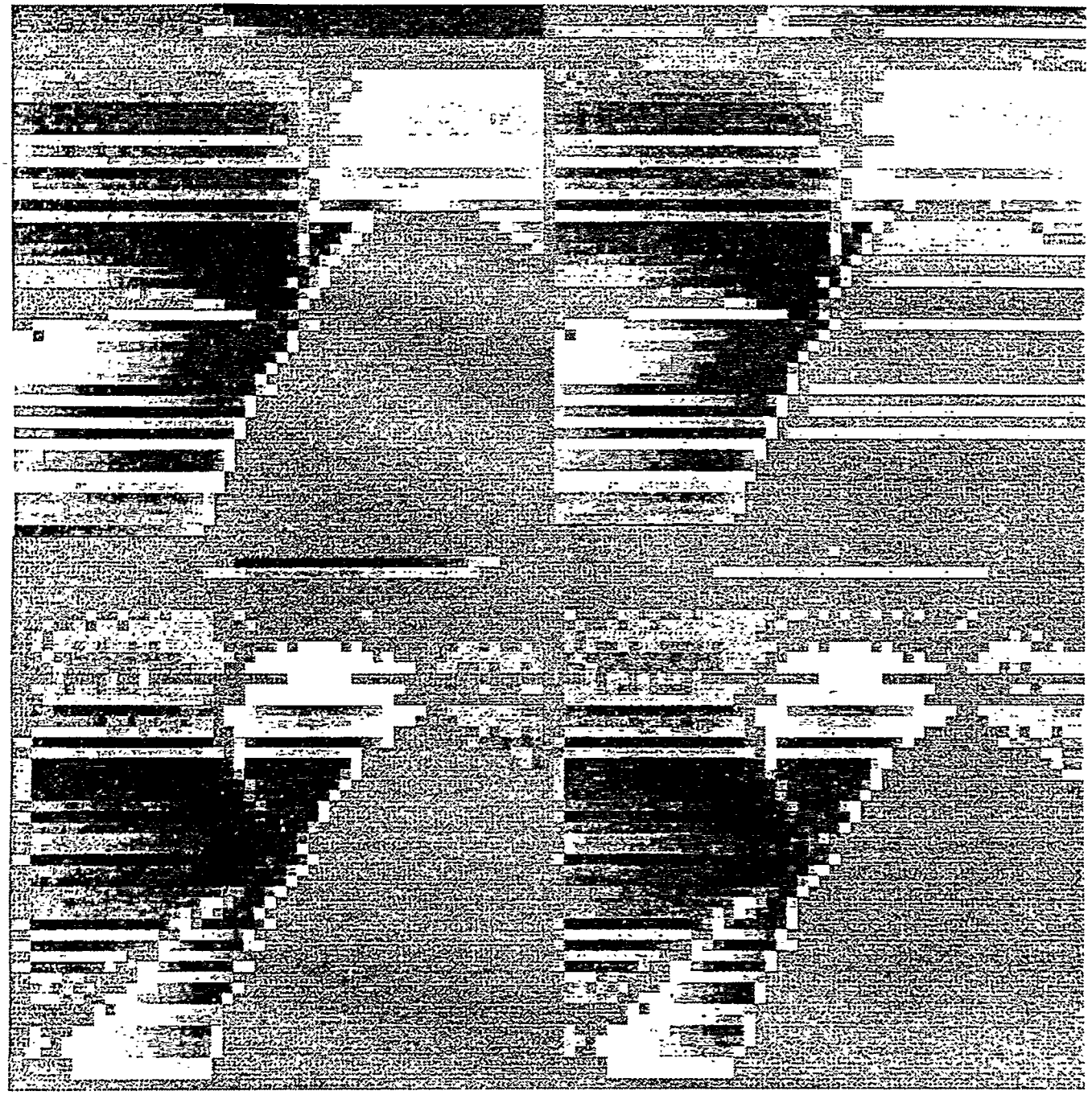

WATER HORIZONTAL VELOCITY GAS HORIZONTAL VELOCITY

Figure 11. Water and gas velocities where the permeability is vertically random on top of the uniform permeability. Each cross-section is 20 km deep by 20 km wide. Upward vertical motions are blue and downward motions red; leftward motions are blue and rightward motions are red.

WATER VERTICAL VELOCITY GAS VERTICAL VELOCITY

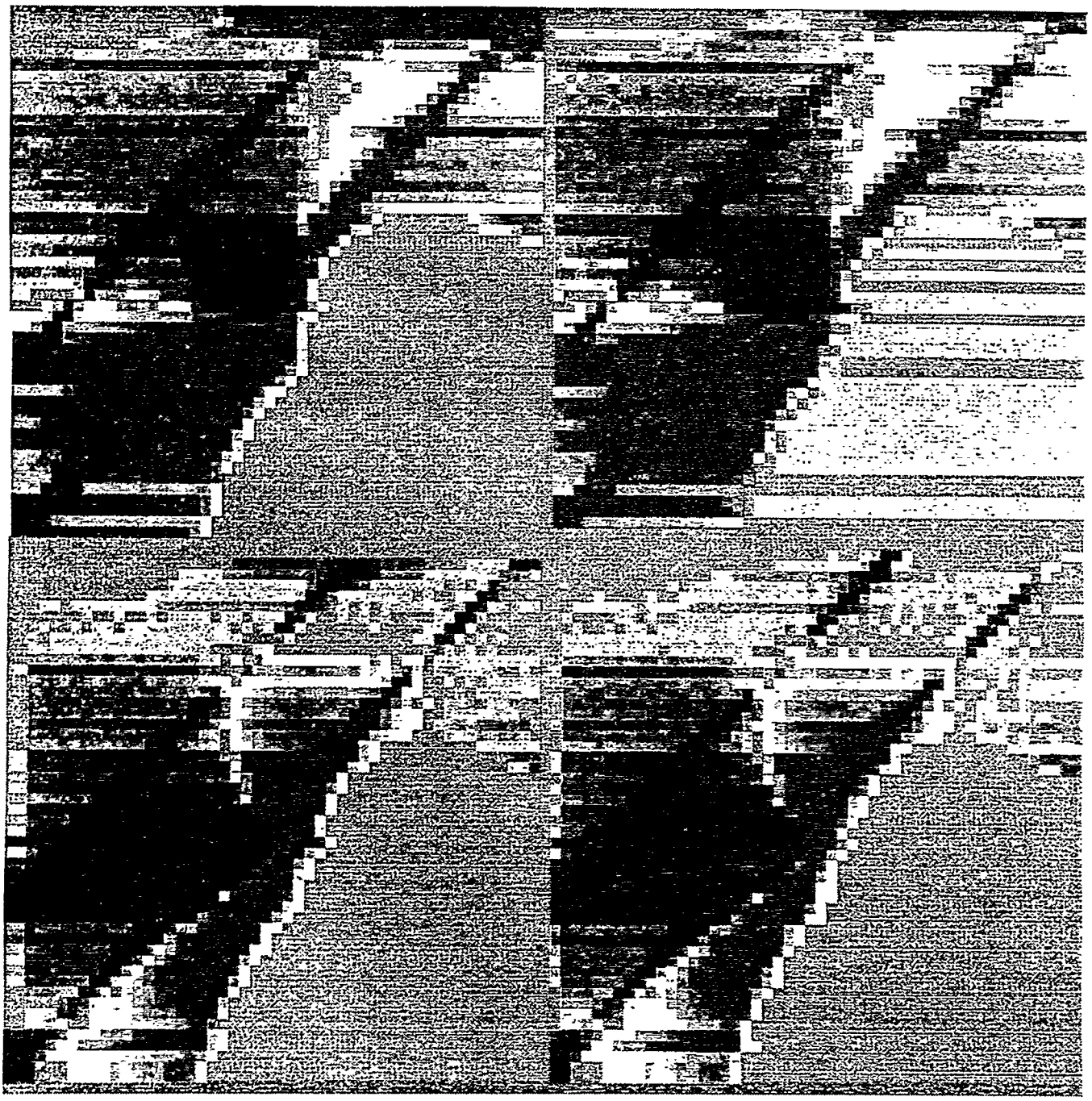

WATER HORIZONTAL VELOCITY GAS HORIZONTAL VELOCITY

Figure 12. Water and gas velocities where the permeability is vertically random on top of the uniform permeability, as well as enhanced on the main and parallel faults. Each cross-section is 20 km deep by 20 km wide. Upward vertical motions are blue and downward motions red; leftward motions are blue and rightward motions are red.

We combine these changing bed permeabilities with enhanced permabilities along the parallel faults, as shown in Figure 12. We see that the fault flows interact strongly with the more permeable beds but we retain the basic result that vertical flows are enhanced along the faults.

COMPARISON WITH OBSERVATIONS

Our simulations show that most of the water ejection occurs on the hanging wall side of the normal fault which is the side on which compressive stresses force the fluid up and away from the fault face, as demonstrated in the above simulation Figures. This phenomena has been observed in numerous cases of normal faulting, Wood and King (1991), and was well-documented at Borah Peak where, Wood (1991): "Principal groundwater effects of the Borah Peak earthquake wera in the hanging wall block within 90 km of the surface rupture."

Initial volume discharge rates were computed for water and gas components, as shown in Figures 13 and 14, for upwelling at the saturated-unsaturated zone boundary above a uniformly permeable medium. In the first minutes, these discharge rates were of the order of 1000 m^3 /(m-day), which for a 10km fault corresponds to $10^7 m^3$ /day. Assuming the flow decays exponentially with a half-life of about 10 days, expected excess flow over 6 months would be in the range of $10^8 m^3$, well within the range of the observed flows from such earthquakes. Thus our estimates of the initial flow rates are of the order expected relative to the long-term discharge rates.

From Figures 13 and 14, we see that the gas moves upward more rapidly than the water. This corresponds with the observations at Borah Peak of Waag (1991), namely:

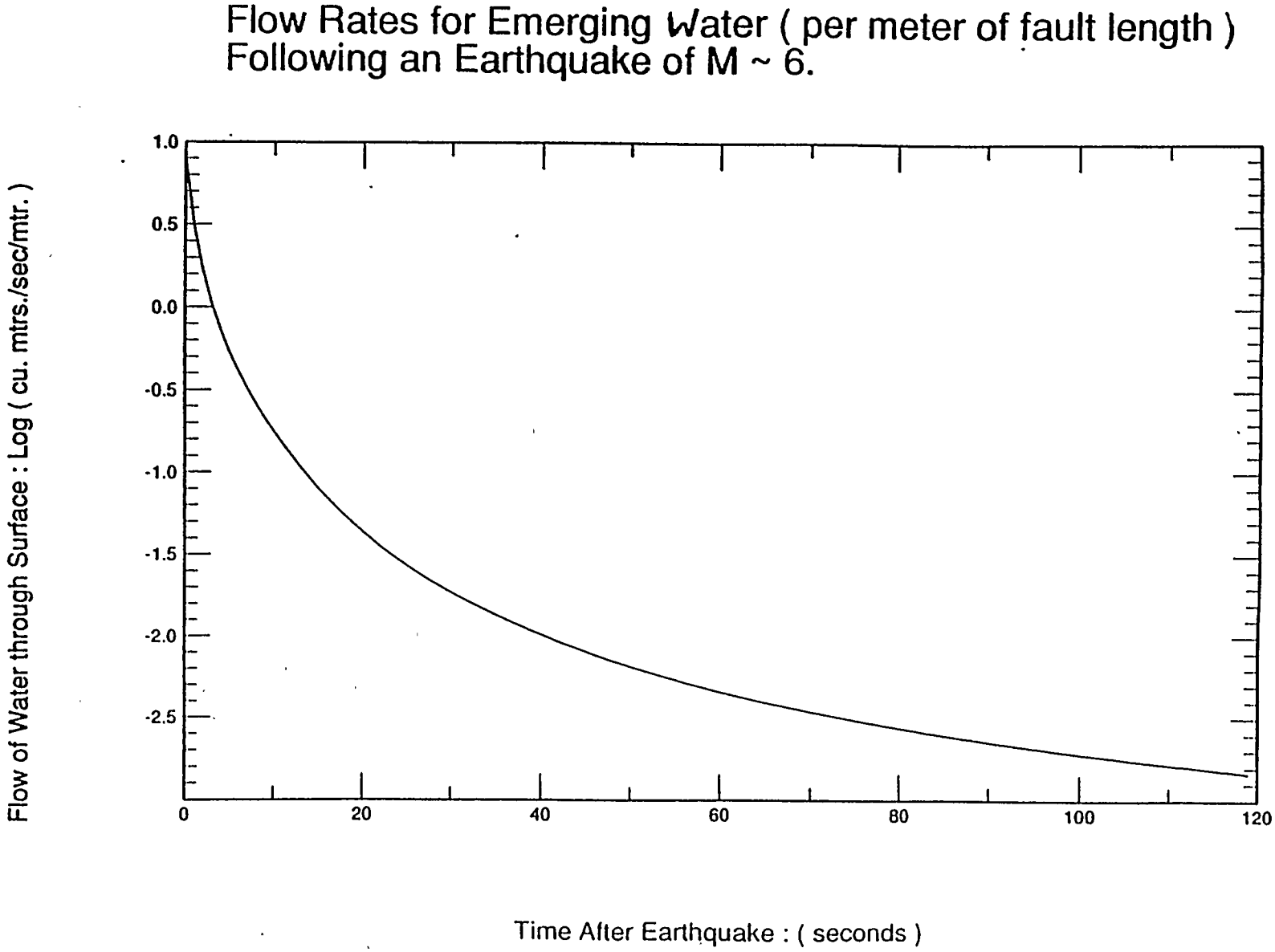

Fig. 13 - Vertical flow rate versus time for water upwelling at the saturated-unsaturated zone boundary in the vicinity of the magnitude 6 dip slip crustal earthquake illustrated in Figures 4, 5.

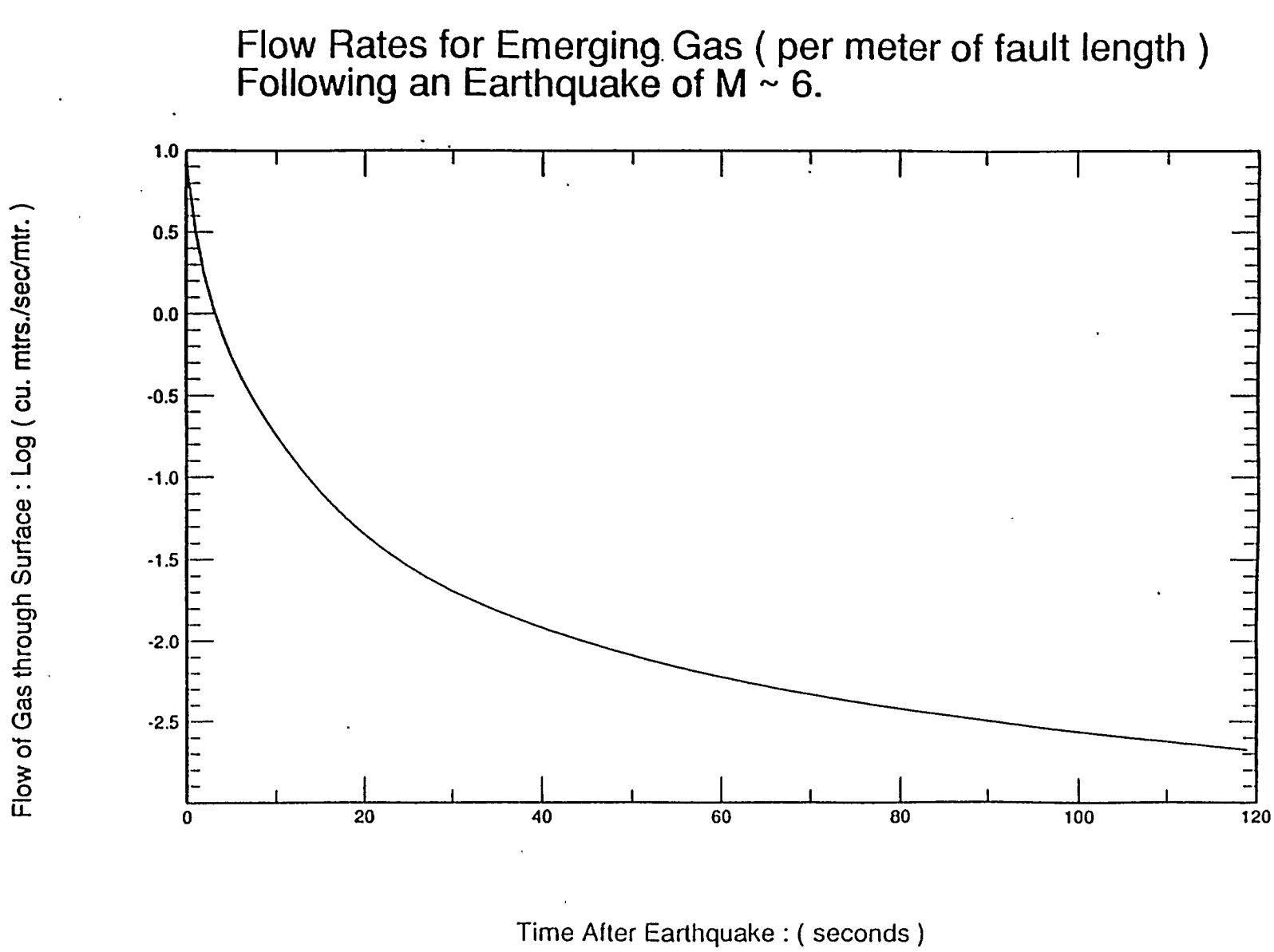

Fig. 14 - Vertical flow rate versus time for CO_2 gas at the saturated-unsaturated zone boundary for the case described in Fig. 13.

"The surge of air ahead of the migrating groundwater pressure wave caused inflation and fluidization of the alluvial confining layer. Elutriation of the fine fraction by air was followed by entrainment of the coarser sediment by waters erupting along the carbonate fracture network."

The 1983 Borah Peak, Idaho, earthquake (M7.3) caused at least a 35 meter increase in water levels about 4km away, Waag (1991), Wood (1991). Carrigan et al. (1991) have numerically developed a model with mainly uniform permeability and a porous rock matrix, and allow some flow in fractures. They concluded that the water level close to the epicenter would only rise at most 5 meters for a typical M7 earthquake. We can thus see that their model and its predictions are in direct contradiction with the above field evidence.

Our simulations show that faults can act as preferential conduits for upward flowing fluids produced by earthquake pressure changes. If the fluids are confined to motions along the open faults, we can expect a much larger rise of the water table in these faults. A simple volumetric argument shows that confined flow along the faults will rise to far greater heights than if the whole water table moves upward en-masse. Carrigan et al. used a porosity of 0.1 for the region at the water table. They claimed that for a uniformly permeable and porous medium the water table would rise about 2 meters for a magnitude 6 earthquake.

Using our fractured medium model, assume a fault every 100 meters parallel to the main fault, and with a fracture aperture of 1 mm. Then the height which the water will travel upto in the faults is given by :

Height = Fault spacing*Porosity*Water Table Rise*Percent in Faults / Fault Aperture

Using the above numbers, this relation gives a rise in the water level in the faults of 2,000 meters, even if we allow only 10% of the water to flow up the faults. Note that just 1% of water flowing up the faults would reach a level 200 meters above the present water table, and at repository depth. Carrigan et al. (1991) argue that fault apertures are much less than 1 mm at Yucca Mountain, implying even higher elevation changes expected of the water table in the faults. This simple volumetric argument for large elevation changes is even more telling at Yucca Mountain, as major fractures there are often much more than 100 meters apart.

CONCLUSIONS

Simulations allow us to comprehend the effects of these earthquake-induced flows on faulted anisotropic media. The simple uniform porous rock model is incapable of predicting the flows along fractures in Yucca Mountain geohydrological structures. Yucca Mountain geohydrology is dominated by a deep water table in volcanic tuffa beds which are cut by numerous faults. Certain zones in these tuffas and most of the fault apertures are filled with a fine-grained calcitic cement. Earthquakes have occurred in this region with the most recent being of magnitude 5.6 and at a distance of about 20 km. Earthquakes in the western U.S.A have been observed to cause fluid flows through and out of the crust of the Earth. These flows are concentrated along the faults with normal faulting producing the largest flows. An earthquake produces rapid pressure changes at and below the ground surface, thereby forcing flows of gas, water, slurries and dissolved salts. In order to examine the properties of flows produced by earthquakes, we have simulated the phenomena using computer-based model-

ing. We investigated the effects of faults and high permeability zones on the pattern of flows induced by the earthquake. We demonstrated that faults act as flow conduits to the surface and that the higher the permeability of a zone, the more the flows will concentrate there. Numerical estimates of flow rates from these simulations compared favorably with data from observed flows due to earthquakes. Simple volumetric arguments demonstrated the ease with which fluids from the deep water table could reach the surface along fault conduits, due to a typical earthquake in a geohydrological environment as found at Yucca Mountain.

REFERENCES

Bear, J., 1972. *Dynamics of Fluids in Porous Media.* Elsevier Press.

Briggs, R. C., and H. C. Troxell, 1955. *Effect of Arvin-Tehachapi Earthquake on Spring and Stream Flow.* in Earthquakes in Kern County, California. 1952. [Bulletin 171 California Division of Mines, 81.]

Carrigan, C. R., G. C. P. King, G. E. Barr, and N. E. Bixler. 1991. *Potential for Water Table Excursions Induced by Seismic Events at Yucca Mountain, Nevada.* Geology. Vol. 19, p. 1157.

Frazier, G. A., and C. M. Petersen. 1974. 3-D Stress Wave Code for the Illiac IV. SSS Final Report to Defense Nuclear Agency.

Jones, C., 1915. *The Pleasant Valley, Nevada, Earthquake of October 2, 1915.* Bulletin of the Seismological Society of America. Vol. 5, p. 190.

Oran, E. S., and J. P. Boris, 1987. *Numerical Simulation of Reactive Flow.* Elsevier Press, New York.

Stewart, H. B., and B. Wendroff, 1984. Two-Phase Flow: *Models and Methods.* Journal of Computational Physics. Vol. 56, p. 363.

Szymanski, J. S., 1989. *Conceptual Considerations of the Yucca Mountain Groundwater System with Special Emphasis on the Adequacy of the System to Accommodate a High-Level Nuclear Waste Repository.* DOE Internal Report, Las Vegas, Nevada.

Wagg, C. J., 1991. *Groundwater Eruptions and Sediment Boil Formation Attendant to the Borah Peak, Idaho, Earthquake.* [Invited paper. AGU Spring Meeting Transactions] EOS. Vol. 72, #17.

Wagg, C. J., and T. G. Lane, 1985. *The Borah Peak, Idaho Earthquake of October 28, 1983 - Structural Control of Groundwater Eruptions and Sediment Boil Formation in the Chilly Buttes Area.* Earthquake Spectra. Vol. 2, p. 151.

Wood, R. M., and G. D. P. King, 1991. *Hydrological Signatures of Earthquake Strain.* Submitted to Journal of Geophysical Research.

Wood, S. H., 1991. *Observations and Subsequent History of Spectacular Grounwater Flows and Aquifer Pressure Increases: 1983 Borah Peak and 1957 Hebgen Lake Earthquakes..* [Invited paper. AGU Spring Meeting Transactions] EOS. Vol. 72, #17.

Zones, C. P., 1957. *Changes in Hydrologic Conditions in the Dixie Valley and Faiview Valley areas, Nevada, after the Earthquake of December 16, 1954.* Bulletin of the Seismological Society of America. Vol. 47, p. 387.